Chemistry of rocky exoplanet atmospheres : towards a better understanding of gas and haze observables in the era of JWST

Thomas Drant

München 2024

Chemistry of rocky exoplanet atmospheres : towards a better understanding of gas and haze observables in the era of JWST

Thomas Drant

Dissertation
an der Fakultät für Physik
der Ludwig-Maximilians-Universität
München

vorgelegt von
Thomas Drant
aus Neuilly-sur-Marne (93, France)

München, den 22.07.2024

Erstgutacher: Prof. Dr. Kevin Heng
Zweitgutachter/in: Prof. Dr. Nathalie Carrasco
Tag der mündlichen Prüfung: 01.10.2024

Summary

Key words : exoplanet atmospheres, chemistry, aerosols, atmospheric modelling, laboratory experiments

In december 2021, the James Webb Space Telescope (JWST) was launched marking the beginning of an active decade of research focusing on the characterization of exoplanet atmospheres. The first observations of JWST already suggest the detection of simple species (CO_2, CH_4 and H_2O) and aerosols in rocky exoplanet atmospheres. These observables hold crucial information on the chemical processes occurring in the atmosphere. Their detection and the quantification of their abundances can help constrain important properties of the atmosphere, its origin and the conditions found at the surface. In this thesis, I focus on three types of observables providing different information on rocky exoplanet atmospheres: gaseous photochemical products in habitable worlds, photochemical hazes with a focus on their intrinsic optical properties, and simple volatiles tracing properties of the rocky interior in warm and non-habitable environments. Using laboratory experiments and theoretical modelling, I studied these different observables to better understand the information they can provide and to improve future interpretation of JWST data. For photochemical products in habitable worlds, I assessed the formation of water vapor by photochemistry in the upper atmosphere, above the cloud cover, and its correlation to the presence of volcanic H_2. For warmer rocky exoplanet atmospheres, I used modelling combining geochemical outgassing, atmospheric chemistry and radiative transfer to assess the correlation between the observed relative molecular abundances of volatiles in the atmosphere (e.g. CO_2/CO) and the interior redox state of the planet. To understand the extinction caused by photochemical hazes in exoplanet atmospheres, I focused on the influence of the particle's composition by deriving the refractive indices of laboratory analogues. I assessed the impact of the optical technique, gas composition and experimental conditions (irradiation, temperature, residence time of the gas) on these refractive indices.

Acknowledgements

This PhD thesis would not have been possible without all the fruitful collaborations and support by family and friends.

I first want to thank the entire team at USM in Munich where I spent most of my PhD. I want to thank the fellow PhD students Aline Novais, Anna Lueber and Can Akin for the great times we had in Munich and during conferences. I also want to thank Meng, Leo, David, Alex, Louise and Surya. I will keep great memories of this time in Munich. This group and the team spirit is fantastic ! I hope I will see you soon, hopefully for a pizza day :) and that we will keep working together in the future.

I want to thank Enrique Garcia-Caurel who kindly worked with me all throughout my PhD and peaked my interest in the world of ellipsometry. I am very happy that we got to work together and I am very grateful for everything you taught me ! It really motivated me to push this work even further and expand it with other collaborations. I hope we will keep working together on other fascinating projects. I want to thank Ella Sciamma-O'brien for joining an ambitious collaboration despite the distance and time difference. Of course, I need to thank Ludovic Vettier for his help all throughout my PhD. There is no Atmosim group without Ludo ! I want to thank Meng and Kevin for the very interesting and productive discussions we had on geochemical outgassing and atmospheric chemistry. I am looking forward to working with both of you on a more experimental project :)

I want to thank the entire NASA Ames group and more specifically Ella, Diane Wooden and Ted Roush, for starting with me a very interesting collaboration and participating to fruitful discussions. I want to thank Ella and Zoé Perrin for their presence and help during the different runs at synchrotron SOLEIL. These were very great experiences despite sometimes the measurements that don't want to work and the brazing cold during winter :) I want to thank Jean-Blaise Brubach and his entire team at the Ailes beamline of synchrotron SOLEIL for welcoming us every time and making our aim possible. I want to thank Zoé Perrin for partnering with me in the challenge of Mueller ellipsometry. I'm very happy that this great endevour ended with great results and taught us a lot on this topic.

I want to thank again Kevin Heng for his implication in my PhD project and organizing a team spirit at USM that taught me a lot and helped me see the bigger picture for my future research in the field. Our discussions taught me a lot about the construction of a scientific question and reasoning to approach a problem in our field. These lessons will stay with me throughout my future career. I want to thank Nathalie Carrasco for making this PhD possible and smooth despite the challenges faced with this cotutelle. I want to thank Nathalie for her help and suggestions during the writing of this thesis.

Je souhaite remercier toute ma famille pour leur soutain pendant ces trois ans de thèse ! En échange, vous avez bénéficier d'un cool séjour pour découvrir la cuture bavaroise ! Je tiens à remercier mes amis et ce super séjour en Espagne qui m'a permit de faire une pause nécessaire pendant cette rédaction. Et merci au soutien de ceux aussi en rédaction de thèse, toujours agréable d'être à plusieurs dans cette épreuve :)

Contents

Page No.

0.1 Objectifs de la thèse

Pendant ces trois années de thèse, j'ai étudié en détail les différents observables permettant de caractériser les atmosphères d'exoplanètes rocheuses actuellement en cours avec le télescope spatial James Webb (JWST) lancé en 2021. Pour ce faire, j'ai utilisé à la fois une approche expérimentale pour étudier la photochimie en phase gaz et les propriétés optiques des aérosols organiques atmosphériques. J'ai également utilisé une approche de modélisation visant à évaluer le rôle de la photochimie et de la thermochimie pour mieux comprendre l'évolution chimique des atmosphères dans différentes conditions mais aussi pour mieux comprendre les informations que les observables atmosphériques peuvent fournir sur les conditions d'habitabilité et les propriétés de l'intérieur planétaire.

Le JWST, avec sa large couverture spectrale allant de 0.8 à 28 μm, permet maintenant de caractériser la présence d'espèces atmosphériques abondantes telles que le CO_2, CH_4 ou encore SO_2 avec également une meilleure observation des signatures d'aérosols atmosphériques comme récemment avec le SiO_2. A partir des données acquises avec le JWST, un certain nombre de propriétés atmosphériques peut être contraint, comme par exemple les abondances moléculaires des espèces majoritaires, la température atmosphérique ou encore la taille de particules atmosphériques. L'objectif principal est de pouvoir interpréter ces observables JWST de manière à déduire les mécanismes physico-chimiques ayant lieu dans l'atmosphère et le lien potentiel avec les propriétés de surface (géologique et biologique notamment). Visant à améliorer notre compréhension des observables atmosphériques et leur lien aux mécanismes physico-chimiques ayant lieu dans l'atmosphère, j'ai utilisé à la fois du modèle numérique et des expériences en laboratoire pour étudier les aérosols organiques atmosphériques et leur propriétés optiques mais également les signatures gazeuses liées à la photochimie et à la thermochimie.

0.2 Projet 1 : importance des signatures photochimiques pour caractériser les mondes habitables

Le premier projet détaillé dans ce manuscrit de thèse a pour objectif de mieux comprendre l'impact de la photochimie sur les observables des exoplanètes rocheuses en zone hab-

itable. Avec cette notion de mondes habitables, on vise les exoplanètes localisées à une distance de leur étoile menant à une température de surface proche de celle de la Terre actuelle et permettant d'avoir de l'eau liquide stable à la surface. La distance à l'étoile est en effet un critère essentiel pour la notion d'habitabilité. La composition des atmosphères de ces planètes est principalement affectée par les cycles géochimiques comme le cycle du carbone sur Terre mais également par la photochimie permettant sur Terre la formation d'ozone et d'autres espèces traces azotées. La photochimie décrit l'ensemble des réactions chimiques liées à l'interaction avec le rayonnement UV de l'étoile. Ce rayonnement énergétique permet en effet de dissocier les molécules de l'atmosphère et d'en créer de nouvelles par réactions chimiques. Comme les observations JWST sondent en général les hautes couches de l'atmosphère où la photochimie est importante, ce processus chimique devient crucial pour comprendre les observables et fournir des informations sur l'habitabilité à la surface à travers la composition atmosphérique.

Pour ce projet, je me suis particulièrement intéressé aux atmosphères dominées par du CO_2 avec de forte concentration d'hydrogène moléculaire H_2 expliquée par un fort dégazage volcanique. Ces objets sont intéressants pour la notion d'habitabilité car la collision entre CO_2 et H_2 mène à un chauffage climatique permettant d'assurer des températures habitables à la surface. Ce scénario a été suggéré pour expliquer la formation de fleuves et rivières à la surface de Mars ancien (il y a 3.8 Ga) et il est important à considérer dans notre définition de la zone habitable. L'effet photochimique reste cependant peu étudié et pourrait révéler de nouveaux observables importants pour les observations de ces mondes avec le JWST.

Pour étudier les produits photochimiques formés dans une atmosphère CO_2-H_2, j'ai tout d'abord utilisé une approche expérimentale avec le réacteur photochimique APSIS (atmospheric chemistry simulated by surfatron) disposé au LATMOS. Pendant ces expériences, un mélange de CO_2-H_2 est injecté dans une chambre à basse pression (1 hPa) et un système énergétique (surfatron) va irradier ce mélange dans l'UV (à 105 nm) de manière à simuler la photochimie des hautes atmosphères planétaires et à former les produits photochimiques attendus. En utilisant de la spectrométrie de masse, j'ai étudié en détail le système chimique et j'ai pu identifier les principaux produits photochimiques

: CO, O_2 et H_2O. Ces expériences ont permis de mettre en avant un processus menant à une production significative d'eau à partir de ce mélange initialement sec. Ce mécanisme est important pour deux raisons. Tout d'abord, cela met en évidence un nouveau processus permettant la formation d'eau dans un monde habitable suggérant que de l'eau peut être produit dans l'atmosphère même par des voies photochimiques. Également, la production d'eau dans la haute atmosphère devient un nouvel observable prometteur car l'eau est généralement séquestré dans les basses couches de l'atmosphère en raison de la condensation, ce qui empêche l'observation des signatures avec le JWST.

De manière à expliquer le mécanisme menant à cette formation d'eau dans la haute atmosphère, j'ai utilisé un modèle visant à reproduire nos conditions expérimentales. Pour cela, j'ai développé la base de données des réactions chimiques pour ajouter les réactions importantes pour notre système. J'ai pu ainsi montrer que la formation d'eau passe par l'oxydation de l'hydrogène moléculaire, possible grâce à la photo-dissociation du CO_2. Ainsi, le H_2 est consommé directement sans être photo-dissocié grâce à la photolyse du CO_2. On a bien ici un puits de H_2, autre que l'échappement atmosphérique, qui permet sa destruction dans l'atmosphère.

Pour étudier l'impact de ce processus sur la formation d'eau dans les atmosphères d'objets connus, j'ai utilisé un modèle atmosphérique 1D en fixant les conditions attendues pour Mars ancien et pour une exoplanète habitable comme Trappist-1e. J'ai montré que pour une atmosphère riche en H_2 comme Mars ancien, la formation photochimique d'eau est extrêmement forte menant à des taux atteignant la saturation très rapidement. Autrement dit, la photochimie du CO_2-H_2 permet de produire de l'eau liquide ce qui a certainement contribué à l'inventaire en eau à la surface de Mars ancien. Pour les exoplanètes, ce mécanisme chimique permet de maintenir une atmosphère oxydante favorisant la stabilité du CO_2 sur le long terme. De plus, cette production d'eau est directement lié à l'abondance de H_2 présente dans l'atmosphère. Autrement dit, si on peut caractériser ce mécanisme, on peut déduire la quantité de H_2 présente dans l'atmosphère malgré le fait de ne pas pouvoir l'observer directement avec le JWST. J'ai pu ainsi faire des simulations d'observations en transit pour un cas Trappist-1e de manière à mettre en évidence les signatures spectrales liées à la photochimie. J'ai

montré que entre 5.5 et 7 microns, l'eau absorbe ce qui permet de mettre en évidence ce processus de manière claire. Avec des observations de qualité dans le futur, on sera ainsi capable de caractériser ce mécanisme et de mettre en évidence la présence de H_2 et donc de mettre sur la table des hypothèses pour expliquer sa présence, notamment le fait que la planète est active d'un point de vue volcanique.

0.3 Projet 2 : observation des atmosphères d'exoplanètes rocheuses pour contraindre l'état redox des intérieurs

Dans ce second projet, je m'intéresse à des objets plus chauds et donc plus faciles à observer car ils sont proches de leur étoile. La plupart des exoplanètes rocheuses confirmées et observées par le JWST ont des températures entre 400 et 1500K, et ne sont donc pas considérées habitables. Ces objets sont intéressants car aucun condensat n'est prédit dans ces conditions donc il n'y a pas d'effet de nuages attendu dans les spectres du JWST mais également la composition ne devrait pas être affectée par des processus géologiques (géochimiques) complexes comme le cycle du carbone. Autrement dit, la composition atmosphérique est contrôlée par l'équilibre entre le dégazage volcanique, la chimie atmosphérique et l'échappement atmosphérique. Les observations par le JWST peuvent donc permettre de contraindre, grâce à la composition de l'atmosphère, les propriétés de l'intérieur planétaire contrôlant le dégazage.

En effet, la théorie prédit que l'état redox de l'intérieur planétaire devrait être très variable pour les différentes exoplanètes rocheuses en raison des variations en masses mais également en raison des variations en compositions rocheuses suggérées par les observations stellaires mettant en évidence une large gamme de possible rapports pour Si/Mg ou encore Fe/Mg. Ces propriétés contrôlent la fugacité d'oxygène (fo_2) qui quantifie la quantité d'oxygène dans le magma mais surtout l'état redox des éléments composant le magma, avec principalement le fer Fe qui peut avoir une forme réduite (Fe^{2+}) ou oxydée (Fe^{3+}). Ce fo_2 est le facteur principal influençant la composition de l'atmosphère dégazée. Ainsi, si on arrive à contraindre les abondances moléculaires des espèces atmosphériques à partir des observations JWST, on peut déduire également les propriétés redox de l'intérieur planétaire et principalement quantifier le fo_2.

Pour ce projet, j'ai utilisé une approche numérique avec modélisation incluant dégazage volcanique, chimie atmosphérique et transfert radiatif (climat). Mes simulations ont montré une forte importance du couplage chimie-climat ce qui m'a motivé à coupler des modèles existants (VULCAN, HELIOS). Pour ces simulations, mon objectif était de mettre en avant les processus chimiques atmosphériques pouvant modifier le fo_2 contrôlé par le dégazage. Vu la variabilité de conditions possibles pour les exoplanètes rocheuses, j'ai exploré l'espace des possibilités en terme de fugacité d'oxygène et pression atmosphérique de surface pour garder une vision large sur l'impact de ces mécanismes affectant la chimie atmosphérique et donc la composition observée par le JWST. L'objectif principal est de mettre en évidence une corrélation claire entre les abondances moléculaires relatives observées dans l'atmosphère et la fugacité d'oxygène du magma. CO_2/CO a été clairement identifié comme étant le traceur le plus fiable permettant de contraindre le fo_2 du magma. Avec mes simulations, j'ai évalué la fiabilité de ce traceur lorsqu'on ajoute la chimie atmosphérique en considérant à la fois la photochimie et la thermochimie.

Avec des simulations 0D, j'ai évalué l'effet du refroidissement atmosphérique. En effet, lorsque le gaz est dégazé de l'intérieur (température du magma), il va se refroidir dans l'atmosphère ce qui entraîne un changement de composition par thermochimie. Mes simulations ont montré que le rapport CO_2/CO peut varier de deux ordres de grandeur si la différence de température entre magma et atmosphère atteint les 1000K. Ce processus de refroidissement atmosphérique permet également de produire du CH_4 de manière abondante dans des conditions réduites (basse fugacité d'oxygène fo_2). En effet, à bas fo_2, l'atmosphère générée sera riche en H_2 et CO, ces deux molécules vont se transformer en méthane à plus basse température dans l'atmosphère. Je met en avant aussi les temps caractéristiques de ce processus qui peut être très rapide, de l'ordre de quelques secondes à quelques années en fonction de la température atmosphérique et du fo_2. Il existe donc des conditions où CO, CH_4 et CO_2 doivent coexister à fortes abondances ce qui pourrait être déduit des observations du JWST et permettre de contraindre efficacement le fo_2.

Avec les simulations 1D, je prend en compte aussi le transport atmosphérique et la photochimie. Je montre que l'effet du transport (vertical) atmosphérique peut faire varier le CO_2/CO d'un facteur 2 à 3 ce qui correspond à un biais sur le fo_2 d'un ordre de grandeur. La photochimie en revanche peut avoir un effet significatif. En effet, la composition atmosphérique dégazée soumise à l'irradiation de l'étoile va tendre à consommer le CO par la photolyse de l'eau et donc produire du CO_2. Cela peut faire varier le rapport CO_2/CO de deux ordres de grandeur sur de longues durées, à l'exception que l'atmosphère soit régénérée de manière continu et rapide par le dégazage. Avec l'effet climatique, je montre que la production de méthane par thermochimie va aussi agir sur le climat et créer un couplage entre les deux mécanismes. Le refroidissement atmosphérique tend à produire du méthane mais ce dernier étant un puissant gaz à effet de serre va tendre à augmenter la température atmosphérique. Ce couplage va limiter l'accumulation de méthane dans l'atmosphère ce qui aura un impact significatif sur les observations. Dans les cas où la production de méthane est importante, je suggère l'utilisation du rapport CO_2/CH_4 pour contraindre le fo_2 au lieu du rapport CO_2/CO. En effet le méthane est plus facilement détectable sur les spectres du JWST en comparaison au CO. Je montre enfin que dans les cas à haut fo_2, les spectres du JWST devraient être dominés par le CO_2 et l'eau avec une contribution très faible du CO ce qui rend la quantification du fo_2 difficile.

0.4 Projet 3 : propriétés optiques des aérosols organiques atmosphériques

En présence de molécules réduites comme le H_2 ou le CH_4, leur photo-dissociation va engendrer une chimie organique complexe qui va éventuellement mener à la formation de particules solides dans l'atmosphère. Ces aérosols organiques, aussi appelés brumes photochimiques, ont un impact significatif sur le climat car ils vont chauffer la haute atmosphère et refroidir la basse atmosphère de manière plus ou moins importante en fonction de leur propriétés optiques. Leur composition, variant fortement avec la température, l'irradiation et la composition atmosphérique, a un effet important qui reste peu compris. Pour ce projet, j'ai utilisé une approche expérimentale visant à produire des analogues de ces aérosols en laboratoire pour déterminer leur propriétés optiques. L'objectif prin-

cipal de ce projet est d'évaluer l'impact de la composition gazeuse, l'irradiation et la température sur les indices optiques des analogues produits. Par indices optiques, on parle de l'indice de réfraction complexe N = n+ik, avec n l'indice de réfraction quantifiant la dispersion de la lumière et k le coefficient d'extinction quantifiant l'absorption.

Avec l'expérience PAMPRE (production d'aérosols en micro-gravité avec plasma réactif) disposé au LATMOS, j'ai commencé par produire des échantillons analogues aux exoplanètes et à la Terre primitive avec différents ratio CO_2/CH_4. J'ai utilisé différentes techniques de mesures et d'analyses pour pouvoir déterminer les indices optiques dans une large gamme spectrale allant de l'UV au lointain IR de manière à couvrir la gamme du JWST. Les données obtenues par les études précédentes, principalement pour les analogues des aérosols de Titan, sont basées sur des techniques de mesures optiques différentes qui peuvent engendrer des biais sur les résultats. Pour ma première étude sur les indices optiques, je compare notamment la sensibilité des deux techniques de mesures principales : l'ellipsometrie et la spectrophotométrie. J'ai observé que la spectroscopie en transmission est généralement plus précise que l'ellipsométrie en réflexion qui est très sensible à la focalisation du faisceau mais aussi à la dégénérescence des paramètres fittés dans l'analyse des données. Pour ces raisons, je suggère une approche efficace utilisant les mesures en transmission dans une large gamme pour déduire les indices optiques. Je montre également que les échantillons analogues pour la Terre primitive deviennent de plus en plus absorbants dans l'infrarouge lorsqu'on augmente le rapport CO_2/CH_4.

Les indices optiques de ces aérosols atmosphériques dépendent de leur composition et donc des conditions de production incluant la température, l'irradiation et la composition atmosphérique. Vu que les études précédentes compilent des données où à la fois la composition du gaz et le setup expérimental varient, il est souvent difficile de contraindre l'impact d'un paramètre en particulier. Pour adresser ce problème, j'ai lancé une collaboration avec l'équipe de NASA Ames travaillant également sur les indices optiques en produisant des analogues avec des conditions expérimentales différentes. Pour cette étude, nous avons utilisé des compositions en gaz similaire en comparant le changement d'indices optiques lié uniquement aux changements de setup (PAMPRE

au LATMOS et COSmIC à NASA Ames). Nous avons produits plusieurs échantillons pour simuler les compositions des différents objets du système solaire (Titan, Pluton et géantes gazeuses) et des exoplanètes. Nos résultats montrent déjà que les propriétés d'absorption des analogues PAMPRE et COSmIC sont très différentes dans l'UV-Visible, même pour une composition gazeuse similaire. En effet, les aérosols COSmIC sont très absorbants dans le visible comparé aux analogues PAMPRE. Cela suggère un effet dans la chimie en phase gaz menant à la formation de l'analogue solide. Ce résultat a un impact important car l'absorption des aérosols dans le visible est la principale contribution au chauffage de la haute atmosphère dans les modèles climatiques. Nos résultats montrent aussi que la présence d'azote a un effet important sur l'absorption dans le visible. En effet, nos analogues produits sans azote (simulant Jupiter et autres objets sans N_2) sont plus transparents dans le visible. Également, la plupart des signatures IR observées sur les analogues azotées disparaissent, laissant uniquement les signatures carbone-hydrogène. De la même manière, nos résultats montrent que la présence de CO a un effet différent sur les indices optiques en comparaison au CO_2. Nos études précédentes montraient une augmentation du k dans l'IR avec plus de CO_2 tandis que cet effet est moins fort avec le CO. Cela provient probablement de la différence dans les propriétés de photo-dissociation de ces deux molécules. Le CO, étant plus résistant aux rayonnements énergétiques, ne vas pas inhiber la croissance organique autant que le CO_2. Toutes ces données fondamentales maintenant fournies à la communauté vont permettre de re-analyser les données des missions spatiales Cassini-Huygens ou encore New Horizons, et permettre de préparer les missions futures comme LIFE ou ARIEL.

Chapter 1

General introduction

1.1 Towards the characterization of exoplanet atmospheres : the lessons of the past three decades

1.1.1 Detection and characterization of exoplanets with state-of-the-art telescopes

The field of exoplanet research is young. It mainly gained momentum in the past two decades with a transition from exoplanet detection to now deeper characterization of their atmospheres made possible by state-of-the-start ground-based and space telescopes. The first exoplanet detection dates back to 1992 when the presence of a planetary system around a pulsar was confirmed using the Arecibo radiotelescope (Wolszczan and Frail 1992). Around a main sequence star, the first exoplanet was inferred from variations in the star's radial velocity suggesting the presence of a planet with a Jupiter-like mass and a very short semi-major axis (Mayor and Queloz 1995). This first detection layed out the principle of planet detection using the radial velocity technique. Since this method is based on the separation between the barycenter of the star and that of the planet-star system, the planet must be massive enough and/or close enough to the star to be detected. In 2002, Udalski et al. 2002 used the transit technique to infer the presence of an exoplanet around a main sequence star. This observational method relies on the decrease in luminosity as the planet orbits in front of the star. This second technique made the detection of small planets possible although it requires that the planet's orbit crosses the field of view between the observed star and the telescope. Fig.1.1 (left) illustrates the principle of the transit method with the star's brightness decreasing as the planet orbits in the line of sight. The Kepler space telescope (Borucki, D. Koch, et al. 2010) was launched in 2009 with the aim to detect small rocky exoplanets. The CHEOPS mission took over more recently to continue the detection and improve planetary radius measurements (Benz et al. 2021). The Kepler

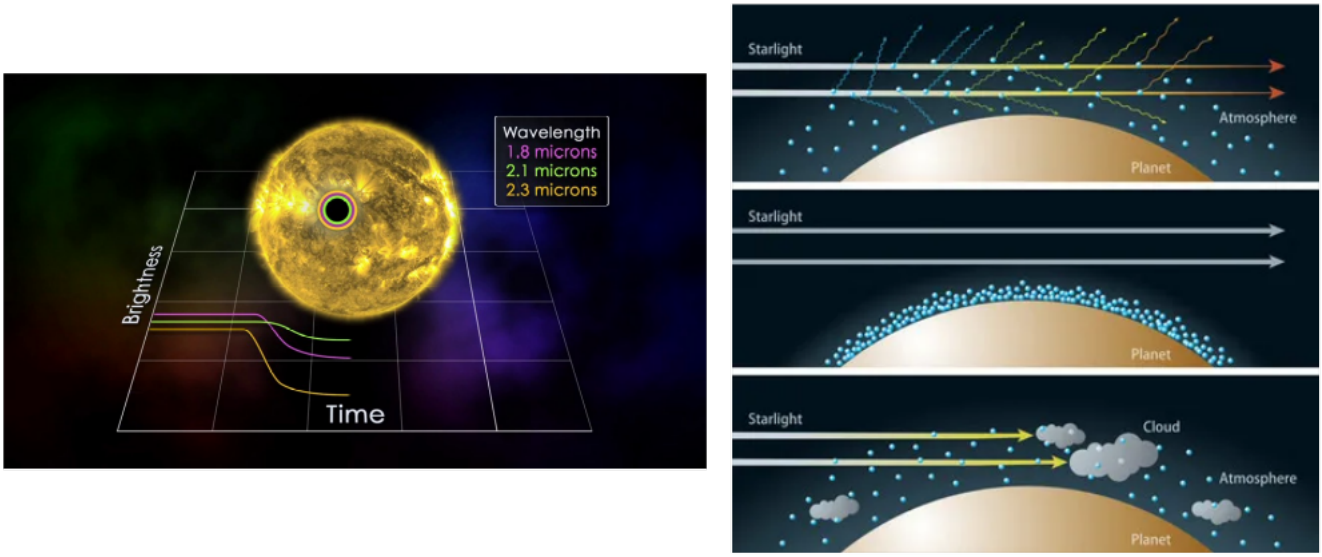

Figure 1.1: (left) Principle of transit observations with the different wavelengths revealing the contribution of the atmosphere. Credit : NASA's Goddard Space Flight Center, Additional animations courtesy ESA/Hubble. (right) Interaction between starlight and exoplanet atmosphere during transit observations. Credit : NASA, NAOJ.

mission alone which lasted almost 10 years lead to the discovery of 2,662 exoplanets. In total, 5,754 exoplanets have been confirmed[1] and this number of is increasing every day.

After using the transit technique to detect exoplanets, observers realized that observations at different wavelengths produce different signals. They understood that these variations are caused by the planet's atmosphere which is probed during the transit observation. Fig.1.1 (left) shows that the atmosphere also contributes to the planet's effective radius blocking the star's luminosity. Charbonneau et al. 2002 reported the first detection of a gaseous species, sodium (Na), in an exoplanet atmosphere. Although this first detection is now widely debated, it marked the beginning of a very active field of research focusing on the characterization of exoplanet atmospheres. Fig.1.1 (right) shows that depending on the atmosphere's thickness, presence/absence of clouds, composition, the interaction between the starlight and the planetary atmosphere is different. These effects are seen in observations as they affect the spectral variations of the signal : this is the principle of exoplanet atmosphere observations with transit spectroscopy. An inten-

[1]Exoplanets catalogue : https://exoplanet.eu/catalog/

sive characterization already started with the Hubble Space Telescope (HST) despite it not being designed for exoplanet observations (Seager and Deming 2010). The narrow spectral range of HST limits the information retrieved but still allowed the detection of water vapor and the quantification of its mixing ratio in several exoplanet atmospheres using the 1.4-μm absorption feature (e.g. Madhusudhan, Crouzet, et al. 2014, Panek et al. 2023). These first results motivated the need for a new space-telescope able to perform transit spectroscopy in a broader spectral range. For that purpose, the James Webb Space Telescope (JWST) (Gardner et al. 2006) was launched in December 2021. The spectral range of JWST extends into the mid-infrared (MIR) compared to HST and rapidly brought forth new molecular detections in exoplanet atmospheres including CO_2 (ERS-Team 2023), SO_2 (Alderson et al. 2023; Powell et al. 2024) and CH_4 (Madhusudhan, Sarkar, et al. 2023). In addition to JWST, ground-based telescopes are used to perform high-resolution spectroscopy thus providing data complementary to what can be obtained at lower resolution from space (Brogi et al. 2017). This specific field of research recently focused on the detection of metals in the atmospheres of Ultra-hot Jupiters (Hoeijmakers et al. 2019), and on the use of He lines to trace atmospheric escape (Oklopčić and Hirata 2018).

1.1.2 Current exoplanet population : what questions do we want to answer ?

Kepler and CHEOPS observations lead to the establishment of a large exoplanet population allowing us to perform statistical analyses. The exoplanet population first tells us that a broad diversity of exoplanet radii exists contrary to what our own Solar System is showing (N.M. Batalha 2014). Mass-radius measurements, although not available for every exoplanet given the need for two independent measurements, provide crucial information on the planet's bulk density allowing us to constrain the interior composition and test planet formation theories (e.g. Betzler and Miranda 2023; Swift et al. 2012). Fig.1.2 (top) shows the exoplanet demographics in the mass - semi-major axis space. Over the last decade, a classification was attempted to better distinguish these objects associated with very different formation mechanisms.

Fig.1.2 (top) shows that the different detection methods are biased, they each favor the detection of specific objects depending on the planet mass, radius and semi-major

axis. The different techniques are thus needed to obtain a population free of observational biases. This current snapshot of the exoplanet population confirmed the common presence of Gas Giant planets with a Jupiter-like mass and a stable orbit close to the host star : these objects are Hot or Ultra-Hot Jupiters depending on the equilibrium temperature. The early discovery of these objects motivated modelers to re-assess the vision of planet formation and migration strongly influenced by the peculiar dichotomy seen in our Solar System (Dawson and Johnson 2018).

The Kepler survey revealed that planets with radii smaller than Neptune are the most abundant in the galaxy (Borucki, D.G. Koch, et al. 2011). It also showed that the rocky/non-rocky dichotomy in our Solar System is not common in exoplanetary systems. In our Solar System, planets transition from rocky with densities around 5-6 g/cm^3 to gas giants with densities around 1.5 g/cm^3. In the exoplanet population, we observe a continuum of radius and density with planets likely composed of a rocky core with a substantial H_2-He envelope captured from the stellar nebulae and preserved over billions of years (Bean, Raymond, and Owen 2021). The planetary radius distribution shown in Fig.1.2 (bottom) however revealed the presence of a radius gap around 1.8 Earth radii (Owen and Wu 2013; Fulton et al. 2017). This feature, observed and predicted by models, results from a continuous mass loss occurring over millions and billions of years. Below this radius gap, planets exhibit high densities suggesting the absence of a thick primitive envelope. These rocky objects vary in mass with some having two or three times the mass and radius of Earth : they are called Super-Earths. Above the radius gap, it seems that planets often preserved their primitive envelope and exhibit densities between Earth-like objects and Saturn-like objects : these are referred to as sub-Neptunes. The transition between Super-Earths and sub-Neptunes lies in the efficiency of the mass loss mechanism controlling the escape of the primitive H_2-He atmosphere. The main mass loss mechanism driving the loss of the primitive envelope is still debated in the literature (Bean, Raymond, and Owen 2021). Two processes are suggested : photo-evaporation causing the loss of H_2 as the upper atmosphere is heated by the extreme ultraviolet (EUV) radiation from the host star (Owen and Wu 2013; Van Eylen et al. 2018), and core-powered mass loss causing an outward flux of H_2 driven by the very hot temperature found in the atmosphere (Ginzburg, Schlichting, and Sari 2018; Gupta and Schlichting 2019). It is likely that both of the processes are involved in the loss of the primitive envelope with the dominant process changing as the planet's

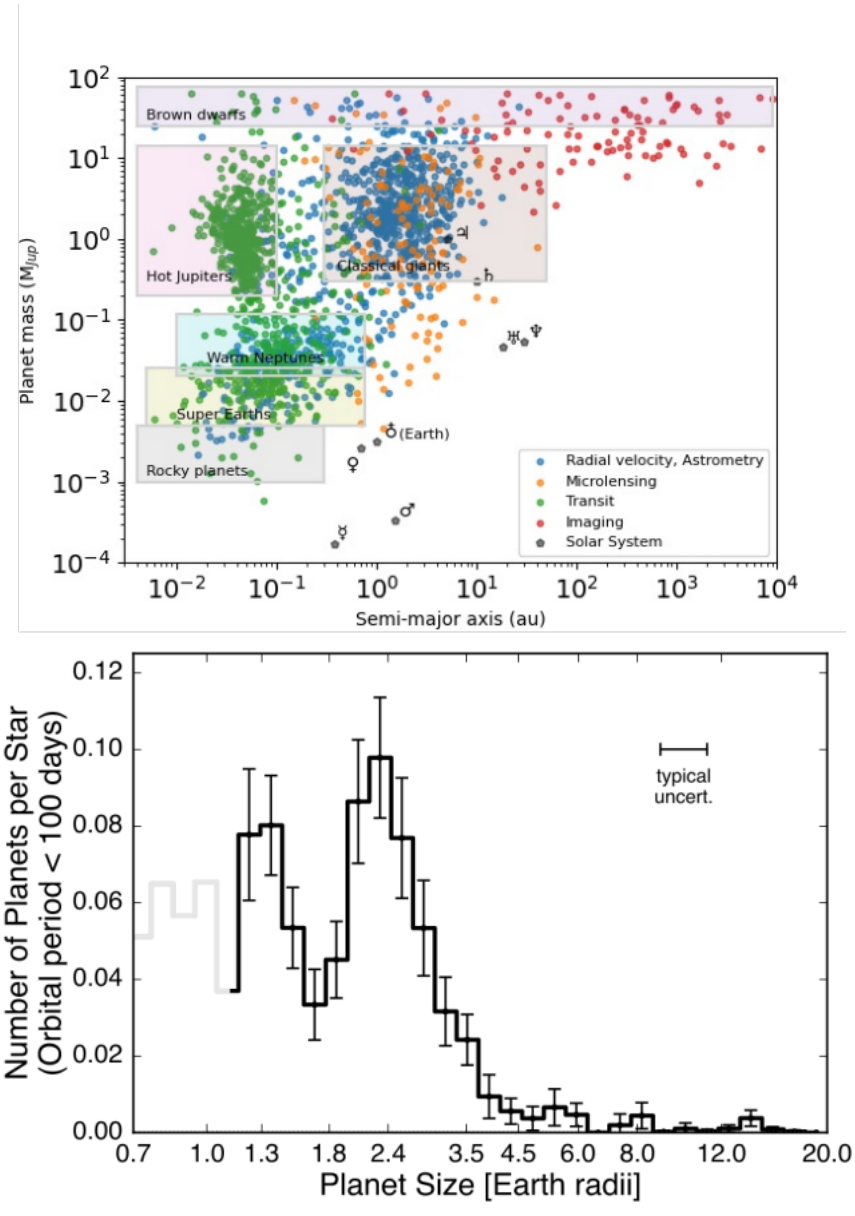

Figure 1.2: (top) Exoplanet demographics displayed in the orbit radius (semi-major axis) - planetary mass space revealing the different types of objects and the observational techniques used for their detection. Credit : Homepage of Gaël Chauvin, adapted from other studies such as Bowler 2016 with data available in the Exoplanets Catalogue (https://exoplanet.eu/catalog/). (bottom) Planetary radius distribution revealing a gap marking the transition between rocky objects and sub-Neptunes. Source : Fulton et al. 2017

atmosphere evolves (Owen and Schlichting 2024).

The nature of sub-Neptune objects is still unknown. Mass-radius measurements result in degenerate outcomes in terms of interior composition (e.g. Howe, Burrows, and Verne 2014). Their intermediate density between Earth-like and Saturn-like values can be explained by a silicate rocky core surrounded by a H_2-He envelope although it can also be explained by a water-rich interior and a more metallic atmosphere (e.g. Valencia et al. 2013). To further understand the composition and nature of these strange objects, atmospheric characterization with JWST is the best diagnostic we currently have. Several observations recently revealed a high metallicity for these sub-Neptune objects (Madhusudhan, Sarkar, et al. 2023; N.F. Wogan et al. 2024; Gao, Piette, et al. 2023) which could point to the fact that the atmosphere is not fully primitive but also affected by a non-negligible contribution of degassing from a rocky interior. Only as we accumulate the number of sub-Neptune observations in the future will we be able to better understand their nature, formation and evolution mechanisms.

For rocky objects, a broad range of properties is observed with masses above that of Earth and equilibrium temperatures ranging from habitable up to several thousands of Kelvins (Borucki, D.G. Koch, et al. 2011; Luque and Pallé 2022). Several close-in rocky exoplanets suggest the presence of a surface magma ocean and a potential atmosphere at equilibrium (e.g. Chao et al. 2021). Several habitable planets were detected (Kane et al. 2016) with a recent excitement for the Trappist-1 planets which make ideal targets. These rocky temperate and habitable worlds are found around stars very different from our Sun which points to a change in atmospheric mechanisms including chemistry. The diversity of these worlds with star-planet light interaction, temperature and composition emphasizes that atmospheric characterization is essential to better understand the physical and chemical processes shaping the atmospheres of the different objects in our galaxy.

During my PhD, I focused on rocky exoplanet atmospheres. Modeling and experimental work for these objects are in high demand to improve our understanding on the chemical mechanisms controlling current observables with JWST. We are at the dawn of rocky exoplanet atmosphere characterization, we need experimental data and modeling predictions if we want to accurately assess what information observations can provide.

1.2 Habitable worlds : How can we infer surface conditions from atmospheric characterization ?

1.2.1 Physical and chemical evolution of atmospheres in habitable conditions

Several rocky exoplanets orbiting in the habitable zone (HZ) of their host star have been reported (Kane et al. 2016). The HZ is defined as a range of distance to the host star where water can be in the liquid phase at the surface of the planet, it does not account for the presence of an atmosphere and its greenhouse properties. As we discuss these habitable worlds, we must refer to the Trappist-1 system. This system presents 7 rocky planets, all of which have semi-major axis below that of Mercury. Three planets in this system are orbiting in the HZ : Trappist-1e, f and g. The Trappist-1 system was the first target of JWST for the characterization of rocky exoplanet atmospheres. In modeling framework, the habitable Trappist-1 planets are typically used as case studies to assess the change in physical and chemical mechanisms for habitable worlds orbiting cooler stars in a tidally locked configuration (e.g. Hu, Peterson, and Wolf 2020; Eager-Nash et al. 2020; Sergeev et al. 2022). Preliminary predictions looked into the likelihood of finding an atmosphere around these objects. It was suggested that despite the strong activity of the host M star, an atmosphere could have been maintained around the habitable Trappist-1 planets (Dong et al. 2017). Our current knowledge on atmospheric escape suggests that a dense atmosphere rich in CO_2 could have been preserved as it is less sensitive to atmospheric escape (Turbet et al. 2020).

The example of Earth taught us that the atmospheric composition is strongly affected by the carbon cycle and thus by surface-atmosphere interactions (Catling and K.J. Zahnle 2020). The carbon-silica cycle on Earth is believed to have regulated the climate over time (Isson et al. 2020). CO_2 present in the atmosphere can react with silica at the surface or dissolve in oceans leading to a depletion of CO_2 in the atmosphere and an increase of the carbon stored in rocks at the surface of the planet. Most of the carbon on Earth is stored in the carbonates and not present in the atmosphere in the form of CO_2 as opposed to Mars or Venus. This carbon cycle is very complex, its efficiency is sensitive to the rocky surface composition which is unknown for exoplanets

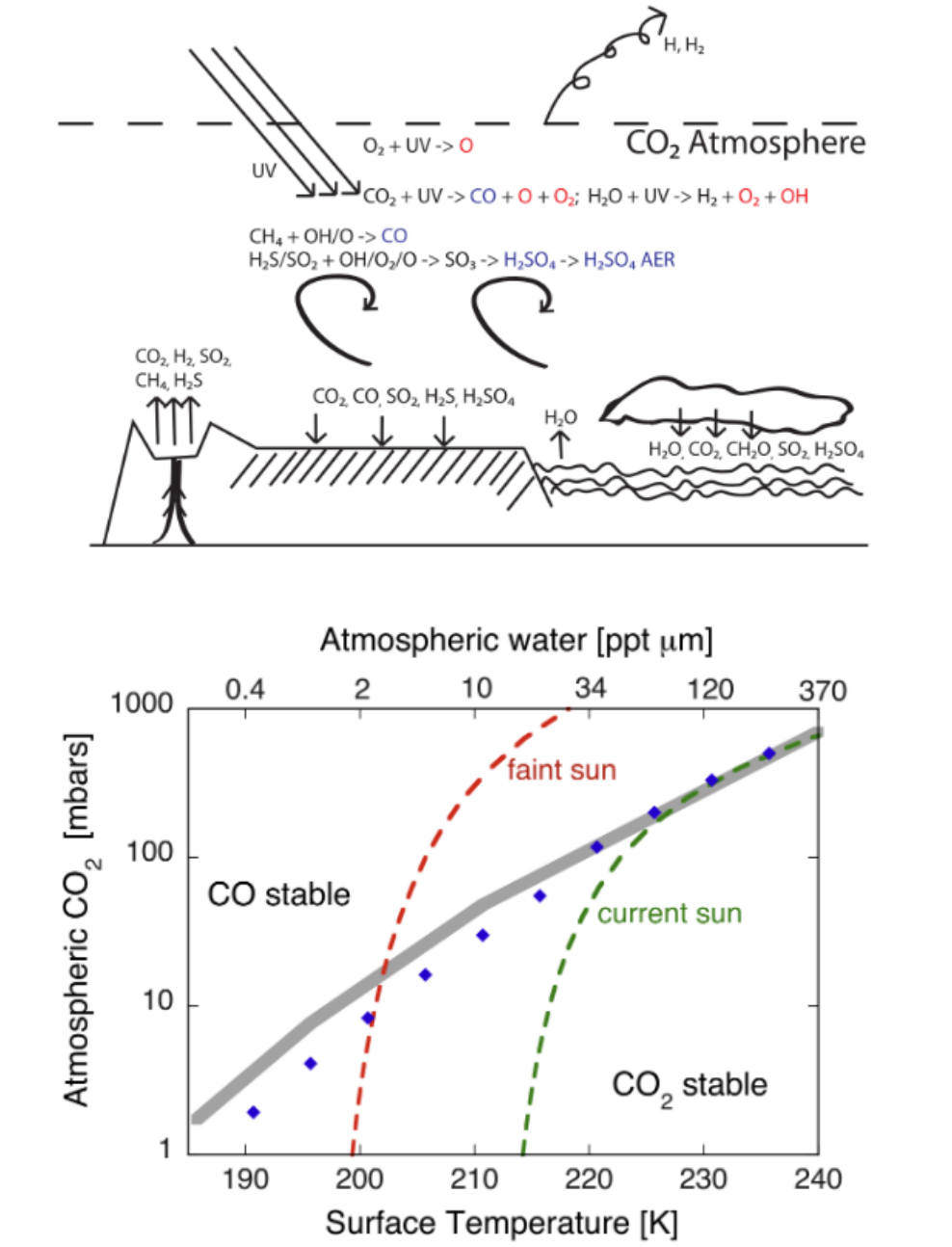

Figure 1.3: (top) Schematic of the main processes affecting the composition and evolution of habitable planetary atmospheres : atmospheric escape, cloud formation, photochemistry, surface-atmosphere interactions including volcanic degassing and surface deposition. Source : Hu, Seager, and Bains 2012. (bottom) Stability of CO_2 and CO atmospheres as a function of water abundance, CO_2 partial pressure and solar luminosity. ppt μm is a unit often used for the water content integrated over the column atmosphere, 1 ppt μm is equivalent to a column density of 3.34 10^{18} cm^{-2}. Source : K. Zahnle et al. 2008.

(e.g. Hakim et al. 2023). If an active carbon cycle is depleting the CO_2 atmospheric abundance in habitable exoplanets, other molecules must be considered to assess the habitability of these worlds and infer the presence of wet surface conditions favorable for life.

In addition to escape and weathering, the atmospheric composition is affected by photochemistry, cloud formation and other surface processes such as volcanic degassing or dry deposition. In our own Solar System, surface deposition is known to be an important sink for specific species although it strongly depends on the composition and redox state of the surface minerals (K. Zahnle et al. 2008). Its consideration in atmospheric models for exoplanets is difficult as the deposition velocities of each gas are highly uncertain and often based on Earth references (Hu, Seager, and Bains 2012; James and Hu 2018). Volcanic degassing is known to shape secondary atmospheres. Even for evolved planets such as Earth, volcanoes are an important source of volatiles that will mix in the atmosphere and build-up limited by their chemical lifetime. Hu, Seager, and Bains 2012 showed that reduced trace species emitted by volcanoes can be long-lived even in oxidized atmospheres, their main sink is surface deposition. Degassing is also difficult to consider in models as the volcanic rate is unknown and the composition of the outgassed volatiles is strongly affected by the interior redox state (Ortenzi et al. 2020). Different C-, N-, and S-bearing species can be produced by volcanoes (Gaillard and Scaillet 2014; Liggins, Shorttle, and Rimmer 2020), all of them will then interact at the surface and contribute to the photochemistry in the upper atmosphere. The different mechanisms affecting the atmospheric composition of habitable exoplanets are illustrated in Fig.1.3 (top).

The first deep study of photochemistry for habitable exoplanet atmospheres was performed by Hu, Seager, and Bains 2012. They pointed out that trace volcanic gases can be long-lived and well-mixed in the atmosphere. More recent work focuses on the stability of CO_2 atmospheres around the cooler M stars to evaluate the build-up of photochemical products such as CO and O_2 (Hu, Peterson, and Wolf 2020; James and Hu 2018; Ranjan et al. 2023). The martian atmosphere taught us that CO_2 is stable despite a continuous destruction by photolysis with vacuum ultraviolet (VUV) photons from the Sun. This is explained by a recycling mechanism induced by the photolysis of water vapor (McElroy and Donahue 1972). The photolysis of H_2O produces the OH

radical that reacts with the CO product of CO_2 photolysis. This cycle reproduces CO_2 and stabilizes the atmosphere as it balances the continuous photolysis sink. In the absence of water vapor in the atmosphere, CO_2 would be continuously destroyed by VUV photons. Fig.1.3 (bottom) quantifies the transition between a stable CO_2 atmosphere towards a CO-dominated atmosphere when the recycling mechanism is not able to balance the CO_2 photolysis. This transition is function of water content in the atmosphere but also function of the stellar flux (or luminosity). For cooler M stars, the near-UV (NUV) stellar flux is lower than the Sun (or other G stars) which lowers the photolysis rate of H_2O relative to CO_2 (Hu, Peterson, and Wolf 2020; Ranjan et al. 2023). The stability of the atmosphere can therefore be strongly affected by the stellar type. Hu, Peterson, and Wolf 2020 first suggested that a CO_2-dominated atmosphere should be unstable around the habitable planet Trappist-1e but more recent work showed that this mechanism is complex and was not correctly modeled in this first study (Ranjan et al. 2023). In general however, CO is seen to build-up to high abundances in these CO_2-dominated atmospheres but O_2 never reaches abundances as high as on Earth (James and Hu 2018; Ranjan et al. 2023).

The definition of habitability and the notion of biosignature have been debated for decades. Recent work on the Solar System planets influenced reasoning now used for exoplanetary systems. There is geomorphological evidence that liquid water was stable and running at the surface of Mars during the Noachian era, around 3.8 Gy ago (Baker 2006). Modelers could not explain however the presence of a warm and wet climate with a surface temperature sufficiently high to have water in the liquid form. The luminosity of the young Sun was indeed 25% lower than the current value making greenhouse warming less efficient even with a 1-bar CO_2 atmosphere (Kasting 1991; Forget et al. 2013; R. Ramirez et al. 2014). This climate puzzle is known as the faint young Sun paradox. More recently, it was suggested that an additional opacity through collision induced absorption (CIA) can explain a surface temperature above the freezing point of water. For early Earth, it would be caused by the collision of N_2 and H_2 (R. Wordsworth and Pierrehumbert 2013) whereas it would be CO_2 and H_2 for early Mars (R. Ramirez et al. 2014). This mechanism is based on the assumption that H_2 accumulated in the atmosphere to hundreds of mbars in a period marked with efficient volcanic degassing. These results emphasized the important role of volcanism to the concept of planetary habitability. Several modeling work focusing on the competition between degassing and

atmospheric escape confirmed that this H_2 build-up is possible (N. Batalha et al. 2015; Liggins, Shorttle, and Rimmer 2020). Some questions remain to be answered, for example why is the martian atmosphere CO_2-dominated and not CO-dominated if volcanoes degassed volatiles in a reduced form (R. Ramirez et al. 2014; Liggins, Shorttle, and Rimmer 2020). This mechanism combining outgassing and warming via CIA has strong implications for the characterization of the HZ in exoplanetary systems. The addition of H_2 in the atmosphere can indeed extend the outer edge of the HZ further away from the star (R.M. Ramirez and Kaltenegger 2017). In the era of JWST, the detection of these worlds would help confirm our current hypotheses regarding the atmosphere and climate of early Mars and Earth. The photochemistry of these atmospheres was however poorly studied. Part of this PhD thesis will focus on the photochemistry of these peculiar atmospheres with intermediate redox conditions to assess the formation of products potentially observable with JWST (see chapter 3).

1.2.2 Strategies of observation : what information could we retrieve by observing these worlds ?

Molecular detections and their retrieved abundances provide information on the chemical and physical mechanisms at play in the observed atmospheres. Often, detection of the species alone is not sufficient to infer its origin. Molecules such as CH_4, HCN or O_2 can be produced by both biotic and non-biotic processes. The abundances of O_2 and O_3 are however crucial as photochemistry alone does not explain percentage levels of O_2 production (James and Hu 2018; Ranjan et al. 2023). It is however difficult to infer the O_2 abundance from that of O_3 as the correlation is non-linear and affected by several parameters including pressure, temperature and stellar VUV flux (Kozakis, Mendonça, and Buchhave 2022). CH_4 can also be produced by non-biotic processes. The high abundance of methane detected in the temperate sub-Neptune K2-18b can for example be explained by biotic emission but also by high-temperature/high-pressure chemistry (N.F. Wogan et al. 2024; Shorttle et al. 2024). There are more complex molecules only produced by life although these species are easily oxidized and photolyzed in the atmosphere making their build-up and thus detection difficult (Seager, Schrenk, and Bains 2012; Seager, Bains, and Hu 2013). The recent suggestion of dimethyl sulfide (DMS) in K2-18b by Madhusudhan, Sarkar, et al. 2023 motivated Tsai, Innes, N.F. Wogan, et al.

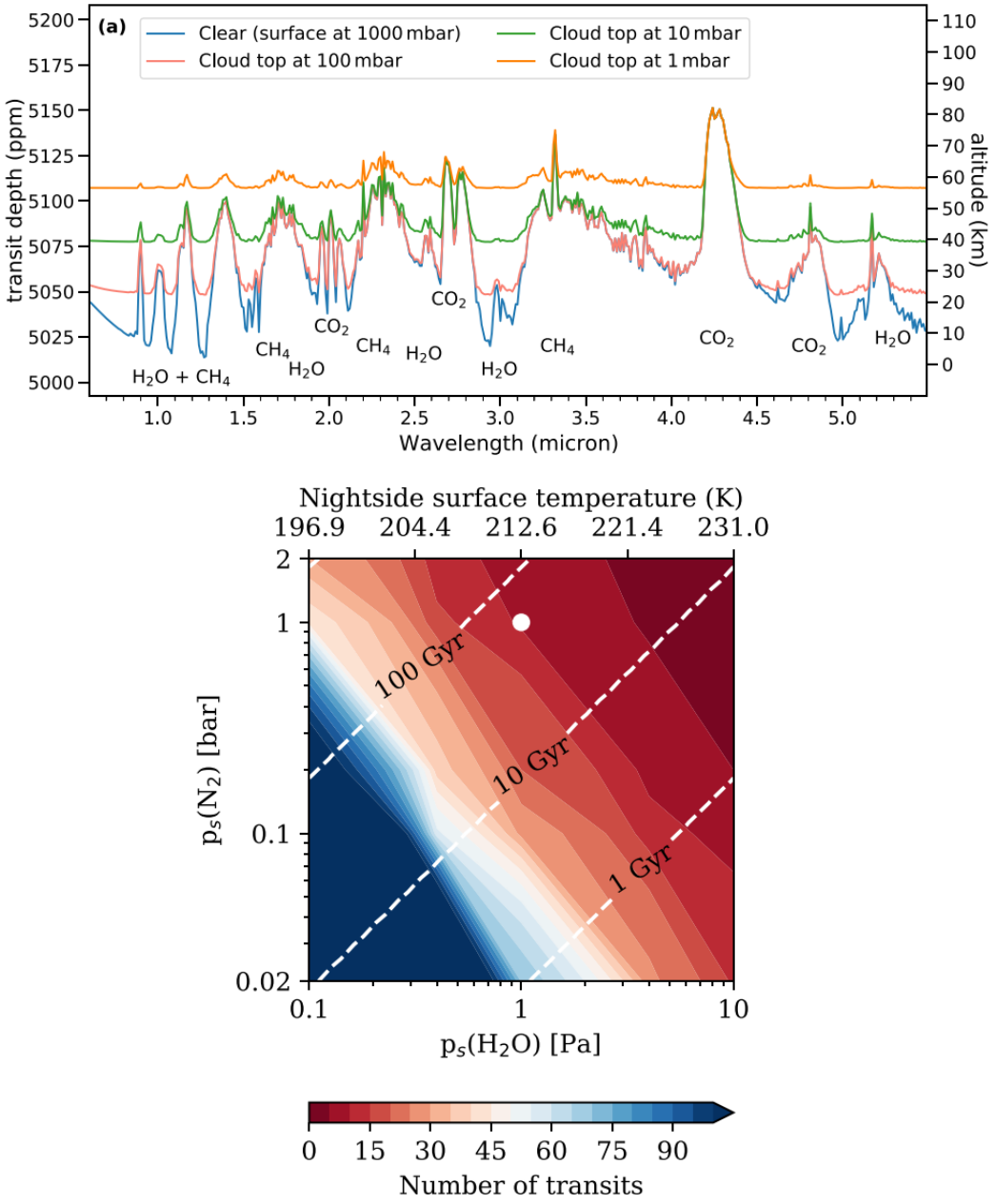

Figure 1.4: (top) Simulated transit spectra of Trappist-1e from a clear atmosphere scenario to a cloudy scenario with different vertical extension of the clouds. Source : Mikal-Evans 2022. (bottom) Number of transits needed to detect the water feature in habitable exoplanet atmospheres as a function of water abundance, N_2 abundance, night-side surface temperature and lifetime of ice deposits. Source : Ding and R.D. Wordsworth 2022.

2024 to assess the biotic emission required to balance destruction by photochemistry. The emission flux needed is typically higher than seen on Earth but values are not unreasonable. More work is needed to study the build-up of biological tracers in exoplanet atmospheres and assess their detectability.

Inferring the presence of a liquid water ocean in an exoplanet atmosphere is also challenging. For habitable planets, the presence of water clouds induces a strong extinction in JWST spectra muting most of the gas signatures (e.g. Mikal-Evans 2022). One would need to probe above the cloud deck to detect tracers indicating the presence of a water ocean. Mikal-Evans 2022 showed that the detection of water, CO_2 and CH_4 features is strongly affected by the top pressure of the cloud deck (see Fig. 1.4, top panel). Bourgalais et al. 2020 suggested the use of the ion pair H_3^+ - H_3O^+ as an indicator of habitability since these species are produced in the upper layers of the atmosphere, above the cloud deck. The build-up of ammonia (NH_3) is unlikely in the presence of a water ocean (Tsai, Innes, Lichtenberg, et al. 2021), its absence in JWST observations could already provide information. On the other hand, the absence of ammonia in observations can also be explained by its strong photolysis rate (Shorttle et al. 2024; N.F. Wogan et al. 2024). Methanol (CH_3OH) could indicate the presence of wet conditions with a surface ocean, its detection in JWST spectra is however unlikely given its low abundance at equilibrium (Tsai, Innes, Lichtenberg, et al. 2021). There is no clear molecule, ion or pair which was identified as an un-debatable biosignature or tracer of surface ocean. More modeling and experimental work are needed to better understand false positives and the conditions in which they are important. On top of the science motivation with these observations, one must be strategic and estimate how many transits are needed to confidently assess the detection of a specific species (Ding and R.D. Wordsworth 2022; Lustig-Yaeger, Meadows, and Lincowski 2019; Wunderlich et al. 2019). Fig.1.4 (bottom) is an example of the number of transits needed to detect the water feature depending on the conditions present in the atmosphere. Currently, the most strategic observation of a habitable planet therefore focuses on a specific species to assess its detection and infer the presence/absence of an atmosphere. In this thesis work, I address the formation of water in the upper layers of habitable CO_2-H_2 atmospheres which could help constrain the bulk atmospheric composition and thus help evaluate

the presence of habitable climate conditions (see chapter 3).

1.3 Non-habitable temperate rocky worlds : what can we learn from their atmospheric characterization ?

The exoplanet population tells us that a broad variety of rocky exoplanets exist with equilibrium temperatures ranging from 200 to ≈2000K. Most rocky exoplanets chosen as targets for atmospheric characterization with JWST are not habitable. For these objects, we are not interested in biosignatures but rather in the bulk composition of volatiles and metal oxides which can help us understand the formation of the atmosphere from the planetary interior. As we are at the dawn of exoplanet atmospheric characterization, we are still focusing on inferring the presence or absence of an atmosphere around these planets. Recent observations of GJ 1132b, 55 cancri e or GJ486b point to the presence of an atmosphere with very different equilibrium temperatures (Moran, Stevenson, et al. 2023; May et al. 2023; Tsiaras et al. 2016). The characterization of Trappist-1c or LHS 475b indicates the absence of a thick atmosphere although a thin atmosphere cannot be excluded (Zieba et al. 2023; Lustig-Yaeger, Fu, et al. 2023). The very few data now available predict that CO_2, CH_4 and H_2O are easily detectable if present in a thick atmosphere. We therefore must understand what we can learn from the detection of these simple molecules before suggesting more complex trace species whose presence will be uncertain.

Rocky exoplanets with equilibrium temperatures above 400K are easier to observe given their higher pressure scale height and the absence of water clouds which tend to mute gas features. In addition, we avoid the wet carbon cycle in these objects which is difficult to model and strongly impacts the chemical evolution of the atmosphere. An atmosphere around these objects must therefore result from volcanic degassing balancing with atmospheric escape. As these planetary systems are several billions of years old, the presence of an atmosphere requires late degassing after the active phase of the star which favors atmospheric evaporation. Dorn, Noack, and Rozel 2018 showed that late

degassing is more likely for Super-Earths with outgassing fluxes correlated to the planetary mass and thermal state of the interior. Estimating the degassing fluxes requires complex interior modelling with knowledge on the core fraction, thermal profile, radiogenic contribution, Rayleigh number, presence or absence of plate tectonics, etc (Quick et al. 2020; Oosterloo et al. 2021). In practice, all of these parameters are unconstrained for exoplanets providing a range of degassing fluxes that can vary by several orders of magnitude from the modern Earth reference. One cannot approach the problem with this quantitative balance between degassing and escape to predict the presence of an atmosphere given the broad parameter space.

The composition of the degassed volatiles or refractories however informs on the properties of the rocky interior. In theory, atmospheric chemistry and escape are the only mechanisms modifying this outgassed composition. Characterizing the composition of these rocky exoplanet atmospheres can thus provide crucial information on interior properties. The main property controlling the composition and redox state of the outgassed species is the oxygen fugacity fo_2 (Gaillard and Scaillet 2014; Tian and Heng 2024). fo_2 is primarily controlled by the redox state of iron in the melt. Iron cations can be in the oxidized form Fe^{3+} (ferric iron) or reduced form Fe^{2+} (ferrous iron). The oxidized form will allow more oxygen to be incorporated in the melt, it thus increases oxygen fugacity. Variations of oxygen fugacity are caused by several mechanisms. First, the stable form of iron (ferrous or ferric) is controlled by the pressure-temperature conditions in the interior. Ferric iron becomes more stable than ferrous iron at high pressure given its smaller molar volume, it will tend to be the main form in the lower mantle. This first equilibrium mechanism teaches us that Fe^{3+} will be more stable for massive planets with high pressure within the mantle (Deng et al. 2020). It points to an increase of oxygen fugacity with planet mass (and size) suggesting that Super-Earths should possess oxidized atmospheres (see illustration in Fig.1.5, bottom panel). A second mechanism is the formation of minerals. Between exoplanetary systems, relative abundances of refractory elements can vary meaning that Mg/Si changes in the rocky interior which affects the incorporation of Fe^{3+} in minerals. Guimond et al. 2023 showed that mineralogy can change the fo_2 by several orders of magnitude. More constraints can be obtained by deriving the relative abundances of refractory elements from stellar observations. Discussions on the

main mechanisms affecting the redox state of exoplanets will be possible once we characterized the atmospheric fo_2 on a large sample of exoplanets with different planetary mass and radius. This is the big picture aim of the future decades of observations with JWST.

The melt fo_2 controls gas-melt partition and speciation within the gas phase. In our own Solar System, we observe degassing dominated by SO_2 for Io, H_2O for Earth and likely CO_2 for Venus. The work of Gaillard and Scaillet 2014 revealed that simple calculations of gas-melt equilibrium for a C-H-O-S system can be used to predict the atmospheric composition. They also emphasize that the solubility of volatile species in the melt is crucial and strongly influenced by the surface pressure. Several studies explored the parameter space of these calculations which includes the melt temperature, oxygen fugacity, degassing pressure and volatile budget (Tian and Heng 2024; Gaillard, Bernadou, et al. 2022; Liggins, Jordan, et al. 2022; Liggins, Jordan, et al. 2023). Their work confirmed that a broad diversity of rocky exoplanet atmospheres is expected. CO-rich exoplanets should exist for rocky interiors with a low fo_2. CH_4-rich exoplanet atmospheres are less likely given its low stability under the high melt temperature (N. Wogan, Krissansen-Totton, and Catling 2020; Tian and Heng 2024). Fig.1.5 (top panel) shows the diversity of atmospheric composition expected depending on the interior fo_2. Tian and Heng 2024 showed that relative abundances between species of opposite redox state can help constrain the interior fo_2. the abundance ratio CO_2/CO was suggested (Tian and Heng 2024) as the most reliable tracer of fo_2. Fig.1.6 (top) shows the strong correlation between fo_2 and the gas phase CO_2/CO. Recently, this tracer was suggested for K2-18b to infer the redox state of a potential surface magma ocean (Shorttle et al. 2024). As we focus on the 4-5.2 μm range where CO_2 and CO features are seen in transit spectra, Fig.1.6 (bottom) compares the data of K2-18b with different simulated spectra using various ratios CO_2/CO. Recent observations of GJ1132b suggest the detection of CH_4 and H_2O if it is not a bias caused by stellar contamination (May et al. 2023). The authors suggest that better data around the CO_2 and CO features are needed to constrain their detection and start discussing the meaning in terms of interior redox state.

To interpret observations of future rocky exoplanet atmospheres and infer interior

fo_2, one needs to understand the physico-chemical mechanisms that affect relative abundances and thus bias detections. The main mechanism is likely atmospheric chemistry. We must understand how atmospheric chemistry can modify the prediction of outgassing. Recent work by Liggins, Jordan, et al. 2023 shows that the lower temperature in the atmosphere compared to the melt leads to the production of CH_4 from conversion with CO and H_2 in low fo_2 conditions. CH_4-rich exoplanet atmospheres are thus possible for reduced redox states and temperatures low enough to be in the stable thermochemical regime of CH_4. The transition between an evolution dominated by photochemistry and thermochemistry is unclear, it is affected by several parameters. In this PhD thesis, I address this issue and evaluate the reliability of molecular relative abundances to infer interior fo_2. For that purpose, I focus on the effect of thermochemistry and photochemistry in a broad range of conditions in terms of surface pressure, surface temperature and fo_2 (see chapter 4).

1.4 Aerosols in exoplanet atmospheres : a tracer of in-situ physico-chemical processes

1.4.1 Observation of aerosols in exoplanet atmospheres

The first observations of exoplanet atmospheres with HST already revealed the strong impact of atmospheric aerosols on the spectra (Gao, Wakeford, et al. 2021). Given the significant fraction of objects observed with evidence of aerosols, these first observations showed that atmospheric particles are common in exoplanet atmospheres. We can distinguish two types of atmospheric aerosols. First, we have condensates which form when the pressure-temperature conditions in the atmosphere reach the saturation vapor pressure of a specific element or molecule. Condensate clouds are ubiquitous in the Solar System, they are made of water on Earth, ammonia on Jupiter, methane and other hydrocarbons on Titan, and sulfuric acid on Venus. As we are now observing exoplanet atmospheres in the MIR with JWST, the vibrational modes of cloud condensates can be detected. For example, quartz clouds were observed in the atmosphere of the hot Jupiter planet WASP-17b (Grant et al. 2023). The second type of atmospheric aerosols is photochemical haze which forms in the upper atmosphere from the photolysis

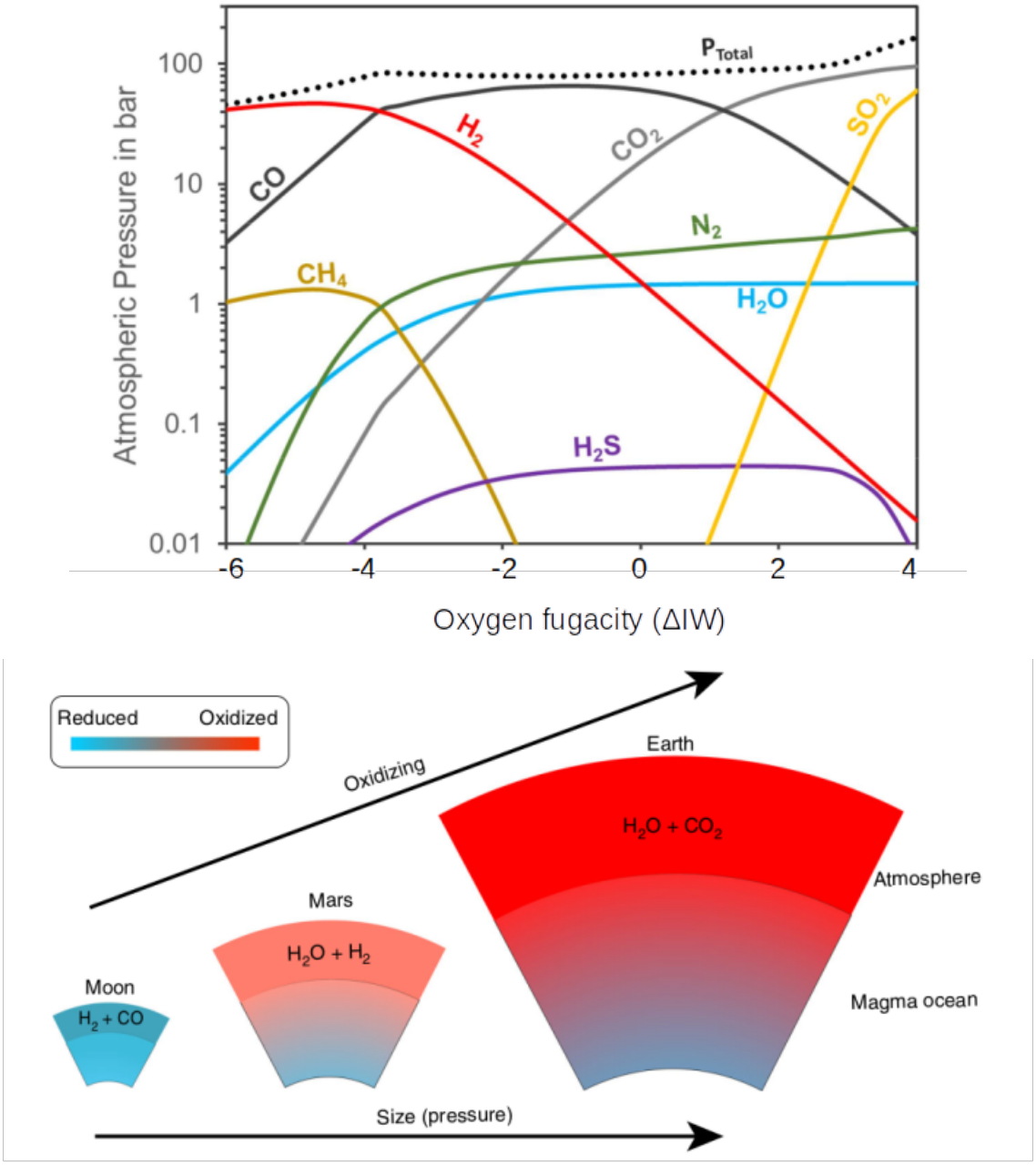

Figure 1.5: (top) Atmospheric composition as a function of oxygen fugacity predicted by gas-melt equilibrium. Oxygen fugacity is expressed using the difference with a reference. The reference here is the iron-wustite buffer controlling the amount of metal iron (Fe) compared oxidized iron (wustite, FeO). This is the primary buffer reaction affecting fo_2 of the Earth's mantle : $Fe + \frac{1}{2} O_2 \longleftrightarrow FeO$. Source : Gaillard, Bernadou, et al. 2022. (bottom) Schematic explaining the expected change of interior fo_2 and thus atmospheric composition with planetary size. Source : Deng et al. 2020.

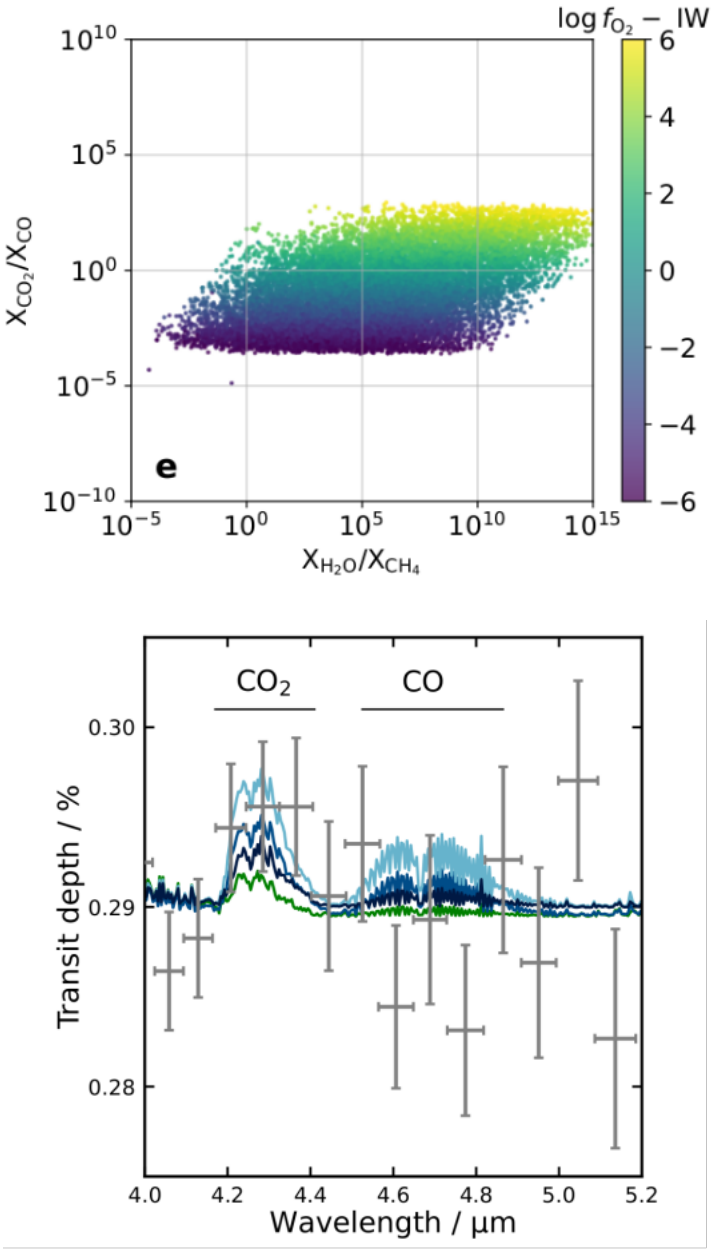

Figure 1.6: (top) Correlated behavior between fo_2 and CO_2/CO suggesting this molecular pair as an atmospheric tracer of interior redox state. Source : Tian and Heng 2024. (bottom) Effect of different CO_2/CO to explain the observations of K2-18b. Source : Shorttle et al. 2024.

of the main molecules and the resulting radical chemistry evolving into a complex polymerization producing solid organic particles. Photochemical hazes are observed in our Solar System, in the atmospheres of Titan, Pluto, Triton and the different Gas Giants (Karkoschka and Tomasko 2011; Ortiz, Moreno, and Molina 1996). They are expected as the primary aerosols in exoplanet atmospheres for objects with an equilibrium temperature lower than ≈1000K (Gao, Thorngren, et al. 2020). The region between 400 and 1000K is indeed largely free of cloud condensates and should be dominated by haze formation (Gao, Wakeford, et al. 2021).

Recent observations of temperate sub-Neptune GJ1214b suggest the presence of a thick haze layer cooling the surface temperature below the equilibrium temperature (Kempton et al. 2023). The combination of HST/WFC3 data and JWST/MIRI data revealed a flat transit spectrum resulting from a significant haze extinction (Kempton et al. 2023). As modelers prepared the observations of GJ1214b, the effect of atmospheric and haze properties on simulated transit spectra was assessed to identify the most important contributions. The atmospheric metallicity is a crucial parameter as it strongly influences the production of haze particles. Often, the haze production rate is parameterized as we have strong uncertainties on its formation mechanisms. Several papers use C_2H_2 as the main gas phase precursors and correlate the loss of C_2H_2 with the production rate of haze particles (Kawashima and Ikoma 2019). Observations of Titan and Pluto hazes taught us that the particles are fractal aggregates and not spherical particles suggesting a complex micro-physical evolution in the atmosphere (Tomasko et al. 2008; Bellucci et al. 2009; Gao, Fan, et al. 2017). The micro-physical model developed by P.P. Lavvas, Coustenis, and Vardavas 2008 for Titan was widely used in the community and later applied to Pluto and now to exoplanets (P. Lavvas and Arfaux 2021) to assess the morphological evolution of haze particles. For aggregates, one must constrain the shape parameters including the number of monomers and fractal dimension to accurately derive the optical properties. For Titan and Pluto aerosols, these parameters are retrieved from different observations. The number of monomers is typically ≈ 3000 and the fractal dimension is debated, sometimes estimated at 2 (Rannou, Cabane, et al. 1997; Gao, Fan, et al. 2017; Sciamma-O'Brien, Roush, et al. 2023) or 2.3-2.4 (Coutelier et al. 2021; Rannou, Coutelier, et al. 2022; Es-sayeh et al. 2023) de-

pending on the observation. One must have intuition on the particle number density of both spherical particles and aggregates as a function of altitude to understand the overall extinction seen in transit spectra. In summary, atmospheric properties (metallicity) and haze properties (monomer size, fractal dimension, number of monomers, production rate) all contribute to the overall haze extinction and its imprint on the observed spectra. For GJ1214b, the flat spectrum suggests a high metallicity (around 1000X solar) and a production rate above 10^{-10} g/cm^2/s (Gao, Piette, et al. 2023). Fig.1.7 (top) shows the effect of atmospheric metallicity and haze production rate on the observed transit spectra for the case of GJ1214b.

One more parameter strongly influences haze extinction : the solid chemical composition. Haze formation is affected by the stellar VUV radiation, atmospheric composition, vertical mixing and temperature. The formation mechanisms strongly vary from one planet to the next leading to haze particles with different compositions. The haze composition controls the intrinsic optical properties known as the refractive indices or optical constants, n and k. n describes dispersion of light and mainly quantifies the attenuation of the speed of light within a medium of specific composition. k describes absorption by the material and thus quantifies the strength of different features as we transition from electronic to atomic polarization. n and k vary with wavelength and are used as input parameters in Mie scattering models to determine the radiative properties of spherical particles and fractal aggregates (Botet, Rannou, and Cabane 1997; Kitzmann and Heng 2017). These refractive indices are largely unknown and become a crucial source of uncertainty in radiative transfer models. With simulations of GJ1214b, it was shown that the effect of k can strongly influence the observed spectra (Kawashima and Ikoma 2019; He, Radke, et al. 2023). Fig.1.7 (bottom) shows the effect of the haze refractive indices on the simulated transit spectra of GJ1214b. A big part of my PhD thesis focuses on these refractive indices given the urgent need for these data to interpret observations (see chapters 5 and 6).

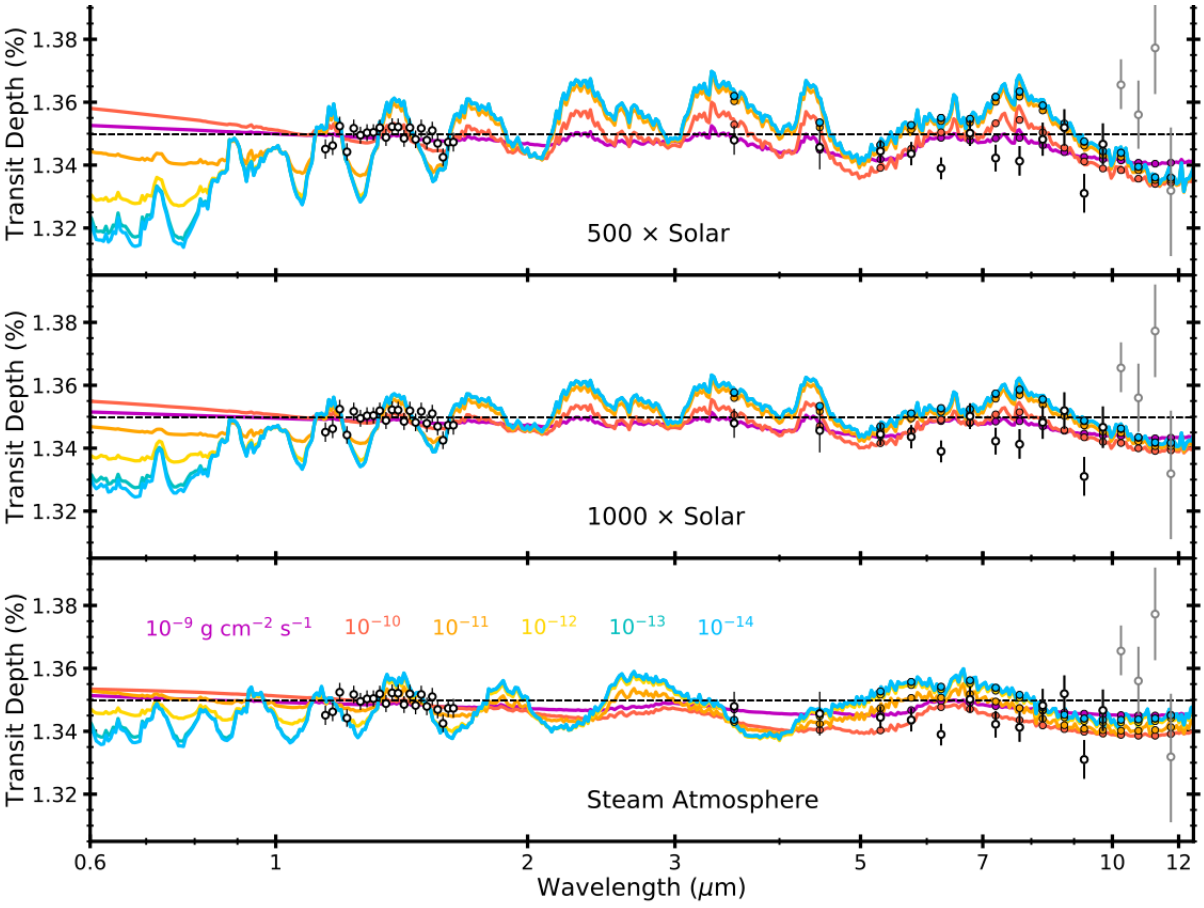

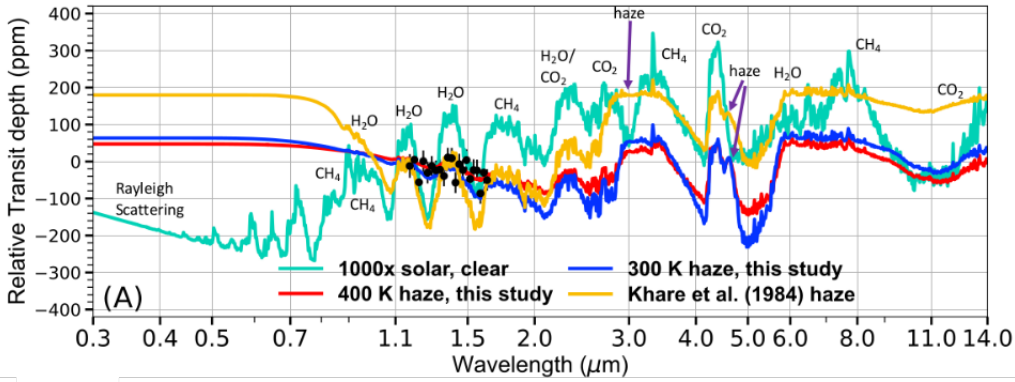

Figure 1.7: (top) Effect of atmospheric metallicty and haze production rate on transit spectra observations of GJ1214b. The HST/WFC3 and JWST/MIRI observations are shown (black circles). Source : Gao, Piette, et al. 2023 and Kempton et al. 2023. (bottom) Effect of the haze composition and thus refractive indices on transit spectra simulations of GJ1214b. Source : He, Radke, et al. 2023.

1.4.2 Laboratory haze analogs : What did we learn on the formation, composition and refractive indices of photochemical hazes ?

Over the past four decades, laboratory setups were developed to simulate the chemistry of planetary atmospheres and more specifically to produce analogs of photochemical hazes. As lamps are not energetic enough to produce high abundances of haze precursors, plasma discharges are used as an energy source. Dissociation of the main molecules is triggered by electron impact instead of VUV photons, it however does not impact the chemical pathways following dissociation. During my PhD, I used the PAMPRE setup (production of aerosols in micro-gravity by a reactive plasma) at LATMOS (France). Other setups exist including the COSmIC setup at the NASA Ames Research Center (Salama et al. 2017) and the PHAZER setup at John Hopkins University (He, Hörst, Riemer, et al. 2017). The aim is to better understand the gas phase chemistry and the formation of precursors leading to haze formation, the composition of the solid material produced, and its optical properties.

Several work revealed that the formation of haze analogs is possible by the production of specific gas phase precursors via photochemistry. It includes C_2H_2 and other complex carbon chains (e.g. benzene C_6H_6) but also nitriles produced in the presence of N_2 (Gautier, Carrasco, Buch, et al. 2011; Perrin et al. 2021; Sciamma-O'Brien, Ricketts, and Salama 2014; He, Serigano, et al. 2022). The different experiments showed that different chemical pathways exist to produce a specific haze precursor, for example nitrile formation is produced by the photolysis of N_2 but also by chemical reactions involving N_2 directly without requiring its photolysis (Trainer, Jimenez, et al. 2012; Berry et al. 2019). The CH_4 abundance relative to N_2 controls the pathways and products which can vary from aliphatics to polycyclic aromatic hydrocarbons (PAHs) (Trainer, Pavlov, et al. 2004). In the presence of O-bearing molecules in the initial gas mixture, complex carbon chains tend be inhibited and replaced with oxygenated molecules (Moran, Hörst, et al. 2022). In the presence of sulfur, organo-sulfuric compounds are seen which suggest a complex chemistry leading to the incorporation of sulfur in the organic precursors (He,

Hörst, Lewis, et al. 2020).

The composition of the haze analogs varies significantly with the initial gas mixture (Carrasco et al. 2016; Jovanovic, Gautier, Vuitton, et al. 2020; Vuitton et al. 2021). N/C changes following the N_2/CH_4 ratio in the initial mixture (Carrasco et al. 2016). This also affects the refractive indices of these haze analogs from UV to near-IR (Mahjoub et al. 2012). As shown in Fig.1.8 (bottom), the MIR relative strength of aliphatic (C-H in CH_2,CH_3) and amine (N-H in NH_3 and NH_2) modes also changes following the initial N_2 and CH_4 abundances (Gautier, Carrasco, Mahjoub, et al. 2012; Mahjoub et al. 2012). Oxygen is also strongly incorporated in the solid material when O-bearing gases are in the mixture (Jovanovic, Gautier, Vuitton, et al. 2020; Moran, Hörst, et al. 2022). It also strongly influences the absorption properties in the UV-Visible (Jovanovic, Gautier, Broch, et al. 2021). For CO_2-rich mixtures representative of early Earth and exoplanet atmospheres, the UV-Visible absorption slope is increased relative to a Titan analog produced from N_2 and CH_4 (see Fig.1.8, top panel, Gavilan, Broch, et al. 2017). MIR absorption is also stronger as CO_2/CH_4 is increased in the initial gas mixture (Gavilan, Carrasco, et al. 2018). Recent work suggests that hazes produced with H_2S as well exhibit higher absorption properties in the visible (Reed et al. 2023). Sulfur was shown to be strongly incorporated in the solid material (Vuitton et al. 2021).

During my PhD, I focused on improving the refractive indices data for exoplanet haze analogs given the current need to analyze and interpret observations. First, the refractive indices are often measured by different techniques and calculations from one group to another. The error and limitations of the technique were shown to be significant in some cases (Tran et al. 2003). I address this issue in detail using several measurements in both the UV-Visible range and MIR. I optimized a series of measurements and developed models to determine reliable refractive indices in a broad spectral range from UV to far-IR to cover the operating range of JWST. I launched a collaboration with the NASA Ames group and assessed the effect of the gas composition and experimental setup on the refractive indices of haze analogs. This last work will provide the community with a large data set that can be used for applications to Titan, Pluto and Exoplanets (see chapter 6).

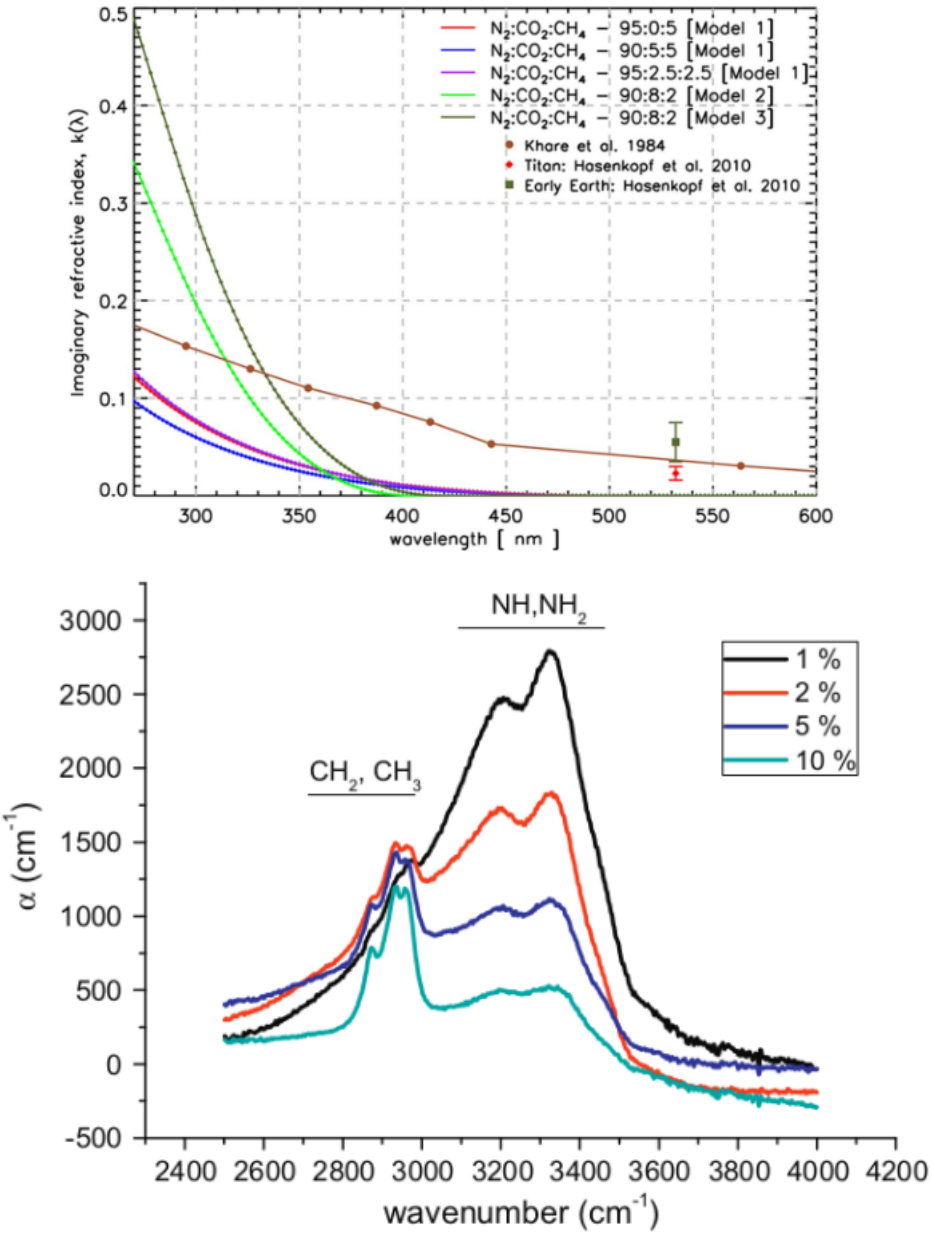

Figure 1.8: (top) UV-Visible extinction coefficient k for exoplanet haze analogs produced with different relative abundances in a N_2-CO_2-CH_4 mixture. Source : Gavilan, Broch, et al. 2017. (bottom) mid-IR absorption coefficient of Titan haze analogs focusing on the variation of aliphatic and amine signatures depending on the initial abundances of N_2 and CH_4. The legend corresponds to the mixing ratio of CH_4 in the initial gas mixture. Source : Mahjoub et al. 2012.

1.5 Focus of this PhD thesis : observables of gases and aerosols to trace atmospheric chemistry

During my PhD, I wanted to improve our understanding on gas and aerosol observables in rocky exoplanet atmospheres by focusing on what information atmospheric chemistry can provide. The general aim is to better understand what can gaseous and solid signatures tell us about the habitability, rocky interior properties, atmospheric conditions and bulk composition. I assessed the effect of several mechanisms from photochemistry, to thermochemistry to aerosol optical properties.

This thesis is written as compilation of journal articles with each chapter corresponding to one paper. The thesis is divided in six chapters. The first chapter of this thesis is the general introduction presenting the big picture around the different types of rocky exoplanets and the different observables we are currently interested in. The second chapter describes the different experimental setups and main measurements performed during my PhD. Chapters 3 to 6 are papers, each is addressing a specific type of observable and answering a specific question. Below is a list of the four following chapters with a small description of the topic of each paper and the questions I wanted to address.

- The third chapter focuses on the photochemistry of habitable CO_2-dominated atmospheres with significant volcanic H_2 build-up. The importance of H_2 to create habitable conditions has been established although the photochemistry and detection of these worlds remain poorly studied. The directing question is : How can we identify these CO_2-H_2 worlds from observations and what information does photochemistry provide ? For this project, I combined photochemical experiments with 0D and 1D chemical kinetics modeling to understand the main chemical network and assess implications for observations.

- The fourth chapter focuses on the effect of atmospheric chemistry on rocky exoplanet atmospheres produced by volcanic outgassing. The directing question is : How can we infer interior redox state properties (oxygen fugacity) from observations and what

constraints are posed by atmospheric chemistry ? For this project, I coupled models of atmospheric chemistry and radiative transfer with simple calculations of geochemical outgassing to assess how atmospheric chemistry and climate modify the outgassed composition.

- The fifth chapter focuses on the refractive indices of exoplanet haze analogs produced in conditions expected for exoplanets and early Earth. The directing question is : What is the effect of the optical method on the accuracy of the retrieved refractive indices and how does the CO_2/CH_4 ratio affect the optical properties in a broad spectral range ? In this paper, I establish the methodology behind different measurements and models to assess the effect of the optical technique (spectrophotometry and ellipsometry) on the derived refractive indices. I also provide refractive indices for haze analogs produced with two different CO_2/CH_4 mimicking different oxidation states in the atmosphere.

- The sixth chapter focuses on a cross-laboratory comparative study to assess the effect of the gas composition and experimental setup on the refractive indices of haze analogs. The leading question is : How does the experimental setup properties (temperature, residence time, irradiation) and the gas composition affect the optical properties of haze analogs from UV to far-IR ? I collaborated with the NASA Ames group to perform several samples with two different setups and compare the optical properties of the analogs. I discuss implications for future modeling work and future observations with JWST.

I finish this thesis report with a general conclusion focusing on the main results, the big picture implications and the remaining questions brought forth during this PhD project.

Chapter 2

Experimental setups and measurements

Since I followed a paper format for this PhD thesis, I provide details on the principles and configurations of the setups and measurements in the different papers but I do not provide a visual description. This section provides a general overview of the different setups and measurements performed during my PhD.

2.1 APSIS

For the photochemical experiments detailed in Chapter 3, I used the APSIS (Atmospheric Photochemistry SImulated by Surfatron) setup shown in Fig.2.1. The chamber is rectangular with a length of 50 cm and a base of dimension 11.4 x 9.2 cm (Peng et al. 2013). The source is not a lamp but a surfatron connected to the chamber on the side, at the base. We do not use a lamp as APSIS has been widely used for Titan applications looking at the photolysis of N_2 which requires energetic photons with wavelengths below 100 nm. With lamps, an optical window is needed between the chamber and the lamp which always filter photons with wavelength below 100 nm (limit with MgF_2 windows). Lamps can therefore not be used to assess mechanisms following N_2 photolysis. With the surfatron, there is no window or other component separating the chamber and the source, energetic photons can thus reach the interior of the chamber and trigger photolysis of N_2. With the surfatron, radiation is monochromatic with a wavelength specific to the main resonance line of the noble gas injected in the surfatron. The noble gas is injected into a quartz tube and excited into a plasma using a microwave generator. For my study, I focused on neutral chemistry and explored the wavelength region of CO_2 photolysis, I thus used argon to have emission at 104.8 nm. An entire thesis was conducted for the design and testing of the surfatron source, we follow the configuration of

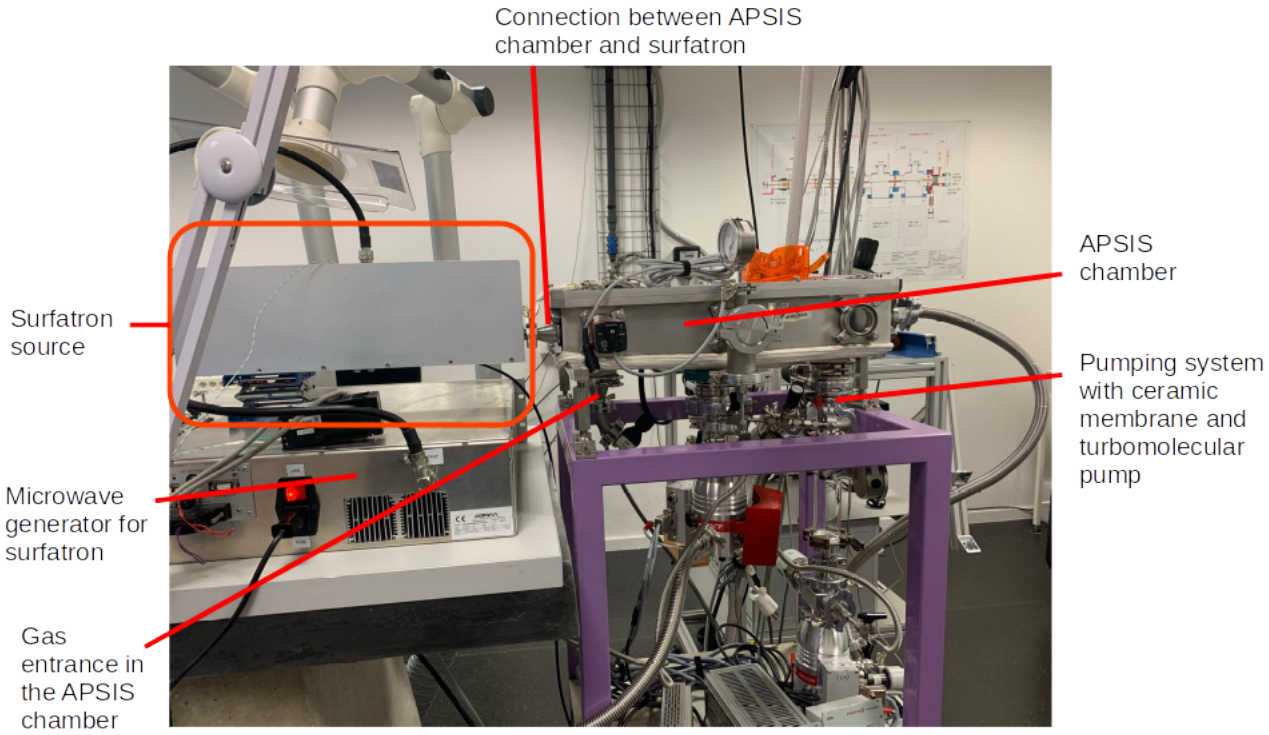

Figure 2.1: Description of the APSIS setup. The quadrupole mass spectrometer is connected behind the APSIS chamber in this image.

Tigrine et al. 2016 to ensure that only photons exit the surfatron towards the chamber making sure that the distance between the plasma discharge and the chamber is sufficient for argon to re-neutralize. The chamber and the surfatron are connected through a 0.5 cm^2 orifice in the center of the chamber base to ensure irradiation only occurs in the center of the chamber. This was designed on purpose to avoid having a reactive medium close to the walls and thus affected by gas-wall reactions. The gas mixture is injected close to the exit of the surfatron source (see Fig.2.1) and the gas exits the chamber through a ceramic membrane with 20-nm orifices followed by a turbo-molecular pump. In this configuration, we obtain a continuous gas flow with a stable pressure around 1 hPa. The APSIS chamber is connected to a quadrupole mass spectrometer to monitor the chemistry during the experiment.

2.2 PAMPRE

I used the PAMPRE setup to produce analogs of photochemical hazes from different gas compositions. More details on the configurations are given in chapters 5 and 6. The setup is shown in Fig.2.2 and was first described in Szopa et al. 2006. The chamber is a cylinder made of stainless steel with a height of 40 cm and a diameter of 30 cm. There are two electrodes within the chamber, one at the top and one at the bottom. During the experiment, electrons are accelerated between the electrodes turning the gas mixture into a cold plasma (room temperature). The potential difference between the electrodes is triggered using a 13.56 MHz radio-frequency generator usually set with a power of 30 W. The plasma can be confined in a stainless steel cage fixed to the upper electrode. With this cage configuration, the bottom of the cage acts as the grounded electrode and the reactive medium is confined in a smaller volume. Different mass flow rate controllers (MFCs) are installed to inject different gases. The gas is sampled directly from high-purity gas bottles (usually from the Air Liquide company). The MFCs allow us to control the abundances in the injected gas mixture. The mixture enters the PAMPRE chamber at the top. The primary pump is connected to the bottom side of the chamber where the gas exits. This configuration creates a continuous flow and stable pressure around 1 hPa depending on the chosen injected flow rate. On the upper side, the mass spectrometer can sample directly the gas within the chamber to monitor the chemistry and characterize the reactive medium.

2.3 Fourier-transform spectrometer at the Ailes beamline of SOLEIL synchrotron

To determine the refractive indices of exoplanet haze analogs, I wrote two proposals as principal investigator (PI) to obtain time at the Ailes beamline of synchrotron SOLEIL. The two proposals were granted (ID20221651, October and March 2023 and ID20231358, january and june 2024) allowing us to access their Fourier-transform spectrometer operating from near-IR to far-IR (1 μm to $\approx$ 200 μm). The instrument setup is shown in Fig.2.3. The source consists of a silicon carbide SiC Globar heated to 1,250 K. Different beamsplitters are used depending on the spectral range. Well-named, the beamsplit-

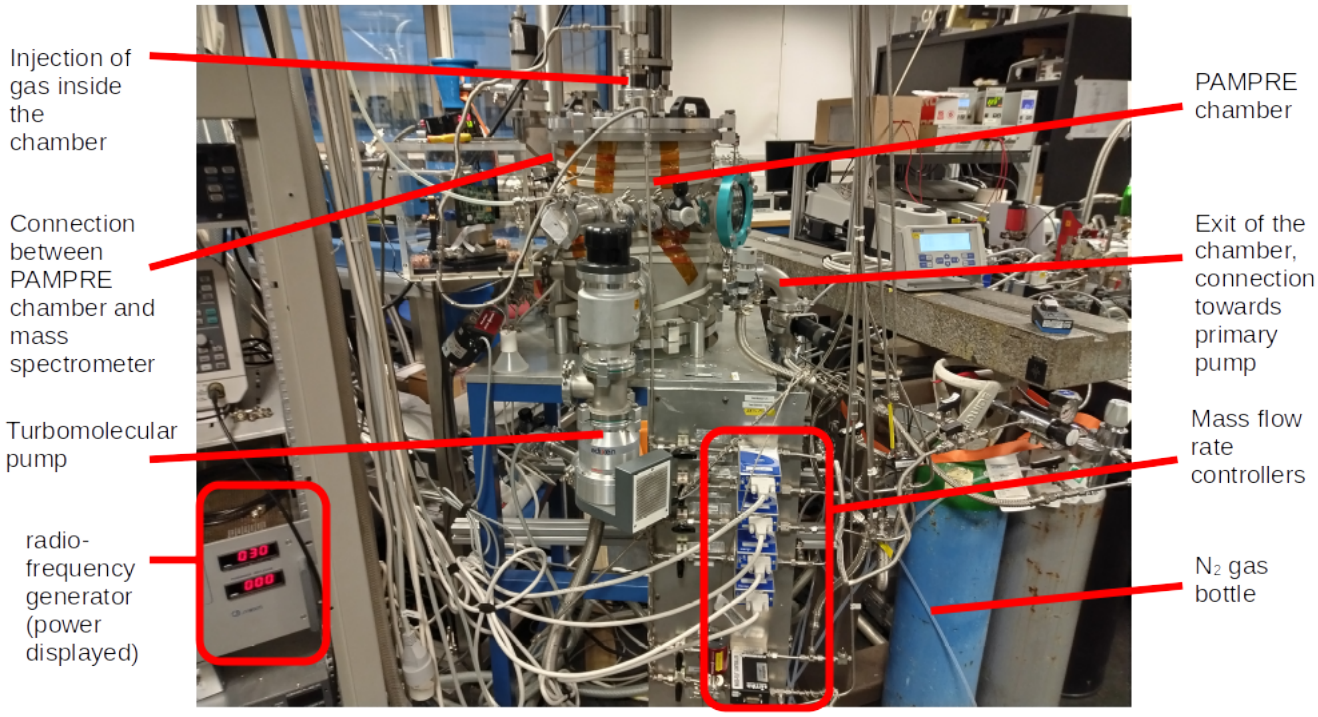

Figure 2.2: Description of the PAMPRE setup.

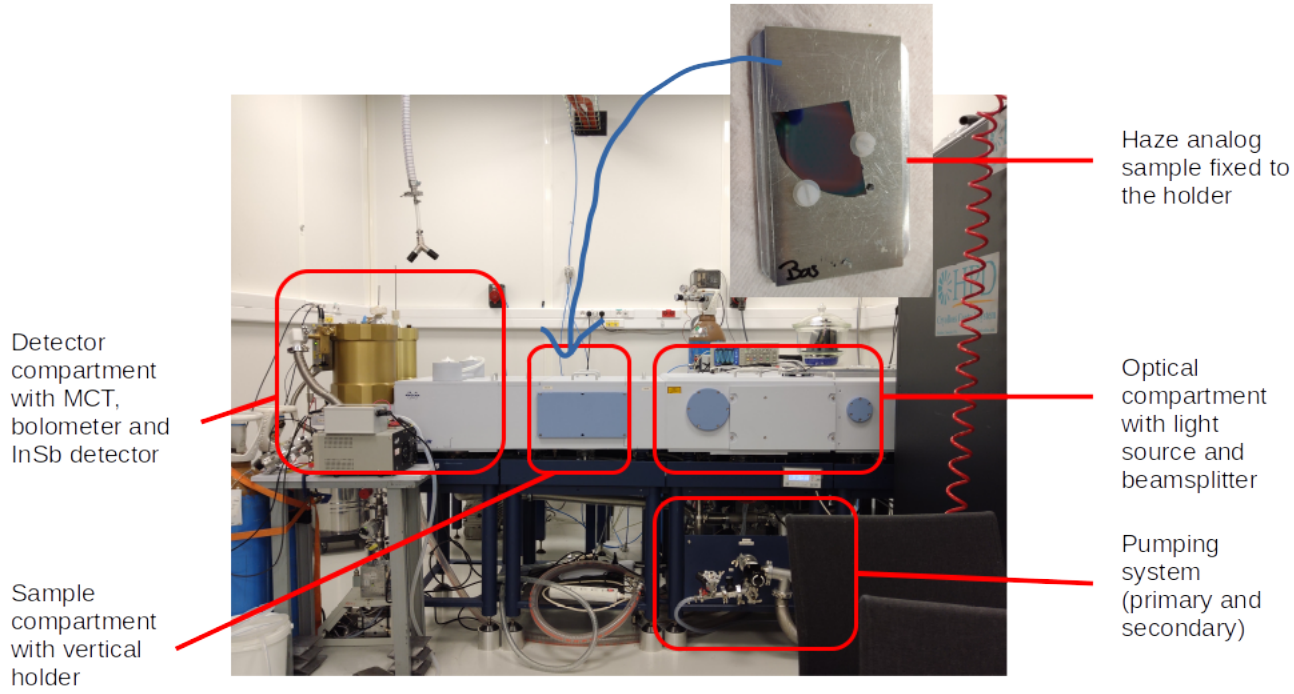

Figure 2.3: Description of the Bruker Fourier-transform spectrometer used at the Ailes beamline of synchrotron SOLEIL to measure spectra from near-IR to far-IR.

ters splits the beam into two new beams. The instruments ensures that the optical path between the two beams is shifted to obtain interferences when the two beams are re-focalized together. Once re-focalized together, the beam reaches the sample compartment. Within this compartment, the sample is fixed onto a vertical holder allowing measurements in both transmission and reflection. The light then reaches the detector compartment. Different detectors are used depending on the wavelength range, more details are given in chapters 5 and 6. The entire instrument is put under vacuum with a pumping system. For convenience, the optical and detector compartments always stay under vacuum. Only the sample compartment is brought back to atmospheric pressure when we need to change samples.

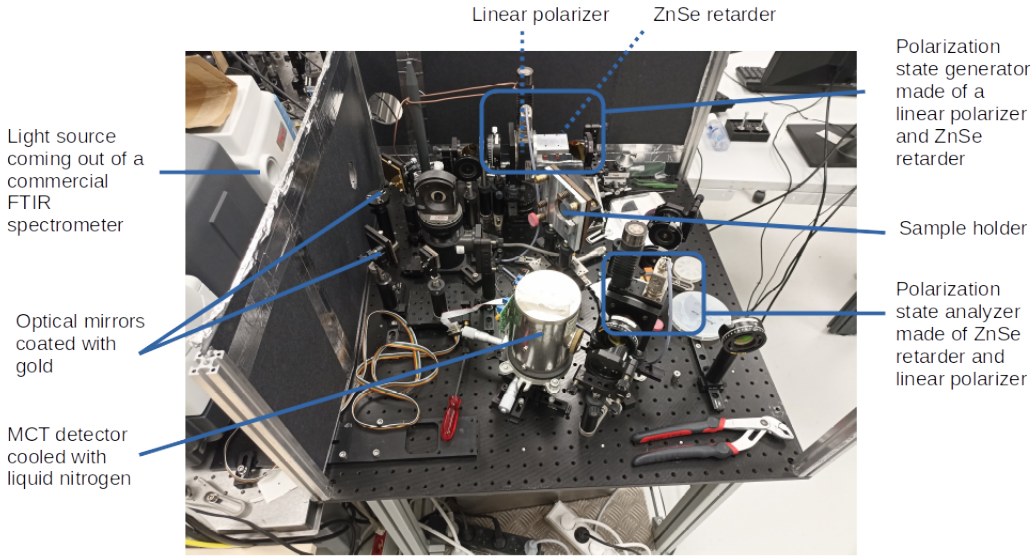

Figure 2.4: Description of the MIR Mueller ellipsometer at the SMIS beamline of synchrotron SOLEIL.

2.4 MIR Mueller ellipsometer at the SMIS beamline of synchrotron SOLEIL

In collaboration with Enrique Garcia-Caurel, I used the MIR Mueller ellipsometer installed at the SMIS beamline of synchrotron SOLEIL. The instrument setup is shown in Fig.2.4. The light source is also a SiC Globar similar to the one used with the Fourier-transform spectrometer at the Ailes beamline. Different mirrors coated with gold guide the beam through the polarization state generator (PSG) made of a linear polarizer and a retarder composed of ZnSe prisms. These prisms induce an elliptic polarization similar in the entire MIR range. In this photograph, we can see clearly the mobile holder of the retarder (metal plaque). This holder onto which the ZnSe prisms are fixed can rotate to create different polarization states. The sample is placed vertically onto the sample holder. The mirror just on the right of the PSG (Fig.2.4) ensures an angle of incidence around 60° on the sample. After reflection on the sample, the beam passes through the polarization state analyzer (PSA) made of the same components as the PSG but with a reversed order. The detector is an MCT cooled with liquid nitrogen.

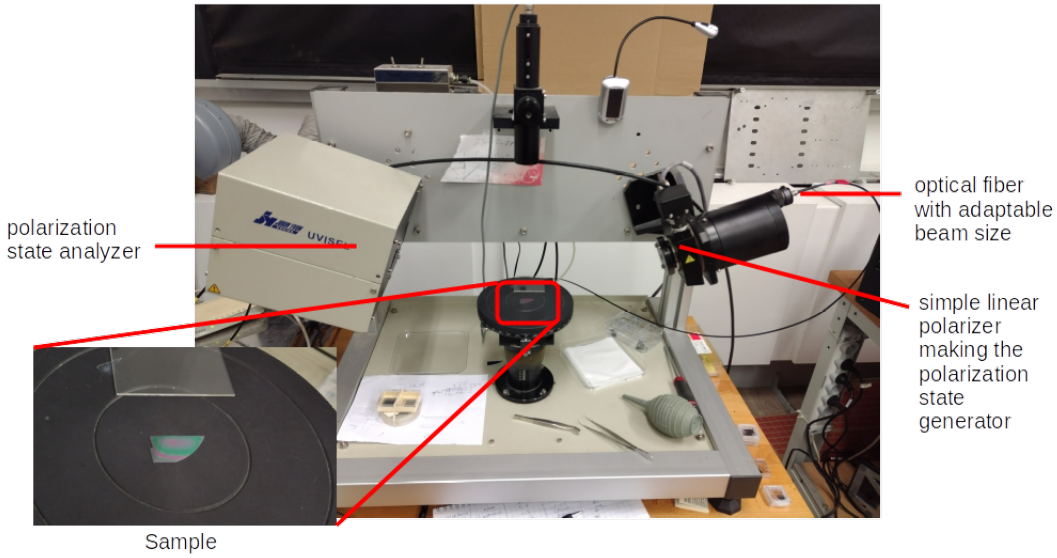

Figure 2.5: Description of the standard UV-Visible ellipsometer at LPICM laboratory of Ecole Polytechnique.

2.5 UV-Visible ellipsometer

In collaboration with Enrique Garcia-Caurel at LPICM of Ecole Polytechnique, I used the commercial standard ellipsometer UVISEL operating in the UV-Visible range. The instrumental setup is shown in Fig.2.5. The light is provided by a halogen lamp followed by an optical fiber to transfer the beam towards the polarization state generator and control the beam size and focalization. The polarization state generator is only made of a linear polarizer contrary to the Mueller ellipsometer described previously. The light is linearly polarized when reaching the sample at an angle of 70°. In practice, we adjust the height of the sample platform to optimize the signal and ensure an accurate focalization. We also align the sample in a region with homogeneous thickness. Different colors can be seen on the sample (see Fig.2.5). This is caused by interference fringes in the film layer and variations of the film thickness. We ensure that the beamspot is localized in a region with only one color. After reflection upon the sample, the beam reaches the polarization state analyzer made of a photo-elastic modulator followed by a linear polarizer. The beam then reaches the monochromator before the photomultiplier detector.

Bibliography

Alderson, L. et al. (2023). "Early Release Science of the exoplanet WASP-39b with JWST NIRSpec G395H". In: *Nature* 614, pp. 664–669. DOI: 10.1038/s41586-022-05591-3.

Baker, V.R. (2006). "Geomorphological Evidence for Water on Mars". In: *Elements* 2.3, pp. 139–143. DOI: 10.2113/gselements.2.3.139.

Batalha, N. et al. (2015). "Testing the early Mars H2–CO2 greenhouse hypothesis with a 1-D photochemical model". In: *Icarus* 258, pp. 337–349. DOI: 10.1016/j.icarus.2015.06.016.

Batalha, N.M. (2014). "Exploring exoplanet populations with NASA's Kepler Mission". In: *Proceedings of the National Academy of Sciences of the United States of America* 111, pp. 12647–12654. DOI: 10.1073/pnas.130419611.

Bean, J.L., S.N. Raymond, and J.E. Owen (2021). "The Nature and Origins of Sub-Neptune Size Planets". In: *JGR : planets* 126. DOI: 10.1029/2020JE006639.

Bellucci, A. et al. (2009). "Titan solar occultation observed by Cassini/VIMS: gas absorption and constraints on aerosol composition". In: *Icarus* 201, pp. 198–216. DOI: 10.1016/j.icarus.2008.12.024.

Benz, W. et al. (2021). "The CHEOPS mission". In: *Experimental Astronomy* 51, pp. 109–151. DOI: 10.1007/s10686-020-09679-4.

Berry, J.L. et al. (2019). "The Influence of Gas-phase Chemistry on Organic Haze Formation". In: *The Astrophysical Journal Letters* 885.1. DOI: 10.3847/2041-8213/ab4b5b.

Betzler, A.S. and J.G.V Miranda (2023). "Relation between Mass and Radius of Exoplanets Distinguished by their Density". In: *Research in Astronomy and Astrophysics* 23.6. DOI: 10.1088/1674-4527/accbb1.

Borucki, W.J., D. Koch, et al. (2010). "Kepler Planet-Detection Mission: Introduction and First Results". In: *Science* 327, pp. 977–980. DOI: 10.1126/science.11854.

Borucki, W.J., D.G. Koch, et al. (2011). "CHARACTERISTICS OF PLANETARY CANDIDATES OBSERVED BY KEPLER. II. ANALYSIS OF THE FIRST FOUR MONTHS OF DATA". In: *The Astrophysical Journal* 736.1. DOI: 10.1088/0004-637X/736/1/19.

Botet, R., P. Rannou, and M. Cabane (1997). "Mean-field approximation of Mie scattering by fractal aggregates of identical spheres". In: *Applied Optics* 36, pp. 8791–8797. DOI: 10.1364/AO.36.008791.

Bourgalais, J. et al. (2020). "Ions in the Thermosphere of Exoplanets: Observable Constraints Revealed by Innovative Laboratory Experiments". In: *The Astrophysical Journal* 895.2. DOI: 10.3847/1538-4357/ab8e2d.

Bowler, B.P. (2016). "Imaging Extrasolar Giant Planets". In: *Publications of the Astronomical Society of the Pacific* 128.968. DOI: 10.1088/1538-3873/128/968/102001.

Brogi, M. et al. (2017). "A Framework to Combine Low- and High-resolution Spectroscopy for the Atmospheres of Transiting Exoplanets". In: *The Astrophysical Journal Letters* 839.1. DOI: 10.3847/2041-8213/aa6933.

Carrasco, N. et al. (2016). "Laboratory analogues simulating Titan's atmospheric aerosols: Compared chemical compositions of grains and thin films". In: *Planetary and Space Science* 128, pp. 52–57. DOI: 10.1016/j.pss.2016.05.006.

Catling, D.C. and K.J. Zahnle (2020). "The Archean atmosphere". In: *Science Advances* 6.9. DOI: 10.1126/sciadv.aax1420.

Chao, K.-H. et al. (2021). "Lava worlds: From early earth to exoplanets". In: *Geochemistry* 81. DOI: 10.1016/j.chemer.2020.125735.

Charbonneau, D. et al. (2002). "Detection of an Extrasolar Planet Atmosphere". In: *The Astrophysical Journal* 568.1. DOI: 10.1086/338770.

Coutelier, M. et al. (2021). "Distribution and intensity of water ice signature in South Xanadu and Tui Regio". In: *Icarus* 364. DOI: 10.1016/j.icarus.2021.114464.

Dawson, R.I. and J.A. Johnson (2018). "Origins of Hot Jupiters". In: *ANNUAL REVIEW OF ASTRONOMY AND ASTROPHYSICS* 56, pp. 175–221. DOI: 10.1146/annurev-astro-081817-051853.

Deng, J. et al. (2020). "A magma ocean origin to divergent redox evolutions of rocky planetary bodies and early atmospheres". In: *Nature Communications* 11. DOI: 10.1038/s41467-020-15757-0.

Ding, F. and R.D. Wordsworth (2022). "Prospects for Water Vapor Detection in the Atmospheres of Temperate and Arid Rocky Exoplanets around M-dwarf Stars". In: *The Astrophysical Journal Letters* 925.1. DOI: 10.3847/2041-8213/ac4a5d.

Dong, C. et al. (2017). "Atmospheric escape from the TRAPPIST-1 planets and implications for habitability". In: *Proceedings of the National Academy of Sciences of the United States of America* 115, pp. 260–265. DOI: 10.1073/pnas.1708010115.

Dorn, C., L. Noack, and A.B. Rozel (2018). "Outgassing on stagnant-lid super-Earths". In: *Astronomy and Astrophysics* 614.A18. DOI: 10.1051/0004-6361/201731513.

Eager-Nash, J.K. et al. (2020). "Implications of different stellar spectra for the climate of tidally locked Earth-like exoplanets". In: *Astronomy and Astrophysics* 639.A99. DOI: 10.1051/0004-6361/202038089.

ERS-Team (2023). "Identification of carbon dioxide in an exoplanet atmosphere". In: *Nature* 614, pp. 649–652. DOI: 10.1038/s41586-022-05269-w.

Forget, F. et al. (2013). "3D modelling of the early martian climate under a denser CO2 atmosphere: Temperatures and CO2 ice clouds". In: *Icarus* 222, pp. 81–99. DOI: 10.1016/j.icarus.2012.10.019.

Fulton, B.J. et al. (2017). "The California-Kepler Survey. III. A Gap in the Radius Distribution of Small Planets". In: *The Astronomical Journal* 154.3. DOI: 10.3847/1538-3881/aa80eb.

Gaillard, F., F. Bernadou, et al. (2022). "Redox controls during magma ocean degassing". In: *Earth and Planetary Science Letters* 577. DOI: 10.1016/j.epsl.2021.117255.

Gaillard, F. and F. Scaillet (2014). "A theoretical framework for volcanic degassing chemistry in a comparative planetology perspective and implications for planetary atmospheres". In: *Earth and Planetary Science Letters* 403, pp. 307–316. DOI: 10.1016/j.epsl.2014.07.009.

Gao, P., S. Fan, et al. (2017). "Constraints on the microphysics of Pluto's photochemical haze from New Horizons observations". In: *Icarus* 287, pp. 116–123. DOI: 10.1016/j.icarus.2016.09.030.

Gao, P., A.A.A. Piette, et al. (2023). "The Hazy and Metal-rich Atmosphere of GJ 1214 b Constrained by Near- and Mid-infrared Transmission Spectroscopy". In: *The Astrophysical Journal* 951.2. DOI: 10.3847/1538-4357/acd16f.

Gao, P., D.P. Thorngren, et al. (2020). "Aerosol composition of hot giant exoplanets dominated by silicates and hydrocarbon hazes". In: *Nature Astronomy* 4, pp. 951–956. DOI: 10.1038/s41550-020-1114-3.

Gao, P., H.R. Wakeford, et al. (2021). "Aerosols in Exoplanet Atmospheres". In: *JGR : planets* 126. DOI: 10.1029/2020JE006655.

Gardner, J.P. et al. (2006). "The James Webb Space Telescope". In: *Space Science Reviews* 123, pp. 485–606. DOI: 10.1007/s11214-006-8315-7.

Gautier, T., N. Carrasco, A. Buch, et al. (2011). "Nitrile gas chemistry in Titan's atmosphere". In: *Icarus* 213, pp. 625–635. DOI: 10.1016/j.icarus.2011.04.005.

Gautier, T., N. Carrasco, A. Mahjoub, et al. (2012). "Mid- and far-infrared absorption spectroscopy of Titan's aerosols analogues". In: *Icarus* 221, pp. 320–327. DOI: 10.1016/j.icarus.2012.07.025.

Gavilan, L., L. Broch, et al. (2017). "Organic Aerosols in the Presence of CO2 in the Early Earth and Exoplanets: UV–Vis Refractive Indices of Oxidized Tholins". In: *The Astrophysical Journal Letters* 848.1. DOI: 10.3847/2041-8213/aa8cc4.

Gavilan, L., N. Carrasco, et al. (2018). "Organic Aerosols in Anoxic and Oxic Atmospheres of Earth-like Exoplanets: VUV-MIR Spectroscopy of CHON Tholins". In: *The Astrophysical Journal* 861.2. DOI: 10.3847/1538-4357/aac8df.

Ginzburg, S., H.E. Schlichting, and R. Sari (2018). "Core-powered mass-loss and the radius distribution of small exoplanets". In: *MNRAS* 476, pp. 759–765. DOI: 10.1093/mnras/sty290.

Grant, D. et al. (2023). "JWST-TST DREAMS: Quartz Clouds in the Atmosphere of WASP-17b". In: *The Astrophysical Journal Letters* 956.2. DOI: 10.3847/2041-8213/acfc3b.

Guimond, C.M. et al. (2023). "A mineralogical reason why all exoplanets cannot be equally oxidizing". In: *MNRAS* 525, pp. 3703–3717. DOI: 10.1093/mnras/stad2486.

Gupta, A. and H.E. Schlichting (2019). "Sculpting the valley in the radius distribution of small exoplanets as a by-product of planet formation: the core-powered mass-loss mechanism". In: *MNRAS* 487, pp. 24–33. DOI: 10.1093/mnras/stz1230.

Hakim, K. et al. (2023). "Diverse Carbonates in Exoplanet Oceans Promote the Carbon Cycle". In: *The Astrophysical Journal Letters* 942.1. DOI: 10.3847/2041-8213/aca90c.

He, C., S.M. Hörst, N.K. Lewis, et al. (2020). "Sulfur-driven haze formation in warm CO2-rich exoplanet atmospheres". In: *Nature Astronomy* 4, pp. 986–993. DOI: 10.1038/s41550-020-1072-9.

He, C., S.M. Hörst, S. Riemer, et al. (2017). "Carbon Monoxide Affecting Planetary Atmospheric Chemistry". In: *The Astrophysical Journal Letters* 841.2. DOI: 10.3847/2041-8213/aa74cc.

He, C., M. Radke, et al. (2023). "Optical properties of organic haze analogues in water-rich exoplanet atmospheres observable with JWST". In: *Nature Astronomy* 8, pp. 182–192. DOI: 10.1038/s41550-023-02140-4.

He, C., J. Serigano, et al. (2022). "Titan Atmospheric Chemistry Revealed by Low-temperature N2-CH4 Plasma Discharge Experiments". In: *ACS Earth Space Chem.* 6, pp. 2295–2304. DOI: 10.1021/acsearthspacechem.2c00164.

Hoeijmakers, J. et al. (2019). "A spectral survey of an ultra-hot Jupiter. Detection of metals in the transmission spectrum of KELT-9 b". In: *Astronomy and Astrophysics* 627.A165. DOI: 10.1051/0004-6361/201935089.

Howe, A.R., A. Burrows, and W. Verne (2014). "MASS-RADIUS RELATIONS AND CORE-ENVELOPE DECOMPOSITIONS OF SUPER-EARTHS AND SUB-NEPTUNES". In: *The Astrophysical Journal* 787.2. DOI: 10.1088/0004-637X/787/2/173.

Hu, R., L. Peterson, and E.T. Wolf (2020). "O2- and CO-rich Atmospheres for Potentially Habitable Environments on TRAPPIST-1 Planets". In: *The Astrophysical Journal* 888.2. DOI: 10.3847/1538-4357/ab5f07.

Hu, R., S. Seager, and W. Bains (2012). "PHOTOCHEMISTRY IN TERRESTRIAL EXOPLANET ATMOSPHERES. I. PHOTOCHEMISTRY MODEL AND BENCHMARK CASES". In: *The Astrophysical Journal* 761.2. DOI: 10.1088/0004-637X/761/2/166.

Isson, T.T. et al. (2020). "Evolution of the Global Carbon Cycle and Climate Regulation on Earth". In: *Global Biogeochemical Cycles* 34. DOI: 10.1029/2018GB006061.

James, T. and R. Hu (2018). "Photochemical Oxygen in Non-1-bar CO2 Atmospheres of Terrestrial Exoplanets". In: *The Astrophysical Journal* 867.1. DOI: 10.3847/1538-4357/aae2bb.

Jovanovic, L., T. Gautier, L. Broch, et al. (2021). "Optical constants of Pluto aerosol analogues from UV to near-IR". In: *Icarus* 362. DOI: 10.1016/j.icarus.2021.114398.

Jovanovic, L., T. Gautier, V. Vuitton, et al. (2020). "Chemical composition of Pluto aerosol analogues". In: *Icarus* 346. DOI: 10.1016/j.icarus.2020.113774.

Kane, S.R. et al. (2016). "A CATALOG OF KEPLER HABITABLE ZONE EXOPLANET CANDIDATES". In: *The Astrophysical Journal* 830.1. DOI: 10.3847/0004-637X/830/1/1.

Karkoschka, E. and M.G. Tomasko (2011). "The haze and methane distributions on Neptune from HST–STIS spectroscopy". In: *Icarus* 211, pp. 780–797. DOI: 10.1016/j.icarus.2010.08.013.

Kasting, J.F. (1991). "CO2 Condensation and the Climate of Early Mars". In: *Icarus* 94, pp. 1–13. DOI: 10.1016/0019-1035(91)90137-I.

Kawashima, Y. and M. Ikoma (2019). "Theoretical Transmission Spectra of Exoplanet Atmospheres with Hydrocarbon Haze: Effect of Creation, Growth, and Settling of Haze Particles. II. Dependence on UV Irradiation Intensity, Metallicity, C/O Ratio, Eddy Diffusion Coefficient, and Temperature". In: *The Astrophysical Journal* 877.2. DOI: 10.3847/1538-4357/ab1b1d.

Kempton, E.M.-R. et al. (2023). "A reflective, metal-rich atmosphere for GJ 1214b from its JWST phase curve". In: *Nature* 620, pp. 67–71. DOI: 10.1038/s41586-023-06159-5.

Kitzmann, D. and K. Heng (2017). "Optical properties of potential condensates in exoplanetary atmospheres". In: *MNRAS* 475, pp. 94–107. DOI: 10.1093/mnras/stx3141.

Kozakis, T., J.M. Mendonça, and L.A. Buchhave (2022). "Is ozone a reliable proxy for molecular oxygen?" In: *Astronomy and Astrophysics* 665.A156. DOI: 10.1051/0004-6361/202244164.

Lavvas, P. and A. Arfaux (2021). "Impact of photochemical hazes and gases on exoplanet atmospheric thermal structure". In: *MNRAS* 502, pp. 5643–5657. DOI: 10.1093/mnras/stab456.

Lavvas, P.P., A. Coustenis, and I.M. Vardavas (2008). "Coupling photochemistry with haze formation in Titan's atmosphere, Part I: Model description". In: *Planetary and Space Science* 56, pp. 27–66. DOI: 10.1016/j.pss.2007.05.026.

Liggins, P., S. Jordan, et al. (2022). "Growth and Evolution of Secondary Volcanic Atmospheres: I. Identifying the Geological Character of Hot Rocky Planets". In: *JGR : planets* 127. DOI: 10.1029/2021JE007123.

— (2023). "Growth and Evolution of Secondary Volcanic Atmospheres: 2. The Importance of Kinetics". In: *JGR : planets* 128. DOI: 10.1029/2022JE007528.

Liggins, P., O. Shorttle, and P.B. Rimmer (2020). "Can volcanism build hydrogen-rich early atmospheres?" In: *Earth and Planetary Science Letters* 550. DOI: 10.1016/j.epsl.2020.116546.

Luque, R. and E. Pallé (2022). "Density, not radius, separates rocky and water-rich small planets orbiting M dwarf stars". In: *Science* 377, pp. 1211–1214. DOI: 10.1126/science.abl7164.

Lustig-Yaeger, J., G. Fu, et al. (2023). "A JWST transmission spectrum of the nearby Earth-sized exoplanet LHS 475 b". In: *Nature Astronomy* 7, pp. 1317–1328. DOI: 10.1038/s41586-023-06232-z.

Lustig-Yaeger, J., V.S Meadows, and A.P. Lincowski (2019). "The Detectability and Characterization of the TRAPPIST-1 Exoplanet Atmospheres with JWST". In: *The Astronomical Journal* 158.1. DOI: 10.3847/1538-3881/ab21e0.

Madhusudhan, N., N. Crouzet, et al. (2014). "H2O ABUNDANCES IN THE ATMOSPHERES OF THREE HOT JUPITERS". In: *The Astrophysical Journal Letters* 791.1. DOI: 10.1088/2041-8205/791/1/L9.

Madhusudhan, N., S. Sarkar, et al. (2023). "Carbon-bearing Molecules in a Possible Hycean Atmosphere". In: *The Astrophysical Journal Letters* 956.1. DOI: 10.3847/2041-8213/acf577.

Mahjoub, A. et al. (2012). "Influence of methane concentration on the optical indices of Titan's aerosols analogues". In: *Icarus* 221, pp. 670–677. DOI: 10.1016/j.icarus.2012.08.015.

May, E.M. et al. (2023). "Double Trouble: Two Transits of the Super-Earth GJ 1132 b Observed with JWST NIRSpec G395H". In: *The Astrophysical Journal Letters* 959.1. DOI: 10.3847/2041-8213/ad054f.

Mayor, M. and D. Queloz (1995). "A Jupiter-mass companion to a solar-type star". In: *Nature* 378, pp. 355–359. DOI: 10.1038/378355a0.

McElroy, M.B. and T.M. Donahue (1972). "Stability of the Martian Atmosphere". In: *Science* 177, pp. 986–988. DOI: 10.1126/science.177.4053.986.

Mikal-Evans, T. (2022). "Detecting the proposed CH4 –CO2 biosignature pair with the James Webb Space Telescope: TRAPPIST-1e and the effect of cloud/haze". In: *MNRAS* 510, pp. 980–991. DOI: 10.1093/mnras/stab3383.

Moran, S.E., S.M. Hörst, et al. (2022). "Triton Haze Analogs: The Role of Carbon Monoxide in Haze Formation". In: *JGR : planets* 127. DOI: 10.1029/2021JE006984.

Moran, S.E., K.B. Stevenson, et al. (2023). "High Tide or Riptide on the Cosmic Shoreline? A Water-rich Atmosphere or Stellar Contamination for the Warm Super-Earth GJ 486b from JWST Observations". In: *The Astrophysical Journal Letters* 948.1. DOI: 10.3847/2041-8213/accb9c.

Oklopčić, A. and C.M. Hirata (2018). "A New Window into Escaping Exoplanet Atmospheres: 10830 Å Line of Helium". In: *The Astrophysical Journal Letters* 855.1. DOI: 10.3847/2041-8213/aaada9.

Oosterloo, M. et al. (2021). "The role of planetary interior in the long-term evolution of atmospheric CO2 on Earth-like exoplanets". In: *Astronomy and Astrophysics* 649.A15. DOI: 10.1051/0004-6361/202039664.

Ortenzi, G. et al. (2020). "Mantle redox state drives outgassing chemistry and atmospheric composition of rocky planets". In: *Scientific Reports* 10.10907. DOI: 10.1038/s41598-020-67751-7.

Ortiz, J.L., F. Moreno, and A. Molina (1996). "Saturn 1991–1993: Clouds and Hazes". In: *Icarus* 119, pp. 53–66. DOI: 10.1006/icar.1996.0002.

Owen, J.E. and H.E. Schlichting (2024). "Mapping out the parameter space for photoevaporation and core-powered mass-loss". In: *MNRAS* 528, pp. 1615–1629. DOI: 10.1093/mnras/stad3972.

Owen, J.E. and Y. Wu (2013). "KEPLER PLANETS: A TALE OF EVAPORATION". In: *The Astrophysical Journal* 775.2. DOI: 10.1088/0004-637X/775/2/105.

Panek, E. et al. (2023). "A re-analysis of equilibrium chemistry in five hot Jupiters". In: *Astronomy and Astrophysics* 677.A51. DOI: 10.1051/0004-6361/202345975.

Peng, Z. et al. (2013). "Titan's atmosphere simulation experiment using continuum UV-VUV synchrotron radiation". In: *JGR : planets* 118, pp. 778–788. DOI: 10.1002/jgre.20064.

Perrin, Z. et al. (2021). "An Atmospheric Origin for HCN-Derived Polymers on Titan". In: *Processes* 9. DOI: 10.3390/pr9060965.

Powell, D. et al. (2024). "Sulfur dioxide in the mid-infrared transmission spectrum of WASP-39b". In: *Nature* 626, pp. 979–983. DOI: 10.1038/s41586-024-07040-9.

Quick, L.C. et al. (2020). "Forecasting Rates of Volcanic Activity on Terrestrial Exoplanets and Implications for Cryovolcanic Activity on Extrasolar Ocean Worlds". In: *Publications of the Astronomical Society of the Pacific* 132.1014. DOI: 10.1088/1538-3873/ab9504.

Ramirez, R. et al. (2014). "Warming early Mars with CO2 and H2". In: *Nature Geoscience* 7, pp. 59–63. DOI: 10.1038/ngeo2000.

Ramirez, R.M. and L. Kaltenegger (2017). "A Volcanic Hydrogen Habitable Zone". In: *The Astrophysical Journal Letters* 837.1. DOI: 10.3847/2041-8213/aa60c8.

Ranjan, S. et al. (2023). "The Importance of the Upper Atmosphere to CO/O2 Runaway on Habitable Planets Orbiting Low-mass Stars". In: *The Astrophysical Journal Letters* 958.1. DOI: 10.3847/2041-8213/ad037c.

Rannou, P., M. Cabane, et al. (1997). "A new interpretation of scattered light measurements at Titan's limb". In: *JGR : planets* 102, pp. 10, 997–11, 013. DOI: 10.1029/97JE00719.

Rannou, P., M. Coutelier, et al. (2022). "Analysis of four solar occultations by Titan's atmosphere with the infrared channel of the VIMS instrument: Haze, CH4, CH3D, and CO vertical profiles". In: *Astronomy and Astrophysics* 666.A140. DOI: 10.1051/0004-6361/202243045.

Reed, N.W. et al. (2023). "The Influence of Hydrogen Sulfide on the Optical Properties of Planetary Organic Hazes: Implications for Exoplanet Climate Modeling". In: *The Astrophysical Journal Letters* 954.2. DOI: 10.3847/2041-8213/acf1a2.

Salama, F. et al. (2017). "Recent Progress in Laboratory Astrophysics Achieved with NASA Ames' COSmIC Facility". In: *Proceedings of the International Astronomical Union* 13, pp. 364–369. DOI: 10.1017/S1743921317011619.

Es-sayeh, M. et al. (2023). "Updated Radiative Transfer Model for Titan in the Near-infrared Wavelength Range: Validation against Huygens Atmospheric and Surface Measurements and Application to the Cassini/VIMS Observations of the Dragonfly Landing Area". In: *The Planetary Science Journal* 4.3. DOI: 10.3847/PSJ/acbd37.

Sciamma-O'Brien, E., C.L. Ricketts, and F. Salama (2014). "The Titan Haze Simulation experiment on COSmIC: Probing Titan's atmospheric chemistry at low temperature". In: *Icarus* 243, pp. 325–336. DOI: 10.1016/j.icarus.2014.08.004.

Sciamma-O'Brien, E., T.L. Roush, et al. (2023). "First Optical Constants of Laboratory-generated Organic Refractory Materials (Tholins) Produced in the NASA Ames COSmIC Facility from the Visible to the

Near Infrared (0.4–1.6 m): Application to Titan's Aerosols". In: *The Planetary Science Journal* 4.7. DOI: 10.3847/PSJ/acd83f.

Seager, S., W. Bains, and R. Hu (2013). "BIOSIGNATURE GASES IN H2 -DOMINATED ATMOSPHERES ON ROCKY EXOPLANETS". In: *The Astrophysical Journal* 777.2. DOI: 10.1088/0004-637X/777/2/95.

Seager, S. and D. Deming (2010). "Exoplanet Atmospheres". In: *ANNUAL REVIEW OF ASTRONOMY AND ASTROPHYSICS* 48, pp. 631–672. DOI: 10.1146/annurev-astro-081309-130837.

Seager, S., M. Schrenk, and W. Bains (2012). "An Astrophysical View of Earth-Based Metabolic Biosignature Gases". In: *Astrobiology* 12.1. DOI: 10.1089/ast.2010.0489.

Sergeev, D.E. et al. (2022). "The TRAPPIST-1 Habitable Atmosphere Intercomparison (THAI). II. Moist Cases—The Two Waterworlds". In: *The Planetary Science Journal* 3.9. DOI: 10.3847/PSJ/ac6cf2.

Shorttle, O. et al. (2024). "Distinguishing Oceans of Water from Magma on Mini-Neptune K2-18b". In: *The Astrophysical Journal Letters* 962.1. DOI: 10.3847/2041-8213/ad206e.

Swift, D.C. et al. (2012). "MASS–RADIUS RELATIONSHIPS FOR EXOPLANETS". In: *The Astrophysical Journal* 744.1. DOI: 10.1088/0004-637X/744/1/59.

Szopa, C. et al. (2006). "PAMPRE: A dusty plasma experiment for Titan's tholins production and study". In: *Planetary and Space Science* 54, pp. 394–404. DOI: 10.1016/j.pss.2005.12.012.

Tian, M. and K. Heng (2024). "Atmospheric Chemistry of Secondary and Hybrid Atmospheres of Super Earths and Sub-Neptunes". In: *The Astrophysical Journal* 963. DOI: 10.3847/1538-4357/ad217c.

Tigrine, S. et al. (2016). "A microwave plasma source for VUV atmospheric photochemistry". In: *J. Phys. D: Appl. Phys.* 49. DOI: 10.1088/0022-3727/49/39/395202.

Tomasko, M.G. et al. (2008). "A model of Titan's aerosols based on measurements made inside the atmosphere". In: *Planetary and Space Science* 56, pp. 669–707. DOI: 10.1016/j.pss.2007.11.019.

Trainer, M.G., J.L. Jimenez, et al. (2012). "Nitrogen Incorporation in CH4-N2 Photochemical Aerosol Produced by Far Ultraviolet Irradiation". In: *Astrobiology* 12.4. DOI: 10.1089/ast.2011.0754.

Trainer, M.G., A.A. Pavlov, et al. (2004). "Chemical composition of Titan's haze: Are PAHs present?" In: *Geophysical Research Letters* 31. DOI: 10.1029/2004GL019859.

Tran, B.N. et al. (2003). "Simulation of Titan haze formation using a photochemical flow reactor The optical constants of the polymer". In: *Icarus* 165, pp. 379–390. DOI: 10.1016/S0019-1035(03)00209-4.

Tsai, S.-M., H. Innes, T. Lichtenberg, et al. (2021). "Inferring Shallow Surfaces on Sub-Neptune Exoplanets with JWST". In: *The Astrophysical Journal Letters* 922.2. DOI: 10.3847/2041-8213/ac399a.

Tsai, S.-M., H. Innes, N.F. Wogan, et al. (2024). "Biogenic Sulfur Gases as Biosignatures on Temperate Sub-Neptune Waterworlds". In: *The Astrophysical Journal Letters* 966.2. DOI: 10.3847/2041-8213/ad3801.

Tsiaras, A. et al. (2016). "DETECTION OF AN ATMOSPHERE AROUND THE SUPER-EARTH 55 CANCRI E". In: *The Astrophysical Journal* 820.2. DOI: 10.3847/0004-637X/820/2/99.

Turbet, M. et al. (2020). "A Review of Possible Planetary Atmospheres in the TRAPPIST-1 System". In: *Space Sci Rev* 216.100. DOI: 10.1007/s11214-020-00719-1.

Udalski, A. et al. (2002). "The Optical Gravitational Lensing Experiment. Search for Planetary and Low-Luminosity Object Transits in the Galactic Disk. Results of 2001 Campaign – Supplement". In: *Acta Astronomica* 52, pp. 115–128. DOI: 10.48550/arXiv.astro-ph/0207133.

Valencia, D. et al. (2013). "BULK COMPOSITION OF GJ 1214b AND OTHER SUB-NEPTUNE EXOPLANETS". In: *The Astrophysical Journal* 775. DOI: 10.1088/0004-637X/775/1/10.

Van Eylen, V. et al. (2018). "An asteroseismic view of the radius valley: stripped cores, not born rocky". In: *MNRAS* 479, pp. 4786–4795. DOI: 10.1093/mnras/sty1783.

Vuitton, V. et al. (2021). "H2SO4 and Organosulfur Compounds in Laboratory Analogue Aerosols of Warm High-metallicity Exoplanet Atmospheres". In: *The Planetary Science Journal* 2.1. DOI: 10.3847/PSJ/abc558.

Wogan, N., J. Krissansen-Totton, and D.C. Catling (2020). "Abundant Atmospheric Methane from Volcanism on Terrestrial Planets Is Unlikely and Strengthens the Case for Methane as a Biosignature". In: *The Planetary Science Journal* 1.3. DOI: 10.3847/PSJ/abb99e.

Wogan, N.F. et al. (2024). "JWST observations of K2-18b can be explained by a gas-rich mini-Neptune with no habitable surface". In: *The Astrophysical Journal Letters* 963.1. DOI: 10.3847/2041-8213/ad2616.

Wolszczan, A. and D.A. Frail (1992). "A planetary system around the millisecond pulsar PSR1257 + 12". In: *Nature* 355, pp. 145–147. DOI: 10.1038/355145a0.

Wordsworth, R. and R. Pierrehumbert (2013). "Hydrogen-Nitrogen Greenhouse Warming in Earth's Early Atmosphere". In: *Science* 339, pp. 64–67. DOI: 10.1126/science.1225.

Wunderlich, F. et al. (2019). "Detectability of atmospheric features of Earth-like planets in the habitable zone around M dwarfs". In: *Astronomy and Astrophysics* 624.A49. DOI: 10.1051/0004-6361/201834504.

Zahnle, K. et al. (2008). "Photochemical instability of the ancient Martian atmosphere". In: *JGR : planets* 113. DOI: 10.1029/2008JE003160.

Zieba, S. et al. (2023). "No thick carbon dioxide atmosphere on the rocky exoplanet TRAPPIST-1 c". In: *Nature* 620, pp. 746–749. DOI: 10.1038/s41586-023-06232-z.

Astronomy & Astrophysics manuscript no. output
November 27, 2024
©ESO 2024

Chapter 3 : Photochemistry of habitable CO_2-H_2 atmospheres explored using experimental and numerical simulations

T. Drant[1,2], N. Carrasco[1,3], P. Pernot[4], S.-M. Tsai[5], L. Vettier[1], T. Gautier[1,6], Z. Perrin[1], M. Maurice[7], M. Turbet[7,8], F. Forget[7], A. Delavois[7], and K. Heng[2,9,10]

[1] LATMOS, Université Paris Saclay, UVSQ, Sorbonne Université, CNRS, 11 Boulevard d'Alembert, 78280 Guyancourt, France.
e-mail: thomas.drant@latmos.ipsl.fr

[2] Ludwig Maximilian University, Faculty of Physics, Observatory of Munich, Scheinerstrasse 1, Munich D-81679, Germany.

[3] ENS Paris-Saclay, 4 avenue des Sciences, 91190 Gif-sur-Yvette, France.

[4] Institut de Chimie Physique, UMR8000 CNRS, Université Paris-Saclay, 91405 Orsay, France.

[5] Department of Earth and Planetary Sciences, University of California, Riverside, CA, USA.

[6] LESIA, Observatoire de Paris, Université PSL, CNRS, Sorbonne Université, 5 place Jules Janssen, 92195 Meudon, France.

[7] Laboratoire de Météorologie Dynamique/IPSL, CNRS, Sorbonne Université, Ecole Normale Supérieure, PSL Research University, Ecole Polytechnique, 75005 Paris, France.

[8] Laboratoire d'astrophysique de Bordeaux, Univ. Bordeaux, CNRS, B18N, allée Geoffroy Saint-Hilaire, 33615 Pessac, France.

[9] University of Bern, ARTORG Center for Biomedical Engineering Research, Murtenstrasse 50, CH-3008, Bern, Switzerland.

[10] University of Warwick, Department of Physics, Astronomy & Astrophysics Group, Coventry CV4 7AL, United Kingdom.

ABSTRACT

Experimental photochemistry is used to characterize the evolution of a room-temperature CO_2-H_2 gas mixture representative of early and/or volcanically active planetary atmospheres similar to current predictions of early Mars. The experiment revealed a significant build-up of water vapor and the absence of hydrocarbon species. Chemical kinetics modelling of the experimental conditions explain the production of water by CO_2 photolysis products reacting with molecular hydrogen. H_2 is identified as a key molecule to produce water vapor in the upper atmosphere and thus increase oxidizing reactions rates. Application of this process to the early martian atmosphere with 1D modelling revealed that the H_2O density reaches the saturation level above the tropospheric cold trap in only a few years. For a hypothetical H_2-rich Trappist-1e planet, the high-altitude formation of water increases CO oxidation rates and therefore prevents the fast photochemical runaway predicted in a H_2-poor scenario. High-altitude build-up of H_2O_2 can exceed the ppm level, its accumulation is higher around Trappist-1 given the lower near-UV flux of the star. In the present study, we apply a quantitative approach to retrieve molecular abundances of stable species from mass spectrometry data acquired during photochemical experiments. Future applications of this method to more complex mixtures will help improve our understanding of exoplanet atmospheric photochemistry and help identify key products relevant for future observations with the James Webb Space Telescope.

Key words. atmospheres, terrestrial planets

1. Introduction

Observations of ancient geological terrains on Mars provided evidence of stable liquid water at the surface around 3.8 Ga (e.g. Carr (1995)). Climate modelling revealed that a CO_2-H_2O atmosphere does not provide sufficient warming to sustain a surface water reservoir under the lower luminosity of the young Sun and lower tropospheric lapse rate induced by CO_2 condensation (Kasting 1991; Wordsworth et al. 2010; Forget et al. 2013; Ramirez et al. 2014). At this early stage in the planet's evolution still marked with an active volcanism, the atmospheric composition can differ significantly from the current state with an enrichment in reduced volcanic greenhouse gases that could compensate the faint luminosity of the Sun and increase surface temperature above the freezing point of water (Sagan 1977). The observations of rocky exoplanet atmospheres now possible with the James Webb Space Telescope (JWST) open a new era where the detection of volcanically active planets could help constrain the feasibility of our current hypotheses regarding the history of Mars' atmosphere and climate.

Decades of research were dedicated to solving the puzzle of the early martian climate, known as the faint young Sun paradox (see review of Haberle et al. (2017)). Scattering-induced warming by atmospheric aerosols was tested although proven to be inefficient for CO_2 ice clouds (Forget et al. 2013; Kitzmann 2016) and sulfuric condensates (Tian et al. 2010; Kerber et al. 2015). Scattering by high-altitude water ice clouds remains a plausible scenario (Urata & Toon 2013; Kite et al. 2021) although a credible source of water is needed above the tropospheric cold trap to maintain a stable cloud cover (Turbet et al. 2020; Ramirez & Kasting 2017). Since the early martian atmospheric composition cannot be constrained directly, different scenarios have been considered to assess their radiative impact. Ramirez et al. (2014) suggested that CO_2-H_2 warming via collision induced absorption (CIA) is efficient assuming a significant build-up of molecular hydrogen through volcanic outgassing. Additional work pointed out that several processes could have driven this high accumulation of atmospheric H_2 including serpentinization and clathtrate destabilisation (Batalha et al. 2015; Chassefière et al. 2016; Wordsworth et al. 2017), radiolysis (Tarnas et al. 2018) or impact-driven thermochemistry (Haberle et al. 2019). The initial calculations of Ramirez et al. (2014) revealed that an atmosphere with 5% H_2 and $\geq$ 1.3 bar of CO_2 would provide sufficient warming to solve the faint young Sun paradox. Motivated by these results, ab-initio calculations and laboratory measurements of the CO_2-H_2 CIA cross sections confirmed the strong radiative effect of this mechanism as it provides a new source of opacity at the peak of the planet's thermal emission, in the transparent windows of CO_2 and H_2O (Wordsworth et al. 2017; Turbet et al. 2019; Godin et al. 2020; Turbet et al. 2020b). Using their own CIA cross sections derived experimentally, Turbet et al. (2020b) found that an early martian atmosphere with 15% H_2 and 1.3 bar of CO_2 can explain the presence of stable liquid water at the surface. CO_2-CH_4 CIA was also suggested although it is not sufficient as the sole source of

warming when $CH_4/CO_2 \leq 0.1$ (Wordsworth et al. 2017; Turbet et al. 2020b; Godin et al. 2020) and the formation of photochemical aerosols is expected to induce an anti-greenhouse effect when $CH_4/CO_2 \geq 0.1$ (Haqq-Misra et al. 2008).

An H_2-rich early martian atmosphere is currently the most likely scenario which can realistically explain a stable, warm and wet early Mars climate. This reasoning first specific to the puzzle of the early Mars motivated further exploration given the important implications to the notion of planetary habitability. The work of Pierrehumbert & Gaidos (2011) and Ramirez & Kaltenegger (2017) pointed out that the radiative effect of H_2 via CIA redefines the outer edge limit of the habitable zone (HZ). CO_2-H_2 CIA-induced warming can extend this limit up to 60% further away from the host star for an atmosphere of 50% H_2 (Ramirez & Kaltenegger 2017). Liggins et al. (2020) confirmed that H_2-rich atmospheres are possible for rocky exoplanets with a reduced mantle although it strongly depends on the planet's volcanic flux and the host star's XUV flux. In the era of JWST, these objects make ideal targets by their high pressure scale height (Ramirez & Kaltenegger 2017), not to mention the spectral features of collision pairs providing crucial constraints on the bulk atmospheric composition (Schwieterman et al. 2015).

Interpreting observations of rocky exoplanet atmospheres requires a good understanding of their chemical evolution under different possible environments. The study of Hu et al. (2012) revealed the long lifetime of outgassed CO and CH_4 mainly affected by atmosphere-surface interactions in oxidized atmospheres. Detection of CO and/or CO_2 in habitable exoplanets informs on the stability of the atmosphere as CO build-up is mainly affected by water photolysis and the HOx cycle (Hu et al. 2012; James & Hu 2018; Ranjan et al. 2020, 2023). O_2-build up to percentage levels was found to be inconsistent with the evolution of CO_2-dominated atmospheres confirming the reliability of O_2 and O_3 as biosignatures (James & Hu 2018; Ranjan et al. 2023). Inferring O_2 concentrations from O_3 detections is however non-trivial as the relationship between these species is non-linear and strongly affected by the stellar type (Kozakis et al. 2022). For rocky habitable planets around M stars, the increased Far-UV to near-UV flux ratio favors the build-up of CO as CO_2 is photolyzed more efficiently than H_2O (Tian et al. 2014; Hu et al. 2020; Ranjan et al. 2020). Both gas composition and stellar environment must be known to interpret the observations of these simple molecules subjected to geochemical and photochemical false positives (Grenfell 2017). Other complex molecular species produced only by life would make better biosignature candidates although these trace gases are often short-lived in the atmosphere given their reduced state and their weak molecular bonds easily dissociated by UV photons (Seager et al. 2012, 2013). Photochemical products can also have important greenhouse properties as seen for nitrous oxide N_2O (Airapetian et al. 2016) and hydrogen peroxide H_2O_2 (Ito et al. 2020) with an accumulation favored in exoplanets orbiting cool stars (Grenfell et al.

2013; Tian et al. 2014). The detection of these different photochemical products would help constrain the chemical and physical mechanisms at play in these potentially habitable atmospheres.

The present study will explore the role of molecular hydrogen in the chemical evolution of early/volcanic atmospheres. In Section 2, we will present experimental photochemistry simulations for a CO_2-H_2 gas mixture representative of the early Mars. Section 3 will focus on chemical kinetics modelling to understand the chemical reactions at play during our experimental simulation. The last section will assess the implications for early Mars and exoplanet atmospheres around M stars.

2. Photochemical experiment of a CO_2-H_2 gas mixture

2.1. APSIS experimental setup

Experimental simulations were performed to better understand the chemistry and identify the main photochemical products likely to build up in volcanic CO_2-H_2 atmospheres. The photochemical reactor APSIS (Atmospheric Photochemistry SImulated by Surfatron), described in detail in Carrasco et al. (2013) and Peng et al. (2013), is used to reproduce the low-pressure chemistry driven by VUV photons in the upper layers of planetary atmospheres. A gas mixture with volume mixing ratios of 85% CO_2 and 15% H_2 is chosen to match the abundances required to warm the surface of early Mars using updated CO_2-H_2 CIA cross sections (Turbet et al. 2020b). VUV irradiation is monochromatic, the wavelength and flux are controlled by the chosen noble gas (Tigrine et al. 2016). We use a primary irradiation at 104.8 nm in the present experiment to focus on neutral chemical reactions where CO_2 photolysis is efficient.

The initial gas mixture of carbon dioxide and molecular hydrogen is injected in the reactor chamber at a total rate of 2 sccm (standard cubic centimeter per minute) from high-purity gas bottles using MKS mass flow rate controllers. A surfatron coupled to the reactor chamber uses a sustained plasma of argon exciting its resonance lines to provide irradiation at 104.8 nm with a smaller contribution at 106.66 nm. Argon is injected in the surfatron at a rate of 2.5 sccm and then flows in the reactor chamber through a 0.5 cm^2 windowless aperture. This specific geometry creates an irradiation cone inside the reactor chamber away from the walls to avoid the effects of heterogeneous catalysis. The configuration and operating parameters of the UV source are chosen to ensure that chemistry is solely initiated by photons (Tigrine et al. 2016). The pressure is kept higher in the surfatron to make sure that the reactive medium does not flow into the UV source. In the APSIS reactor chamber, an outward flow is maintained through the 20-nm orifices of a ceramic membrane followed by a turbomolecular pump. The membrane creates an appropriate intake pressure for efficient functioning of the pump and it increases the residence time of the gas mixture in the reactor to $\approx$ 90s leading to higher abundances

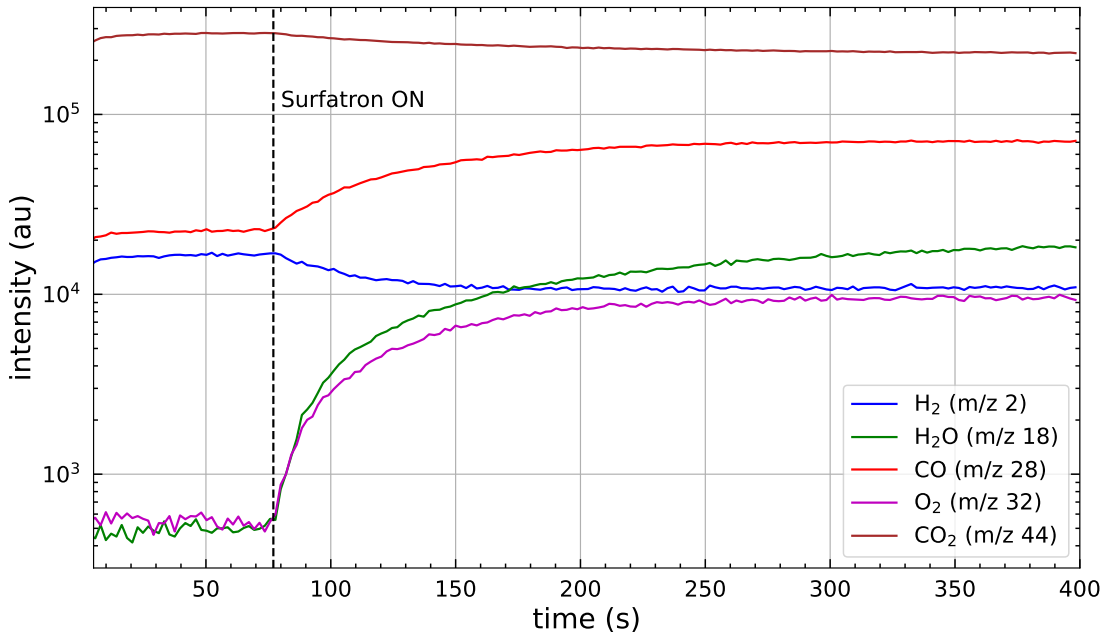

Fig. 1: Temporal evolution of measured intensities (in arbitrary units) following the production and consumption of specific species during the photochemical experiment. The initial gas composition is made of 85% CO_2 and 15% H_2. The vertical dashed line marks the activation of the surfatron UV source.

and thus better detection of photochemical products. During the experiments, continuous injection and pumping provide a constant flow that stabilizes the pressure at 1hPa.

A Hiden EQP200 quadrupole mass spectrometer (QMS) is coupled to the reactor chamber and used to sample gas species flowing through a 100-micron entrance aperture. During the experiment, the gas phase chemistry can be monitored using mass spectrometry and thus reveal the formation of photochemical products. Before each experiment, the APSIS reactor and the QMS are pumped down to approximately 10^{-7} and 5.10^{-9} hPa respectively.

2.2. Experiment : identification of photochemical products

During the experiment, the multiple ion detection (MID) mode of the QMS is used to moniter the intensity at specific chosen *m/z*. The production and consumption of stable species can therefore be assessed as the UV source is turned on using their characteristic *m/z*. Fig.1 presents the temporal evolution of the chemical system as the surfatron is activated. Only the *m/z* for which we observed notable variations of the signal are shown. The measurement is stopped as the system reaches equilibrium between the continuous gas flow and the VUV-driven chemistry which we will refer to as the steady-state.

The photochemical experiment revealed CO, O_2 and H_2O as the main photochemical products accumulating to large abundances (Fig.1). No C2 hydrocarbon species are identified given the absence

of intensity variations at *m/z* 26 or 30. Although the main contribution of C_2H_4 at *m/z* 28 overlaps with CO, the absence of fragment contributions at *m/z* 26 and 27 suggest the absence of C_2H_4 in the mixture. H_2O_2 at *m/z* 34 and O_3 at *m/z* 48 are also absent in the data suggesting a weak production rate despite the significant production of O_2. Although CO and O_2 are direct photochemical products of CO_2, the significant production of water points to a chemistry that involves molecular hydrogen. The experiment therefore suggests the presence of a chemical pathway leading to the formation of water in an initially dry CO_2-H_2 mixture. This last result is in agreement with a previous early-Earth study that observed a less significant water formation in an N_2-dominated plasma experiment that includes percentage levels of CO_2 and H_2 (Fleury et al. 2015). This result also indicates that the chemical system presents competitive pathways involving O. The large accumulation of CO points to a strong UV flux making CO_2 photolysis largely dominant over CO oxidation. On the other hand, the oxidation rate of CO might be reduced if the hydroxyl radical is efficiently used for the production of molecular oxygen and water.

To better understand these competitive chemical pathways and evaluate the implications for planetary atmospheres of similar composition, comparison between our experimental results and a chemical kinetics model is necessary. The next step is to quantify the relative abundances of our photochemical products and compare these results with the predictions by a chemical kinetics model.

2.3. Retrieval of molecular abundances using mass spectrometry data : model description

The theoretical approach to retrieve molecular abundances from mass spectra is detailed in Gautier et al. (2020), it fundamentally relies on solving the linear relationship between the abundance of each species and the resulting intensities measured at different *m/z* by a low-resolution mass spectrometer :

$$\begin{pmatrix} I_{m/z1} \\ I_{m/z2} \\ \vdots \\ I_{m/zj} \end{pmatrix} = \begin{pmatrix} F_{1,1} & F_{1,2} & F_{1,i} \\ F_{2,1} & F_{2,2} & F_{2,i} \\ \vdots & \ddots & \vdots \\ F_{j,1} & \dots & F_{j,i} \end{pmatrix} \times \begin{pmatrix} N_1 \\ N_2 \\ \vdots \\ N_i \end{pmatrix} \quad (1)$$

Where I is the intensity at *m/z* j, F is the fragment intensity of species i at *m/z* j, and N is the "uncorrected" abundance.

The retrieved abundance is said 'uncorrected' at first as it does not yet correspond to the abundance of the neutral species prior to ionization within the instrument. These abundances must be corrected by the ionization cross section at 70 eV to account for the ionization efficiency of the different species in the ion source of the QMS. The final relative abundances are expressed as follows in Gautier et al. (2020) :

$$\frac{C_1}{C_2} = \frac{N_1 \times \sigma_2}{N_2 \times \sigma_1} \tag{2}$$

Where C is the abundance of species i and σ is the ionization cross section at 70 eV.

The calculation relies on the use of a fragmentation pattern for each species which describes its imprint on a mass spectrum with unit resolving power (F matrix in Eq.1). To understand this concept, one must understand what happens to the neutral molecules in the mass spectrometer. The gas molecules sampled through the entrance aperture reach the ion source and cross path with an electron-beam produced by a filament and accelerated to 70 eV. The interaction between electrons and molecules, often referred to as "electron impact", leads to ionization. The interaction can result in the loss of one electron from the molecule's outermost orbital. The cation formed by direct ionization is called the parent ion (e.g. CO_2^+ for CO_2). However, the excess of energy from the interaction can lead to dissociative ionization forming fragment ions (e.g. CO^+, C^+ or O^+ for CO_2) or double ionization forming doubly charged ions (e.g. CO_2^{++} for CO_2). These ionization processes and the impact on the measured mass spectra are summarized in McLafferty & Tureček (1993). From now on, the mention of fragment ions refers to every ion with a *m/z* lower than the parent ion, it thus includes doubly charged cations. The parent and fragment ions all contribute to the measured mass spectrum at different *m/z*, their relative intensities make up the fragmentation pattern. In the case of our photochemical experiment, CO^+ at *m/z* 28 combines two contributions : parent ion of CO produced in the reactor chamber by photochemistry and the fragment ion of CO_2. One must distinguish between these contributions to accurately retrieve the abundance of CO in the reactive medium. In a complex gas mixture, the patterns of all species will overlap given the typical low mass resolution of a QMS. In other words, ions of different chemical nature can have a similar *m/z* and therefore contribute to the same peak intensity. Accurate data is therefore needed for the fragmentation pattern database to decompose the measured mass spectrum using Eq.1 with the correct contribution of each molecule.

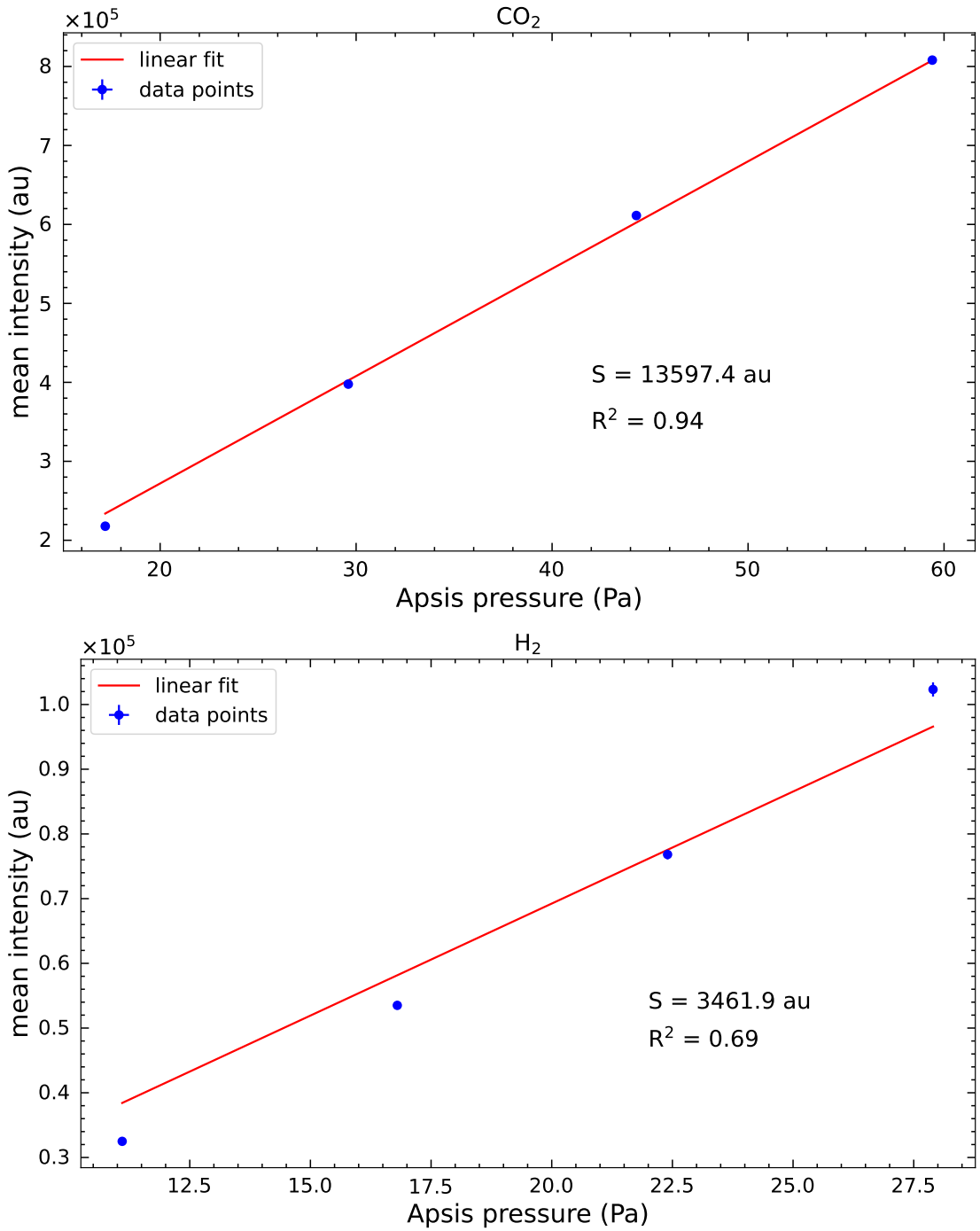

Fig. 2: Calibration of instrument sensitivity S for CO_2 and H_2 with the EQP200 Quadrupole Mass Spectrometer. Linear fit provides the I/P correction factor used in the retrieval model. The quality of the fit is reflected in R^2.

The algorithm described in Gautier et al. (2020) solves Eq.1 using non-negative linear least-square fitting to retrieve the "uncorrected" abundance from the measured mass spectrum and the constructed fragmentation pattern database of potential candidates. This mathematical procedure decomposes the mass spectrum to quantify the contribution of each species listed in the database. The resulting residual is highly sensitive to the accuracy of the fragmentation patterns. The model performs Monte Carlo simulations to propagate the uncertainties on the fragment relative intensities into the retrieved 'un-

corrected' abundance. It is rather difficult to define a prior uncertainty on the fragmentation pattern. Very few data are publicly available, one must often use data from the NIST Chemistry WebBook[1]. The fragmentation pattern of a single molecule is indeed significantly different from one instrument to the next. Gautier et al. (2020) attributed this to the change of geometry of the ion source. In practice, several other instrumental effects can explain these variations. For the purpose of the present study, we were able to create our own fragmentation pattern database with the same instrument used for the photochemical experiment. We obtained data for CO_2, H_2, CO, H_2O, O_2 and Ar (flowing in the mixture from the UV source). Comparison between our own database and one constructed using data available on the NIST Chemistry WebBook taught us that variations as high as 80% can be found. This can introduce large errors during the retrieval calculations, it is thus crucial to have a database constructed with the same instrument used to measure the analyzed mass spectrum.

For the present application of the model, we found that several instrumental effects introduce large uncertainties on the retrieved abundances if not accounted for. In the following, we describe the experimental protocol and formalism used to consider these effects in the model in addition to the fundamental theory described in Eq.1 and 2. These corrections are always needed in practice to analyze measured data (e.g. Serigano et al. (2022), Leseigneur et al. (2022) and Gautier et al. (2024)).

First, an additional correction was added to account for the fact that each fragmentation pattern spectrum is normalized with its peak of maximum intensity. If not corrected for, the sum of all peak intensities in the pattern will differ from one species to the next and therefore introduce an error in the retrieved 'uncorrected' abundance (Eq.1). The normalization of the database can be a large source of error when considering species prone to significant fragmentation in the ion source.

The instrumental effects important to consider are those that exhibit mass-dependent efficiencies. Starting even before the ionization process, the transfer of neutral species from the APSIS reactor through the 100-micron aperture of the QMS can be described by a molecular flow (Knudsen number around 1). The gas flux becomes inversely proportional to the square-root of the mass meaning that H_2 diffuses more efficiently in the instrument compared to the other heavier gases. After the ionization process, the transmission of cations through the quadrupole mass filter (QMF) also exhibits mass-dependent efficiency caused by geometrical effects on the electric field (Ehlert 1970; Antony Joseph et al. 2018). After the mass filter, the ions arrive at the secondary electron multipler (SEM) detector also characterized by a mass-dependent gain (Barnett 1954; Van Gorkom & Glick 1970; Reagan et al. 1987). Light gases, such as H_2, can also be affected by a lower pumping efficiency within the instrument.

[1] NIST chemistry WebBook : https://webbook.nist.gov/chemistry/

Species	*m/z* calibrated	I/P	R^2	σ_{max}
CO_2	44	13597.4	0.94	933.4
H_2	2	3461.9	0.69	534.4
CO	28	6312.6	1.03	116.7
O_2	32	4430.6	1.59	851.3
He	4	3189.4	0.86	299.4
Ne	20	4370.0	0.89	344.4
Ar	40 (Ar^+)	9482.3	0.89	758.9
	20 (Ar^{++})	1575.7	0.88	121.8
N_2	28	12847.2	0.94	632.2

Table 1: Instrument sensitivities (I/P) of the calibrated gases. σ_{max} is the maximum deviation from the fitted slope (Fig.2).

These effects are complex and difficult to assess accurately individually. On first approximation, they can however be all accounted for using a single correction factor which we will refer to as the instrumental response or sensitivity. This assumption is reasonable as most instrumental effects will exhibit an efficiency linearly proportional to the species density. In other words, the measured intensity of a species can in principle be calculated directly using its partial pressure in the APSIS reactor and its instrumental sensitivity. This linear coefficient corresponds to the constant intensity to pressure ratio (I/P) determined during a calibration procedure. For the present photochemical experiment, every gas except water could be calibrated thus providing accurate instrumental sensitivities with our EQP200 Hiden QMS. The experimental procedure consists of measuring the intensity of the parent ion at different pressures and calculate the I/P. The pressure range for the measurements was chosen based on a first guess for the partial pressure of the given species. The calibration measurements of CO_2 and H_2 are given as examples in Fig.2. H_2 is the species that presents the highest error on the slope as this light species is strongly affected by all the mass-dependent physical processes occuring in the QMS. If the instrument sensitivity cannot be determined for every species, an alternative is to obtain a transmission function of the instrument using the I/P of the available gases and interpolating for the missing uncalibrated *m/z* (Chatain et al. 2020). The water sensitivity was derived using this approach although it is subjected to a larger uncertainty as the detector gain for example is not only function of the *m/z* but also function of the chemical nature of the ion (Barnett 1954; Reagan et al. 1987). The instrument sensitivities of the different calibrated gases are listed in Table 1.

Using the instrument sensitivity, the relative abundance of neutral species in the APSIS reactor can be expressed as :

$$\frac{C_1}{C_2} = \frac{N_1 \times S_2 \times \sum_{j,i=1} F_{1,j}}{N_2 \times S_1 \times \sum_{j,i=2} F_{2,j}}$$
$$\text{With : } S_i = \frac{I_j}{P_i \times A_i} \tag{3}$$

Where S_i is the instrumental response specific to species i using its parent ion. The sum of $F_{i,j}$ corresponds to the normalization correction using the sum of all fragment peak intensities in the fragmentation pattern. I_j is the intensity of the fragment used for the calibration (usually parent ion), P_i is the partial pressure of species i in the APSIS reactor, and A_i is the abundance of its main isotope. The ionization cross section is now included in the instrument sensitivity.

The retrieval model was also equipped with a bootstrap analysis on the Monte Carlo runs to ensure that the sample size is sufficient and statistically representative. In practice, we re-sample amongst all the retrieved abundances obtained for the different Monte Carlo runs and ensure that the mean abundance of each species is constant within an error of 0.001%. As a post-processing analysis of the posteriors, we calculate a correlation matrix using the abundances of the different species to assess degeneracy and evaluate the accuracy of the model solutions. This last feature is particularly useful when considering different species with overlapping patterns which can lead to correlated abundances sensitive to the uncertainty on the fragmentation patterns. Hydrocarbons for example tend to overlap at similar *m/z*, correlation analyses might help understand the less accurate quantification of C_2H_6 in the sensitivity study of Gautier et al. (2020) on simulated mass spectra.

As this model was developed to analyze mass spectra of photochemical mixtures with gases unknown a priori, it can be used to test the detection of trace species and provide upper limits of their mixing ratios. We assess the correlation between the retrieved abundance of potential trace species and the fragment intensities of more abundant species sharing similar *m/z*. This approach evaluates the sensitivity of the detection to other species present in the mixture with similar *m/z* contributions. The different features of the model are summarized in Fig.3. The current model considering instrumental effects is validated on simple laboratory gas mixtures in Appendix A.

2.4. Retrieval of molecular abundances using mass spectrometry data : application to the CO_2-H_2 photochemical experiment

The retrieval model was used on the two measured spectra. First, we acquired a spectrum before activating the surfatron to quantify the mixing ratios of CO_2 and H_2 in the initial gas mixture. The second spectrum is acquired during irradiation, once the chemical system reached a steady-state as evaluated in Fig.1. This last spectrum holds information on the abundances of photochemical products. Each spectrum is the mean of 8 spectra acquired consecutively from *m/z* 1 to 50.

For the data analysis of the photochemical experiment, we use a sample size of 300,000 Monte Carlo runs to account for the higher number of species compared to the validation experiments (see Appendix A). The prior uncertainty on the fragmentation patterns is set to 10% with the exception of H_2 and water set to 20%. The fragmentation pattern of water was retrieved using residual water

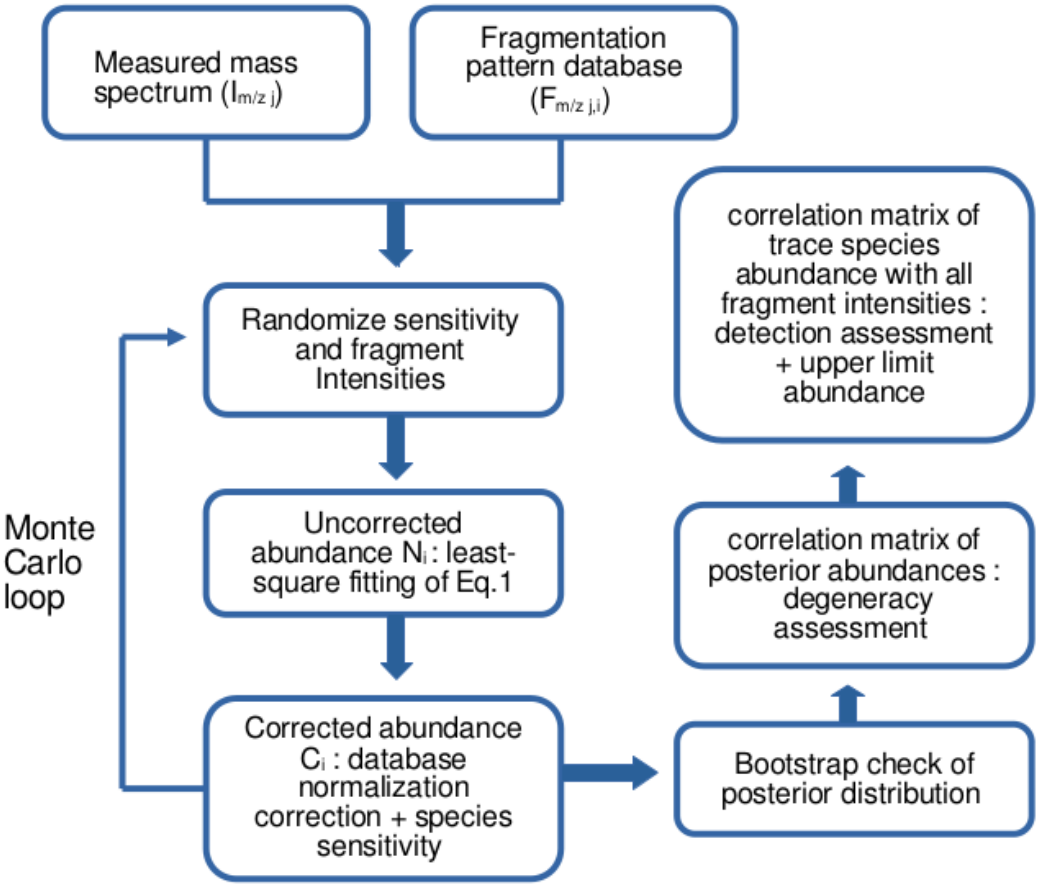

Fig. 3: Flow schematic of the current algorithm to retrieve abundances from mass spectra with unit resolving power (adapted from Gautier et al. (2020)).

signatures observed during the model validation experiment (e.g. *m/z* 17 and 18 in Fig.A.3). The prior uncertainties on the instrument sensitivities are given in Table 1. A uniform law is used during sampling for both fragment relative intensities and instrument sensitivities to not under-estimate these uncertainties.

Fig.4 shows the results of the analysis for the first mass spectrum obtained on the initial gas mixture without irradiation. The retrieved abundance of H_2 is very close to the known injected abundance, we emphasize that a slight deviation is expected as pumping effect can lower the CO_2 to H_2 abundance ratio (explanations in Appendix A). Fig.5 shows the results for the irradiated gas mixture once it reached a dynamical-chemical steady-state.

The model efficiently reproduces the measured spectrum with a very low residual given the accuracy of our fragmentation pattern database. The top right panel shows the strong correlation between the posterior abundances of CO and CO_2 with a Pearson coefficient of -0.77. This result stems from the common CO^+ ion contributing at *m/z* 28. A higher uncertainty on their fragmentation pattern would thus lead to an even stronger degeneracy in the retrieved abundances. This result emphasizes

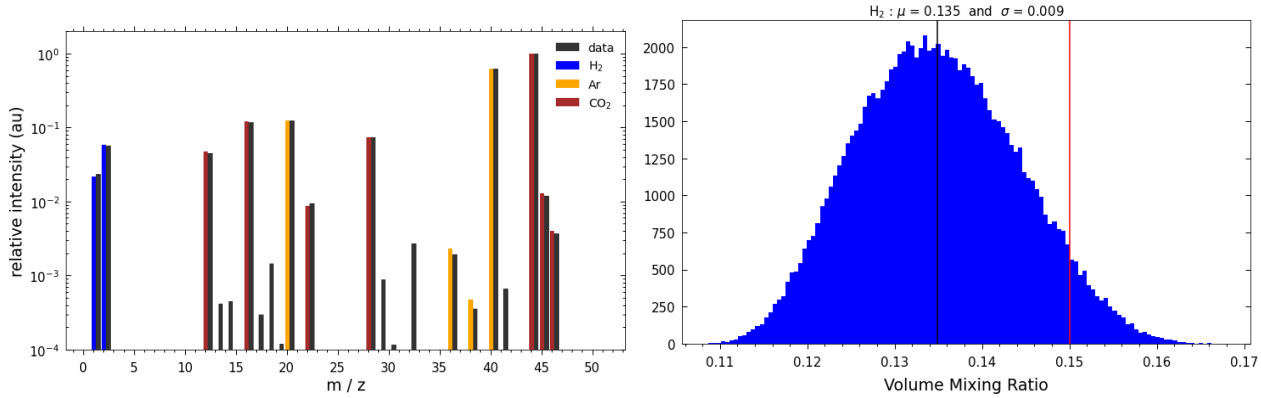

Fig. 4: Retrieval of H_2 mixing ratio in the photochemical experiment with 85% CO_2 and 15% H_2, before activation of the UV source. (left) Measured mass spectrum and best fit showing the contribution of each species. (right) Probability density function of the retrieved H_2 mixing ratio compared to the known abundance in the injected gas mixture (red line).

the need to perform a meticulous calibration of the main species to avoid accumulating these correlated behaviors in complex mixtures.

To evaluate the accuracy of the retrieved abundances, one can also look at the chemical balance. The loss of CO_2 and H_2 by photochemistry must be compensated by high abundances of photochemical products. Around 20% of CO_2 is lost by photochemistry, the lost C is going in CO with an abundance around 18%. For the O, it goes in both O_2 and H_2O. The abundance of water summed with twice the abundance of O_2 result in a total abundance of 17%. The C-O balance is very reasonable. The loss of H_2 by photochemistry should approximately reflect the production of water to conserve H balance. Around 7% of H_2 is lost by photochemistry which approximately corresponds to the amount of water formed. The hydrogen balance is also reasonable. The three photochemical products are clearly produced at percentage levels. Our result predict a more significant production of water relative to oxygen. A higher uncertainty is seen on the retrieved abundance of H_2O (Fig.5) explained by a larger error on its sensitivity. No other trace product could be clearly identified, we examine this result in more details using a chemical kinetics code in the next section.

3. Interpretation of experimental results with 0D chemical kinetics modelling

The photochemical experiment revealed the accumulation of CO, O_2 and H_2O at percentage levels from an initially dry CO_2-H_2 gas mixture (Fig.5). These high abundances and the absence of hydrocarbon species suggest that specific pathways seem to largely dominate the chemical network. In the following, we aim to identify the key pathways using 0D chemical kinetics modelling with the open-

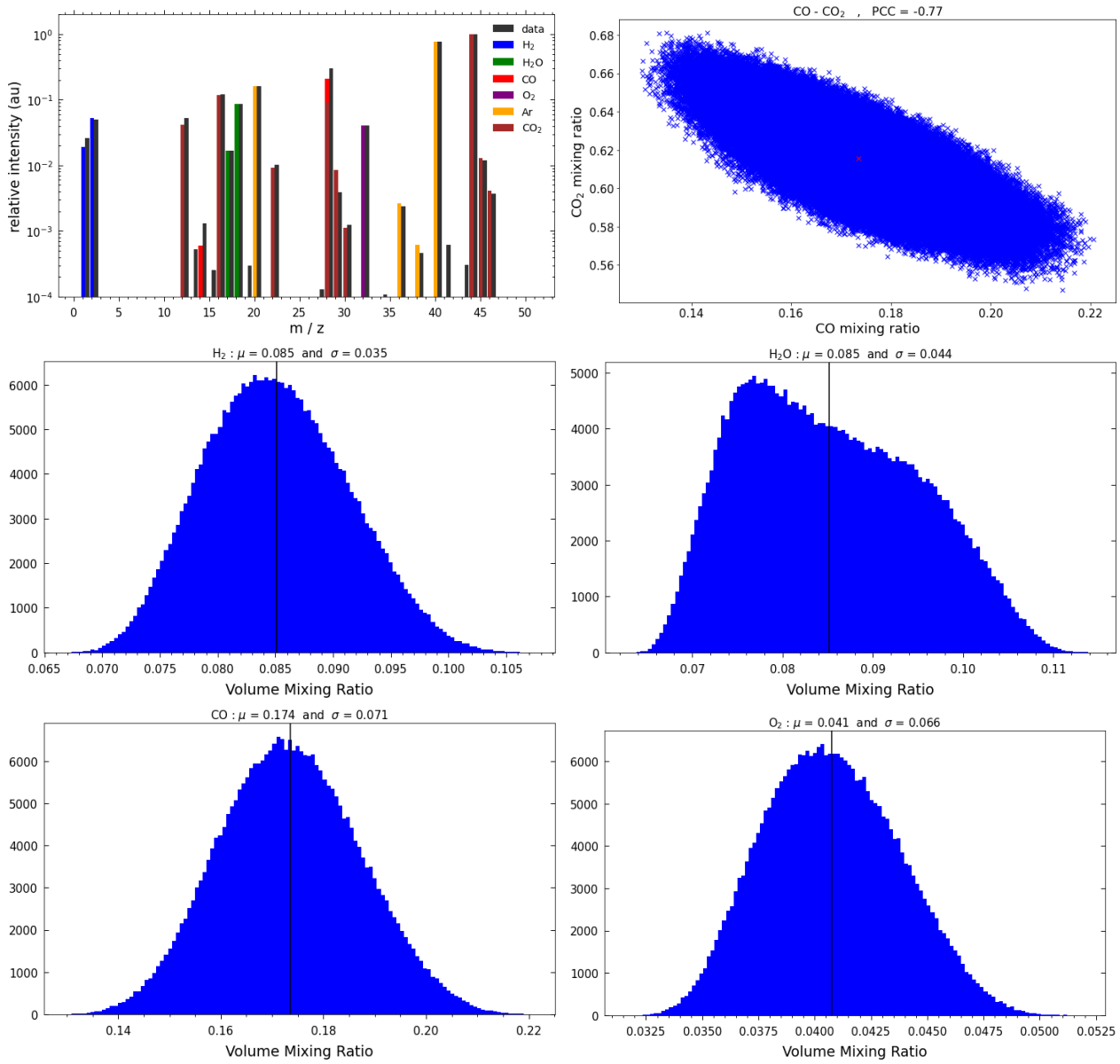

Fig. 5: Retrieved mixing ratios of photochemical products in an irradiated gas mixture with 85% CO_2 and 15% H_2. (top left) Measured and fitted mass spectra with the contribution of each species. (top right) Posterior correlation between the abundances of CO and CO_2. The Pearson correlation coefficient (PCC) is estimated at -0.77. (middle + bottom) Probability density function of the retrieved mixing ratios for H_2, H_2O, CO and O_2.

source ReactorUI[2] code described in Peng et al. (2014) and constructed with a parametrization for the APSIS reactor.

Inputs of the model include the UV flux of the surfatron source at the resonance lines of Ar (104.8 and 106.66 nm). The mean flux of the surfatron was determined from a separate experiment using the photolysis rate of CO_2 monitored with mass spectrometry (details in Appendix B). A unique mean flux of 5.10^{13} photons/cm^2/s is used for the chemical calculations after correcting the 3D geometry of the chamber using the total flux at the exit of the surfatron and the optical depth along the length of the reactor chamber (Peng et al. 2014). The photo-absorption and photo-dissociation cross sections

[2] ReactorUI : https://doi.org/10.5281/zenodo.3946078

of the different gases at room temperature are taken from the Leiden Observatory database[3]. The branching ratios of photolysis reactions are taken from the Phidrates database[4]. The list of chemical reactions initially constructed to study the reduced N_2-CH_4 atmosphere of Titan (Peng et al. 2014) was extended to include oxidizing reactions relevant for a CHO gas mixture (see Appendix C). The model uses a Monte Carlo samping approach to consider uncertainties on the rate constants, cross sections and branching ratios. 500 runs were performed to assess the propagation of these errors in the final steady-state abundances. The Arrhenius coefficients of the rate constants and the uncertainty factors are mainly taken from the Kinetics Database for Astrochemistry (KIDA)[5] when available (see Appendix C for more details). The theory behind the chemical calculations and uncertainty considerations are explained in Appendix C. The model iterates in time for 5,000 s which is sufficient to reach a steady-state.

The results of the simulations are shown in Fig.6. The chemical system reached a steady-state after $\approx$ 100 s following the same order of magnitude seen with the experiment (Fig.1). The simulation clearly shows that CO, H_2O and O_2 are the main species formed by photochemistry. The uncertainty on the mixing ratios is significant given the strong UV flux of the surfatron. The predicted steady-state mixing ratios are compared to the retrieved experimental values in Table 2. Experiment and model predict reasonably similar mixing ratios within the range of uncertainties, both reveal an accumulation of CO, H_2O and O_2 to several percents. The model predicts a significant accumulation of atomic hydrogen. It is explained by the strong UV flux dissociating H_2 efficiently at the chosen wavelength. Recombination of two atomic hydrogen into H_2 is poorly efficient on the other hand. Atomic oxygen does not accumulate as much as it is more reactive. The model simulation also predicts a more significant mixing ratio of O_2 relative to H_2O. We believe this difference to originate from a measurement bias. The very reactive medium indeed accumulates atomic H that can react with O_2 producing first HO_2 followed by water. Radical species are not observed in mass spectrometry given their chemical lifetime shorter than the transfer time from the reactive medium to the ion source of the instrument. The reactive medium is thus not observed directly and a measurement bias arises explaining the higher H_2O/O_2 predicted by the mass spectrometry analysis. Wall catalysis can also cause an increase in H_2O/O_2 abundance ratio although it is unlikely to occur in the current setup as its configuration focuses the monochromatic irradiation in the center of the chamber, away from the walls.

Sensitivity analysis was performed using the 500 Monte Carlo runs, it consists of determining the Spearman correlation coefficient between the rate of a specific reaction and the final predicted abundance of a species. The correlation can therefore reveal how sensitive the abundance is to the

[3] Leiden Observatory database : https://home.strw.leidenuniv.nl/~ewine\/photo/
[4] Phidrates : https://phidrates.space.swri.edu/
[5] KIDA : https://kida.astrochem-tools.org/

uncertainties on the rate constants, branching ratios and cross sections. The analysis revealed that every photochemically-produced species (O_2, CO and H_2O) is mainly sensitive to the photolysis of CO_2 and H_2O. Given the strong UV flux, uncertainties on the photolysis cross sections are important to consider for the prediction of the steady-state abundances.

We performed a rate analysis of the different reactions in the chemical network to identify the main pathways affecting the abundance of water, O_2 and CO. The analysis revealed that all of these species are produced or consumed significantly using the hydroxyl radical OH and therefore compete kinetically at this center of the network. Once the steady-state is reached, OH is produced mainly via the photolysis of water. The dry initial mixture however produces this water using molecular hydrogen and photolysis products of CO_2 following :

$$CO_2 + h\nu \longrightarrow CO + O(1\,D) \quad (1)$$

$$O(1\,D) + H_2 \longrightarrow OH + H \quad (2)$$

$$OH + H_2 \longrightarrow H_2O + H \quad (3)$$

Two molecules of H_2 are consumed for the formation of water via the OH radical. In an H_2-rich gas mixture, the rates of (2) and (3) are high leading to an efficient build-up of water despite its strong dissociation at the current wavelength. The formation of water can occur without the photolysis of H_2, this pathway should therefore be efficient in the entire VUV spectral range where CO_2 photodissociates. The oxidation of H_2 along with the photolysis of water continuously produce OH which is controlling the abundance of the main stable molecules in the mixture. The oxidizing mixture inhibits the formation and accumulation of reduced hydrocarbon species such as CH_4, C_2H_4 or C_2H_6. The hydroxyl radical also controls the formation of O_2 and oxidation of CO through :

$$O + OH \longrightarrow O_2 + H \quad (4)$$

$$CO + OH \longrightarrow CO_2 + H \quad (5)$$

As photolysis of CO mainly occurs at higher photon energies than the present experiment, oxidation by OH represents its only chemical sink although it is here efficiently balanced by the photolysis of CO_2. The production and consumption of H_2O_2 is an essential part of HOx cycle following :

$$H + O_2 + M \longrightarrow HO_2 + M \quad (6)$$

$$OH + OH + M \longrightarrow H_2O_2 + M \quad (7)$$

$$HO_2 + HO_2 \longrightarrow H_2O_2 + O_2 \quad (8)$$

$$H_2O_2 + h\nu \longrightarrow OH + OH \quad (9)$$

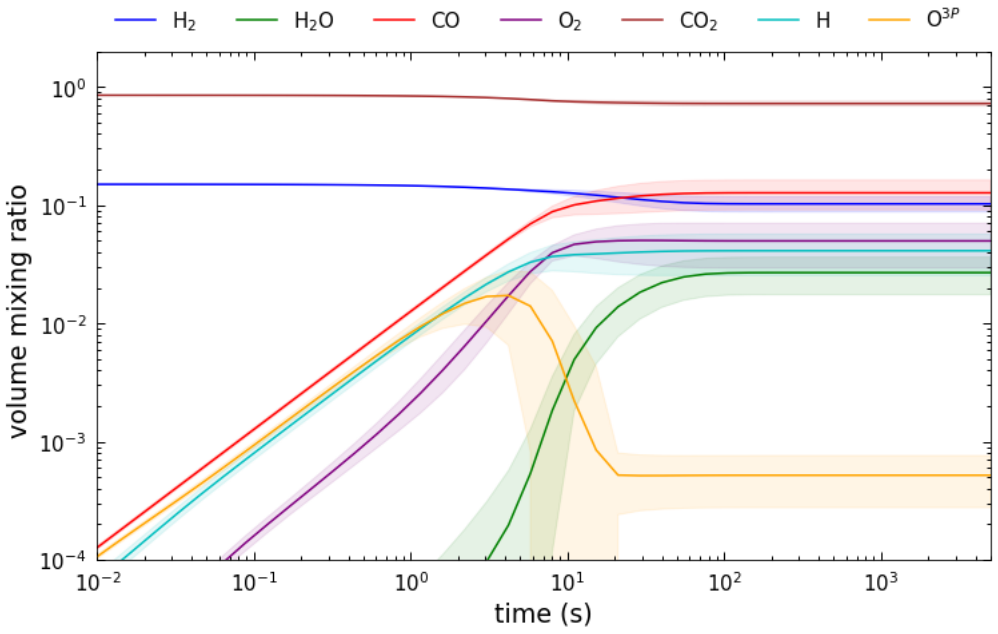

Fig. 6: Temporal evolution of the mixing ratios ($\pm 1\sigma$) during the 0D numerical simulation for an initial gas mixture with 85% CO_2 - 15% H_2. 500 Monte Carlo simulations were performed to account for the uncertainties on the rate constants, branching ratios and cross sections.

The final predicted abundances of H_2O_2 and O_3 at 10^{-8} and 10^{-10} respectively explain their non-detection in the mass spectra during the experiment (Fig.5) given the instrumental detection limit around a few tens of ppm. The consumption of HO_2 to produce water explains the low abundance of H_2O_2 in the present experiment. H_2O_2 build-up could however occur at lower photon energies, where H_2 photolysis is not permitted.

The results shown in this analysis raise several questions regarding the role of H_2 in the chemistry of volcanic atmospheres. In the presence of H_2, the formation of water by photochemistry becomes an additional source at high altitude unrelated to the potential presence of liquid water at the surface of the planet. The photochemical oxidation of molecular hydrogen in CO_2-dominated atmosphere is identified here as an additional sink of H_2 along with atmospheric escape. As stated, the presence of molecular hydrogen renders the atmosphere wet and could therefore play a significant role in the stability of CO_2 atmospheres, preventing a significant and continuous build-up of CO. For exoplanet atmospheres, since the efficiency of this photochemical process becomes stellar-type-dependent, the aim is to predict differences in final outcomes to test these theories with JWST observations in the near future. 1D photochemical simulations are performed in the following section to address these different points.

Species	Retrieved abundances	1σ	Predicted abundances	1σ
CO_2	0.61	0.04	0.722	0.04
H_2	0.08	0.01	0.102	0.01
CO	0.17	0.01	0.127	0.03
H_2O	0.08	0.01	0.027	0.01
O_2	0.04	0.01	0.050	0.02

Table 2: Comparison between the retrieved abundances in the photochemical experiment and the predicted abundances with the 0D chemical kinetics model.

4. Implications for early Mars and habitable planets around M stars

4.1. A photochemical source of water in the early Martian atmosphere

1D simulations are performed using the open source 1D chemical kinetics code VULCAN described in Tsai et al. (2017) and Tsai et al. (2021). The initial gas composition is varied using different volume mixing ratios of molecular hydrogen to assess its role on the photochemical accumulation of water in the upper atmosphere and its redistribution towards the lower atmosphere. We will distinguish between a dry and wet scenario : the dry scenario refers to an atmosphere initially deprived of water, the wet scenario considers the presence of water vapor following its saturation curve in the lower atmosphere with a vertically quenched mixing ratio around 10^{-5} above the cold trap. The temperature profile follows Batalha et al. (2015) considering a moist adiabat of water and CO_2 in the troposphere. We mimick vertical mixing using the K_{zz} profile derived by Massie & Hunten (1981) for modern Earth and often considered for rocky planets under habitable conditions (Hu et al. 2012; Batalha et al. 2015). We use the stellar spectrum of an Early Sun (0.6 Ga) modeled in Claire et al. (2012) which exhibits a higher extreme ultra-violet (EUV) to far UV (FUV) flux ratio compared to modern Earth. We focus on a 1 bar early Martian atmosphere following previous paleopressure estimations based on crater size distributions (Kite et al. 2014; Kurokawa et al. 2018; Warren et al. 2019). Given the poor constraints on the nitrogen partial pressure in the early martian atmosphere (Adams et al. 2021), we focus on a CHO system.

360 chemical reactions are considered in the network including the different pathways to form methane and hydrocarbons. C_2H_6 is the most complex hydrocarbon species considered in the network, the oxidizing nature of the studied atmosphere would not allow a more complex atmospheric chemistry. Kinetic constants of two- and three-body reactions are taken from KIDA which mainly compiles data from Tsang & Hampson (1986); Baulch et al. (1992, 1994, 2005); Atkinson et al. (2004); Harada et al. (2010); Sander et al. (2011); Loison et al. (2014), valid at cool temperatures and used in the Titan chemistry simulations of Hébrard et al. (2009). Photo-absorption and dissociation cross sections along with branching ratios are taken from the Leiden Observatory database. We consider the Rayleigh scattering cross sections of CO_2, CO, H_2, O_2 for the calculation of the optical depth. Molecular hydrogen is assumed to escape at diffusion-limited rate (Ramirez et al. 2014;

Batalha et al. 2015; Liggins et al. 2020). No surface emissions are considered, the feasibility of building H_2-rich atmosphere was already assessed (Batalha et al. 2015; Liggins et al. 2020), the present study focuses on the photochemical mechanisms induced by the presence of H_2. Photochemical products such as O_2, H_2O_2 and CO can react with minerals, these surface sinks are important although deposition velocities are largely unknown and dependent on the surface composition (Zahnle et al. 2008; Hu et al. 2012). No surface sinks are considered, we will discuss their potential influence on the build-up of photochemical products in the lower atmosphere.

The results of the different dry simulations are shown in Fig.7. The top panel describes the mixing ratios of water and CO after $\approx$ 25 years using different initial mixing ratios of H_2. We emphasize that the model is not coupled to a radiative transfer calculator at the time, we therefore assume a similar P-T profile regardless of the initial mixing ratio of H_2. The bottom panel shows the abundance of hydrogen peroxide recently proposed as an important warming agent for early Mars (Ito et al. 2020).

We observe an abundance of water in the upper atmosphere strongly correlated to the initial concentration of H_2. Our results show that a 10% H_2 atmosphere could accumulate enough water vapor in several years to reach the condensation level above the cold trap. We find a similar effect if the atmosphere is initially wet close to the surface. Photochemistry is identified as a key source of water, above the cold trap, in H_2-rich atmospheres. Recent studies proposed high-altitude water ice clouds as candidates to warm the surface of the early Mars (Segura et al. 2008; Urata & Toon 2013; Kite et al. 2021). Given the high sedimentation rate of ice cloud particles and the low water vapor concentration above the cold trap, this process would not be efficient in the absence of an additional high-altitude source of water (Turbet et al. 2020). We find that a wet H_2-rich atmosphere could significantly increase the water concentration above the cold trap. More work is needed to assess the efficiency and sustainability of this process against the kinetics of condensation and sedimentation.

We performed a rate analysis of the chemical network and confirmed that H_2 oxidation is the primary pathway to form water. Although the 0D chemical kinetics of the experiment previously revealed that the hydroxyl radical is initially produced from the unstable O(1D) radical reacting with H_2, the 1D analysis now considering a realistic solar spectrum shows that the same reaction with the more stable O(3P) radical is more efficient as O(1D) is only produced efficiently at very low pressures. The analysis also confirms that two-body reactions with the OH radical are the main pathways to O_2 formation and CO destruction with a weak contribution of three-body reactions. We confirm that H and O are the main reactive species accumulating to high abundances in the upper atmosphere as discussed in Hu et al. (2012). Although the system reached a steady-state after a few hundred years, H_2 is still continuously consumed by photochemistry with a slightly weaker effect of atomic hydrogen recombination. We calculated the lifetime of H_2 controlled by its conversion into water by photochemistry using column integration of the rates and concentrations, we find that H_2 would remain in

the atmosphere for ≈ 200,000 years after the end of the volcanically active period. Diffusion-limited escape would therefore overcome the photochemical destruction of H_2 with a rate of the order of 10^{12} $cm^{-2}.s^{-1}$, so one order of magnitude higher than the overall loss rate by photochemistry. The oxidation rate of H_2 is still significant which explains this strong build-up of water in the upper atmosphere. The chemical pathway controlling the formation of CO and H_2O in the dry early martian atmosphere follows :

$$CO_2 + h\nu \longrightarrow CO + O(3\,P)$$
$$O(3\,P) + H_2 \longrightarrow OH + H$$
$$OH + H_2 \longrightarrow H_2O + H$$
$$H + H + M \longrightarrow H_2 + M$$
$$\text{Net} : CO_2 + H_2 \longrightarrow CO + H_2O$$

The photolysis of one molecule of CO_2 therefore leads to the formation of one molecule of CO and one molecule of H_2O. H_2O and CO build-up is similar initially with similar abundances for both in the upper atmosphere, for the high H_2 abundances scenarios (see Fig.7). For low H_2 abundances (blue and red curves in Fig.7), the CO abundance increases above the abundance of H_2O. This stems from the lack of balance between water photolysis and CO oxidation in the upper atmosphere following :

$$H_2O + h\nu \longrightarrow OH + H$$
$$CO + OH \longrightarrow CO_2 + H$$
$$H + H + M \longrightarrow H_2 + M$$
$$\text{Net} : CO + H_2O \longrightarrow CO_2 + H_2$$

If the production of OH by water photolysis is too slow, the sink of CO by oxidation with OH is weaker than the production of CO via CO_2 photolysis. This kinetic competition controls the stability of CO_2 atmospheres. These chemical mechanisms are summared in Fig.8. If the production of CO dominates over its sink, the atmosphere enters into a photochemical runaway regime where CO_2 is completely consumed over time to produce a CO-dominated atmosphere. This mechanism is affected by the stellar type as water and CO_2 photolysis efficiencies depend on the near-UV to far-UV flux ratio of the star (Hu et al. 2020; Ranjan et al. 2023). In the present work, H_2 abundance is identified as an important factor for runaway given its correlation to water production. The CO build-up rate is also affected by surface sinks (Zahnle et al. 2008) although they are largely unknown for exoplanets.

The bottom panel of Fig.7 shows that hydrogen peroxide reaches abundances above the ppm level at pressures below 0.1 mbar given the high abundances of water vapor. An H_2-poor wet early martian atmosphere could also build-up H_2O_2 above the ppm level in the upper atmosphere. More work is needed to assess the radiative feedback of H_2O_2 using self-consistent calculations of photochemistry

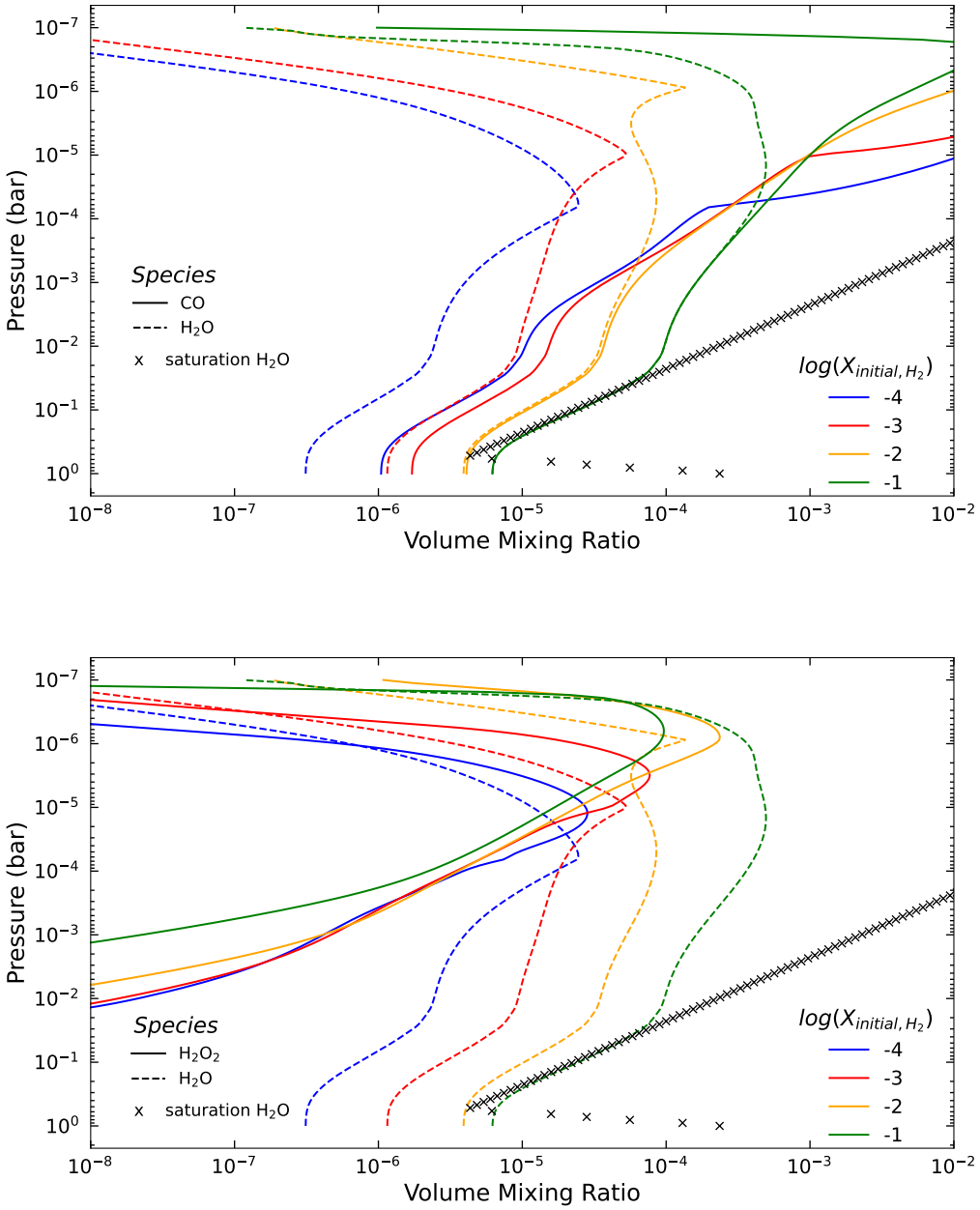

Fig. 7: Mixing ratios of water, carbon monoxide and hydrogen peroxide produced by photochemistry in an initially dry CO_2-dominated early martian atmosphere with different mixing ratios of H_2. The results are shown at a time of 25.7 years when the mixing ratio of water reaches the saturation level for the 10% H_2 scenario.

and radiative transfer.

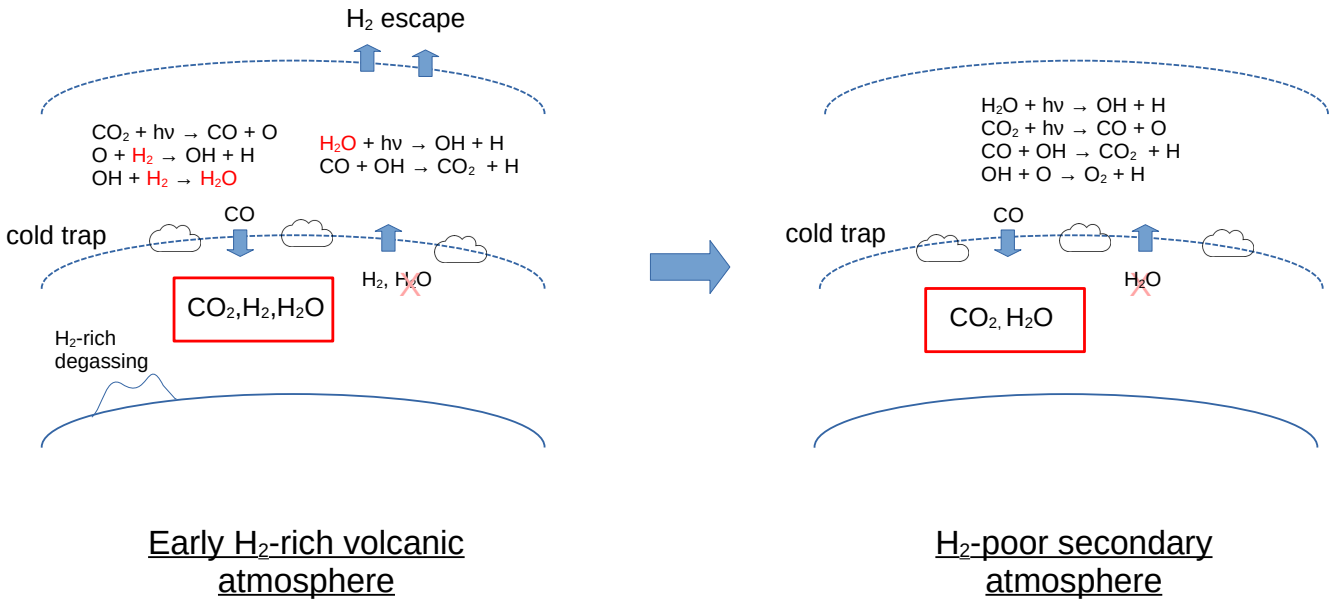

Fig. 8: Schematic summarizing the main mechanisms and chemical reactions affecting the high-altitude abundances of water in volcanic atmospheres.

4.2. H_2-rich atmosphere around Trappist-1e : implication for photochemical runaway and H_2O_2 formation

To assess implications for future observations of exoplanets, we focus on Trappist-1e as it is our best target with an equilibrium temperature suggesting habitable conditions and a cool host star suggesting a difference in the photolysis rates of water and CO_2 compared to Mars. The Trappist-1e simulations are performed using a similar parametrization in VULCAN with only a few changes. The stellar spectrum of Trappist-1 is taken from the MUSCLES survey (France et al. 2016). Surface gravity, planet and orbit radii of Trappist-1e are taken from Gillon et al. (2017). For this case study, we focus on a 10% H_2 atmosphere which would suggest the presence of active volcanism in the recent history of the planet. The aim is to understand the role of molecular hydrogen in the accumulation of photochemical products potentially observable. We want to answer the following questions : Can we infer the large abundance of the spectrally transparent H_2 using specific photochemical products ? Is H_2 controlling the chemical evolution of the atmosphere ?

Fig.9 compares the mixing ratios of water, CO and H_2O_2 between the H_2-rich Trappist-1e and early-mars atmospheres. We confirm previous predictions by Hu et al. (2020) that the accumulation of CO and O_2 is favored around M stars given the lower NUV to FUV flux ratio. The higher CO_2 to H_2O photolysis rate ratio compared to a planet around a Sun-like star should in theory modify the chemical evolution of the atmosphere (Hu et al. 2020). In a H_2-rich scenario, our simulations

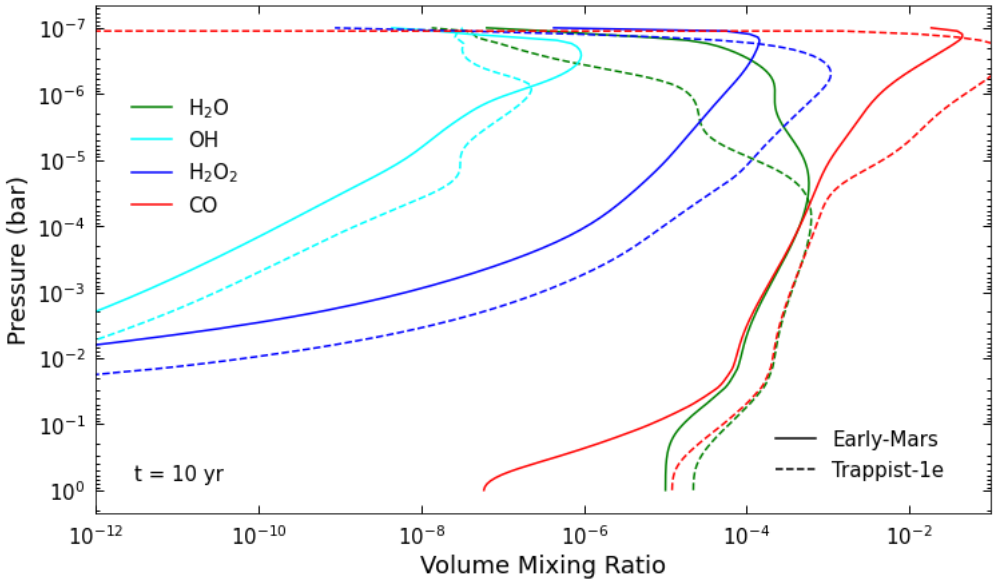

Fig. 9: Comparison of molecular abundances for CO, H_2O and H_2O_2 (after 10 years) between the simulations of the 10% H_2 early Mars and Trappist-1e atmospheres.

show that the significant production of water vapor above the cold trap (Fig.9) constrains the increasing abundance of CO in the upper atmosphere. The strong oxidation of CO in the upper atmosphere bounds its accumulation in the lower atmosphere to the vertical mixing ratio of water. CO can still accumulate to a mixing ratio of 10^{-4} in about 100 years (without surface deposition) but fast runaway is inhibited by the production of water in the upper atmosphere. O_2 runaway is also inhibited and cannot accumulate to percentage levels as predicted in Hu et al. (2020). During its volcanically active period, Trappist-1e could have sustained an H_2-rich atmosphere which prevented photochemical runaway. The confirmation of a habitable CO_2-dominated atmosphere orbiting an M-dwarf with future JWST observations can constrain the presence of an effective process stabilizing the atmosphere. Detection of water vapor in the atmospheres of habitable exoplanets will be challenging given the formation of clouds (Ding & Wordsworth 2022). For the H_2-rich atmosphere, the strong accumulation of water vapor above the cloud cover along with the higher scale height could help observations of these worlds. More work is needed to assess the detectability of water vapor with JWST in H_2-rich exoplanet atmospheres.

Fig.9 also shows that H_2O_2 build-up is higher for the Trappist-1e H_2-rich scenario compared to the early Mars case. The lower NUV flux of the Trappist-1 M star reduces the photolysis rate of hydrogen peroxide still easily dissociated at these wavelengths. The present results highlight that H_2-rich atmosphere could have other greenhouse contributions with H_2O_2 and high-altitude water clouds in addition to CIA.

5. Conclusions

Experimental photochemistry of a CO_2-H_2 gas mixture revealed a significant build-up of water. A side analysis of the chemical network with 0D kinetic modelling proved that key pathways involving molecular hydrogen render the mixture wet thus inhibiting the production of reduced hydrocarbon species. These results suggest the presence of a high-altitude source of water in the upper atmosphere of H_2-rich habitable planets. The application of this process in a 1D column atmosphere representative of an initially dry early Mars proved that the build-up of water can reach the saturation level over several years at an altitude above the tropospheric cold trap. Mixing of the photochemically-produced water to the lower atmosphere leads to condensation and suggest that the water budget of early Mars likely includes a photochemical origin.

H_2-rich atmosphere can be sustained if the active volcanism balances with atmospheric escape. The significant build-up of water in the hypothetical H_2-rich upper atmosphere of Trappist-1e reach detectable levels over several years and might help infer the presence of molecular hydrogen despite the presence of a cloud cover. This additional source of water is also shown to inhibit photochemical runaway and might play a crucial role in the early evolution of secondary atmospheres during the phase of active volcanism. H_2O_2 is found to build-up efficiently in H_2-rich atmospheres around M-dwarf stars given the high abundance of water and the lower near-UV stellar flux compared to Sun-like stars. More studies are needed to assess the climate feedback of high-altitude water clouds and H_2O_2 build-up shown to be possible in H_2-rich atmospheres.

Experimental photochemistry will be needed in the near future to identify key photochemical species that can be used as tracers to infer the presence of a rocky surface on sub-Neptunes or infer the presence of liquid water at the surface of rocky exoplanets. The present work validates and applies a quantitative model to retrieve the abundances of stable species from mass spectrometry data acquired during photochemical experiments. Future applications of the model on more complex mixture will help us improve our knowledge on nitrogen and sulfur photochemistry along with photochemical haze precursors which can have significant implications for future observations of cool and temperate exoplanet atmospheres.

References

Adams, D., Luo, Y., Wong, M.L. et al. 2021, Astrobiology, 21(8), 968-980, doi : 10.1089/ast.2020.2273

Airapetian, V.S., Glocer, A., Gronoff, G., Hébrard, E., Danchi, W. 2016, Nat. Geo., 9, 452-455, doi : 10.1038/ngeo2719

Antony Joseph, M.J., McIntosh, D.G., Raymond Gibson, J., Taylor, S. 2018, Rapid Commun Mass Spectrom, 32, 677-685, doi : 10.1002/rcm.8094

Arney, G., Domagal-Goldman, S.D., Meadows, V.S., Wolf, E.T. et al. 2016, Astrobiology, 16(11), 873-899, doi : 10.1089/ast.2015.1422

Atkinson, R., Baulch, D.L., Cox, R.A. et al. 1989, International Journal of Chemical Kinetics, 21, 115-150, doi : 10.1002/kin.550210205

Atkinson, R., Baulch, D.L., Cox, R.A., Crowley, J.N. et al. 2004, Atmos. Chem. Phys., 4, 1461–1738, doi : 10.5194/acp-4-1461-2004

Atkinson, R., Baulch, D.L., Cox, R.A., Crowley, J.N. et al. 2006, Atmos. Chem. Phys., 6, 3625–4055, doi : 10.5194/acp-8-4141-2008

Barnett, C.F. 1954, Oak Ridge National Laboratory, Carbide and Carbon Chemicals Company

Batalha, N., Domagal-Goldman, S.D., Ramirez, R., Kasting, J.F., Icarus, 258, 337-349, doi : 10.1016/j.icarus.2015.06.016

Baulch, D.L., Cobos, C.J., Cox, R.A. et al. 1992, J. Phys. Chem. Ref. Data, 21, doi : 10.1063/1.555908

Baulch, D., Cobos, C., Cox, R., Frank, P., Hayman, G. et al. 1994, J. Phys. Chem. Ref. Data, 23, 847–1033, doi : 10.1063/1.555953

Baulch, D.L., Bowman, C.T., Cobos, C.J. 2005, J. Phys. Chem. Ref. Data, 24, doi : 10.1063/1.1748524

Burkholder, J.B., Abbatt, J.P.D., Huie, R.E. et al. 2015, JPL publications 15-10

Carr, M.H. 1995, JGR, 100, 7479-7507, doi : 10.1029/95JE00260

Carrasco, N., Giuliani, A., Correia, J.-J., Cernogora, G. 2013, J. Synchrotron Rad., 20, 587-590, doi : 10.1107/S0909049513013538

Chassefière, E., Lasue, J., Langlais, B., Quesnel, Y. 2016, M&PS, 51, doi : 10.1111/maps.12784

Chatain, A., Jiménez-Redondo, M., Vettier, L. et al. 2020, PSST, 29, doi : 10.1088/1361-6595/ab9b1a

Claire, M.W., Sheets, J., Cohen, M., Ribas, I., Meadows, V.S., Catling, D.C. 2012, ApJ, 757, doi : 10.1088/0004-637X/757/1/95

Ding, F. & Wordsworth, R. 2022, ApJL, 925, doi : 10.3847/2041-8213/ac4a5d

Ehlert, T.C. 1970, J. Phys. E: Sci. Instrum., 3, doi : 10.1088/0022-3735/3/3/418

Fleury, B., Carrasco, N., Marcq, E., Vettier, L., Määttänen, A. 2015, ApJL, 807:L29, doi : 10.1088/2041-8205/807/2/L29

Forget, F., Wordsworth, R., Millour, E., Madeleine, J.-B., Kerber, L., Leconte, J., Marcq, E., Haberle, R.M. 2013, Icarus, 222, 81-99, doi : 10.1016/j.icarus.2012.10.019

France, K., Loyd, R.O.P., Youngblood, A., Brown, A. et al. 2016, ApJ, 820, doi : 10.3847/0004-637X/820/2/89

Gans, B., Peng, Z., Carrasco, N., Gauyacq, D., Lebonnois, S., Pernot, P. 2013, Icarus, 223, 330-343, doi : 10.1016/j.icarus.2012.11.024

Gautier, T., Serigano, J., Bourgalais, J., Hörst, S.M., Trainer, M.G. 2020, Rapid Commun Mass Spectrom, 34, doi : 10.1002/rcm.8684

Gautier, T., Serigano, J., Das, K., et al. 2024, A&A, In review.

Gillon, M., Triaud, A., Demory, B.-O. et al. 2017, Nature, 542, 456-460, doi : 10.1038/nature21360

Godin, P.J., Ramirez, R.M., Campbell, C.L. et al. 2020, JGR Planets, 125, doi : 10.1029/2019JE006357

Grenfell, J.L., Gebauer, S., Godolt, M. et al. 2013, Astrobiology, 13, doi : 10.1089/ast.2012.0926

Grenfell, J.L. 2017, Physics Report, 713, 1-17, doi : 10.1016/j.physrep.2017.08.003

Haberle, R.M., Catling, D.C., Carr, M.H., Zahnle, K.J. 2017, The Early Mars Climate System, In: Haberle, R.M., Clancy, R.T., Forget, F., Smith, M.D., Zurek, R.W., eds., The Atmosphere and Climate of Mars, Cambridge Planetary Science. Cambridge University Press, 526-568, doi : 10.1017/9781139060172.017

Haberle, R.M., Zahnle, K., Barlow, N.G., Steakley, K.E. 2019, Geophys. Res. Lett., 46, doi : 10.1029/2019GL084733

Haqq-Misra, J.D., Domagal-Goldman, S.D., Kasting, P.J., Kasting, J.F. 2008, Astrobiology, 8(6), 1127-1137, doi : 10.1089/ast.2007.0197

Harada, N., Herbst, E., Wakelam, V. 2010, ApJ, 721, 1570-1578, doi : 10.1088/0004-637X/721/2/1570

Hébrard, E., Dobrijevic, M., Bénilan, Y., Raulin, F. 2006, J. Photochem. Photobiol., A, 7:211–230, doi : 10.1016/j.jphotochemrev.2006.12.004

Hébrard, E., Dobrijevic, M., Pernot, P., Carrasco, N. et al. 2009, J. Phys. Chem. A, 113, doi : 10.1021/jp905524e

Hébrard, E., Dobrijevic, M., Loison, J.C. et al. 2013, A&A, 552, doi : : 10.1051/0004-6361/201220686

Hu, R., Seager, S., Bains, W. 2012, ApJ, 761, doi : 10.1088/0004-637X/761/2/166

Hu, R., Peterson, L., Wolf, E.T. 2020, ApJ, 888, doi : 10.3847/1538-4357/ab5f07

Ito, Y., Hashimoto, G.L., Takahashi, Y.O., Ishiwatari, M., Kuramoto, K. 2020, ApJ, 893, doi : 10.3847/1538-4357/ab7db4

James, T.S. & Hu, R. 2018, ApJ, 867, doi : 10.3847/1538-4357/aae2bb

Kasting, J.F. 1991, Icarus, 94, 1-13, doi : 10.1016/0019-1035(91)90137-I

Kerber, L., Forget, F., Wordsworth, R. 2015, Icarus, 261, 133-148, doi : 10.1016/j.icarus.2015.08.011

Kite, E.S., Williams, J.-P., Lucas, A., Aharonson, O. 2014, Nat. Geo., 7, doi : 10.1038/NGEO2137

Kite, E.S., Steele, L.J., Mischna, M.A., Richardson, M.I. 2021, PNAS, 118(18), doi : 10.1073/pnas.2101959118

Kitzmann, D. 2016, ApJL, 817, doi : 10.3847/2041-8205/817/2/L18

Kozakis, T., Mendonça, J.M., Buchhave, L.A. 2022, A&A, 665, doi : 10.1051/0004-6361/202244164

Kurokawa, H., Kurosawa, K., Usui, T. 2018, Icarus, 299, 443-459, doi : 10.1016/j.icarus.2017.08.020

Leseigneur, G., Bredehöft, J.H., Gautier, T., et al. 2022, Angewandte Chemie International Edition, 61, doi : 10.1002/anie.202201925

Liggins, P., Shorttle, O., Rimmer, P.B. 2020, EPSL, 550, doi : 10.1016/j.epsl.2020.116546

Lindemann, F.A., Arrhenius, S., Langmuir, I. et al. 1922, Tran. Faraday Soc., 17

Loison, J.-C., Wakelam, V., Hickson, K.M., Bergeat, A., Mereau, R. 2014, MNRAS, 437, 930–945, doi : 10.1093/mnras/stt1956

McLafferty, F.W. & Tureček, F. 1993, Interpretation of Mass Spectra, University Science Books

Massie, S.T. & Hunten, D.M. 1981, JGR, 86(C10), 9859-9868, doi : 10.1029/JC086iC10p09859

Peng, Z., Gautier, T., Carrasco, N., Pernot, P., Giuliani, A., Mahjoub, A., Correia, J.-J., Buch, A., Bénilan, Y., Szopa, C., Cernogora, G. 2013, JGR : planets, 118, 778-788, doi : 10.1002/jgre.20064

Peng, Z., Carrasco, N., Pernot, P. 2014, GeoResJ, 1-2, 33-53, doi : 10.1016/j.grj.2014.03.002

Pierrehumbert, R. & Gaidos, E. 2011, ApJL, 734, doi : 10.1088/2041-8205/734/1/L13

Ramirez, R.M., Kasting, J.F. 2017, Icarus, 281, 248-261, doi : 10.1016/j.icarus.2016.08.016

Ramirez, M.R., Kopparapu, R., Zugger, M.E., Robinson, T.D., Freedman, R., Kasting, J.F. 2014, Nat. Geo., 7, 59-63, doi : 10.1038/NGEO2000

Ramirez, R.M. & Kaltenegger, L. 2017, ApJL, 837, doi : 10.3847/2041-8213/aa60c8

Ranjan, S., Schwieterman, E.W., Harman C. et al. 2020, ApJ, 896, doi : 10.3847/1538-4357/ab9363

Ranjan, S., Schwieterman, E.W., Leung, M., Harman, C.E., Hu, R. 2023, ApJL, 958, doi : 10.3847/2041-8213/ad037c

Reagan, N.R., Frees, L.C., Gray, J.W. 1987, J. Vac. Sci. Technol. A, 5, 2389-2392, doi : 10.1116/1.574460

Ruaud, M., Loison, J.-C., Hickson, K.M., Gratier, P., Hersant, F., Wakelam, V. 2015, MNRAS, 447, 4004–4017, doi : 10.1093/mnras/stu2709

Sagan, C. 1977, Nature, 269, 224-226, doi : 10.1038/269224a0

Sander, S.P., Abbatt, J., Barker, J. R., Burkholder, J. B., Friedl, R. et al. 2011, JPL publication, 10-6

Seager, S., Schrenk, M., Bains, W. 2012, Astrobiology, 12, doi : 10.1089/ast.2010.0489

Seager, S., Bains, W., Hu, R. 2013, ApJ, 777, doi : 10.1088/0004-637X/777/2/95

Segura, T.L., Toon, O.B., Colaprete, A. 2008, JGR, 113, doi : 10.1029/2008JE003147

Serigano, J., Hörst, S.M., He, C. 2022, JGR planets, 127, doi : 10.1029/2022JE007238

Schwieterman, E.W., Robinson, T.D., Meadows, V.S. 2015, ApJ, 810, doi : 10.1088/0004-637X/810/1/57

Tarnas, J.D., Mustard, J.F., Lollar, B.S. et al. 2018, EPSL, 502, 133-145, doi : 10.1016/j.epsl.2018.09.001

Tian, F., Claire, M.W., Haqq-Misra, J.D., Smith, M. et al. 2010, EPSL, 295, 412-418, doi : 10.1016/j.epsl.2010.04.016

Tian, F., France, K., Linsky, J.L., Mauas, P.J.D., Vieytes, M.C. 2014, EPSL, 385, 22-27, doi : 10.1016/j.epsl.2013.10.024

Tigrine, S., Carrasco, N., Vettier, L., Cernogora, G. 2016, J. Phys. D: Appl. Phys., 49, doi : 10.1088/0022-3727/49/39/395202

Tsai, S.-M., Lyons, J.R., Grosheintz, L., Rimmer, P.B., Kitzmann, D., Heng, K. 2017, ApJS, 228, doi : 10.3847/1538-4365/228/2/20

Tsai, S.-M., Malik, M., Kitzmann, D., Lyons, J.R., Fateev, A., Lee, E., Heng, K. 2021, ApJ, 923(2), doi : 10.3847/1538-4357/ac29bc

Tsang, W. & Hampson, R.F. 1986, J. Phys. Chern. Ref. Data, 15, doi : 10.1063/1.555759

Turbet, M., Tran, H., Pirali, O., Forget, F., Boulet, C., Hartmann, J.-M. 2019, Icarus, 321, 189-199, doi : 10.1016/j.icarus.2018.11.021

Turbet, M., Gillmann, C., Forget, F., Baudin, B., Palumbo, A., Head, J., Karatekin, O. 2020, Icarus, 335, doi : 10.1016/j.icarus.2019.113419

Turbet, M., Boulet, C., Karman, T. 2020b, Icarus, 346, doi : 10.1016/j.icarus.2020.113762

Urata, R.A. & Toon, O.B. 2013, Icarus, 226, 229-250, doi : 10.1016/j.icarus.2013.05.014

Van Gorkom, M. & Glick, R.E. 1970, Int. J. Mass Spectrom. Ion Phys., 4, 203-218, doi : 10.1016/0020-7381(70)85038-0

Warren, A.O., Kite, E.S., Williams, J.-P., Horgan, B. 2019, JGR planets, 124(11), 2793-2818, doi : 10.1029/2019JE006178

Wordsworth, R., Forget, F., Eymet, V. 2010, Icarus, 210, 992-997, doi : 10.1016/j.icarus.2010.06.010

Wordsworth, R., Kalugina, Y., Lokshtanov, S. et al. 2017, Geophys. Res. Lett., 44, 665-671, doi : 10.1002/2016GL071766

Zahnle, K., Haberle, R.M., Catling, D.C., Kasting, J.F. 2008, JGR, 113, doi 10.1029/2008JE003160

Appendix A: Retrieval of molecular abundances using mass spectrometry data : model validation using calibration gas mixtures

Gautier et al. (2020) validated the original model using simulated spectra to assess the accuracy of retrieved abundances when considering complex mixtures with overlapping fragments. The model was however not validated with our instrument using a calibration procedure. In this section, we validate the model using simple mixtures to assess the accuracy of the quantification now considering instrumental effects.

The model validation experiments are conducted with the same APSIS setup used during the photochemical CO_2-H_2 experiment, with the exceptions that the UV source is not used and the chamber configuration is static. In other words, the pumping valve is closed when a specific mixture with known relative abundances is injected in the reactor chamber until the pressure reaches 1 hPa. This static configuration is necessary as the differential pumping can modify the known abundances especially when using light gases such as He or H_2. Once the chosen pressure is reached, mass spectra are acquired from *m/z* 1 to 50 with unit resolving power.

Three mixtures are used to perform the model validation. A first mixture contains only noble gases with *m/z* from 4 to 40. This experiment is performed to assess alone the importance of the instrument sensitivity as these gases do not fragment and do not overlap in *m/z* with the exception of Ar^{++} and Ne^{+}. The second mixture is made of CO_2 and N_2 to validate the retrieval of abundances when species have overlapping fragments (N_2^+ and CO^+). The last mixture containing CO and H_2 aims at validating accurate quantification of the H_2 abundance despite the higher uncertainty on its calibration constant (Chatain et al. 2020).

For the data analysis, we chose a sample size of 100,000 which is sufficient given the low uncertainties on the fragmentation pattern and the low number of gases in the mixture. The prior uncertainty on the fragmentation patterns is set to 10% with the exception of H_2 set at 20% to account for the larger measurement error at *m/z* 1. The prior uncertainties on the instrument sensitivities listed in Table 1 are derived for each gas using the maximum deviation between the linear fit and the calibration data points (Fig.2). The errors on the sensitivity and fragmentation patterns are assumed to follow a uniform law as to not under-estimate these important instrumental effects.

The first mixture is made of 75% He, 15% Ne, 5% Ar and other heavier noble gases (Kr, Xe) at higher *m/z* that we did not consider in the analysis as our photochemical experiment will only produce species with *m/z* below that of CO_2. The retrieved abundances of Ne and Ar (relative to He) are shown in Fig.A.1 along with the measured mass spectrum and the fitted mass spectrum of the Monte Carlo run presenting the lowest residual. We find a very accurate retrieved abundance for Ne with a small effect of the instrumental corrections since He and Ne have relatively similar sensitivities (see Table

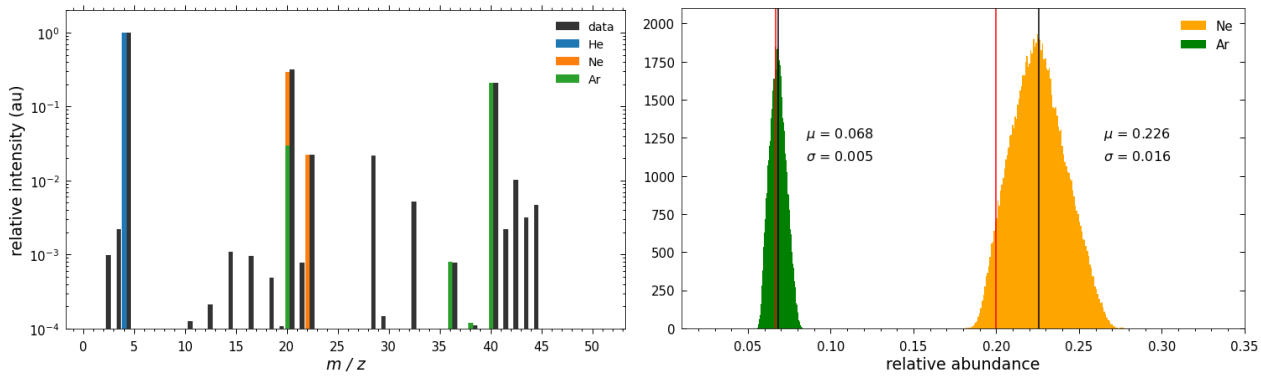

Fig. A.1: Retrieval of relative abundances for the first model validation mixture with 75% He, 15% Ne and 5% Ar. (left) Measured mass spectrum in black and the contribution of each species in the fitted mass spectrum. (right) Probability density function of the retrieved abundances of Ne and Ar relative to He. The known abundances and the retrieved mean abundances are shown with the vertical red and black lines respectively.

1). For argon, we find a significant effect of the sensitivity on the retrieved relative abundance. The sensitivity of Ar is indeed three times lower than the sensitivity of He after correcting for their large difference in ionization efficiency. We observed that a mass spectrum acquired on the same mixture with a Faraday detector will present a peak of argon at *m/z* 40 higher than the peak of Ne at *m/z* 20. We can thus attribute the low Ar sensitivity to its lower gain with the SEM detector compared to He and Ne.

The second mixture contains 60% N_2 and 40% CO_2. These species have relatively similar sensitivities given their close *m/z* but their fragmentation efficiencies are different with the main fragment of CO_2 overlapping with the parent ion of N_2. The retrieved relative abundance of CO_2 is shown in Fig.A.2 along with the mass spectra (measured and best fit). The results teach us that the abundance of CO_2 is under-estimated if the normalization of the database is not corrected for, this stems from the fact that CO_2 presents several fragments whereas N_2 fragments poorly. The normalization correction is not however sufficient as it leads to an over-estimation of the abundance. This result is explained by the sensitivity difference between the fragment ions of CO_2. Indeed, the increased sensitivity of the lower mass fragment ions of CO_2 (CO^+, C^+, O^+ and $CO_2{}^{++}$) leads to an overestimated sum of intensities in the fragmentation pattern. This unknown sensitivity of the fragments is uncorrected and therefore propagates during the normalization correction leading to an over-estimated CO_2 abundance. The error is not significant and will not affect the aim of our photochemical experiment but future applications might require improving the model by considering a fragment-dependent sensitivity instead of unique species-dependent sensitivity.

The last mixture contains 70% of H_2 and 30% of CO. Both molecules don't present many fragments. H_2 is however a difficult molecule to quantify with mass spectrometry given its low mass. In Section 2.3, we showed that the calibration of H_2 is more subjected to errors. The aim is to show

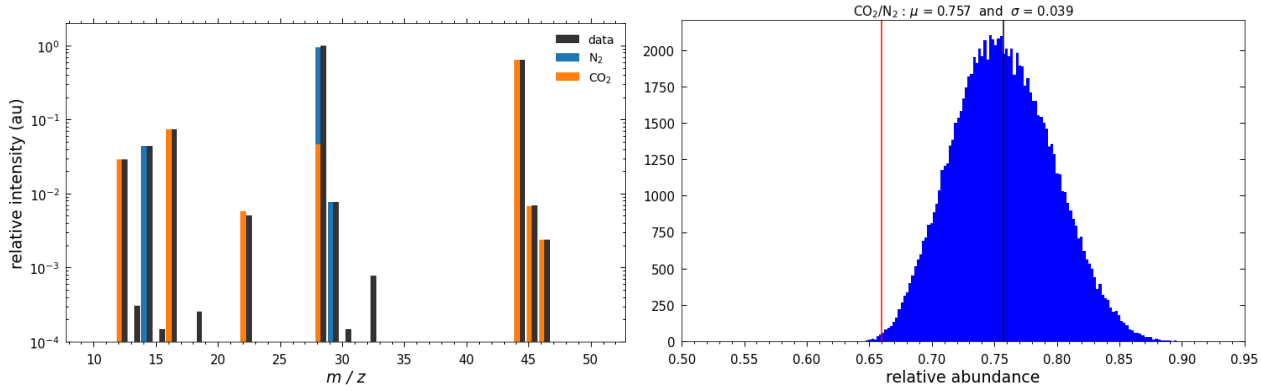

Fig. A.2: Retrieval of relative abundances for the second model validation mixture with 60% N_2 and 40% CO_2. (top) Measured mass spectrum in black and the contribution of each species in the fitted mass spectrum. (bottom) Probability density function of the retrieved abundance of CO_2 relative to N_2. The known abundance and the retrieved mean abundance are shown with the vertical red and black lines respectively.

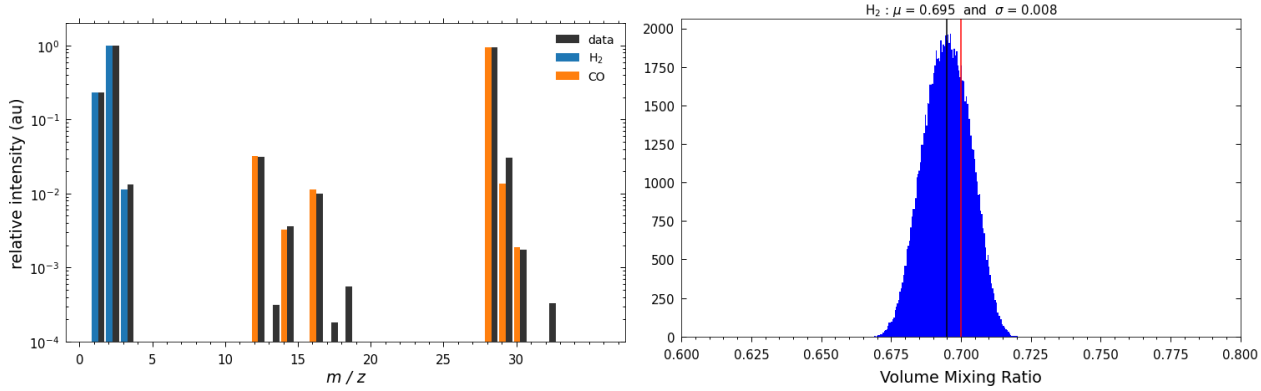

Fig. A.3: Retrieval of abundances for the third model validation mixture with 70% H_2 and 30% CO. (top) Measured mass spectrum in black and the contribution of each species in the fitted mass spectrum. (bottom) Probability density function of the retrieved mixing ratio of H_2. The known abundance and the retrieved mean abundance are shown with the vertical red and black lines respectively.

that H_2 can still be accurately quantified using its sensitivity. The retrieved abundance of H_2 and the mass spectra (measured and best fit) are shown in Fig.A.3. The sensitivity is again identified as the primary parameter affecting the retrieved abundance. We show that the abundance of H_2 is accurately retrieved using the measured sensitivity and its uncertainty. This result confirms that H_2 should be quantified accurately during the data analysis of the CO_2-H_2 photochemical experiment.

The validation experiments proved that the database normalization correction and the instrument sensitivity are the two main parameters affecting the accuracy of the retrieval since our fragmentation pattern are well constrained. Given the range of sensitivities measured for the different species (Table 1), the retrieved abundances can be off by a factor of two to four depending on the gases if this effect is not considered. We emphasize that the sensitivity factor is mainly species-dependent and therefore does not affect the quality of the mass spectrum fit (Eq.1) as opposed to the fragmentation pattern uncertainties, this source of error can thus easily come unnoticed.

Appendix B: UV flux of the surfatron

A preliminary experiment focusing on the photolysis of CO_2 was performed to derive the mean UV flux. We used pure CO_2 injected in the reactor chamber at a rate of 2 sccm. Ar is injected in the surfatron at a rate of 2.5 sccm. The pressure in the APSIS reactor stabilizes at 1hPa. We purposefully used conditions similar to the photochemical experiment as the surfatron flux varies with pressure (Tigrine et al. 2016).

The consumption of CO_2 by photolysis in the chamber is monitored by mass spectrometry following the temporal evolution of intensity at *m/z* 44. The raw data is shown in blue in Fig.B.1 (top panel). The signal often exhibits a temporal drift caused by the electronics of the QMS (see Fig.B.1, top panel). The signal drift is assessed prior to activating the UV source, it usually follows a linear evolution with time which can be easily corrected and extrapolated (see Fig.B.1, top panel). Once the UV source is turned on, the exponential evolution of the intensity at *m/z* 44 directly reflects the evolution of the CO_2 density. This density can be expressed as :

$$N_{CO_2}(t) = N_{CO_2,\infty}\ e^{at+b} \tag{B.1}$$

Where a and b are coefficients quantifying the combined effect of flow and chemistry.

As the photolysis of CO_2 largely dominate the evolution with a negligible contribution of the recombination reaction CO + O + M $\longrightarrow$ CO_2 + M, the time derivation of the CO_2 density can be written as follows,

$$\frac{dN_{CO_2}}{dt} = -N_{CO_2}(\frac{1}{\tau_r} + J_{CO_2})\ + \frac{\phi}{L} \tag{B.2}$$

Where τ_r is the residence time of the gas in the APSIS reactor chamber (s), J_{CO_2} is the photolysis rate constant of CO_2 (s^{-1}), ϕ is the outward flux driven by pumping ($cm^{-2}.s^{-2}$), and L is the length of the reactor chamber (cm).

One can solve B.2 and show that solution is expressed as :

$$N_{CO_2}(t) = N_{CO_2,\infty}\ e^{-(\frac{1}{\tau_r}+J_{CO_2})t+\frac{\phi}{L}} \tag{B.3}$$

The fitted slope in Fig.B.1 (bottom panel) thus equals $-(\frac{1}{\tau_r} + J_{CO_2})$. The residence time of the gas in the reactor chamber (around 90 s) is derived using the injected flow rate and the stabilized 1

hPa pressure assuming ideal gas behavior. The photolysis rate constant of CO_2 at a wavelength of 104.8 nm can be directly estimated. The mean UV flux is hidden in this total photolysis rate constant expressed as (Peng et al. 2014) :

$$J_{CO_2}(\lambda) = \int_0^{\infty} I(\lambda)\ \sigma_{CO_2}(\lambda)\ d\lambda \tag{B.4}$$

Where I is the mean flux at wavelength λ.

For monochromatic irradiation, the flux can be directly calculated using the estimation of the photolysis rate constant and the photodissociation cross section of CO_2 at 104.8 nm taken from the Leiden Observatory database. The total mean flux is estimated at 5.10^{13} photons/cm^2/s. It can also be seen as the effective flux in the reactor chamber that accounts for the geometrical effects, i.e. the smaller volume of the irradiatied medium compared to the volume of the entire chamber.

Appendix C: chemical network and kinetic calculations in ReactorUI

The ReactorUI kinetic database was initially constructed to study the chemistry of the N_2/CH_4 atmosphere of Titan (Peng et al. 2014). New reactions relevant for a CHO chemical system were added to the original network. The kinetic constants and uncertainty parameters of each added reaction are listed in Table C.1 for two-body reactions and Table C.2 for three-body reactions. The reference used for the data is also specified, most of these data are available in KIDA. The three kinetic constants A, B and E_a correspond to the parameters of the Arrhenius law describing the rate constant. For 2-body reactions, the temperature-dependent rate constant is expressed as,

$$K_i(T) = A_i\ (\frac{T}{T_0})^{-B_i}\ e^{-\frac{Ea}{T}} \tag{C.1}$$

Where T_0 is the reference room temperature (300 K).

The rate constant of three-body reactions is expressed following (Hébrard et al. 2013) :

$$K_i(T) = \frac{(K_0(T)\ n_M\ F + K_r)\ K_\infty}{K_0(T)\ n_M + K_\infty} \tag{C.2}$$

where K_0 and K_∞ are the low and high pressure rate constants, both expressed following the Arrhenius law. n_M is the total number density. K_r is the radiative association rate. F is an additional factor to characterize the behavior of K_i at pressures between the high and low pressure limits. F = 1 in the

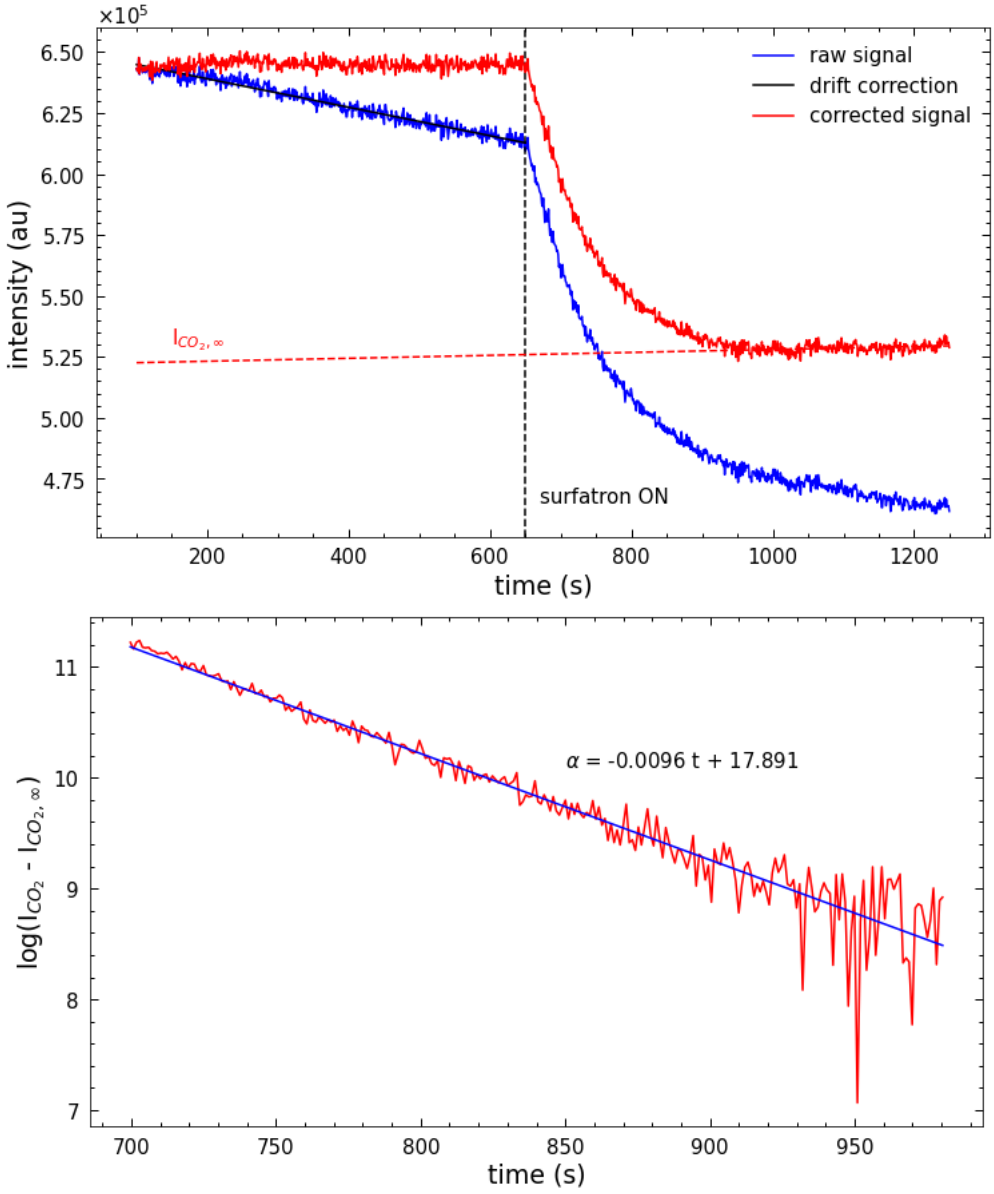

Fig. B.1: Photolysis of CO_2 monitored to derive the mean UV flux of the surfatron. (top) Evolution the measured intensity at *m/z* 44. (bottom) Linear fit of the CO_2 consumption to derive the photolysis rate constant.

standard Lindemann formalism (Lindemann et al. 1922) used in the 1D atmospheric model VULCAN (Tsai et al. 2017). This semi-empirical calculation of the rate constant is detailed in Hébrard et al. (2013). The empirical F factor is non-trival and cannot be expressed from first principles (Hébrard et al. 2009, 2013). It is expressed as :

$$log(F) = \frac{log(F_c)}{1 + (\frac{log(K_0(T)\ n_M + K_{capture}(T))}{N})^2} \quad \text{(C.3)}$$

where F_c and N are constants usually set to 0.6 and 1 respectively. $K_{capture}$ is the rate constant derived from classical capture theory.

For a similar reaction, different rate constants have been reported in the literature, most of them can be found in the NIST Chemical Kinetics database[6]. Uncertainties can be large and vary with temperature. The review of Burkholder et al. (2015) presents a comparative analysis of the different data and provides estimated uncertainties. The uncertainty on the rate constant increases as we depart from room temperature given the lack of data and the additional experimental complexities (Burkholder et al. 2015). This error is not estimated using standard statistics given the few data available, it involves a case by case estimation based on the temperature, the complexity of the experimental setup, and the potential for systematic errors (Hébrard et al. 2006, 2009; Burkholder et al. 2015). The uncertainty factor f derived from this comparative analysis and used in the chemical kinetics model is expressed as,

$$f(T) = f(T_0)\ e^{|g\ (\frac{1}{T}-\frac{1}{T_0})|} \tag{C.4}$$

where $f(T_0)$ is the uncertainty factor at room temperature and g is the uncertainty propagation factor. g quantifies the increase in experimental errors and the lower amounts of available data when temperature departs from 300K.

In the ReactorUI model, the probability density function of each rate constants is expressed using a lognormal law to ensure using positive values during the Monte Carlo sampling. The rate constant considering uncertainties K' can be expressed as :

$$K'(T) = K(T)\ u_k(T)$$
$$\text{With : } u_k(T) = e^{N(0,1)\ log(f(T))} \tag{C.5}$$

Where N(0,1) is a normal distribution.

For each Monte Carlo run, the rate constant of a specific reaction is generated using the principle in C.5. A similar approach is used to consider the uncertainty on cross sections and branching ratios, with the added complexity that these parameters are wavelength-dependent (Gans et al. 2013). For the purpose of the present study, we added O_2 and H_2O_2 photolysis in the ReactorUI cross section and branching ratio database using available data in the Leiden Observatory database and Phidrates.

[6] NIST chemical kinetics database : https://kinetics.nist.gov/kinetics/

Reaction	A	B	E_a	f_{300K}	g	Valid temperature range	reference
$O^{1D} + H_2O \longrightarrow OH + OH$	$1.63\ 10^{-10}$	0	-60	1.08	20	217-453 K	Burkholder et al. (2015)
$O^{3P} + OH \longrightarrow O_2 + H$	$1.8\ 10^{-11}$	0	-180	1.15	50	136-515 K	Burkholder et al. (2015)
$HO_2 + HO_2 \longrightarrow H_2O_2 + O_2$	$3.0\ 10^{-13}$	0	-460	1.15	100	222-1120 K	Burkholder et al. (2015)
$OH + HO_2 \longrightarrow H_2O + O_2$	$4.8\ 10^{-11}$	0	-250	1.15	50	252-420 K	Burkholder et al. (2015)
$OH + H_2O_2 \longrightarrow H_2O + HO_2$	$1.8\ 10^{-12}$	0	0	1.15	45	200-300 K	Burkholder et al. (2015)
$OH + OH \longrightarrow H_2O + O^{3P}$	$1.8\ 10^{-12}$	0	0	1.25	50	233-580 K	Burkholder et al. (2015)
$H_2O_2 + H \longrightarrow OH + H_2O$	$1.7\ 10^{-11}$	0	1800	1.26	0	300-1000 K	Burkholder et al. (2015)
$H_2O_2 + H \longrightarrow H_2 + HO_2$	$2.8\ 10^{-12}$	0	1890	1.47	0	280-1000 K	Burkholder et al. (2015)
$O^{3P} + HO_2 \longrightarrow OH + O_2$	$3.0\ 10^{-11}$	0	-200	1.05	50	229-391 K	Burkholder et al. (2015)
$O^{3P} + H_2O_2 \longrightarrow OH + HO_2$	$1.4\ 10^{-12}$	0	2000	1.2	100	283-386 K	Burkholder et al. (2015)
$CO_2 + O^{1D} \longrightarrow O^{3P} + CO_2$	$7.5\ 10^{-11}$	0	-115	1.15	20	195-370 K	Burkholder et al. (2015)
$CO_2 + O^{3P} \longrightarrow CO + O_2$	$2.46\ 10^{-11}$	0	26600	2.0	0	10-800 K	Harada et al. (2010)
$O^{3P} + H_2 \longrightarrow OH + H$	$8.5\ 10^{-20}$	2.67	3160	3.16	100	300-2500 K	Baulch et al. (1992)
$CO + HO_2 \longrightarrow OH + CO_2$	$5.6\ 10^{-10}$	0	12200	2	0	10-800 K	Harada et al. (2010)
$H + O_3 \longrightarrow OH + O_2$	$1.4\ 10^{-10}$	0	470	1.1	40	196-424 K	Burkholder et al. (2015)
$O^{1D} + O_3 \longrightarrow O_2 + O_2$	$1.2\ 10^{-10}$	0	0	1.2	50	103-393 K	Burkholder et al. (2015)
$O^{1D} + O_3 \longrightarrow O_2 + O^{3P} + O^{3P}$	$1.2\ 10^{-10}$	0	0	1.2	50	103-393 K	Burkholder et al. (2015)
$OH + O_3 \longrightarrow HO_2 + O_2$	$1.7\ 10^{-12}$	0	940	1.15	50	190-357 K	Burkholder et al. (2015)
$HCO + O_2 \longrightarrow CO + HO_2$	$5.2\ 10^{-12}$	0	0	1.4	100	200-2000 K	Atkinson et al. (2006)
$HO_2 + O_3 \longrightarrow OH + O_2 + O_2$	$1.0\ 10^{-14}$	0	490	1.15	80	197-413 K	Burkholder et al. (2015)
$O^{1D} + O_2 \longrightarrow O^{3P} + O_2$	$3.3\ 10^{-11}$	0	-55	1.1	10	104-424 K	Burkholder et al. (2015)
$O^{3P} + O_3 \longrightarrow O_2 + O_2$	$8.0\ 10^{-12}$	0	2060	1.1	200	220-409 K	Burkholder et al. (2015)
$HCO + OH \longrightarrow CO + H_2O$	$1.8\ 10^{-10}$	0	0	2.0	0	296-2500 K	Baulch et al. (2005)
$C + CH \longrightarrow C_2 + H$	$2.4\ 10^{-10}$	0	0	2.0	0	10-300 K	Loison et al. (2014)
$CH_3 + C \longrightarrow C_2H_2 + H$	$1.0\ 10^{-10}$	0	0	2.0	0	10-280 K	KIDA
$H + C_2H_5 \longrightarrow CH_3 + CH_3$	$5.99\ 10^{-11}$	0	0	0	0	10-300 K	Ruaud et al. (2015)
$HCO + HCO \longrightarrow CO + H_2CO$	$4.48\ 10^{-11}$	0	0	1.32	100	10-300 K	Hébrard et al. (2009)
$HCO + HCO \longrightarrow CO + CO + H_2$	$3.64\ 10^{-11}$	0	0	2.0	100	50-200 K	Hébrard et al. (2009)

Table C.1: Chemical kinetic constants of two-body reactions added to the ReactorUI database.

Reaction	A_0	B_0	$E_{a,0}$	$f_{300K,0}$	g_0	A_∞	B_∞	E_a, ∞	$f_{300K,\infty}$	g_∞	F	Valid temperature range	reference
$OH + OH + M \longrightarrow H_2O_2 + M$	$6.9\ 10^{-31}$	-1	0	1.5	100	$2.6\ 10^{-11}$	0	0	1.5	100	0.6	200-400 K	Burkholder et al. (2015)
$H + O_2 + M \longrightarrow HO_2 + M$	$4.4\ 10^{-32}$	-1.3	0	1.3	50	$7.5\ 10^{-11}$	0.2	0	1.3	50	0.6	298-200 K	Burkholder et al. (2015)
$O^{3P} + O_2 + M \longrightarrow O_3 + M$	$5.7\ 10^{-34}$	-2.8	0	1.26	100	$2.8\ 10^{-12}$	0	0	1.6	100	0.65	200-300 K	Atkinson et al. (1989)
$O^{3P} + CO + M \longrightarrow CO_2 + M$	$1.7\ 10^{-33}$	0	1510	2.5	100	$1.0\ 10^{-10}$	0	0	2	100	1.0	50-200 K	Tsang & Hampson (1986)
$OH + H + M \longrightarrow H_2O + M$	$6.78\ 10^{-31}$	-2	0	2	100	$1.0\ 10^{-10}$	0	0	2	100	1.0	50-200 K	Tsang & Hampson (1986)
$O^{3P} + H + M \longrightarrow OH + M$	$4.33\ 10^{-32}$	-1	0	5	100	$1.0\ 10^{-10}$	0	0	2	100	1.0	50-200 K	Tsang & Hampson (1986)

Table C.2: Chemical kinetic constants of three-body reactions added to the ReactorUI database. K_r=0 for each reaction.

Astronomy & Astrophysics manuscript no. output
November 27, 2024
©ESO 2024

Chapter 4 : Inferring interior oxygen fugacity of rocky exoplanets from observations : assessing biases by atmospheric chemistry

T. Drant[1,2], M. Tian[2], N. Carrasco[1,3], and K. Heng[2,4,5,6]

[1] University of Paris Saclay, OVSQ, LATMOS, 11 Boulevard d'Alembert, 78280 Guyancourt, France.
e-mail: thomas.drant@latmos.ipsl.fr

[2] Ludwig Maximilian University, Faculty of Physics, Observatory of Munich, Scheinerstrasse 1, Munich D-81679, Germany.

[3] ENS Paris-Saclay, 4 avenue des Sciences, 91190 Gif-sur-Yvette, France.

[4] University of Bern, ARTORG Center for Biomedical Engineering Research, Murtenstrasse 50, CH-3008, Bern, Switzerland.

[5] University College London, Department of Physics & Astronomy, Gower St, London, WC1E 6BT, United Kingdom.

[6] University of Warwick, Department of Physics, Astronomy & Astrophysics Group, Coventry CV4 7AL, United Kingdom.

ABSTRACT

In the era of the James Webb Space Telescope, inferring the presence and bulk composition of temperate rocky exoplanet atmospheres is now possible. The primary targets typically present equilibrium temperatures ranging from 400 to 1500K for which a balance between geochemical outgassing and escape is required to maintain an atmosphere. The composition of these exoplanet atmospheres hold crucial information on the redox state of the planetary interior characterized by the oxygen fugacity (fo_2). The relative molecular abundances of species with opposite redox states inferred from observations can help constrain an effective interior fo_2. Using outgassing and atmospheric chemistry calculations that self-consistently iterate with radiative transfer, we assess the reliability of different relative abundances in a C-H-O system that could be used to retrieve fo_2. CO_2/CO, previously suggested as the most reliable tracer of fo_2, is increased by atmospheric cooling (thermochemistry) and photochemistry which would cause a bias of $\approx$ 1-2 orders of magnitude on the retrieved fo_2. Constraints on the atmospheric temperature can help correct the effect of atmospheric cooling and improve the retrieval of fo_2. The increase of CO_2/CO driven by photochemistry is dominant for thin atmospheres although it occurs over long timescales (tens/hundreds of thousands of years) and therefore would be negligible if the atmosphere is continuously replenished by volcanism. The transition between a chemical regime dominated by atmospheric thermochemistry towards a regime dominated by photochemistry is controlled not only by pressure and temperature but also by oxygen fugacity itself (i.e. O/H). Inferring CO_2/CO from the data might be challenging given the low contribution of CO in transit and emission spectra for objects with high CO_2 and H_2O abundances. We suggest CO_2/CH_4 as a more reliable tracer of fo_2 for reducing conditions (< IW) and high pressure-temperature surface conditions favoring the build-up of CH_4 by atmospheric cooling.

Key words. atmospheres, terrestrial planets

1. Introduction

The NASA Kepler mission dedicated for the search of exoplanets (Borucki et al. 2010) showed that objects with radii smaller than Neptune are the most abundant, representing ≈ 3/4 of the entire population (Borucki et al. 2011). Analyses of the exoplanet radii measured with Kepler revealed the presence of a gap in the population around 1.5 $R_\oplus$ (Fulton et al. 2017) referred to in the literature as the 'radius gap'. This gap marks the transition between the category of Super-Earth (R_p < 1.5 $R_\oplus$) and sub-Neptunes (R_p > 1.5 $R_\oplus$), the latter likely composed of a rocky core surrounded by a H_2-He primitive envelope that survived erosion during the early active phase of the star. Current models explain the radius gap using two main mass loss mechanisms : photo-evaporation (Owen & Wu 2013; Lopez & Fortney 2013; Fulton & Petigura 2018; Van Eylen et al. 2018; MacDonald 2019) and core-powered mass loss (Gupta & Schlichting 2019; Owen & Schlichting 2024). In the radius - orbital period parameter space, the "radius valley" is characterized by a negative slope as both photo-evaporation and core-powered mass loss efficiencies decrease with orbital period given their dependency to the XUV stellar flux and internal atmospheric temperature respectively (Owen & Schlichting 2024). The dominant process shaping the radius valley is still debated in the literature, several works pointed out that each process individually can reproduce the negative slope of the radius valley (Van Eylen et al. 2018; MacDonald 2019; Gupta & Schlichting 2019) and no clear stellar mass - radius gap correlation is seen to suggest a predominance by photo-evaporation (Parke Loyd et al. 2020).

Sub-Neptune planets around 2-3 $R_\oplus$, not found in our Solar System, are the most abundant objects in the galaxy (Borucki et al. 2011). The lower frequency of bigger objects could be explained by the presence of a magma ocean at equilibrium with the primitive envelope which dissolves efficiently for $R_p > 3R_\oplus$ driven by the high pressure and high hydrogen solubility at the surface (Kite et al. 2019). The nature of sub-Neptune planets is still debated, they are possibly hydrid atmospheres which preserved the primitive atmosphere with a later contribution by geochemical outgassing (Tian & Heng 2024). This later contribution leads to higher atmospheric metallicities compared to hot Jupiters in agreement with recent observations of GJ 1214b (Kempton et al. 2023; Gao et al. 2023) and K2-18b (Madhusudhan et al. 2023). Sub-Neptunes could also host shallow atmospheres allowing habitable surface conditions (Tsai et al. 2021a; Hu et al. 2021; Yu et al. 2021).

Even for objects below the radius gap, a broad range of bulk densities is reported suggesting variations from water worlds, to Earth-like objects, to Super-Mercuries (Luque & Pallé 2022). In addition, rocky exoplanets are found around stars with a broad range of metallicities (Buchhave et al. 2012). Planetary mass and radius measurements along with the relative abundances of refractory elements from the host star provide constraints to deduce the composition of the rocky interior (Dorn et al. 2015). A large fraction of rocky planets seems to be enriched in Fe compared to their host star (Liu & Ni 2023). Recent analyses suggest a correlated behavior in the relative abundance of refractories between the planet and the star although the correlation is not 1:1 and likely affected by planet formation mechanisms (Adibekyan et al. 2021).

Interior properties of rocky exoplanets (composition, temperature, variability) are thus largely unknown. The likelihood of finding an atmosphere around these objects relies on the efficiency of late degassing to balance atmospheric escape (Ortenzi et al. 2020). The degassing rate is mainly controlled by planet mass and internal heating via tidal or radiogenic processes (Dorn et al. 2018; Quick et al. 2020; Oosterloo et al. 2021). For $M_p < 3M_\oplus$, degassing rate increases with planet mass making secondary atmospheres around Super-Earths more likely (Dorn et al. 2018). An increased core fraction however reduces convection efficiency and thus degassing rate (Oosterloo et al. 2021). In simplified models, degassing rate is derived using mantle melt fraction, rock-melt partition coefficients and approximated mantle convection rate (Ortenzi et al. 2020; Liggins et al. 2022). The process of degassing is thus subjected to too many unknown variables although the outgassed composition is mainly controlled by the volatile budget and the oxygen fugacity (fo_2) (Gaillard & Scaillet 2014; Gaillard et al. 2022; Guimond et al. 2023; Tian & Heng 2024). For lava worlds, the atmosphere in equilibrium with the magma ocean directly reflects the interior redox state (or fo_2). The relative abundances of volatiles or metal oxides (e.g. CO_2-CO or SiO-SiO_2) in the fluid phase is a consequence of melt redox state suggesting that the interior fo_2 can be derived by characterization of the atmospheric composition (Wolf et al. 2023; Gaillard et al. 2022; Tian & Heng 2024). Several of the simple volatile molecules outgassed into the atmosphere and observable with the James Webb Space Telescope (JWST) can co-exist depending on the temperature and elemental budget (Woitke et al. 2020). These detections should help constrain interior redox state of temperate rocky exoplanet atmospheres.

The mantle redox state controlling the composition of the atmosphere informs on the formation and evolution history of the interior. Most scenarios suggest an increase in oxidation state over time caused by the degassing of reduced species and a potential metal density deficit resulting from the primordial H_2 envelope partially dissolving into the magma ocean and reacting at the core-mantle boundary (Young et al. 2023). Mantle fo_2 mainly reflects the relative abundance of ferric iron relative to the total iron content ($Fe^{3+}/\Sigma Fe$) in the mantle, with high fo_2 favoring the oxidation of metallic iron

in the buffer reaction $Fe + \frac{1}{2} O_2 \longleftrightarrow FeO$ or the oxidation of ferrous iron in the buffer reaction $FeO + \frac{1}{4} O_2 \longleftrightarrow FeO_{3/2}$ (Frost & McCammon 2008; Burgisser et al. 2015; Deng et al. 2020; Ortenzi et al. 2020; Liggins et al. 2022; Guimond et al. 2023). The interior mineralogy dictated by the relative abundances of refractories (e.g. Mg/Si) incorporates ferric iron and can significantly modify the mantle fo_2, more constraints on these processes can be obtained if the stellar refractory abundances are derived from observations (Guimond et al. 2023). Theoretical calculations show that the lower molar volume of Fe^{3+} relative to Fe^{2+} under high pressure favors high redox state and thus suggest that exoplanets with a more massive mantle should exhibit higher fo_2 (Deng et al. 2020). However, a more massive mantle also reduces the efficiency of core-mantle differentiation with large abundances of Fe remaining in the mantle and decreasing the mean fo_2 (Noack et al. 2023). Future atmospheric characterization of a large rocky exoplanet population will help us better understand these interior formation and evolution mechanisms.

The atmospheric composition and relative abundances of volatile species with different redox states is first set by geochemical outgassing but modified by atmospheric chemistry (photochemistry and equilibrium chemistry). In the present study, we assess the biases caused by these chemical processes and their influence on future atmospheric characterization to constrain interior fo_2. In Section 2, we present our model combining geochemical outgassing with self-consistent calculations of atmospheric chemistry and radiative transfer. In Section 3, we describe the effect of atmospheric cooling (thermochemistry or equilibrium chemistry) on relative molecular abundances used as tracers of interior fo_2. In section 4, we assess the effect of atmospheric cooling, photochemistry and vertical mixing on the relative abundances for a 1D case study simulation of the super-Earth GJ1132b. In Section 5, we discuss the implications for future observations with JWST.

2. Model description

2.1. 0D calculations of atmospheric cooling

Exoplanets currently observed with JWST exhibit very different densities ranging from 5-6 $g.cm^{-3}$, values suggesting a silicate rocky interior, to 3-4 $g.cm^{-3}$, suggesting either a water-rich interior or the presence of a substantial H_2 envelope around a rocky core (Luque & Pallé 2022). The present study focuses on secondary atmospheres where the primitive H_2-He envelope was initially lost by escape. To avoid the large unknowns required to compute outgassing and escape fluxes, we consider a state where both mechanisms balance using a parametrized surface pressure. Both boundary conditions are thus not considered in the present study as we focus on the effect of atmospheric chemistry. Most rocky exoplanets observed with JWST present equilibrium temperatures between 400K and 1500K. If these objects maintained an atmosphere, the volatiles outgassed from the interior will cool to the

new temperature found in the atmosphere. The molecular abundances of the different species will change according to the atmospheric temperature-pressure conditions, we will refer to this process as atmospheric cooling.

After atmospheric cooling, the molecular abundances might change significantly compared to the prediction of the outgassing model. Tian & Heng (2024) explored the parameter space in 0D outgassing calculations describing a C-H-O-N-S fluid system at equilibrium with a carbon-bearing melt. The model uses a degassing pressure, melt temperature, oxygen fugacity and activity of graphite to assess the speciation of the stable molecules at chemical equilibrium. Tian & Heng (2024) showed that only the molecular abundance ratio CO_2/CO directly correlates to oxygen fugacity and can be used to infer fo_2 from observations. Given the high temperature of melts, CH_4-rich degassing is unlikely unless speciation occurs under high pressure (Wogan et al. 2020; Tian & Heng 2024).

To assess the change in molecular abundances of a volcanic mixture subjected to atmospheric cooling, we combine the geochemical outgassing calculations of Tian & Heng (2024) with atmospheric thermochemical calculations performed using FastChem and VULCAN. FastChem, described in detail in Stock et al. (2018) and Stock et al. (2022), uses a semi-analytical approach to determine the molecular abundances at chemical equilibrium for a given pressure, temperature and set of elemental abundances. VULCAN, described in Tsai et al. (2017) and Tsai et al. (2021b), is a 1D chemical kinetics code used to study equilibrium chemistry and/or photochemistry. We use FastChem for direct calculations of molecular abundances. VULCAN is used to understand the change in molecular abundances using a detailed analysis of the chemical network and timescales. The C-H-O chemical network was validated in Tsai et al. (2017) and Tsai et al. (2018). We updated the chemical kinetic constants taken from the NIST chemical kinetics database[1]. A few reactions were added following the work of Liggins et al. (2023). Most kinetic constants used are compiled in the reviews of Tsang & Hampson (1986), Tsang (1987) and Baulch et al. (1992) as they were validated in a broad range of gas temperature ranging from 300 to 2500K. For a few reactions, we were compelled to use kinetic constants derived from theoretical calculations when experimental data were not available in a broad range of temperature. The database counts 427 chemical reactions (forward and reverse) and 39 photolysis reactions involving only C-H-O species.

The aim of this first 0D analysis is to assess the reliability of CO_2/CO as an atmospheric tracer for interior fo_2 despite the change in temperature between melt and atmosphere. We focus only on the C-H-O system as nitrogen would only affect N_2-NH_3 conversion which alone is not a good indicator of fo_2. Additionally, the current model does not consider solubility in the melt which is essential to

[1] NIST chemical kinetics database : https://kinetics.nist.gov/kinetics/

understand the atmospheric abundances of ammonia (Shorttle et al. 2024). We explore the parameter space of the model now including the surface temperature T_s (temperature of the atmosphere) in addition to the parameters of the outgassing model. Degassing is assumed to occur under atmospheric pressure, a reasonable assumption discussed in Gaillard & Scaillet (2014). To avoid biases caused by the lack of melt solubility in our calculations, we limit the pressure range below 100 bars. Solubility of CO_2 is low (Gaillard & Scaillet 2014) and the calculations of Tian & Heng (2024) simplify to an ideal gas problem where the fugacity of gas species can be approximated with the partial pressure (French 1966). We perform random sampling using log-uniform and uniform laws to cover the entire parameter space : activity of graphite A_c between 10^{-7} and 1, T_s between 700 and 1600K, P_s in 10^{-3}-100 bar range, and fo_2 between IW-6 and IW+5. The melt temperature T_m is set to 1600K. 10,000 Monte Carlo runs are performed in total.

2.2. 1D calculations combining radiative transfer and atmospheric chemistry

The 0D calculations provide crucial insights into the main chemical mechanisms resulting from atmospheric cooling. In a 1D atmosphere however, atmospheric temperature and composition are strongly correlated. The abundances of atmospheric species are affected by the atmospheric temperature changing throughout the column atmosphere. The composition and more specifically the greenhouse properties of the atmospheric mixture also controls the temperature profile. This complexity compels us to combine different calculations using a climate-chemistry model. For that purpose, we coupled the radiative-convective model HELIOS (Malik et al. 2017, 2019a) with the chemistry model VULCAN to perform self-consistent calculations including both radiative transfer and chemical kinetics (photochemistry and equilibrium chemistry). The geochemical calculations of Tian & Heng (2024) are used to set the initial atmospheric composition. It can also be used as a lower boundary condition in VULCAN using a parameterized volcanic flux. As stated previously, we refrain from using this continuous outgassing feature in this work given the large unknown regarding the flux. Given the broad range of temperature encountered in our case study, competition between mixing, radiative and chemical timescales are expected which strengthens the need to use a self-consistent model. In our atmospheric model, the temperature profile is changed by HELIOS during the VULCAN simulation using the radiative timescale as an iteration time step. The radiative timescale is updated throughout the simulation to modify the time step if needed, it is expressed following :

$$t_{rad} = \frac{C_p P}{\sigma g T^3} \tag{1}$$

where P is the pressure, C_p is the heat capacity, σ is the Stefan-Boltzmann constant, g is the gravity and T the atmospheric temperature.

The mean heat capacity of the atmosphere is derived using the abundances of the main atmospheric molecules (CO, CO_2, CH_4, H_2 and H_2O) and their C_p at the given surface temperature. C_p(T) of each species is calculated using the thermodynamic data (polynomial constants) from Holland & Powell (1998) also used in the geochemical outgassing calculations (Tian & Heng 2024). The change in temperature is read by VULCAN to update the kinetic constants and reaction rates. Temperature-dependent photo-absorption cross sections and molecular diffusion rates are also changed according to the new temperature conditions.

We include a transit spectra simulator to read the outputs of the atmospheric model. We use the forward model of HELIOS-T first described in Fisher & Heng (2018) which we modified to apply generally for any atmospheric composition and consider temperatures and mixing ratios varying with pressure. HELIOS provides the secondary eclipse emission spectrum of the planet along with the contribution function of different spectral bins to assess the pressure range probed.

This tool combining outgassing, atmospheric chemistry and radiative transfer is essential to assess the influence of surface pressure on the dominant chemical regime (photochemistry or equilibrium chemistry) affecting molecular abundances. The structure of the model is illustrated in Fig.1. We explore the parameter space of the atmospheric model guided by a specific question : how can relative molecular abundances help constrain interior fo_2 from observations ? We want to clarify the role of photochemistry and thermochemistry. If deterministic mechanisms are at play, our aim is to identify how we can correct for them in a retrieval framework.

The outgassing calculations are used to predict the initial composition of the atmosphere which will be modified by atmospheric chemistry. Atmospheric escape is not considered and we restrain from using a constant volanic flux at the surface since this value would be strongly unconstrained. Our aim is to focus on the influence of atmospheric chemistry. We focus on the case study of GJ 1132b as recent observations suggest the presence of an atmosphere (May et al. 2023). The results and underlying mechanisms identified can be generalized to other objects. We will focus on three oxygen fugacity end-members : IW-3, IW and IW+3. The iron-wustite (IW) buffer is a reference commonly used in the Earth science community. For each redox state, three surface pressure scenarios are considered : 0.01 (Mars-like), 1 (Earth-like) and 100 (Venus-like) bars. Atmospheric pressure is one of the main parameters as it strongly affects surface temperature.

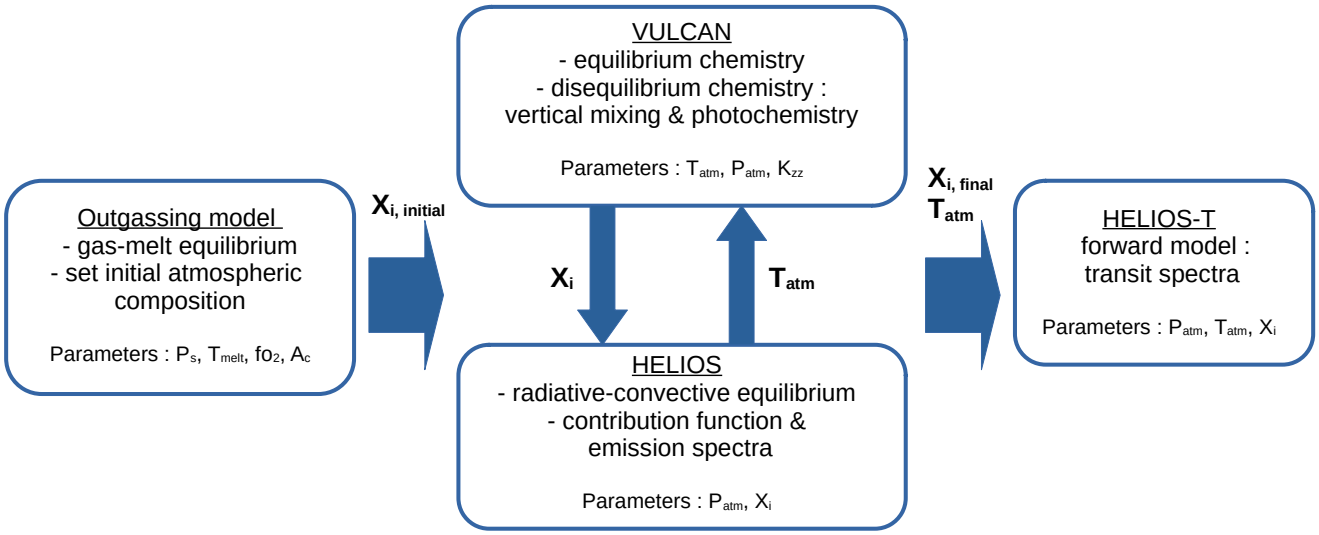

Fig. 1: Description of the atmospheric model. Each section of the model is shown with its purpose and the atmospheric parameters needed for the simulations. Using iterations between VULCAN and HELIOS following the radiative timescale, the model performs self-consistent calculations of atmospheric chemistry and radiative transfer. The different model parameters mentioned are : melt temperature T_m, melt oxygen fugacity fo_2, activity of graphite A_c, degassing pressure here assumed similar to surface pressure P_s, vertical profile of temperature T_{atm} and pressure P_{atm} in the atmosphere, eddy mixing coefficient K_{zz} and vertical profile of volume mixing ratio X_i for each species i.

In the outgassing calculation, melt temperature is kept fixed at 1600K following Gaillard & Scaillet (2014). The melt temperature is unknown, the difference between melt temperature and atmospheric temperature is the important parameter hence our choice to only vary atmospheric temperature. Activity of graphite is set to ensure an atmosphere rich in carbon : 10^{-6} for IW+3, 10^{-4} for IW and 10^{-2} for the low fo_2 scenario (IW-3). For a carbon-poor degassing, only H_2 and H_2O present high abundances that could be detected limiting our ability to infer a quantitative redox state. In the atmospheric model, photochemical haze formation is not included, the surface albedo does not impact our simulations as surface emissivity is set accordingly (albedo = 1 - emissivity). Stellar temperature, radius and mass are set for GJ 1132 (Berta et al. 2015) and used to produce the blackbody spectrum in HELIOS. Surface pressure is set according to our three different scenarios, top pressure is set to 10^{-7} bar to ensure the accuracy of the VUV optical depth and vertical profile of actinic flux in the 1D photochemical calculations. The stellar flux of GJ 1132 is subjected to negative values, we thus use the stellar flux of GJ 1214 which presents a similar temperature and radius, with data available as part of the MUSCLES survey (France et al. 2016). The climate model and transit spectra generator includes the opacities of CO (Rothman et al. 2010; Li et al. 2015), CO_2 (Rothman et al. 2010), CH_4 (Rothman et al. 2010; Hargreaves et al. 2020), H_2O (Polyansky et al. 2018) along with collision-induced absorption (CIA) by H_2-H_2. Other CIAs are not included given the lack of data in a broad spectral and temperature range (Chubb et al. 2024). Rayleigh scattering is considered in the atmospheric model (VULCAN, HELIOS, HELIOS-T) for the different species following the formu-

lation in MacDonald & Lewis (2022) using the King factor, refractive index and reference number density with most data taken from Sneep & Ubachs (2005). The water refractive index is pressure-temperature dependent, the data is taken from Murphy (1977) and Schiebener et al. (1990). Vertical mixing described by the eddy diffusion coefficient K_{zz} is one of the main sources of uncertainty in the chemical model, especially since the temperature is not known a priori. The role of K_{zz} is assessed and discussed in Section 4.1 and 4.2. Molecular diffusion is considered in VULCAN (Tsai et al. 2021b), the diffusion coefficients are taken from Marrero & Mason (1972) following the formalism in Hu et al. (2012). Photo-absorption and -dissociation cross sections were compiled from the Leiden Observatory database[2] in the original study of Tsai et al. (2021b). Temperature-dependent cross sections are available for CO_2 (150-800K) (Venot et al. 2018) and water (273-573K) (Fateev et al. 2019) although not in the entire range of temperature covered with our simulations ($\approx$ 400-1600K). The reaction database is similar to the one used for the 0D chemical analyses (Section 2.1).

3. Influence of atmospheric cooling on CO_2/CO and CH_4 production

3.1. Relative molecular abundances : inferring fo_2 and temperature using CO, CO_2 and CH_4

The relative molecular abundances obtained with the atmospheric cooling simulations are shown in Fig.2. Even after atmospheric cooling, CO_2/CO and fo_2 remain strongly correlated with a Pearson coefficient at 0.92. The lower correlation compared to the outgassing prediction is explained by a decrease of CO_2/CO as T_s increases for a given fo_2 (top right panel, Fig.2). The correlation decreases as the atmospheric temperature departs from the melt temperature, it is thus caused by atmospheric cooling. For T_s between 700 and 1600K, CO_2/CO varies by up to two orders of magnitude for a given fo_2. A constraint on the temperature is therefore essential to correct biases induced by atmospheric cooling.

Fig.2 shows that a single CO_2/CO can correspond to a broad range of atmospheric temperature. In other words, this molecular pair cannot be used in observations to infer atmospheric temperature. CO-CH_4 conversion is however very sensitive to atmospheric temperature (top right panel, Fig.2). The methane abundance can thus be used to constrain the atmospheric temperature and improve the retrieved fo_2. Using the abundances of CO, CO_2 and CH_4, one can in theory retrieve accurately the oxygen fugacity and atmospheric temperature (top panels, Fig.2). The feasibility of this later statement lies in the absolute abundances of each species and their detectability in the spectral range of JWST. In practice, high abundances of methane are found only under reducing conditions. Inferring

[2] https://home.strw.leidenuniv.nl/~ewine/photo/cross_sections.html

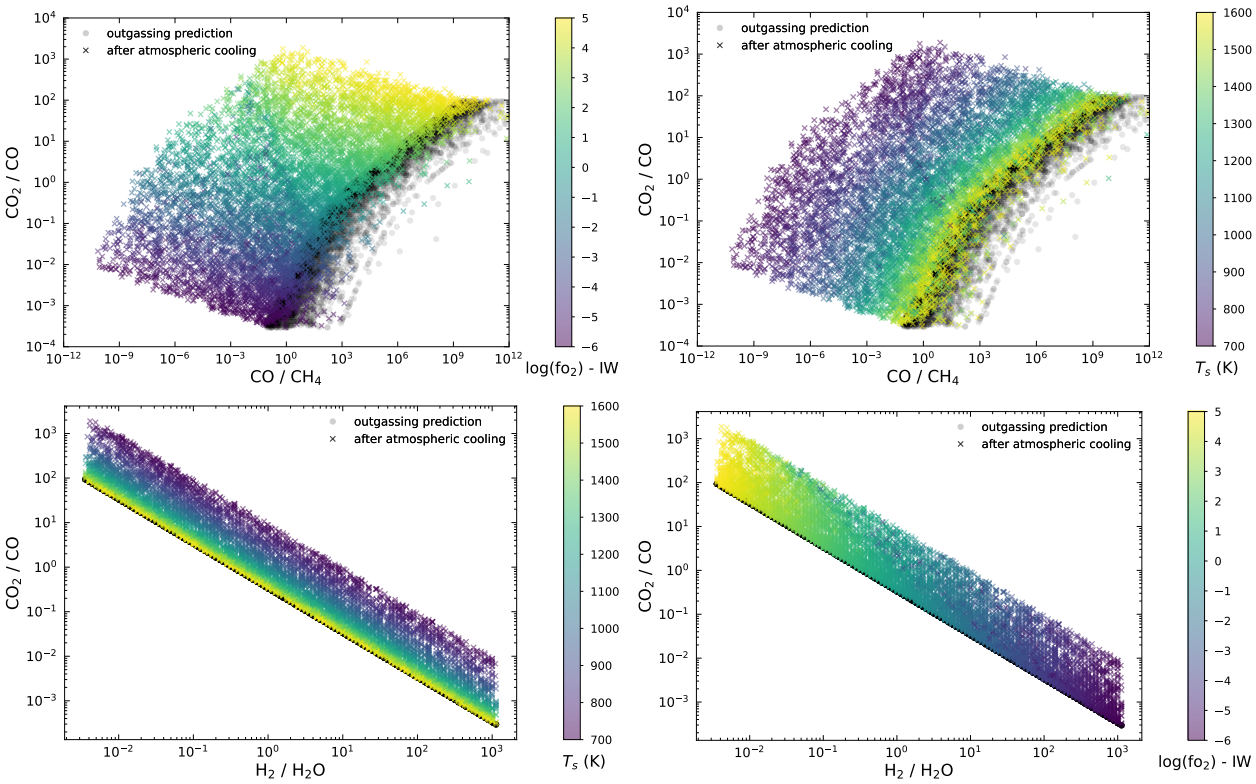

Fig. 2: Relative molecular abundances for the different simulations considering a geochemical outgassed mixture cooling to a different atmospheric temperature. The following model parameters are explored using 10,000 Monte Carlo simulations with uniform and log-uniform sampling : activity of graphite, degassing pressure (or atmospheric pressure), oxygen fugacity and atmospheric temperature (see main text Section 2.1 for the parameter range). The atmospheric temperature T_s is kept below the melt temperature T_m set to 1600K. The black dots show the prediction by outgassing alone. The colored crosses show the predictions with atmospheric cooling.

temperature would be more difficult for oxidized atmospheres. In theory, H_2/H_2O provides a similar information on fo_2 as CO_2/CO (bottom left panel, Fig.2). Although the H_2 abundance cannot be retrieved from observations, it suggests that low oxygen fugacity objects would create thicker atmospheres which would affect transit observations through the scale height as discussed in Ortenzi et al. (2020).

3.2. Chemical network and timescales

For a fluid mixture at equilibrium with a carbon-bearing melt, the C-H-O system can be described using four independent chemical reactions (French 1966; Tian & Heng 2024) :

$$C + O_2 \longleftrightarrow CO_2 \qquad \text{(R1)}$$

$$C + \tfrac{1}{2} O_2 \longleftrightarrow CO \qquad \text{(R2)}$$

$$C + 2\,H_2 \longleftrightarrow CH_4 \qquad \text{(R3)}$$

$$H_2 + \tfrac{1}{2} O_2 \longleftrightarrow H_2O \qquad \text{(R4)}$$

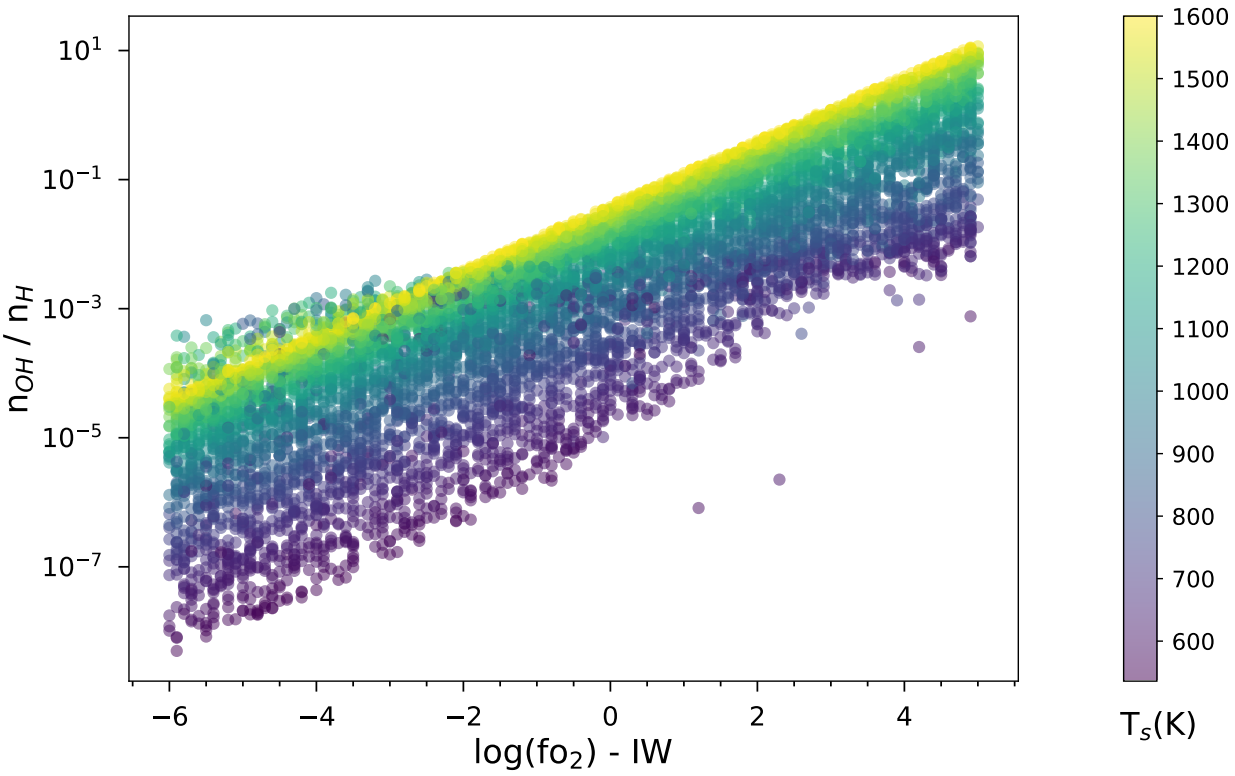

Fig. 3: Density ratio OH/H at chemical equilibrium as a function of oxygen fugacity and atmospheric temperature. The following model parameters are explored using 10,000 Monte Carlo simulations with uniform and log-uniform sampling : activity of graphite, degassing pressure (or atmospheric pressure), oxygen fugacity and atmospheric temperature (see main text Section 2.1 for the parameter range). The atmospheric temperature T_s is kept below the melt temperature T_m set to 1600K.

By calculating the Gibbs free energy and equilibrium constant of each reaction, one can derive the partial pressures of the main stable species involved in the network (French 1966; Tian & Heng 2024). The calculation is analytical for a C-H-O system under the ideal gas assumption. For the atmospheric calculations, one could use a similar approach where the activity of graphite and oxygen fugacity are replaced by the elemental abundances of the gas mixture (Heng & Tsai 2016; Heng et al. 2016). With chemical kinetics, one understands that the partial pressures of the stable molecules and the timescales of chemical equilibrium are controlled by reactions with the radical products of thermal dissociation, e.g. $H_2O \longrightarrow OH + H$. The abundances of these radicals is changed with temperature. Since we previously showed that atmospheric cooling can strongly modify CO_2/CO, we can look at the radicals and reactions to understand why. Fig.3 shows the density ratio OH/H as a function of oxygen fugacity and temperature for the different Monte Carlo simulations performed. The results teach us that OH/H is correlated to both fo_2 and atmospheric temperature. For a given temperature, the fo_2 can be seen as a specific O/H or OH/H. We now need to look at the chemical network to understand why the change in radical density also affects molecular abundances such as CO_2/CO.

For each simulation, we have a specific atmospheric/degassing pressure, atmospheric temperature and elemental abundances predicted by the outgassing calculations. Using kinetic simulations performed with VULCAN, we evaluate the different reaction rates and find the fastest chemical pathway between two molecules, e.g. CO and CH_4, using a Dijsktra algorithm (Dijkstra 1959). This analysis gives us the main chemical pathway controlling a specific conversion at a given pressure-temperature and for a given set of elemental abundances. Within this fastest pathway, we identify the rate limiting step (RLS) or slowest reaction which bottlenecks the chemical pathway and controls the timescale. In most scenarios, the chemical timescale can approximated as :

$$t_{eq,X} = \frac{n_X}{V_{RLS,X}} \tag{2}$$

Where n is the number density (molecules.cm^{-3}) of species X at chemical equilibrium and V_{RLS} is the slowest reaction rate in the fastest pathway (molecules.cm^{-3}.s^{-1}).

The outgassing model predicts a broad range of elemental abundances although C/O is usually below 1 given the difficulty in producing CH_4-rich atmospheres. O/H varies significantly depending on fo_2 giving very high metallicities poorly studied as previous work focused on hot Jupiters or hot Neptunes and the effect of C/O (Moses et al. 2011, 2013a,b; Venot et al. 2015; Tsai et al. 2018). Our network analysis shows that CO-CO_2 and H_2-H_2O conversions are always controlled by the following scheme in the entire parameter space (pressure, temperature, elemental abundances) :

$$CO + OH \longleftrightarrow CO_2 + H \qquad \text{(R5)}$$

$$H_2O + H \longleftrightarrow H_2 + OH \qquad \text{(R6)}$$

$$\text{net} : CO + H_2O \longleftrightarrow CO_2 + H_2$$

From this pathway, one can understand why variations of CO_2/CO and OH/H are directly correlated. First, the increase in CO_2/CO with fo_2 at a given temperature is caused by the increase in OH/H favoring the oxidation of CO. An increase in fo_2 corresponds to an increase in O/H and therefore OH/H. OH/H however also varies with temperature for a given O/H as thermal dissociation rates of water and molecular hydrogen vary differently with temperature (Fig.3). Since our outgassing calculations mainly predict O/H < 1, H_2/H_2O is controlled by OH/H and therefore decreases with fo_2 and temperature. This analysis explains the trends of relative abundances as a function of fo_2 and temperature in Fig.2 (bottom panels). CO_2/CO on the other hand increases with fo_2 but decreases with temperature. This result can seem counter-intuitive but is explained by the balance in elemental abundances. The decrease in OH/H and H_2O/H_2 with temperature at a given fo_2 leads to an increase of CO_2/CO to conserve elemental abundances and especially O/H. The trends of relative molecular

abundances for CO_2, CO, H_2 and H_2O are completely controlled by the change of the radical density ratio OH/H with temperature and fo_2.

CO-CH_4 conversion is also evaluated for the different simulations, the following scheme is identified :

$$CO + H + M \longleftrightarrow HCO + M \quad \text{(R7)}$$
$$HCO + H_2 \longleftrightarrow H_2CO + H \quad \text{(R8)}$$
$$H_2CO + H + M \longleftrightarrow CH_3O + M \quad \text{(R9a)}$$
$$H_2CO + H + M \longleftrightarrow CH_2OH + M \quad \text{(R9b)}$$
$$CH_3O + H_2 \longleftrightarrow CH_3OH + H \quad \text{(R10a)}$$
$$CH_3O + H_2O \longleftrightarrow CH_3OH + OH \quad \text{(R10b)}$$
$$CH_3OH + M \longleftrightarrow CH_3 + OH + M \quad \text{(R11a)}$$
$$CH_3OH + H \longleftrightarrow CH_3 + H_2O \quad \text{(R11b)}$$
$$CH_2OH + H \longleftrightarrow CH_3 + OH \quad \text{(R12)}$$
$$CH_3 + H_2 \longleftrightarrow CH_4 + H \quad \text{(R13a)}$$
$$CH_3 + H_2O \longleftrightarrow CH_4 + OH \quad \text{(R13b)}$$
$$OH + H_2 \longleftrightarrow H_2O + H \quad \text{(R14)}$$
$$H + H + M \longleftrightarrow H_2 + M \quad \text{(R15)}$$

$$\text{net} : CO + 3\,H_2 \longleftrightarrow CH_4 + H_2O$$

This general scheme is valid for the different simulations performed although some steps can be associated to different reactions depending on the temperature, pressure and elemental abundances. The oxygenated species produced during CO-CH_4 conversion are however similar. As our outgassing calculations predict C/O$\leq$1, the CO-CH_4 scheme involves primarily oxygenated species such as methanol and formaldehyde. For C/O$\geq$1, the fastest pathway would also involve saturated and unsaturated reduced hydrocarbons (Moses et al. 2011, 2013a; Venot et al. 2015; Tsai et al. 2018).

The reaction converting CH_3O-CH_3OH involves either H_2 and H (R10a) or H_2O and OH (R10b) depending on the oxygen content in the atmosphere and more specifically depending on O/H. The reaction R10a dominates for O/H < 0.5 whereas R10b dominates for higher O/H. A similar result is found for the CH_3-CH_4 conversion. For high O/H, oxidation of methane dominates through reaction R13b whereas hydrogenation dominates for lower O/H (R13a). The CH_3-CH_4 reaction might be changed with H_2S when sulfur is included (Liggins et al. 2023) although this depends on the sulfur

content in the mixture.

The reaction converting CH_3-CH_3OH or CH_3-CH_2OH depends on the temperature-pressure conditions. At temperatures above 900K, R11a and R12 are competing. R11a dominates at high pressure as methanol formation/dissociation is pressure-dependent. R11a is indeed a three-body reaction which becomes inefficient at low pressures. The two-body reaction R12 becomes more efficient than R11a at low pressures. The fastest pathway is thus going directly from CH_2OH to CH_3 without methanol at low pressure. The pressure value marking the transition from R11a to R12 depends on the temperature. This pressure value increases with temperature from about 10^{-2} bar at 900K to 10 bars at 1600K in agreement with the analysis of Tsai et al. (2018). At temperatures below 900K, R11a and R11b are competing. For a high OH/H, R11a would dominate as it involves OH compared to R11b involving H. The transition between R11a and R11b for the limiting reaction depends on both temperature and O/H since both parameters affect OH/H.

For every simulation, either R11a, R11b or R12 is identified as the limiting reaction (RLS). The CO-CH_4 conversion requires the dissociation of three bonds binding C and O together. The timescale of this conversion is limited by the dissociation of the last bond in methanol or CH_2OH. These results are in agreement with previous analyses of CO-CH_4 conversion for exoplanet atmospheres (Moses et al. 2011; Tsai et al. 2018; Liggins et al. 2023).

Our results show that the change in OH/H controlled by oxygen fugacity and temperature has a significant impact on the CO-CH_4 and CO-CO_2 conversions. Differences are thus expected in terms of timescales. Fig.4 shows the chemical timescales of CO derived for each simulation. We observe that the timescale is mainly controlled by fo_2 and the atmospheric temperature.

It was previously shown that the timescale of CO can be derived by identifying the RLS of the CO-CH_4 conversion for low metallicity atmospheres representative of hot Jupiters (Tsai et al. 2018). For high O/H, that statement is no longer valid as the oxidation of CO with the radical OH becomes more efficient than its hydrogenation initiating the CO-CH_4 conversion. The timescale of CO can be approximated using R5 as RLS in Eq.2 when the rate of R5 is higher than the rate of R7. We note that the timescale of CO at low temperatures and high fo_2 joins the timescales obtained for low fo_2, this stems from the decrease in OH/H with temperature and the resulting decrease in CO oxidation relative to hydrogenation. When the rate of R7 is higher than R5, the timescale of CO is controlled by CO-CH_4 conversion and thus by the RLS in the given pressure-temperature conditions.

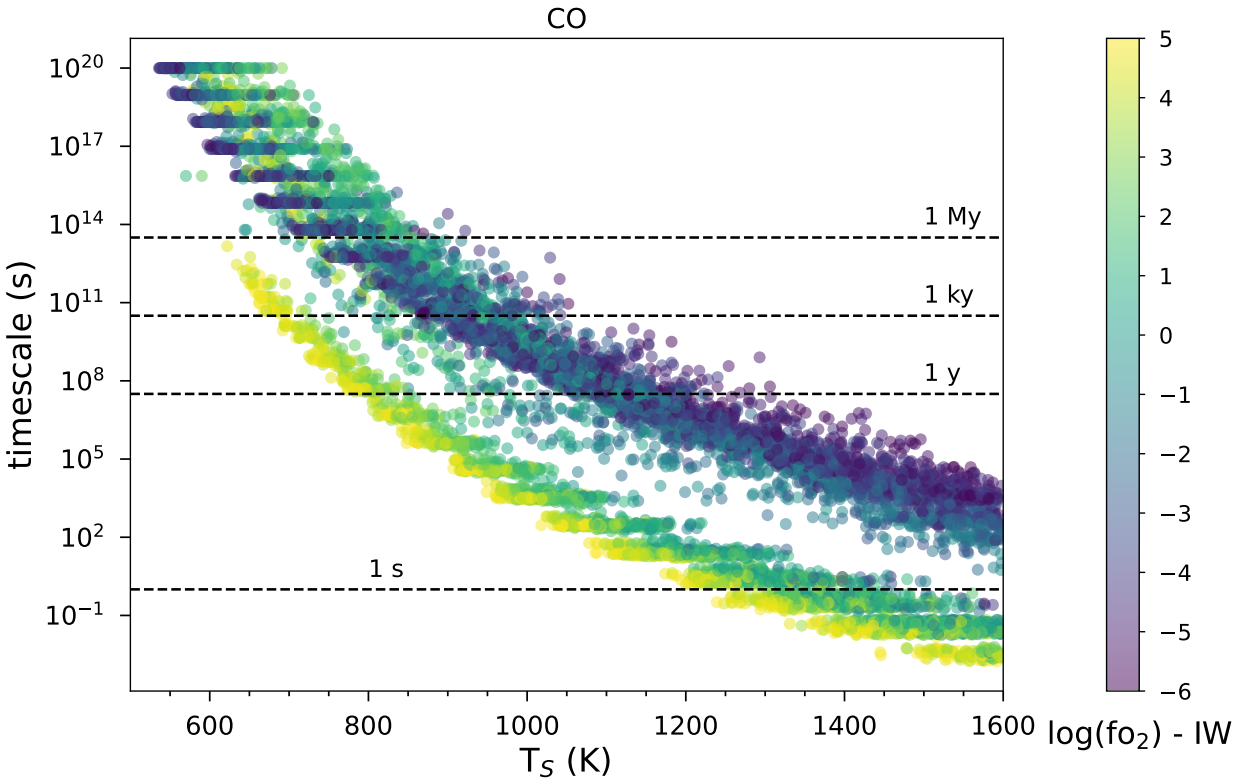

Fig. 4: Thermochemical timescales of CO as a function of temperature and fo_2 for the different simulations. Two branches are observed as the timescale is controlled by CO-CO_2 conversion at high fo_2 (high O/H) and CO-CH_4 conversion at low fo_2 (low O/H). The following model parameters are explored using 10,000 Monte Carlo simulations with uniform and log-uniform sampling : activity of graphite, degassing pressure (or atmospheric pressure), oxygen fugacity and atmospheric temperature (see main text Section 2.1 for the parameter range). The atmospheric temperature T_s is kept below the melt temperature T_m set to 1600K.

4. Case study using a climate-chemistry model : How does pressure, temperature, mixing and UV photons impact the atmospheric tracers of fo_2 ?

The trends in relative molecular abundances and timescales observed in Fig.2 and Fig.4 with atmospheric cooling (thermochemistry alone) are caused by the changes in OH/H with both temperature and fo_2. It is thus important to constrain atmospheric temperature from observations to improve the retrieval of fo_2. Generally speaking, the thermochemical timescales are short for temperatures above 1000K. Around 700-800K, the timescale can be very long depending on O/H (Fig.4). At these temperatures, equilibrium chemistry might not dominate over photochemistry and both must be considered carefully. The generalization of the timescales for photochemistry is difficult as it depends on several parameters including atmospheric composition, temperature, pressure, orbit radius and the distribution of stellar flux across the 1D column atmosphere. In this section, we perform 1D modelling including climate and chemical calculations to understand the combined role of photochemistry and equilibrium chemistry and their influence on the molecular abundances of C-H-O species.

4.1. Production of methane in volcanic atmospheres : a chemistry-climate feedback

Previous outgassing calculations showed that methane-rich degassing only occurs at low melt temperature and high degassing pressure (Wogan et al. 2020; Tian & Heng 2024). However, methane can be produced by thermochemistry in the atmosphere using CO and H_2 (Liggins et al. 2023). CH_4 is a strong greenhouse gas that can significantly affect the temperature profile. For our simulation with a surface pressure of 0.01 bar, thermochemistry is not efficient given the low surface temperature around 650K and CH_4 build-up is inefficient. CH_4 is produced efficiently in the 1 and 100 bar simulations however. Fig.5 shows the evolution of temperature and CO-CH_4 mixing ratios during the process of atmospheric cooling for the two end-member fo_2 (IW-3 and IW+3) with a surface pressure of 1 bar. We focus on this 1-bar surface pressure simulation to describe the mechanism forming methane. In the low fo_2 scenario (IW-3), the initial atmosphere presents a surface temperature much cooler than the high fo_2 scenario. An oxidized atmosphere made of CO_2-H_2O indeed possesses a higher IR opacity compared to the reduced CO-H_2 atmosphere. The 900K initial surface temperature of the low fo_2 scenario is explained by the high abundance of water in the atmosphere with a smaller contribution of H_2-H_2 CIA. The surface temperature of the low fo_2 atmosphere however increases by 300K in only a few years whereas the high fo_2 surface temperature is stable over time (top panels, Fig.5). Both simulations converge to a similar final surface temperature although warming is driven by CO_2-H_2O in the high fo_2 case and by H_2O-CH_4 in the low fo_2 case.

Fig.5 (left panels) shows that the increase in surface temperature in the low fo_2 scenario is correlated to the increase in CH_4 and decrease in CO mixing ratios. CO-CH_4 conversion indeed favors methane at a temperature of 900K and the chemical timescale is still short (Fig.4) allowing a fast methane build-up. At 900K, chemical equilibrium would however predict a methane mixing ratio above the CO mixing ratio (see dashed black curve, Fig.5, middle left panel) whereas our simulation shows that methane abundance stabilizes around 5.10^{-3}. This is explained by the radiative properties of methane limiting its own build-up as the abundance of CH_4 is very sensitive to the temperature. The increase of temperature caused by the increase in methane mixing ratio indeed changes the CO-CH_4 conversion making CO more stable at the final temperature of 1200K. In other words, the strong IR opacity of methane prevents its build-up above percentage level. This statement is true as the radiative timescale is here shorter than the chemical timescale leading to a climate feedback evolving progressively with the chemistry. In the high fo_2 scenario, the higher O/H and lower C/O favors oxidation of CO (R5) over hydrogenation (R7) making methane build-up less efficient (right panels, Fig.5). Liggins et al. (2023) showed that high methane abundances can be obtained in low fo_2 conditions by atmospheric cooling although their simulations do not consider this climate feedback which likely lead to biases in the final abundances. In both fo_2 scenarios, equilibrium chemistry would predict

high methane abundances in the upper atmosphere, at pressures below 0.1 bar, given the lower atmospheric temperature (middle panels, black dashed curves, Fig.5). Vertical mixing however quenches the methane abundance at higher pressures making the observed abundances dominated by disequilibrium chemistry. In other words, one must know the pressure-temperature conditions in the lower atmosphere close to the surface to interpret the methane abundance.

For low fo_2 (IW-3) and higher surface pressure (100 bars), methane is more stable and can build-up to higher abundances reaching percentage levels. In general, the methane build-up and lower ratio CO/CH_4 suggest the presence of a high pressure atmosphere (above 0.01 bar) leading to high temperatures at the surface. High-pressure/High-temperature chemistry dominates the observables as thermochemistry and mixing-driven quenching is faster than photochemistry in these conditions. K_{zz} does not affect the final outcome of the feedback in terms of temperature and mixing ratio. It however affects the evolution over time as the mixing and radiative timescales are competing. For low K_{zz} values, the CH_4 build-up starting in the lower atmosphere at higher pressures is not transported upwards fast which affects the radiative feedback. In the 100 bar scenario, the chemical timescale is lower than the radiative timescale making the model converge fast, with less iterations. The dominant chemical mechanism changes for lower pressures where photochemistry dominates the evolution, this is discussed in Section 4.2. If one would change the planet's orbit radius, the resulting effect on the surface temperature would also modify the outcome of the climate-chemistry feedback induced by methane. This process is therefore sensitive to the atmospheric redox state and surface temperature. This latter parameter is itself controlled by the abundances of greenhouse gases, the surface pressure and the orbit radius.

4.2. Atmospheric CO_2/CO as a tracer of interior fo_2 : effect of thermochemistry and photochemistry

As discussed in Section 3, CO_2/CO decreases with temperature driven by the change in OH/H. In a 1D column atmosphere the CO-CO_2 abundances will change throughout the atmosphere given the decrease of temperature with altitude. The vertical abundances of the main species involved in the net reaction $CO + H_2O \longleftrightarrow CO_2 + H_2$ are shown in Fig.6 for the two end-member fo_2 (IW-3 and IW+3) scenarios in a 1-bar atmosphere. Since CO and CO_2 quench at lower pressure than CH_4, the change of temperature in the lower atmosphere is important and will control their constant abundance in the upper atmosphere. For both fo_2 scenarios, we see that CO_2/CO increases with altitude caused by the decrease in temperature. K_{zz} controls the quench point and thus the CO_2/CO in the upper atmosphere.

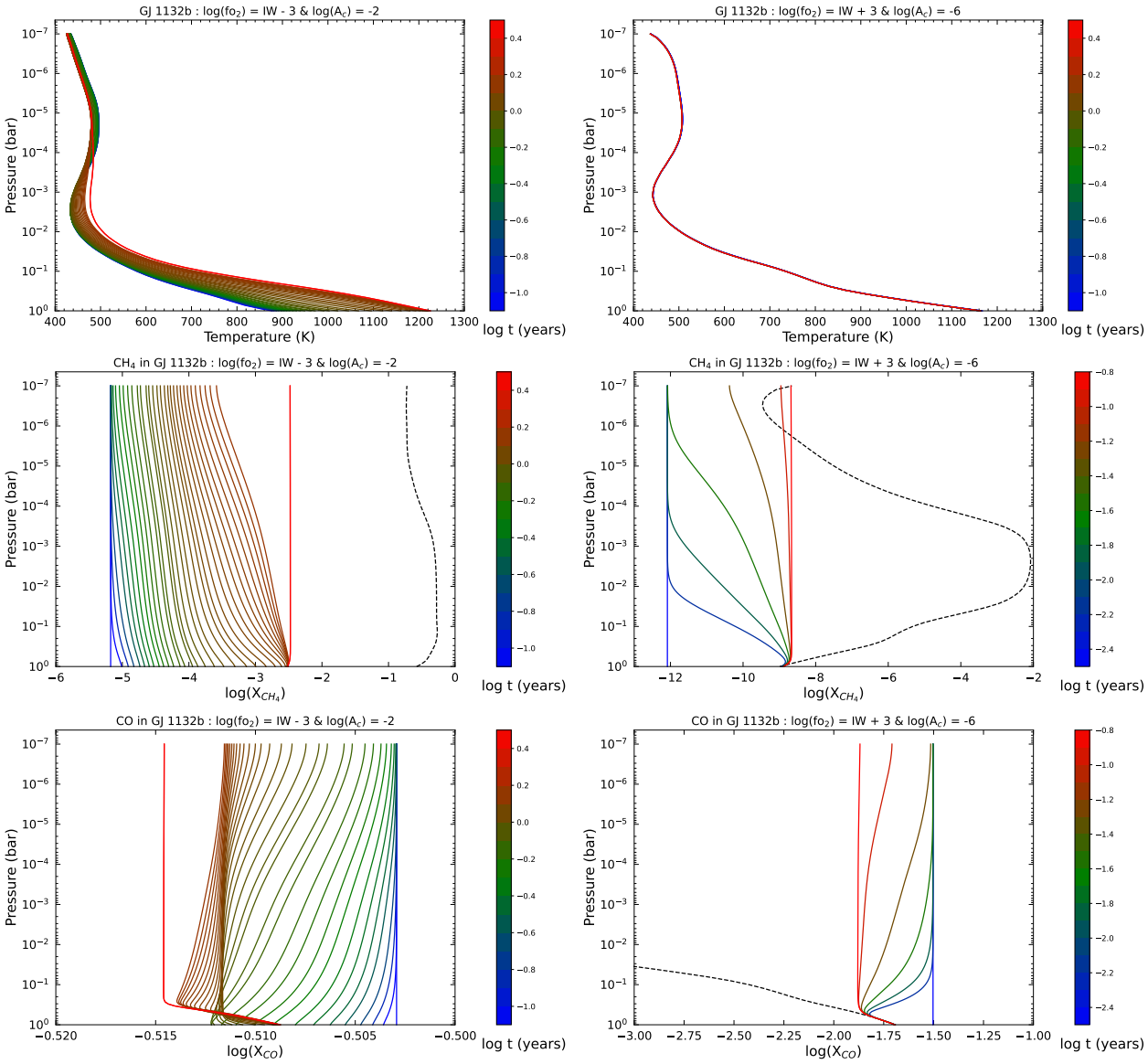

Fig. 5: Temporal evolution of temperature and CO-CH_4 volume mixing ratios in a 1-bar atmosphere around GJ 1132b considering two end-member oxygen fugacities. K_{zz} = 10^7 cm^2/s is assumed. The initial atmospheric composition is set by outgassing. We consider fo_2 = IW-3 and A_c = 10^{-2} for the low oxygen fugacity end-member (left panels) and fo_2 = IW+3 and A_c = 10^{-6} for the high oxygen fugacity end-member (right panels). The dashed black curve shows the prediction of chemical equilibrium without vertical mixing computed with FastChem using the initial state of the atmosphere (abundances predicted by outgassing).

In our simulations, the CO_2/CO predicted by outgassing can change in the atmosphere by a factor of 2-3 depending on the temperature and mixing rate. In theory, CO_2/CO could change by up to two orders of magnitude (Fig.2) as discussed in Section 3 but the high chemical timescales obtained for the low temperature simulations make thermochemistry inefficient relative to photochemistry. This change of CO_2/CO by a factor of 2-3 is reasonable and suggest that the molecular abundances in the atmosphere still hold crucial information on the redox state of the interior.

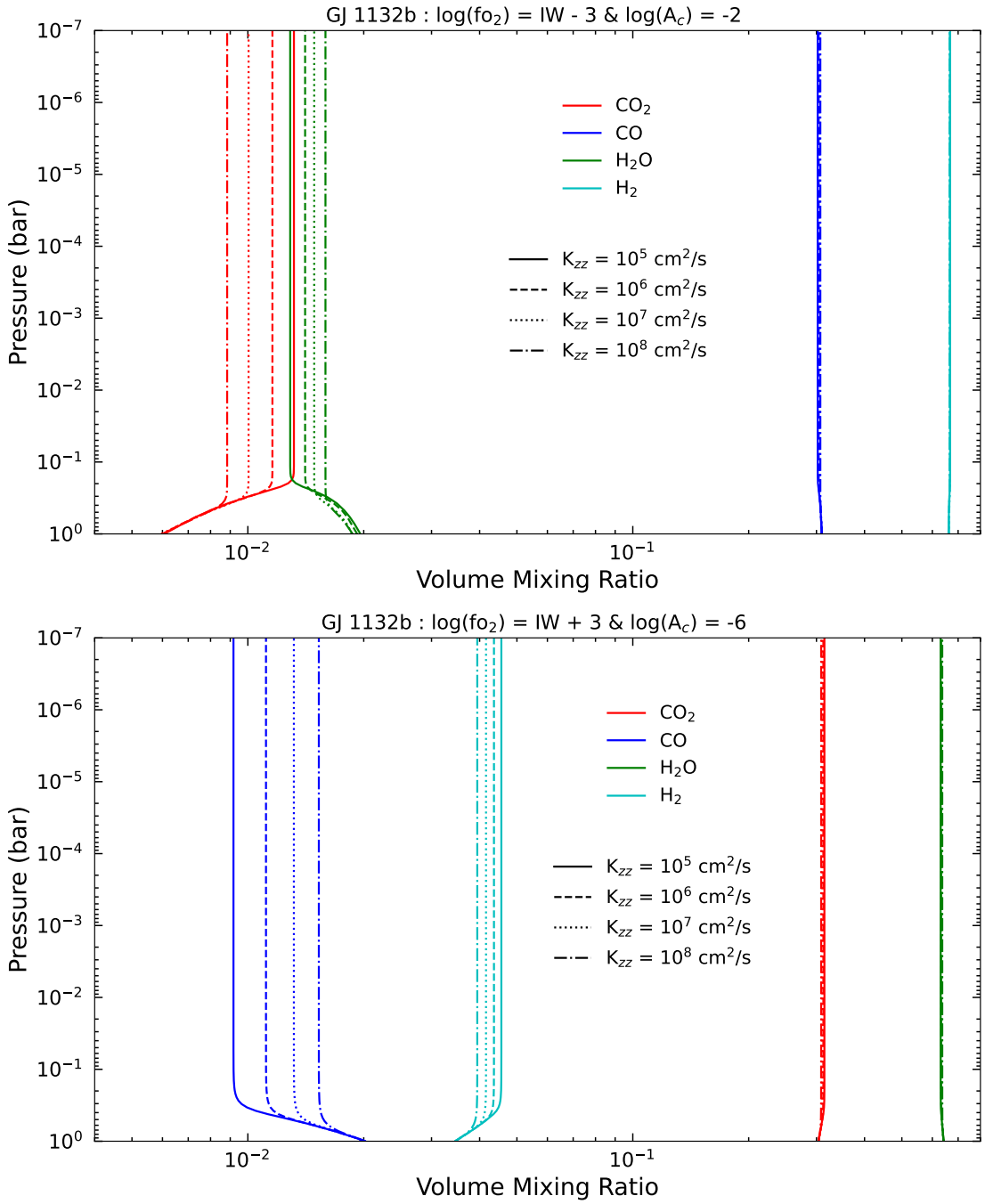

Fig. 6: Vertical volume mixing ratios of CO, CO_2, H_2 and H_2O for the 1-bar atmosphere scenario of GJ 1132b with two end-member oxygen fugacities. The initial atmospheric composition is set by outgassing. We consider fo_2 = IW-3 and $A_c = 10^{-2}$ for the low oxygen fugacity end-member (top panel) and fo_2 = IW+3 and $A_c = 10^{-6}$ for the high oxygen fugacity end-member (bottom panel). Different mixing efficiencies are shown (eddy coefficient K_{zz}) affecting the molecular abundances at the quench point (e.g. CO_2/CO). The pressure-temperature profiles of both scenarios are shown in Fig.5 (top panels).

Although thermochemistry dominates the vertical abundances of the species in the 1-bar and 100-bar simulations given the high pressure and temperature, photochemistry dominates the evolution in the 0.01-bar simulation. The temporal evolution of the temperature profile and vertical mixing ratios

of CO_2 and H_2O are shown in Fig.7. Analysis of the chemical network reveals an evolution similar to thermochemistry with $CO + H_2O \longleftrightarrow CO_2 + H_2$ as a net reaction :

$$H_2O + h\nu \longrightarrow OH + H \qquad \text{(R16)}$$

$$CO + OH \longrightarrow CO_2 + H \qquad \text{(R17)}$$

$$H + H + M \longrightarrow H_2 + M \qquad \text{(R18)}$$

$$\text{net} : CO + H_2O \longrightarrow CO_2 + H_2$$

The change here is that radicals OH and H are produced by photo-dissociation in the upper atmosphere instead of thermo-dissociation in the lower atmosphere. In the low fo_2 scenario (IW-3), the abundance of CO exceeds that of water. The high abundance of water however leads to an efficient production of the OH radical which oxidizes and destroys CO. Over long periods of time (tens to hundreds of thousands of years), the loss of water and CO becomes significant with the oxidation of CO leading to an increase of CO_2 abundances. The photolysis of CO_2 reproduces CO but this process is less efficient than the water photolysis and oxidation of CO. As the system evolves over time, water mixing ratio decreases and CO will stabilize to an abundance resulting from a balance between destruction by oxidation and production by CO_2 photolysis. Overall, CO_2/CO increases by $\approx$ 1-2 orders of magnitude. The temperature profile changes over time but only in the upper atmosphere (Fig.7, top left panel) since the initial stratospheric inversion induced by water (Malik et al. 2019b) is removed as a result of its photochemical loss. This photochemical mechanism suggest that photochemistry can introduce a bias in CO_2/CO although the long timescale of this process would make it inefficient if the planet is still volcanically active.

The chemical regime controlling CO_2/CO (photochemistry or thermochemistry) is mainly influenced by oxygen fugacity itself (i.e. O/H), orbit radius and surface pressure. For a given orbit radius, surface pressure controls surface temperature and thus the efficiency of thermochemistry. For a given surface pressure, the timescales of equilibrium chemistry increase with orbit radius. Since the stellar flux and orbit radius are well constrained for the different rocky objects, the main parameters one should assess to interpret relative molecular abundances are surface pressure and fo_2. Mixing can be important although it should affect the relative abundances by a factor of 2-3 at the most. In the outgassing model, a change of CO_2/CO by a factor of 2-3 would correspond to a change of fo_2 by one order of magnitude approximately. The lack of constraints on mixing and atmospheric temperature at the quench point would introduce a bias of approximately one order of magnitude on the retrieved fo_2. If the atmosphere is thin (low surface temperature) and continuously replenished by geochemical outgassing, the CO_2/CO will be preserved given the long timescales of the photochemical mechanism.

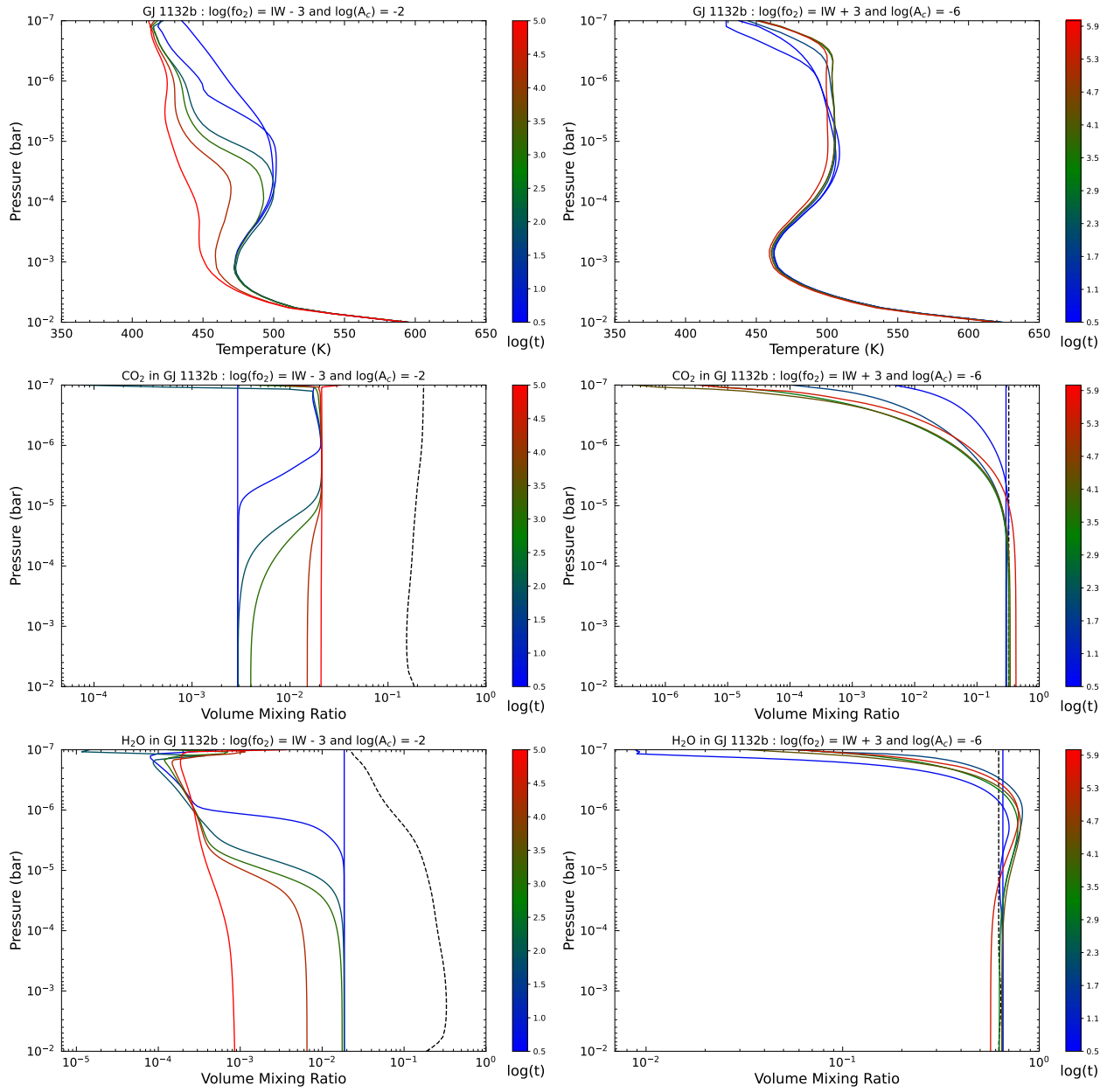

Fig. 7: Temporal evolution of temperature and CO_2-H_2O volume mixing ratios in the 0.01-bar atmosphere scenario of GJ 1132b (with $K_{zz} = 10^5$ cm^2/s). The dashed back curve shows the prediction by equilibrium chemistry without mixing and computed with FastChem using the initial abundances predicted by outgassing. Left panels : low fo_2 scenario (IW-3). Right panels : high fo_2 scenario (IW+3).

4.3. Summary of the different scenarios and implications for observations

The previous section revealed that CO_2/CO varies in the lower atmosphere following the change in temperature until the quench point is reached. For each scenario, we calculate with HELIOS the contribution function at different spectral bins to assess the pressure and temperature probed in emission. The result is shown in Fig.8 (top left panel) for the high fo_2 (IW+3) 1-bar scenario. For the two fo_2 end-member cases (IW-3 and IW+3), we simulate emission and transmission spectra to cover the

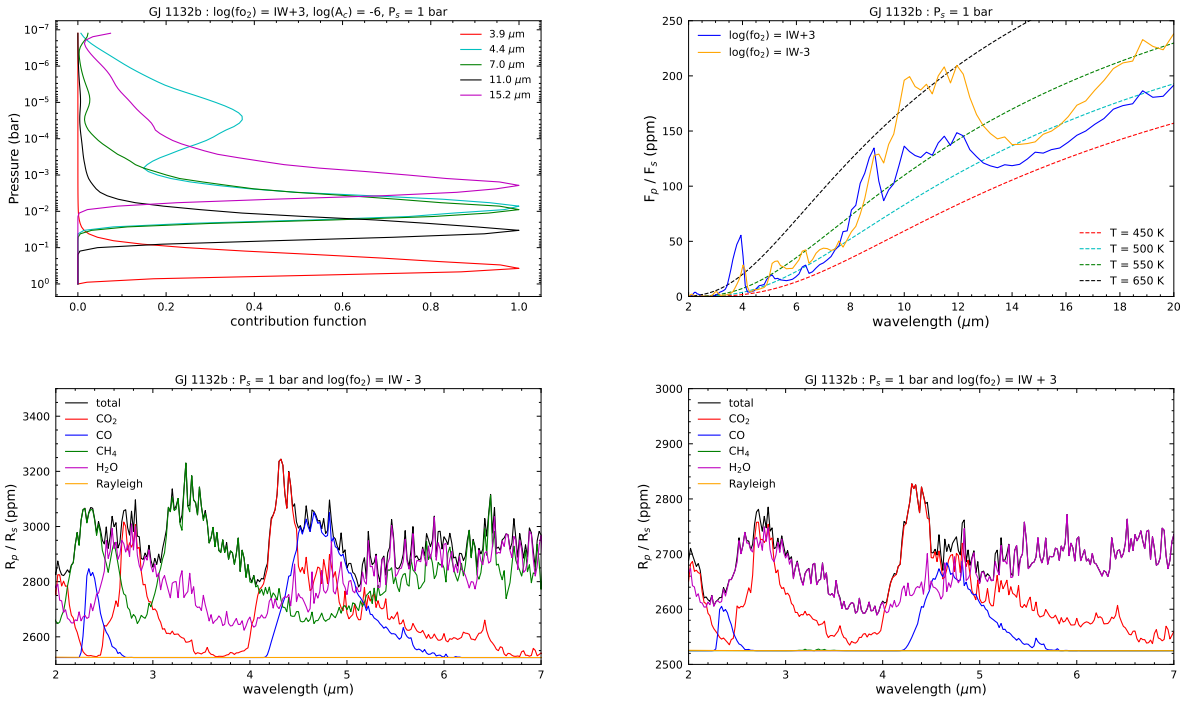

Fig. 8: Predictions of observation for low fo_2 and high fo_2 atmospheres around GJ 1132b. (Top left panel) Contribution function calculated with HELIOS to assess the pressure and temperature probed in emission with different spectral bins. (Top right panel) Emission spectra of the high fo_2 and low fo_2 1-bar atmosphere. (bottom panels) Transit spectra focusing on the NIRSpec range of JWST, with the contribution of the different species on the observed signatures for the low fo_2 scenario (left) and high fo_2 scenario (right).

spectral range of NIRSpec (transmission) and MIRI (emission) on JWST.

Let's start by looking at emission spectra and the information they can provide. We observe in Fig.8 (top right) that the deep atmosphere is only probed in the spectral range separating the water and CO_2 bands between $\approx$ 3.2 and 4 μm. Given the presence of methane in the low fo_2 case and its significant contribution around 3.5 μm, the pressure probed is highest around 3.9 μm between the CH_4 and CO_2 bands. In the simulated emission spectra (top right panel, Fig.8), the change between the fo_2 scenarios in the NIRSpec range is seen in this spectral window. The lack of methane in the high fo_2 scenario leads to a higher signal as emission mainly comes from a deeper atmospheric layer with a higher temperature. The spectral window is also larger in the high fo_2 case given the lack of methane build-up. We remind the reader that the absence of methane can also be explained by a thin atmosphere with low surface temperature in a low fo_2 scenario.

In the region between 10 and 15 μm previously used to assess the presence of a CO_2 thick atmosphere around Trappist-1c (Zieba et al. 2023), we observe a change between the low fo_2 and high fo_2 scenarios. In both cases, the 15-μm CO_2 band is observed but the ratio of signal between 12 and 15 μm is different and traces the high abundances of water in the high fo_2 scenario. For IW-3, the spectral region around 10-12 microns probes deep atmospheric layers leading to a difference above

50 ppm with the 15-μm CO_2 band. For IW+3, the steam atmosphere absorbing at 10-12 μm reduces the difference with the CO_2 band to $\approx$ 25 ppm. In the future, one should consider using this ratio to provide first insights on the partial pressures of CO_2 and water in the atmosphere.

Now, let's look at simulated transit spectra. In transmission, variations between low fo_2 and high fo_2 scenarios mainly lie in the abundance of methane and carbon monoxide as shown in Fig.8 (bottom panels). In the low fo_2 case, the CO-H_2 atmosphere is seen with the clear signatures of methane at 2.3 and 3.4 μm and CO dominating the contribution at 4.7 μm. CO_2 is still abundant and detected in the low fo_2 case using its 4.4 μm feature. In the high fo_2 scenario (bottom right panel, Fig.8), the high abundances of CO_2 and H_2O dominate the spectrum and contribute significantly at 4.7 μm given the lower opacity and abundance of CO. Retrieving accurately high CO_2/CO might be challenging as the data would probably be fitted efficiently without contribution from CO. Future work should assess in detail the limitations in inferring CO_2/CO for rocky exoplanet atmospheres using a retrieval framework. Only with this detailed retrieval analysis, one could evaluate how accurate the CO_2/CO value can be.

In our analysis, we see that the probed pressure at the peak of the opacity bands of CO_2, CO, CH_4 and H_2O is below 0.1 bar (top left panel, Fig.8). The probed mixing ratio thus corresponds to the quenched value controlled by vertical mixing. Our analysis suggest that the effect of K_{zz} has negligible impact on the transit spectra as the variation in mixing ratios are small for the dominant atmospheric species and usually within 50% for the secondary species (CO-H_2 in high fo_2 case and H_2O-CO_2 in low fo_2 case). In Fig.9, we review the quenched abundances of the different simulations across the P_s-fo_2 space and summarize the changes in CO_2/CO compared to the outgassing prediction. We also assess the changes in CO_2/CH_4 as the distinct signatures of methane make it easier to observe compared to CO.

In all the scenarios, CO_2/CO is increased (Fig.9) by atmospheric chemistry compared to the outgassing prediction following the chemical mechanisms described in Section 3.2 and 4.2. With thermochemistry, the change in CO_2/CO remains below one order of magnitude as the high abundances of greenhouse gases in volcanic atmospheres (CH_4, CO_2 and H_2O) tend to produce high surface temperatures with a relatively low difference with the melt temperature. Photochemistry can modify CO_2/CO for thin atmospheres although this process occurs over timescales likely longer than the replenishment by outgassing. Following the outgassing calculations, CO_2/CO changes by one order of magnitude when fo_2 varies by two orders of magnitude. The effect of atmospheric chemistry introduces a limit into how accurate one can be in inferring fo_2 if the temperature of the quench point cannot be constrained. We estimate this bias around one order of magnitude, two if photochemistry is

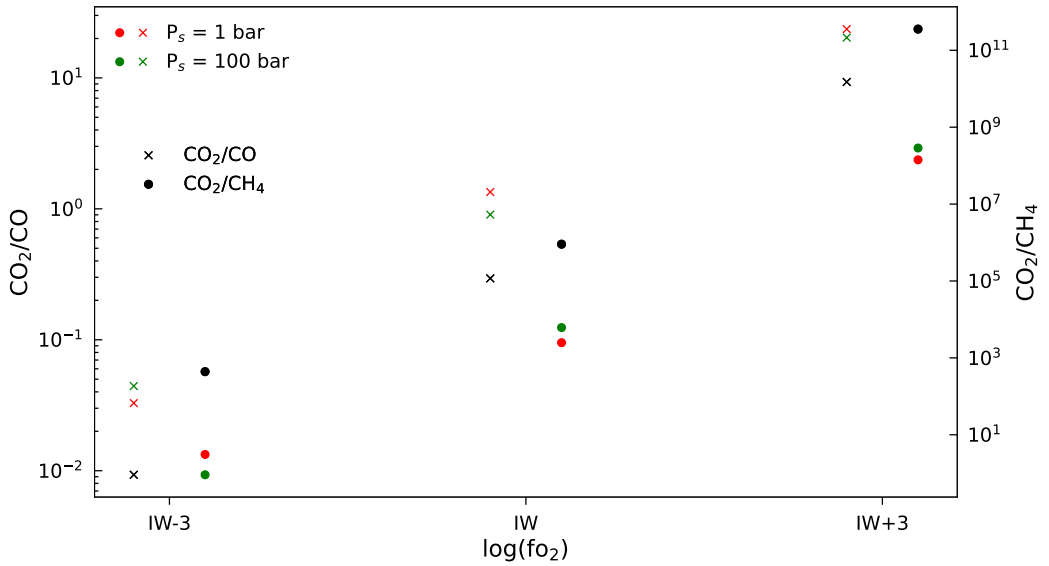

Fig. 9: Relative molecular abundances of the different P_s and fo_2 simulations at the quench point. Crosses correspond to CO_2/CO and dots correspond to CO_2/CH_4. The black marker shows the prediction by outgassing alone and the colored markers show the prediction including atmospheric chemistry.

considered.

Fig.9 shows that CO_2/CH_4 decreases significantly as a result of atmospheric cooling. At fo_2 around IW and below, CO_2 and CH_4 coexist and reach detectable levels. CO_2/CH_4 can help infer atmospheric fo_2 if the CO abundance cannot be retrieved accurately. Above IW, CO_2/CH_4 is very high and methane will likely not be observed given its low stability in an atmosphere with high O/H. The high abundance of water and CO_2 and the absence of methane might be the best indicator of high fo_2 scenarios although constraining the exact fo_2 value is limited by the detection efficiency of CO. At low fo_2, the co-existence of CO, CH_4 and CO_2 could be constrained and provide crucial information on interior fo_2 and atmospheric temperature. CO/CH_4 can help constrain the atmospheric temperature whereas CO_2/CO or CO_2/CH_4 can be used to constrain fo_2. Fig.10 summarizes the different mechanisms affecting the observables of volcanic atmospheres and the strategy of observations suggested by this work. Fig.9 also shows that the difference in methane abundances between the 1-bar and 100-bar scenarios is small, below the expected accuracy with JWST. Using CH_4, one could infer the presence of a thick atmosphere with high surface pressure and temperature although a reliable value of surface pressure cannot be inferred. P_s is one of the main parameters affecting the outcome of atmospheric chemistry as it also controls temperature. Since retrieving P_s from observations is difficult (e.g. Heng & Kitzmann (2017)), retrieval framework and fo_2 inference should consider this parameter carefully.

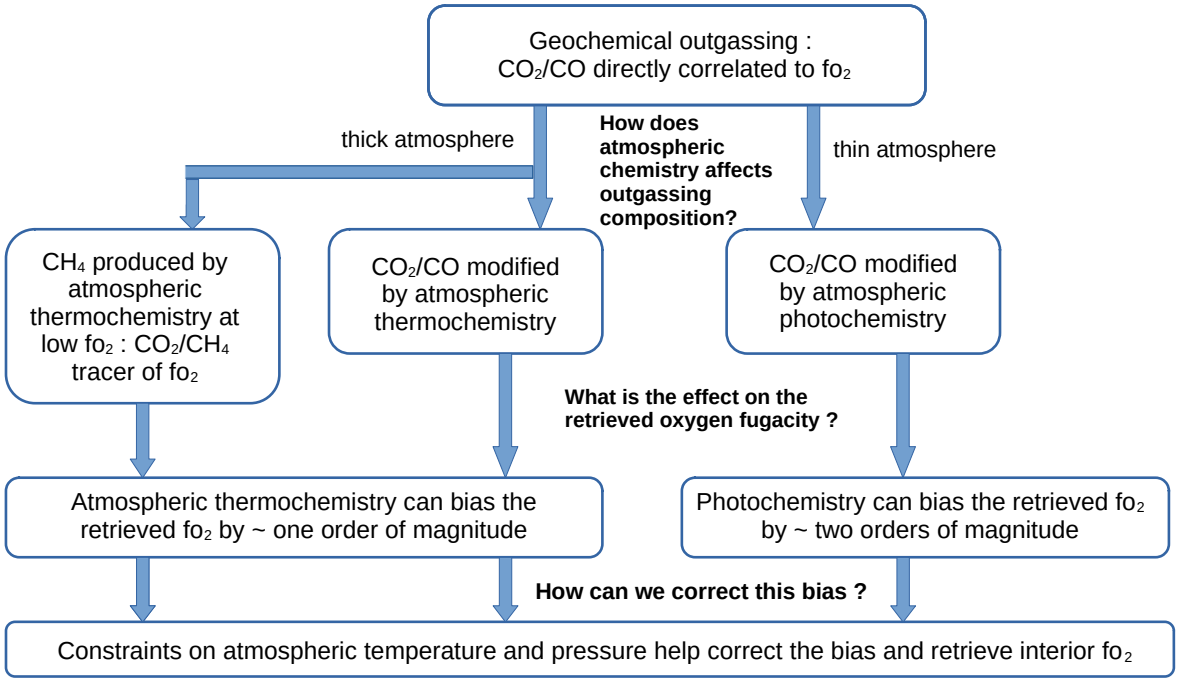

Fig. 10: Flow chart summarizing the effect of atmospheric chemistry on the tracers of interior oxygen fugacity (CO_2/CO and CO_2/CH_4). The terms 'thick' and 'thin' atmospheres are used respectively to mark the transition from a regime dominated by equilibrium chemistry towards a regime dominated by photochemistry. This transition is not quantified using pressure ranges as other variables must be considered including distance to the star and O/H (see main text).

5. Model limitations and discussions

5.1. Limitations of the model

The geochemical outgassing calculations following the approach of French (1966) provide a simple solution for the partial pressure of volatiles in the C-H-O fluid system although it does not consider their solubility in a silicate melt. In practice, one needs to extend the simple system in French (1966) to include gas-melt equilibria, e.g. for water (dissolved as OH^-) and CO_2 (dissolved as carbonate CO_3^{2-}), following the formalism in Iacono-Marziano et al. (2012), Gaillard & Scaillet (2014), Burgisser et al. (2015) or Liggins et al. (2020). Ascension of magma and surface degassing is typically simulated by solving the set of gas-gas and gas-melt equilibria equations at decreasing pressure until soluble species ex-solve from the melt and the surface pressure is reached. This approach is used in the D-compress and EVolve models of Burgisser et al. (2015) and Liggins et al. (2022) respectively, both used for applications in planetary and exo-planetary sciences.

The added complexity in these calculations leads to additionnal model parameters including mantle melt fraction, partition coefficients of the species and volatile budget, all of which are largely unconstrained for exoplanets. Our approach focuses on the main parameter affecting gas speciation, oxygen fugacity, using simple calculations that can be easily included in the analysis of JWST data

to assess the error on the retrieved fo_2. The solubility of water could however affect the O/H budget of the atmosphere and change the outcome of thermochemistry and photochemistry. Water is indeed favored at higher pressures in the gas phase (Tian & Heng 2024) although water solubility becomes important above 1 bar (Gaillard & Scaillet 2014). In a similar way, atmospheric escape can change the O/H atmospheric budget over time. Given the conclusions of this study, both melt solubility and atmospheric escape should be considered in future work to assess in greater details their influence on the variations of O/H compared to fo_2. This complexity increases the difficulty in inferring interior fo_2 from observations especially since the surface pressure (controlling solubility) and the escape history are not constrained from observations.

Given the high solubility of N in the melt at low fo_2 (Bernadou et al. 2021) and its significant impact on the atmospheric abundances of NH_3 (Shorttle et al. 2024), we leave these calculations for a future study where solubility will be included in the calculations. N-rich volcanic atmospheres are expected (Liggins et al. 2022, 2023), one might foresee a similar effect of O/H on the N_2-NH_3 conversion with N_2 favored at high O/H. The effect of NH_3 on the radiative-chemical feedback discussed for CH_4 (Fig.5, Section 4.1) should be assessed given its high IR opacity and its thermochemical stability also strongly dependent on temperature.

5.2. Implications for JWST observations

For rocky exoplanets, recent observations of 55 Cancri e (Tsiaras et al. 2016; Hu et al. 2024), GJ 486b (Moran et al. 2023) or GJ 1132b (Swain et al. 2021; May et al. 2023) suggest the presence of an atmosphere where the main gas components can be identified. Although the observations of Trappist-1c (Zieba et al. 2023) and LHS 475b (Lustig-Yaeger et al. 2023) point to a thin atmosphere or no atmosphere, the data quality suggest that a thick atmosphere should be detected if present. Even in emission, one should expect to resolve CO_2 and H_2O bands efficiently if enough transits were accumulated (Piette et al. 2022). The current observations are limited by the spectral range and the presence of cool stellar spots leading to detections of methane and water bands that might not originate from the planet's atmosphere (May et al. 2023; Moran et al. 2023). Despite these limitations, interpretation of molecular detections in rocky exoplanet atmospheres is starting including reasoning around the interior redox state (Heng 2023; May et al. 2023). The variations in the secondary eclipse observations of 55 Cancri e could be caused by transient degassing unbalanced with atmospheric escape given the very short orbital period of the planet (Heng 2023). Recent observations suggest an atmosphere rich in CO_2 and/or CO (Hu et al. 2024). Additional observations might help constrain their relative abundances and infer the redox state of the magma ocean. On the other hand, the detection of H_2O and CH_4 in GJ 1132b, if not caused by stellar spots, raises questions on the redox state as CO_2 and CO abundances are not well constrained (May et al. 2023).

Our work is also relevant for sub-Neptune planets as recent observations suggest that a magma ocean could be present beneath the thick H_2 envelope with degassing explaining a high metallicity (Shorttle et al. 2024). In addition, the high atmospheric pressure scale height of these objects make them ideal targets with JWST. The high abundances of CH_4 and CO_2 inferred from JWST observations of K2-18b are compatible with biotic methane emissions in an ocean planet with a shallow H_2 envelope and habitable surface temperature (Madhusudhan et al. 2023). The data could also be explained by a deeper H_2 atmosphere with high metallicity around 100X solar (Wogan et al. 2024). The co-existance of CO_2-CH_4 and the absence of ammonia can be explained by a deep magma ocean with reducing conditions and thus high ammonia solubility (Shorttle et al. 2024). Following our study, this can be explained at relatively low OH/H in the atmosphere although one would need to constrain the atmospheric temperature to retrieve the fo_2 with greater accuracy. At these high metallicities and low oxidation states, abundances of CO higher than CO_2 are expected (Shorttle et al. 2024) but not suggested by the retrieval analysis of Madhusudhan et al. (2023). The difference in the habitable shallow atmosphere and warm deep atmosphere scenarios lies in the CO abundance relative to CO_2 and CH_4. As described in Section 4.3, CO could be unconstrained given its low IR opacity and its main band overlapping with that of CO_2. CO_2/CH_4 can however be seen as a tracer of fo_2 as well (see Section 4.3) with the low ratio in K2-18b suggesting very low fo_2 conditions in agreement with the interpretation of Shorttle et al. (2024). More quantitatively, Madhusudhan et al. (2023) suggested $CO_2/CH_4 \approx 0.1$ which correspond to a fo_2 around IW-3 (see Fig.9). The nature of K2-18b is still debated, one would need to look for specific features which might confirm an atmospheric composition controlled by equilibrium chemistry and pointing to the presence of a deep-hot atmosphere. One would need to assess the CO_2/CH_4 and if possible CO_2/CO for several sub-Neptunes objects with different equilibrium temperatures to confirm a predominance by thermochemistry.

6. Conclusions

Using relative abundances of simple molecules (CO, CO_2, CH_4 and H_2O) now constrained from the observations of rocky exoplanet atmospheres with JWST, we can start to discuss implications for the redox state of the rocky interior. The relative molecular abundance CO_2/CO provides crucial information given the direct correlation with oxygen fugacity. We assess the effect of atmospheric chemistry on the molecular abundances to highlight the main mechanisms and suggest corrections and reasoning for future applications. For high temperatures ($\approx$ 700-800K) and high fo_2 (high O/H), thermochemistry and mixing controls the vertical abundances in the atmosphere modifying CO_2/CO by atmospheric cooling. The lower atmospheric temperature at the quench point compared to the melt temperature leads to an increase in CO_2/CO making inference of fo_2 biased by one order of magnitude approximately if the atmospheric temperature cannot be constrained accurately. In low fo_2

and high pressure conditions, CO and CH_4 can co-exist at high abundances and their ratio can help constrain the atmospheric temperature. The primary limitation in the temperature correction is the inability to infer surface pressure from observations. Methane build-up creates a climate-chemical feedback under high pressure and high temperature ($\approx$ 700-800K) although the final mixing ratio does not vary significantly with pressure and therefore does not provide a reliable constraint for surface pressure. Given the weak contribution of CO in transit spectra for high CO_2 or H_2O abundances, CO_2/CH_4 is suggested as a more reliable tracer to infer interior oxygen fugacity although the lack of methane build-up under high O/H budget make the quantification of high fo_2 conditions difficult. In theory, photochemistry dominates over thermochemistry for thin and cool (below $\approx$ 700K) atmospheres with low fo_2 (low O/H) leading to an increase of CO_2/CO caused by the oxidation of CO via water photolysis. In practice, a recently replenished atmosphere preserves the composition set by outgassing given the long timescales of photochemistry (tens to hundreds of thousands of years). The timescales of equilibrium chemistry vary significantly with the O/H budget making the transition to a photochemistry-dominated regime dependent on distance to the star, pressure, composition (and thus temperature) and oxygen fugacity. Although the current sample of rocky exoplanet atmospheres observed is sparse, several detections of CO_2, H_2O and CH_4 were already suggested. These promising results emphasize the need to understand how chemical abundances can be used to infer properties of the atmosphere and explain them using the combined effect of outgassing, atmospheric chemistry and escape.

References

Adibekyan, V., Dorn, C., Sousa, S.G., et al. 2021, Science, 374, 330–332, doi : 10.1126/science.abg8794

Batalha, N., Domagal-Goldman, S.D., Ramirez, R., Kasting, J.F., Icarus, 258, 337-349, doi : 10.1016/j.icarus.2015.06.016

Baulch, D.L., Cobos, C.J., Cox, R.A. et al. 1992, J. Phys. Chem. Ref. Data, 21, doi : 10.1063/1.555908

Bernadou, F., Gaillard, F., Füri, E., Marrocchi, Y., Slodczyk, A. 2021, Chemical Geology, 573, doi : 10.1016/j.chemgeo.2021.120192

Berta-Thompson, Z.K., Irwin, J., Charbonneau, D. 2015, Nature, 527, 204–207, doi : 10.1038/nature15762

Borucki, W.J., Koch, D., Basri, G. 2010, Science, 327, 977-980, doi : 10.1126/science.118540

Borucki, W.J., Koch, D., Basri, G. 2011, ApJ, 736, doi : 10.1088/0004-637X/736/1/19

Buchhave, L.A., Latham, D.W., Johansen, A. 2012, Nature, 486, 375-377, doi : 10.1038/nature11121

Burgisser, A., Alletti, M., Scaillet, B. 2015, Computers & Geosciences, 79, 1-14, doi : 10.1016/j.cageo.2015.03.002

Chubb, K.L., Robert, S., Sousa-Silvia, C., et al., 2024, ArXiv, submitted to RASTI, doi : 10.48550/arXiv.2404.02188

Deng, J., Du, Z., Karki, B.B., Ghosh, D.B., Lee, K.K.M. 2020, Nat Com, 11, doi : 10.1038/s41467-020-15757-0

Dijkstra, E. W. 1959, NuMat, 1, 269-271, doi : 10.1007/BF01386390

Dorn, C., Khan, A., Heng, K., et al. 2015, A&A, 577, A83, doi : 10.1051/0004-6361/201424915

Dorn, C., Noack, L., Rozel, A.B. 2018, A&A, 614, doi : 10.1051/0004-6361/201731513

Fateev, A. 2019

Fisher, C. & Heng, K. 2018, MNRAS, 481, 4698–4727, doi : 10.1093/mnras/sty2550

France, K., Loyd, R.O.P., Youngblood, A., Brown, A. et al. 2016, ApJ, 820, doi : 10.3847/0004-637X/820/2/89

French, B. 1966, Rev. of Geoph., doi : 10.1029/RG004I002P00223

Frost, D.J. & McCammon, C.A. 2008, Annual reviews of Earth and Planetary Sciences, 36, 389-420, doi : 10.1146/annurev.earth.36.031207.124322

Fulton, B.J. & Petigura, E.A. 2018, AJ, 156, doi : 10.3847/1538-3881/aae828

Fulton, B.J., Petigura, E.A., Howard, A.W. 2017, AJ, 154, doi : 10.3847/1538-3881/aa80eb

Gaillard, F., Bernadou, F., Roskosz, M., et al. 2022, EPSL, 577, doi : 10.1016/j.epsl.2021.117255
Gaillard, F. & Scaillet, B. 2014, EPSL, 403, 307-316, doi : 10.1016/j.epsl.2014.07.009
Gao, P., Piette, A.A.A., Steinrueck, M.E. et al. 2023, ApJ, 951, doi : 10.3847/1538-4357/acd16f
Guimond, C.M., Shorttle, O., Jordan, S., Rudge, J.F. 2023, MNRAS, 525, 3703–3717, doi : 10.1093/mnras/stad2486
Gupta, A. & Schlichting, H.E. 2019, MNRAS, 487, 24–33, doi : 10.1093/mnras/stz1230
Hargreaves, R.J., Gordon, I.E., Rey, M., et al. 2020, ApJS, 247, doi : 10.3847/1538-4365/ab7a1a
He, C., Radke, M., Moran, M., et al. 2023, Nat Astron, 8, 182-192, doi : 10.1038/s41550-023-02140-4
Heng, K., Lyons, J.R., Tsai, S.-M. 2016, ApJ, 816, doi : 10.3847/0004-637X/816/2/96
Heng, K. & Tsai, S.-M. 2016, ApJ, 829, doi : 10.3847/0004-637X/829/2/104
Heng, K. 2023, ApJL, 956, doi : 10.3847/2041-8213/acfe05
Holland, T.J.B. & Powell, R. 1998, J. metamorphic Geol., 16, 309-343, doi : 10.1111/j.1525-1314.1998.00140.x
Hu, R., Bello-Arufe, A., Zhang, M., et al. 2024, Nature, 630, 609-612, doi : 10.1038/s41586-024-07432-x
Hu, R., Damiano, M., Scheucher, M., et al. 2021, ApJL, 921, doi : 10.3847/2041-8213/ac1f92
Hu, R., Seager, S., Bains, W. 2012, ApJ, 761, doi : 10.1088/0004-637X/761/2/166
Hu, R., Peterson, L., Wolf, E.T. 2020, ApJ, 888, doi : 10.3847/1538-4357/ab5f07
Iacono-Marziano, G., Gaillard, F., Scaillet, B., et al. 2012, EPSL, 357-358, 319-326, doi : 10.1016/j.epsl.2012.09.052
James, T.S. & Hu, R. 2018, ApJ, 867, doi : 10.3847/1538-4357/aae2bb
Kempton, E.M.R., Zhang, M., Bean, J.L. 2023, Nature, 620, 67-71, doi : 10.1038/s41586-023-06159-5
Kite, E.S., Fegley, B., Schaefer, L., Ford, E.B. 2019, ApJL, 887, doi : 10.3847/2041-8213/ab59d9
Heng, K. & Kitzmann, D. 2017, MNRAS, 470, 2972–2981, doi : 10.1093/mnras/stx1453
Li, G., Gordon, I.E., Rothman, L.S., et al. 2015, Astrophys. J. Supp. Ser., 216, doi : 10.1088/0067-0049/216/1/15
Liggins, P., Shorttle, O., Rimmer, P.B. 2020, EPSL, 550, doi : 10.1016/j.epsl.2020.116546
Liggins, P., Jordan, S., Rimmer, P.B., Shorttle, O. 2022, JGR planets, 127, doi : 10.1029/2021JE007123
Liggins, P., Jordan, S., Rimmer, P.B., Shorttle, O. 2023, JGR : planets, 128, doi : 10.1029/2022JE007528
Liu, Z. & Ni, D. 2023, A&A, 674, A137, doi : 10.1051/0004-6361/202245387
Lopez, E.D. & Fortney, J.J. 2013, ApJ, 776, doi : 10.1088/0004-637X/776/1/2
Luque, R. & Pallé, E. 2022, Science, 377, 1211-1214, doi : 10.1126/science.abl7164
Lustig-Yaeger, J., Fu, G., May, E.M. 2023, Nature Astronomy, 7, 1317-1328, doi : 10.1038/s41550-023-02064-z
MacDonald, M.G. 2019, MNRAS, 487, 5062–5069, doi : 10.1093/mnras/stz1480
MacDonald, R.J. & Lewis, N.K. 2022, ApJ, 929, doi : 10.3847/1538-4357/ac47fe
Madhusudhan, N., Sarkar, S., Constantinou, S., Holmberg, M., Piette, A.A.A., Moses, J.I. 2023, ApJL, 956, doi : 10.3847/2041-8213/acf577
Malik, M., Grosheintz, L., Mendonça, J.M. et al. 2017, AJ, 153, doi : 10.3847/1538-3881/153/2/56
Malik, M., Kitzmann, D., Mendonça, J.M. et al. 2019, AJ, 157, doi : 10.3847/1538-3881/ab1084
Malik, M., Kempton, E.M.-R., Koll, D.D.B., Mansfield, M., Bean, J.L., Kite, E. 2019, ApJ, 886, doi : 10.3847/1538-4357/ab4a05
Marrero, T.R. & Mason, E.A. 1972, J. Phys. Chem. Ref. Data, 1
May, E.M., MacDonald, R.J., Bennett, K.A. 2023, ApJL, 959, doi : 10.3847/2041-8213/ad054f
Moran, S.E., Stevenson, K.B., Sing, D.K. et al. 2023, ApJL, 948, doi : 10.3847/2041-8213/accb9c
Moses, J.I., Visscher, C., Fortney, J.J. 2011, ApJ, 737, doi : 10.1088/0004-637X/737/1/15
Moses, J.I., Line, M.R., Visscher, C., et al. 2013b, ApJ, 777, doi : 10.1088/0004-637X/777/1/34
Moses, J.I., Madhusudhan, N., Visscher, C., Freedman, R.S. 2013a, ApJ, 763, doi : 10.1088/0004-637X/763/1/25
Murphy, W. F. 1977, The Journal of Chemical Physics, 67, 5877–5882, doi : 10.1063/1.434794
Noack, L. 2023, 55th Annual Meeting of the Division for Planetary Sciences, 55
Oosterloo, M., Höning, D., Kamp, I.E.E., van der Tak, F.F.S. 2021, A&A, 649, A15, doi : 10.1051/0004-6361/202039664
Ortenzi, G., Noack, L., Sohl, F., et al. 2020, scientific reports, 10, doi : 10.1038/s41598-020-67751-7
Owen, J.E. & Schlichting, H.E. 2024, MNRAS, 528, 1615–1629, doi : 10.1093/mnras/stad3972
Owen, J.E. & Wu, Y. 2013, ApJ, 775, doi : 10.1088/0004-637X/775/2/105
Parke Loyd, R.O., Shkolnik, E.L., Schneider, A.C., et al. 2020, ApJ, 890, doi : 10.3847/1538-4357/ab6605
Piette, A.A.A., Madhusudhan, N., Mandell, A.M. 2022, MNRAS, 511, 2565–2584, doi : 10.1093/mnras/stab3612
Polyansky, O.L., Kyuberis, A.A., Zobov, N.F., Tennyson, J., Yurchenko, S.N., Lodi, L. 2018, MNRAS, 480, 2597–2608, doi : 10.1093/mnras/sty1877
Quick, L.C., Roberge, A., Mlinar, A.B., Hedman, M.M. 2020, Publications of the Astronomical Society of the Pacific, 132, doi : 10.1088/1538-3873/ab9504
Rothman, L.S., Gordon, I.E., Barber, R.J., et al. 2010, J. Quant. Spectrosc. Radiat. Transfer, 111, 2139-2150, doi : 10.1016/j.jqsrt.2010.05.001
Schiebener, P., Straub, J., Levelt Sengers, J.M.H., Gallagher, J.S. 1990, J. Phys. Chem. Ref. Data, 19, 677-717, doi : 10.1063/1.555859
Shorttle, O., Jordan, S., Nicholls, H., Lichtenberg, T., Bower, D.J. 2024, ApJL, 962, doi : 10.3847/2041-8213/ad206e

Sneep, M. & Ubachs, W. 2005, Journal of Quantitative Spectroscopy & Radiative Transfer, 92, 293-310, doi : 10.1016/j.jqsrt.2004.07.025

Stock, J.W., Kitzmann, D., Patzer, A.B.C., Sedlmayr, E. 2018, MNRAS, 479, 865-874, doi : 10.1093/mnras/sty1531

Stock, J.W., Kitzmann, D., Patzer, A.B.C. 2022, MNRAS, 517, 4070-4080, doi : 10.1093/mnras/stac2623

Swain, M.R., Estrela, R., Roudier, G.M., et al. 2021, ApJ, 161, doi : 10.3847/1538-3881/abe879

Tian, M. & Heng, K. 2024, A&A, 963, doi : 10.3847/1538-4357/ad217c

Tsai, S.-M., Lyons, J.R., Grosheintz, L., Rimmer, P.B., Kitzmann, D., Heng, K. 2017, ApJS, 228, doi : 10.3847/1538-4365/228/2/20

Tsai, S.-M., Kitzmann, D., Lyons, J.R., Mendonça, J., Grimm, S.L., Heng, K. 2018, ApJ, 862, doi : 10.3847/1538-4357/aac834

Tsai, S.-M., Innes, H., Lichtenberg, T., et al. 2021a, ApJL, 922, doi : 10.3847/2041-8213/ac399a

Tsai, S.-M., Malik, M., Kitzmann, D., Lyons, J.R., Fateev, A., Lee, E., Heng, K. 2021b, ApJ, 923(2), doi : 10.3847/1538-4357/ac29bc

Tsang, W. & Hampson, R.F. 1986, J. Phys. Chem. Ref. Data, 15, doi : 10.1063/1.555759

Tsang, W. 1987, J. Phys. Chem. Ref. Data, 16, 471–508, doi : 10.1063/1.555802

Tsiaras, A., Rocchetto, M. Waldmann, I.P., et al. 2016, ApJ, 820, doi : 10.3847/0004-637X/820/2/99

Van Eylen, V., Agentoft, C., Lundkvist, M.S. 2018, MNRAS, 479, 4786–4795, doi : 10.1093/mnras/sty1783

Venot, O., Hébrard, E., Agúndez, M., Decin, L., Bounaceur, R. 2015, A&A, 577, doi : 10.1051/0004-6361/201425311

Venot, O., Bénilan, Y., Fray, N. et al. 2018, A&A, 609, doi : 10.1051/0004-6361/201731295

Wogan, N., Krissansen-Totton, J., Catling, D.C. 2020, PSJ, Planet. Sci. J., 1(58), doi : 10.3847/PSJ/abb99e

Wogan, N.F., Batalha, N.E., Zahnle, K., Krissansen-Totton, J., Tsai, S.-M., Hu, R. 2024, ArXiv, doi : 10.48550/arXiv.2401.11082

Woitke, P., Herbort, O., Helling, C., et al. 2020, A&A, 646, A43, 10.1051/0004-6361/202038870

Wolf, A.S., Jäggi, N., Sossi, P.A., Bower, D.J. 2023, ApJ, 947, doi : 10.3847/1538-4357/acbcc7

Young, E.D., Shahar, A., Schlichting, H.E. 2023, Nature, 616, 306-311, doi : 10.1038/s41586-023-05823-0

Yu, X., Moses, J.I., Fortney, J.J., Zhang, X. 2021, ApJ, 914, doi : 10.3847/1538-4357/abfdc7

Zahnle, K., Haberle, R.M., Catling, D.C., Kasting, J.F. 2008, JGR, 113, doi 10.1029/2008JE003160

Zieba, S., Kreidberg, L., Ducrot, E. 2023, Nature, 620, 746-749, doi : 10.1038/s41586-023-06232-z

Astronomy & Astrophysics manuscript no. output
November 27, 2024
©ESO 2024

Chapter 5 : Optical constants of exoplanet haze analogs from 0.3 to 30 microns⋆ - comparative sensitivity of spectrophotometry and ellipsometry

T. Drant[1,2], E. Garcia-Caurel[3], Z. Perrin[1], E. Sciamma-O'Brien[4], N. Carrasco[1], L. Vettier[1], T. Gautier[1,5], J.-B. Brubach[6], P. Roy[6], D. Kitzmann[7], and K. Heng[2,8,9]

[1] University of Paris Saclay, OVSQ, LATMOS, 11 Boulevard d'Alembert, 78280 Guyancourt, France.
e-mail: thomas.drant@latmos.ipsl.fr

[2] Ludwig Maximilian University, Faculty of Physics, Observatory of Munich, Scheinerstrasse 1, Munich D-81679, Germany.

[3] Ecole Polytechnique, LPICM, Route de Saclay, 91120 Palaiseau, France.

[4] NASA Ames Research Center, Space Science and Astrobiology Division, Code ST, Moffett Field, CA 94035, USA.

[5] LESIA, Observatoire de Paris, Université PSL, CNRS, Sorbonne Université, 5 place Jules Janssen, 92195 Meudon, France.

[6] Synchrotron SOLEIL, L'Orme des Merisiers, 91190 Saint-Aubin, France.

[7] University of Bern, Center for Space and Habitability, Gesellschaftsstrasse 6, CH-3012, Bern, Switzerland.

[8] University of Bern, ARTORG Center for Biomedical Engineering Research, Murtenstrasse 50, CH-3008, Bern, Switzerland.

[9] University of Warwick, Department of Physics, Astronomy Astrophysics Group, Coventry CV4 7AL, United Kingdom.

ABSTRACT

We report new optical constants (refractive index n and extinction coefficient k) of exoplanet haze analogs from 0.3 to 30 microns. The samples are produced in a simulated N_2-dominated atmosphere with two different abundance ratios of CO_2 and CH_4 using the PAMPRE plasma reactor at LATMOS. We find that our haze analogs present a significantly lower extinction coefficient in the optical and near-infrared (NIR) range compared to the seminal data obtained on Titan haze analogs. We confirm the stronger IR absorption expected for hazes produced in a gas mixture with higher CO_2 abundances. Given the strong impact of the atmospheric composition on the absorbing power of hazes, these new data should be used to characterize early-Earth and CO_2-rich exoplanet atmospheres. The data presented in this paper can be found in the Optical Constants Database. Using ellipsometry or spectrophotometry, the retrieved optical constants are affected by the sensitivity of the measurement and the accuracy of the calculations. A comparative study of both techniques was performed to identify limitations and better understand discrepancies in previous data. For the refractive index n, errors of 1-3% are observed with both optical techniques and the different models, caused by the correlation with the film thickness. We find that UV-Visible reflection ellipsometry provides similar n values regardless of the model used whereas the Swanepoel method on transmission is more subjected to errors in the UV. In the UV and mid-infrared (MIR), the different calculations lead to rather small errors on k. Larger errors of k arise in the region of weak absorption where calculations become sensitive to errors on the refractive index n.

Key words. atmospheres, terrestrial planets

1. Introduction

Past observations and modelling predictions taught us that aerosols are ubiquitous in exoplanet atmospheres (Gao et al. 2021). Their scattering-induced opacity mutes gaseous signatures challenging our effort to unveil the atmospheric composition (e.g., Wakeford & Sing 2015; Sing et al. 2016; Bruno et al. 2018). The process of aerosol formation is directly related to the physical-chemical properties of the atmosphere. Following future ambitions with the James Webb Space Telescope (JWST) and the Atmospheric Remote-sensing Infrared Exoplanet Large-survey (ARIEL), the characterization of aerosols represents an essential step in understanding the diversity and complexity of exoplanet atmospheres (Beichman et al. 2014; Heng & Showman 2015; Zellem et al. 2019; Lacy & Burrows 2020).

Photochemical hazes are direct evidence of a complex disequilibrium chemistry triggered by energetic photons in the upper atmosphere. They are expected in the H_2-dominated atmospheres of relatively cold gas giants where methane is the main form of carbon (Gao et al. 2020). Laboratory experiments also revealed that a broad variety of bulk compositions can lead to the formation of hazes, including CO_2- and H_2O-rich atmospheres (He et al. 2018a; Hörst et al. 2018). Given the large diversity of atmospheric compositions predicted for rocky exoplanets (Gaillard & Scaillet 2014; Deng et al. 2020; Gaillard et al. 2022; Tian & Heng 2023), the presence of hazes is expected for numerous objects.

In atmospheric science, gas phase chemistry is described using a generalized framework based on first principles that can be used to predict the composition of exoplanet atmospheres (e.g., Heng et al. 2016). The complexity of haze formation precludes a similar description and requires the use of heavy assumptions for its physical parametrization (e.g., Morley et al. 2015; Lavvas & Koskinen 2017; Kawashima & Ikoma 2018, 2019; Gao et al. 2020). Laboratory analyses of the gas phase chemistry and its complex effect on haze production clearly point to the presence of multiple chemical pathways depending on the initial gas mixture (Sciamma-O'Brien et al. 2017; He et al. 2018a,b; Hörst et al. 2018; Berry et al. 2019; Moran et al. 2020; Perrin et al. 2021). Our current knowledge on haze composition and optical properties therefore mainly relies on experimental data. Intrinsic properties of photochemical hazes are described with their refractive indices (n and k), also called optical constants, used as an input parameter to Mie theory (e.g., Kitzmann & Heng 2018). The data is however scarce and often limited to a narrow spectral range (Gao et al. 2021).

The pioneering study of Khare et al. (1984) motivated the emergence of a field focusing on the formation of laboratory haze analogs, also called tholins, to retrieve their optical constants in support to observations and atmospheric modelling. Despite the different gas compositions expected for exoplanet atmospheres, the data of Khare et al. (1984) obtained on Titan haze analogs remain used for its broad spectral range (Arney et al. 2016; Kawashima & Ikoma 2018, 2019). Departure from a reduced N_2/CH_4 (Titan) composition towards more oxidizing conditions revealed an increased absorbing power of haze analogs (Gavilan et al. 2017, 2018; Jovanović et al. 2021) which can be partly explained by the incorporation of oxygen in the solid (Jovanović et al. 2020). A surprisingly high production rate of haze analogs with lower IR absorption properties is expected in H_2O-rich atmospheres (He et al. 2018a; Hörst et al. 2018). Recent simulations suggest that these different absorbing properties would significantly impact IR transit spectra (He et al. 2023). In the era of the JWST, haze particles could in theory be observed using their vibrational modes in the MIR in addition to the scattering slope in the visible and NIR (Wakeford & Sing 2015; Pinhas & Madhusudhan 2017; Mai & Line 2019; He et al. 2023). Optical constants of exoplanet haze analogs are therefore needed in a broad spectral range for future analyses of JWST spectra.

Following the seminal work of Khare et al. (1984), more data was acquired on laboratory haze analogs though often limited to either the MIR (Imanaka et al. 2012) or the UV-Vis-NIR (Ramirez et al. 2002; Mahjoub et al. 2012; Sciamma-O'Brien et al. 2012; Gavilan et al. 2017; Jovanović et al. 2021; He et al. 2022). The discrepancies in the reported optical constants are significant and largely overcome the uncertainties given by each study, even for haze analogs produced from a similar gas composition. The extinction coefficient (k) of Titan haze analogs measured by different groups varies by up to two orders of magnitude in the optical-NIR range (Brassé et al. 2015; He et al. 2022). UV absorption is also significantly different (Brassé et al. 2015) with only a few groups that observed a peak of absorption around 300-400 nm (Ramirez et al. 2002; He et al. 2022).

These discrepancies can be explained by three factors : the composition of the gas mixture, the experimental conditions (gas flow rate, pressure, temperature, energy distribution of the source), and the optical technique used to derive the refractive indices (Brassé et al. 2015). It was shown that relative abundances in the initial gas mixture affect the optical properties of hazes in the entire range (Mahjoub et al. 2012; Gautier et al. 2012; Gavilan et al. 2017, 2018). This assessment was possible as the analogs were produced using the same experimental setup and the measurements were performed using the same optical technique. Current data were however obtained by different groups, the literature is thus split between optical constants measured with ellipsometry and spectrophotometry. To the best of our knowledge, comparison of ellipsometric and spectrophotometric calculations using a similar analog and spectral range were only reported by Tran et al. (2003). Their results, limited to the refractive index n in the optical range, suggest variations between both techniques. A study is long

overdue to assess the effect of the optical method and better understand the current inconsistencies in the data.

The aim of the present study is two-fold.
First, we assess the effect of the optical technique providing a new baseline study to guide future calculations of optical constants for exoplanet aerosol analogs. The sensitivities and limitations of the different methods are investigated to better understand the discrepancies in the existing data.
We provide new optical constants (n and k) for exoplanet haze analogs from 0.3 to 30 microns thus covering the entire spectral range of JWST and ARIEL. Our analogs are produced using different oxidations in the gas mixture to quantify the increased absorption expected for oxygenated hazes. Following the work of Gavilan et al. (2018), we provide additional refractive index calculations and expand the spectral coverage in the far-infrared (FIR). Our new data are compared to the seminal work of Khare et al. (1984) for Titan haze analogs as we discuss implications for future observations.

2. Haze analogs

2.1. Production with PAMPRE

Haze analogs are produced using the PAMPRE (french acronym for "production of aerosols in micro-gravity by a reactive plasma") experimental setup described in detail in Szopa et al. (2006). This plasma reactor triggers disequilibrium chemical reactions from electron impact at energies equivalent to vacuum-ultraviolet photons. The relative electron energy distribution compares to a solar spectrum with an increased high-frequency tail enhancing dissociation and ionization of the gas molecules (Szopa et al. 2006; Alves et al. 2012). The plasma is confined in a stainless-steel cage with the base acting as the grounded electrode onto which we place optical substrates. During the experiment, an organic film grows on top of the substrates and pseudo-spherical grains deposit on the reactor walls. To avoid intricate treatment of the grain geometry, the refractive indices are only measured on thin films.

Experiments are performed at room temperature. The plasma is generated using a fixed radio-frequency power of 30 W and frequency of 13.56 MHz. The gas mixture is injected in the PAMPRE reactor chamber from high-purity gas bottles ($\geq$ 99.995% for CO_2, $\geq$ 99.9999% for N_2 and $\geq$ 99.9995% for CH_4) using MKS mass flow rate controllers. Continuous injection at 60 sccm (standard cubic centimeter per minute) and primary pumping generate a gas flow and ensure a stable pressure of 0.85 hPa in the reactor chamber. The haze analogs are collected at the end of the experiment. The chamber is then pumped down to $\sim 10^{-6}$ hPa using a turbo-molecular pump and the reactor walls are heated to prevent water contamination in the next experiments.

2.2. Gas mixture and samples

We mimic the composition of an oxidized Titan-like exoplanet atmosphere using the CO_2-CH_4 molecular pair recently proposed and currently debated as a potential biosignature (Arney et al. 2016, 2018; Krissansen-Totton et al. 2018; Woitke et al. 2021; Mikal-Evans 2022). The chosen gas composition is somewhat arbitrary given the wide diversity expected for exoplanet atmospheres (Gaillard & Scaillet 2014; Deng et al. 2020; Gaillard et al. 2022; Tian & Heng 2023), and is mainly inspired by our current knowledge on the chemical reactivity of N_2 and CH_4 (Sciamma-O'Brien et al. 2010). Our gas mixture is composed of 95% N_2 with two different abundance ratios of CO_2 and CH_4. We focus on CHON haze analogs formed in N_2-dominated gas mixtures to (1) compare our optical constants obtained in a broad spectral range with the seminal data of Khare et al. (1984), (2) assess the sensitivity of the different optical methods and calculations to understand discrepancies in the existing data and (3) quantify over a broad spectral range the change in optical properties emerging with higher abundances of CO_2 (Gavilan et al. 2017, 2018).

The properties of the two haze analogs, including the composition of the gas mixtures, are detailed in Table 1. From now on, the analogs produced in a 1% and 3% CO_2-rich gas mixture will be referred to as the reduced and oxidized analog respectively. For each gas mixture, thin films were deposited onto three different substrates during a single experiment. The substrates were specifically chosen to ensure the reliability of the subsequent ex-situ spectroscopic and ellipsometric measurements. We used an MgF_2 optical window (Crystran) for spectroscopic measurements in the UV-MIR range, an intrinsic silicon wafer (Sil'Tronix) with both sides polished for infrared spectroscopy, and a P-doped (boron) single side polished Si wafer (Sil'Tronix) for ellipsometric measurements. The different samples were produced with a thickness higher than 500 nm to avoid the formation of a non-negligible oxidized layer when they are exposed to air to carry out the optical measurements (Nuevo et al. 2022). The study of Gavilan et al. (2017) showed that an additional oxidized layer can be a limiting factor leading to model-dependent solutions when determining the refractive indices. Between the different optical measurements performed in this study, our samples were kept under primary vacuum to avoid continuous oxidation.

Gas composition	Substrate	Production[a] (hours)	Film thickness[b] (nm)	Film thickness uncertainty[c]
95% N_2 / 4% CH_4 / 1% CO_2	MgF_2	8	1375	$\leq 1\%$
(reduced analog)	doped Si	8	1566	$\leq 1\%$
	intrinsic Si	8	1445	$\leq 3\%$
95% N_2 / 2% CH_4 / 3% CO_2	MgF_2	57	750	$\leq 3\%$
(oxidized analog[d])	intrinsic Si	57	855	$\leq 3\%$

Notes.
[a] The production refers to the duration of the experiment.
[b] The film thickness are measured with the Swanepoel method or with UV-Vis ellipsometry depending on the sample (see main text).
[c] The uncertainty on the film thickness is determined using 6-7 measurements at different positions on the samples.
[d] As only spectroscopic measurements were performed on the oxidized analog, the doped Si substrate was not used.

Table 1: Different samples of our two haze analogs.

3. Optical measurements and calculations

3.1. Characterizing haze analogs with spectrophotometry and ellipsometry

3.1.1. Optical constants : intrinsic optical properties

Even though the composition of hazes remains largely unknown, their intrinsic properties can be described by the refractive indices, also referred to as optical constants, that physically quantify dispersion and absorption of radiation independently of the particles' geometry.

Dispersion and absorption result from dielectric polarization that occurs as electric dipoles within the material align with the electric field and oscillate following the frequency of the incident wave. In response to these forced oscillations, the dipoles radiate in all directions creating a secondary wave that interferes with the primary wave.

Sequential dielectric polarization reduces the speed of light in the material giving rise to the phenomenon of dispersion. The temporal frequency of light is unchanged in any medium but the wavelength is modified as λ/n, λ being the vacuum wavelength and n the real part of the complex refractive index.

Resonant oscillations occur as the natural frequencies of the dipoles are approached, it leads to destructive interference between the primary and secondary waves thus giving rise to the phenomenon of absorption. Electronic polarization occurs at optical and UV frequencies whereas atomic polarization leads to absorption at infrared frequencies.

The complex refractive index is expressed as N = n + ik. n is the refractive index and k is the extinction coefficient. Both are dimensionless parameters function of the composition, describing dispersion and absorption respectively.

Absorption and dispersion occur at the same time, their causal relationship is expressed by the Kramers-Kronig equation (Kronig 1926; Kramers 1927):

$$n(\nu_i) = n_\infty + \frac{2}{\pi} P \int_0^\infty \frac{\nu\, k(\nu)}{\nu^2 - \nu_i^2}\, d\nu \quad (1)$$

where ν is the vacuum wavenumber (cm^{-1}, defined as $1/\lambda$), and n_∞ is the refractive index at infinite wavenumber. P is the Cauchy principal value of the integral.

3.1.2. Spectrophotometry vs. Ellipsometry

Spectrophotometry and ellipsometry are the two main techniques used in material science to measure the refractive indices. Currently, the optical constants of haze analogs have been equally obtained with spectrophotometry (Khare et al. 1984; Ramirez et al. 2002; Tran et al. 2003; Imanaka et al. 2012; He et al. 2022) and ellipsometry (Khare et al. 1984; Mahjoub et al. 2012; Sciamma-O'Brien et al. 2012; Gavilan et al. 2017; Jovanović et al. 2021). The theory behind both techniques is very mature, we do not claim to bring any new theoretical contributions to the field but rather review the concepts that are relevant to understand the calculations discussed in the present study. Most of these concepts are adapted from the textbooks of Tompkins & Irene (2005) and Fujiwara (2007).

In practice, both methods rely on reflectance and/or transmittance measurements. Calculations account for the layered structure of the sample illustrated in Fig.1. Reflection and transmission at the different interfaces between media is only function of the refractive indices (and incident angle) as described by the well-known Fresnel coefficients.

Spectrophotometry and ellipsometry however differ in the description of the intrinsic properties. In spectrophotometry, we use the complex refractive index to describe how a medium affects the propagation of the wave. This physical description is commonly used in astronomy and planetary science, taking its root in the fundamental wave equation. In practice, spectrophotometric measurements are usually performed under unpolarized light. In ellipsometry, intrinsic optical properties are defined by the dielectric constant ε ($\varepsilon = \varepsilon_1 + i\varepsilon_2$), also called dielectric function for $\varepsilon(\nu)$. Commonly used in material science, this formalism describes the behavior of oscillating electric dipoles in a solid structure. In practice, ellipsometry uses a grazing geometry and different polarization states of light to understand the behavior of the dipoles.

The difference between both methods therefore essentially emerges from the physical description, whether we focus on the wave or the material. Both definitions describe dispersion and absorption by the material using a different formalism. Calculations should in principle provide similar intrinsic properties to satisfy the known relation between ε and N :

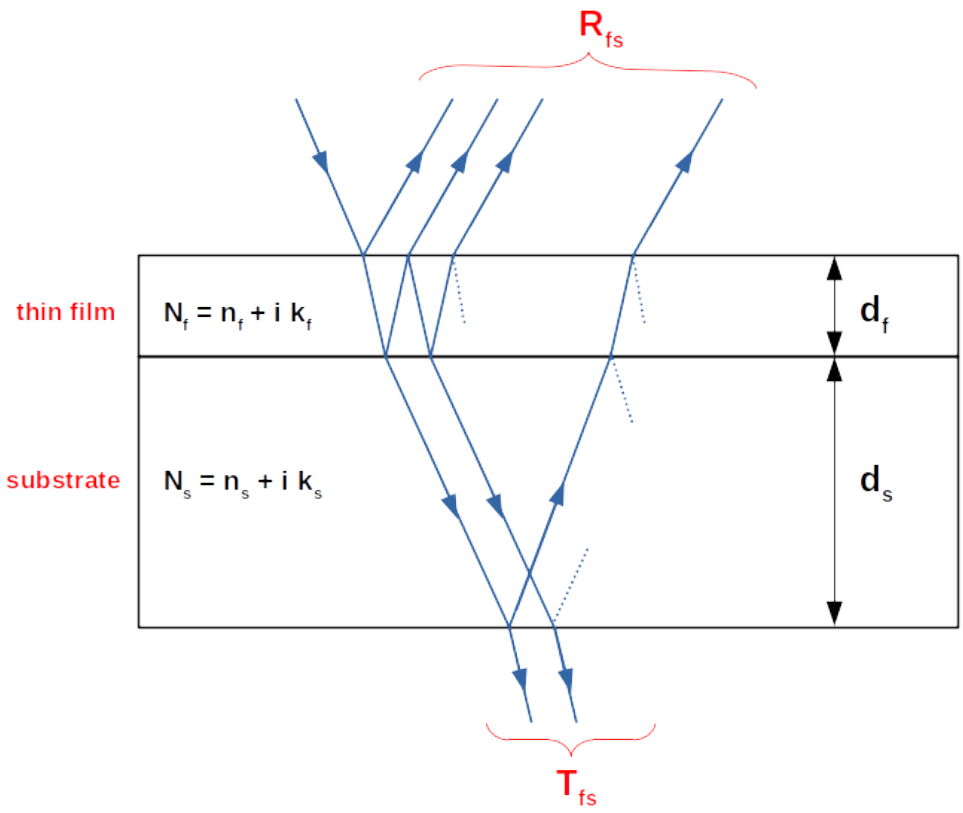

Fig. 1: Haze analog : thin film (f) overlaying a substrate (s). Each medium (or layer) is characterized by its thickness (d) and complex refractive index (N). $d_f \ll d_s$ in practice, the scale is changed for clarity. The measured reflection and transmission of the film/substrate sample, R_{fs} and T_{fs} respectively, are affected by multiple reflections at the different interfaces.

$$\varepsilon_1 = n^2 - k^2$$
$$\varepsilon_2 = 2nk \tag{2}$$

In practice, the different models used for data analysis rely on specific assumptions that can lead to discrepancies in the retrieved optical constants. One aim of this study is to assess the limitations and sensitivities of the different methods applied to our haze analogs in a broad spectral range. In the next sections, we describe in detail the different measurements and calculations performed to retrieve the refractive indices from UV to FIR. For that comparative study of spectrophotometry and ellipsometry, we focus on the reduced analog (Table 1).

3.2. UV-Vis-NIR spectrophotometry

3.2.1. Measurements

Measurements were performed using a PerkinElmer UV-Vis-NIR High-Performance Lambda 1050+ instrument at LATMOS (Laboratoire ATmosphères, Milieux, Observations Spatiales), in Guyan-

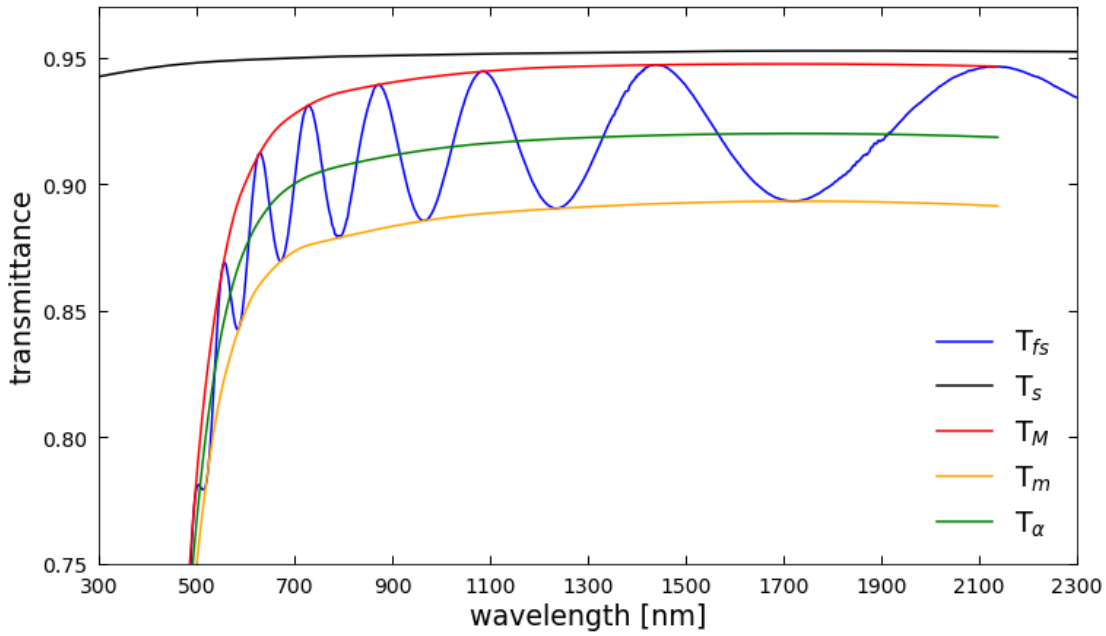

Fig. 2: Measured transmittance of the reduced analog deposited on a MgF_2 substrate (T_{fs}, blue curve). The transmission of the substrate alone is shown with the black curve. The transmission envelopes (T_M and T_m) and the interference-free transmission (T_α) are constructed based on the Swanepoel method.

court (France). The light source consists of two lamps: a halogen and a deuterium lamp used for wavelengths above and below 319 nm respectively. The instrument uses a double beam and double monochromator to ensure high spectral resolution and accurate absolute measurements. A common beam depolarizer is placed before the sample compartment to correct partial polarization induced by the different optical components. The size of the beam spot is reduced to $\sim$ 4 mm on the sample using an optical mask. Different modules are loaded in the detector compartment to perform reflection and transmission measurements.

We used the Three Detector module that combines a photo-multiplier tube (for UV-Vis), and PbS and InGaAs detectors (for NIR), thus covering a wide spectral range from 200 to 3300 nm. This module is used exclusively for transmittance measurements at normal incidence. The measured transmittance of the reduced haze analog (deposited on MgF_2 substrate) is shown in Fig.2. Different measurements were performed at different locations on the same sample to estimate an uncertainty on the film thickness.

We also used the Total Absolute Measurement System (TAMS) goniometer module to perform reflectance measurements at different angles. The single Si detector limits measurements below 1100 nm. The baseline is obtained in transmission making absolute measurements more reliable than an integrating sphere as it does not rely on the use of a reflecting standard. Measurements are made at incident angles from 10 to 50° using an angular step of 10°. Reflectance spectra of the reduced analog (deposited on MgF_2 substrate) are shown in Fig.3 for incident angles from 10 to 40°.

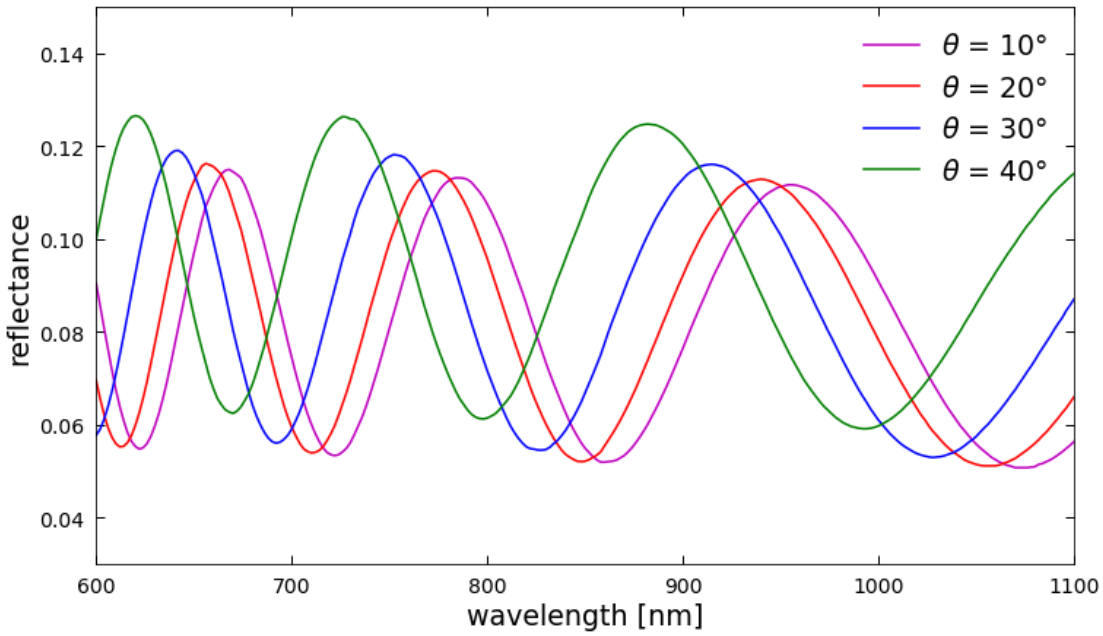

Fig. 3: Reflectance spectra measured on the reduced analog (deposited on MgF_2 substrate) with the TAMS goniometer module for different incident angles (θ = 10, 20, 30 and 40°).

3.2.2. Optical models

The goniometry and Swanepoel methods are used to derive the refractive indices of the reduced analog from the measured spectra. The aim is to evaluate the accuracy of these approaches.

First, we calculated the refractive index and film thickness (n_f and d_f) using the goniometry approach in the NIR. Interference fringes are observed on the measured reflectance spectra (Fig.3) as a result of coherent multiple reflection within the thin haze layer. On the other hand, the large thickness of the substrate only leads to incoherent multiple reflection at these low wavelengths. The oscillating frequency of the observed fringes is function of film thickness, refractive index n_f and incident angle following the law of interference :

$$2d_f\sqrt{n_f^2 - \sin(\theta_i)^2} = m\lambda \tag{3}$$

where m is the order of interference and θ_i is the angle of incidence.

A change in the incident angle modifies the optical path within the film and consequently introduces a shift in the position of fringe extrema (Reizman 1965; Ayupov et al. 2011). The refractive index of the film is calculated using a system of Eq.3 for two incident angles as we measure the shift of fringe extrema on our reflectance spectra (Fig.3). For reflection measurements with $n_s \leq n_f$, constructive interference (fringe maxima) are described by half-integer orders (m) whereas destructive

interference (fringe minima) are described by integer orders. In a manner similar to the calculation of the refractive index, the order of interference m is calculated using a system of Eq.3 for two adjacent maxima or minima, assuming that the refractive index remains constant in the spectral range separating these fringe extrema. The calculated m value is then rounded to the nearest integer if we use adjacent minima or half-integer if we use adjacent maxima. The film thickness is then calculated directly using Eq.3. We performed several calculations focusing on similar fringes (m = 4 and 4.5) and using different sets of spectra, with different incident angles, to estimate uncertainties on n_f and d_f. The results are discussed in Section 4.1.

Compared to the goniometry method, the Swanepoel method uses the theoretical expression of transmission and reflection for a thin layer deposited on a substrate. This theoretical description includes the role of multiple reflection within the film and substrate, illustrated in Fig.1, and absorption by the thick under-laying substrate (Stenzel et al. 1991; Imanaka et al. 2012) :

$$
\begin{aligned}
T_{fs} &= \frac{|t_{afs}|^2|t_{sa}|^2 e^{-2\beta_{s,im}}}{1-|r_{sfa}|^2|r_{sa}|^2 e^{-4\beta_{s,im}}} \\
R_{fs} &= |r_{afs}|^2 + \frac{|t_{afs}|^2|r_{sa}|^2|t_{sfa}|^2 e^{-4\beta_{s,im}}}{1-|r_{sfa}|^2|r_{sa}|^2 e^{-4\beta_{s,im}}} \\
\text{With : } \beta &= \frac{2\pi d}{\lambda}\sqrt{n^2-\sin(\theta_i)^2}
\end{aligned}
\tag{4}
$$

where T_{fs} and R_{fs} are respectively the transmission and reflection of the film/substrate sample, β is the phase, $\beta_{s,im}$ is the imaginary part of the phase for the substrate, t and r are the transmission and reflection Fresnel coefficients between the different media (air, film, substrate). The phase of the thin film is included in the expression of these Fresnel coefficients.

We developed an optical model based on the analytical approach of Swanepoel (1983) to retrieve the optical constants using the transmittance spectrum. This method was only validated on a simulated spectrum at the time but it is now widely used on experimental data (Al-Ani 2008; El-Naggar et al. 2009; Bakr et al. 2011; Dorranian et al. 2012; Ozharar et al. 2016; Jin et al. 2017). We validated our model using the simulated spectra presented in Swanepoel (1983, 1984).

Two criteria are required to reduce the expression of transmission in Eq.4 and calculate the optical constants of the film analytically. First, the substrate must be transparent ($k_s = 0$) hence our choice of MgF_2. Second, the film must be weakly absorbing ($k_f^2 \ll n_f^2$). An accurate first estimation of the refractive index therefore relies on the absence of absorption in the optical and NIR range as we transition between atomic and electronic polarization. This assumption is reasonable as transmission

is often not sensitive to weak overtone features. Assuming these criteria met, the transmission is expressed as follows (Swanepoel 1983),

$$T_{fs} = \frac{A\ x}{B - C\ x\ \cos(2\beta) + D\ x^2}$$

With : $A = 16\ n_f^2\ n_s$

$$B = (n_f + 1)^3\ (n_f + n_s^2)$$

$$C = 2\ (n_f^2 - 1)\ (n_f^2 - n_s^2)$$

$$D = (n_f - 1)^3\ (n_f - n_s^2)$$

$$x = e^{-\alpha_f d_f}$$

$$\alpha_f = \frac{4\ \pi\ k_f}{\lambda} \tag{5}$$

where α is the absorption coefficient and n_s is the refractive index of the substrate.

For transmission measurements and $n_s \leq n_f$, constructive interference (fringe maxima) are described by integer orders (m) whereas destructive interference (fringe minima) are described by half-integer orders. The cosine of the phase therefore varies from positive to negative. The transmission envelopes of maxima T_M and minima T_m are defined for $\cos(2\beta)$ equals to 1 and -1 respectively (Manifacier et al. 1976; Grigorovici et al. 1982; Swanepoel 1983, 1984) :

$$T_M = \frac{Ax}{B - Cx + Dx^2}$$

$$T_m = \frac{Ax}{B + Cx + Dx^2} \tag{6}$$

Our optical model constructs the transmission envelopes of maxima and minima using the measured transmittance as illustrated in Fig.2. The interference-free transmission is also calculated using the geometric mean of T_M and T_m.

The refractive index of the film is expressed analytically as follows (Swanepoel 1983),

$$n_f = \sqrt{C + \sqrt{(C^2 - n_s^2)}}$$
$$\text{With : } C = 2\, n_s\, \frac{T_M - T_m}{T_M T_m} + \frac{n_s^2 + 1}{2} \tag{7}$$

Indeed, the Fresnel coefficients teach us that the fraction of light reflected at the film/substrate interface only depends on the difference in refractive index between the two media. The height of interference fringes observed in Fig.2 and constrained by the transmission envelopes can thus provide a first estimation of n_f theoretically independent of the film thickness.

The refractive index of the transparent substrate is directly calculated from its measured transmittance (Fig. 2) as follows,

$$n_s = \frac{1}{T_s} + \sqrt{\frac{1}{T_s^2} - 1}, \tag{8}$$

where T_s is the transmittance of the substrate alone.

The refractive index of our MgF_2 optical window exhibits a spectral dispersion matching the Sellmeier description of Dodge (1984) (data available in the Refractive.Info database[1]). This result confirms the absolute accuracy of the measured transmission.

Using the first estimation of n_f, the film thickness is calculated with adjacent extrema following the law of interference (Eq.3). Once n_f and d_f are known, the order of interference is calculated for each fringe. The m values are rounded to the nearest integer for maxima and half-integer for minima. d_f and n_f are finally re-calculated with the rounded m value to reduce the uncertainty.

Several estimations of d_f are obtained depending on the number of fringes. A mean value of thickness is taken and the uncertainty is estimated using the maximum deviation. As this uncertainty depends on the number of fringes considered in the spectrum, we focus on the uncertainty given by additional measurements which is a better indicator of the thickness homogeneity within the size of the beam spot. The uncertainties are obtained using 7 different measurement on the reduced analog and 6 on the oxidized analog (Table 1).

n_f is fitted to a first-order Cauchy law to extrapolate at lower wavelengths and allow calculations of k_f in the entire spectral range. k_f is calculated as follows (Swanepoel 1983),

[1] https://refractiveindex.info/

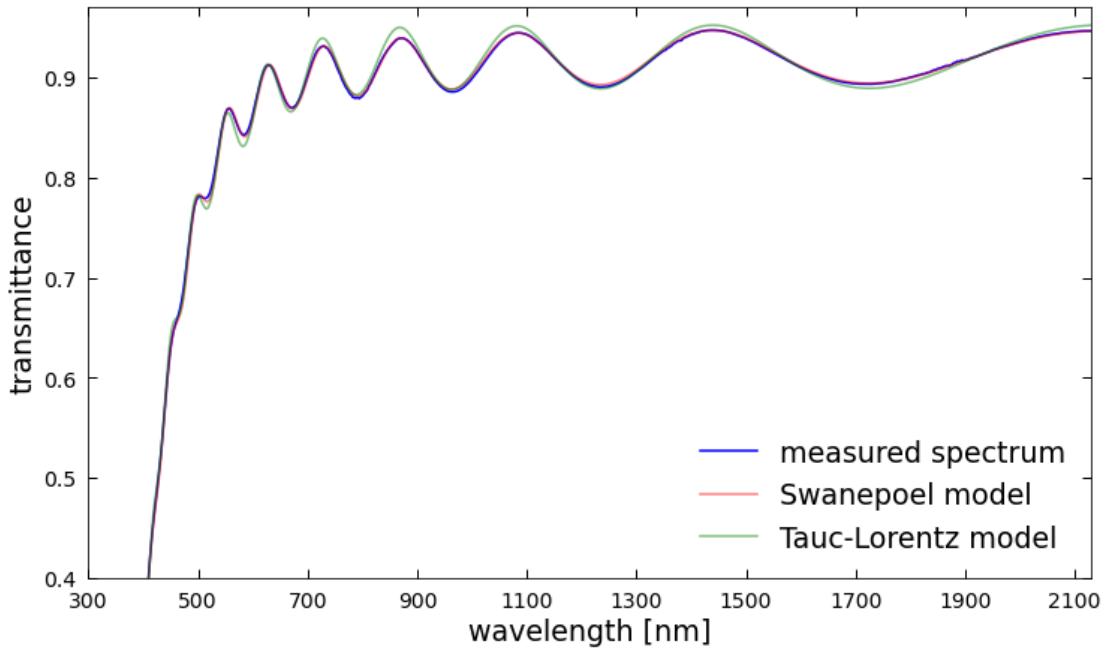

Fig. 4: Measured transmittance of the reduced analog deposited on a MgF_2 substrate (blue curve) compared to the simulated spectrum of the Swanepoel method (pink curve) and Tauc-Lorentz model (green curve). The fitted parameters of the Tauc-Lorentz model are : A = 1.92 eV, C = 0.32 eV, Eo = 3.86 eV, E_g = 1.31 eV and ε_∞ = 2.34. The Swanepoel method and Tauc-Lorentz model predict a film thickness of 1375 and 1351 nm respectively.

$$k_f = \frac{-\lambda}{4\,\pi\,d_f}\ln\left(\frac{E_M - \sqrt{E_M^2 - (n_f^2-1)^3(n_f^2-n_s^4)}}{(n_f-1)^3\,(n_f-n_s^2)}\right)$$
$$\text{With :}\;\; E_M = \frac{8\,n_f^2\,n_s}{T_M} + (n_f^2-1)(n_f^2-n_s^2) \tag{9}$$

k_f values essentially reflect the difference between T_s and T_M in Fig.2. In theory, the extinction coefficient can also be calculated using the transmission envelope of minima or the interference-free transmission (Fig.2). The analytical expression function of T_M is chosen as it is less sensitive to uncertainties on the refractive index (Swanepoel 1983).

Using the film thickness and optical constants calculated with the Swanepoel method, a simulated spectrum can be reproduced and compared to our measurement. The simulated spectrum obtained with the Swanepoel method is shown in Fig.4. Results are discussed in Section 4.1.

We also developed the model to account for a non-homogeneous film thickness using the description in Grigorovici et al. (1982) and Swanepoel (1984). This formalism introduces the surface roughness as an average departure from the mean thickness at the scale of the beam spot. The refractive index n_f is no longer calculated analytically but retrieved using a root-finding algorithm. We

emphasize that this description does not account for surface scattering and the effect on specular reflectance, it rather describes the shrinking of interference fringes towards higher frequencies caused by a non-constant optical path. The effect of a non-homogeneous film thickness can lead to significant errors in the estimated optical constants (Swanepoel 1984; Ramirez et al. 2002). Results are discussed in Section 4.3.

3.3. IR spectroscopy

3.3.1. Measurements

We performed IR measurements using a Bruker IFS125HR Fourier-Transform (FT) interferometric spectrometer at the AILES beamline of Synchrotron SOLEIL, in Saint-Aubin (France). The sample compartment and optical system are put under a primary vacuum ($\sim$ 0.04 hPa) to avoid atmospheric contamination in the spectra. A silicon carbide Globar heated to 1,250 K provides energy in the entire spectral range. Transmission spectra are acquired at an incident angle of 11°. In the MIR, we measure from 400 to 10,000 cm^{-1} with a step of 4 cm^{-1} using a KBr beam-splitter and an MCT detector cooled with liquid nitrogen. In the FIR, we measure from 100 to 400 cm^{-1} with a spectral resolution of 4 cm^{-1} using a 6-micron mylar beam-splitter with deposits of germanium and a bolometer detector cooled with liquid helium. Because of the low intensity of the source at FIR wavelengths and the lack of absorption of our haze analog in that spectral region, absolute transmission is less accurate. We therefore have limited our analysis of the FIR data to wavelengths below 30 μm.

FT infrared spectroscopy does not operate in double-beam mode and therefore does not provide absolute transmission directly. A reference spectrum without the sample is therefore required to retrieve the baseline. Baseline correction alone is very sensitive and therefore introduces large errors in the absolute transmission unless we perform an additional reliable correction. As a second correction, we scale our spectra to the absolute transmission obtained with spectrophotometry at the amine band (around 3.1 microns) where both measurements overlap. We use a similar scaling factor for the substrate spectrum. This scaling factor could also be obtained by comparing the measured transmission of the MgF_2 with a simulated transmission as the optical constants of MgF_2 are known. Both corrections provide similar results. For the sample deposited on the intrinsic Si substrate, the correction is also performed using the known optical properties of Si. In the FIR, interference fringes caused by multiple reflection within the 300-μm thick Si substrate were also removed following the procedure in Swanepoel (1983). This sample is used as the substrate is transparent in the MIR and FIR whereas the MgF_2 substrate limits our measurement below 6-7 microns. The transmission of the reduced analog deposited on the Si substrate from 1.5 to 30 microns is shown in Fig. 5.

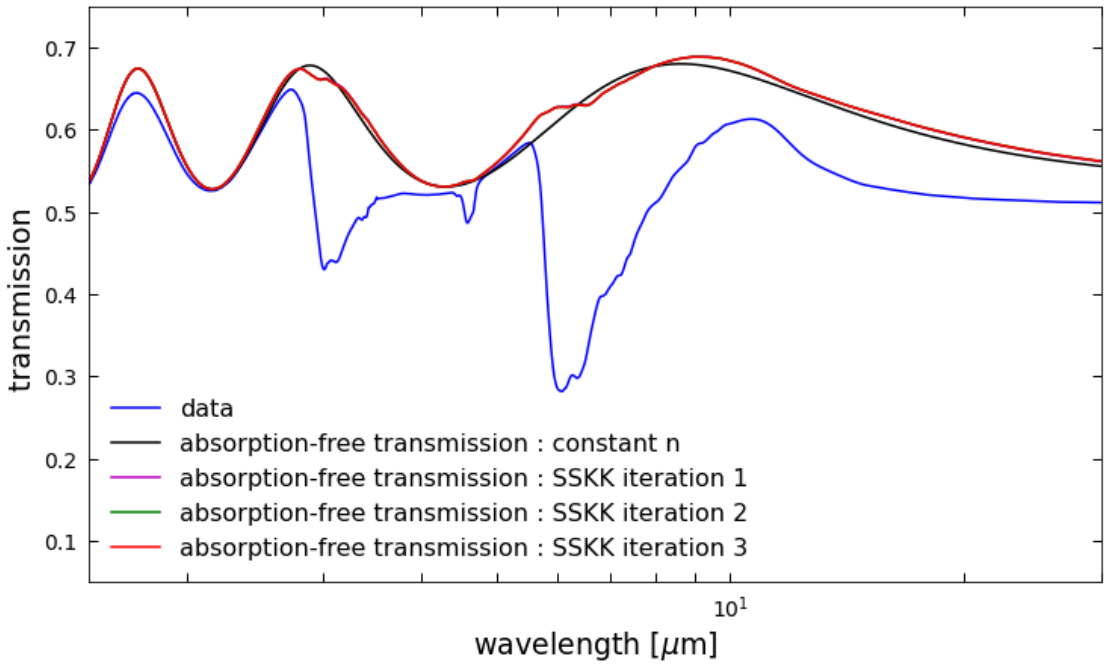

Fig. 5: MIR-FIR transmission of the reduced analog (blue curve) deposited on the intrinsic Si substrate. The first absorption-free transmission used as a baseline for Beer-Lambert calculation is shown in black. The updated baselines generated by the SSKK iteration model are shown, only 3 iterations are required to reach the chosen tolerance.

3.3.2. Calculations

The extinction coefficient of the film (k_f) is derived from the absolute transmission using a Beer-Lambert model that considers coherent multiple reflection within the film:

$$k_f = \frac{\lambda \, cos(\theta_i)}{4 \, \pi \, d_f} \ln\left(\frac{T_o}{T_{fs}} \right) \tag{10}$$

where T_{fs} and T_o are respectively the measured transmittance and the simulated absorption-free transmittance of the film/substrate sample. In this calculation of k, the optical path accounts for the 11° incident angle used during the measurements.

Using the first-order Cauchy fit of the refractive index and the film thickness from the Swanepoel method, a first simulated absorption-free transmission T_o (assuming k_f = 0, black curve in Fig.5) is calculated from Eq.4. This initial calculation assumes a refractive index rather constant in the IR to calculate k_f. This approach provides more accurate k_f values in the MIR as we account for the coherent behavior of the film rather than assuming $T_o = T_s$.

Using these first estimations of k_f, n_f can then be calculated more accurately to satisfy Kramers-Kronig causality. A singly-substractive Kramers-Kronig (SSKK) algorithm is used to derive the refractive index in the IR. The KK equation in Eq.1 teaches us that the refractive index can in principle be calculated as a function of wavelength using n_∞ and $k(\lambda)$. Eq.1 can be rewritten to scale n in the

entire range using an anchor point at a specific wavenumber (or wavelength) and thus replace the ambiguous n_∞ term. This expression known as the singly-substractive Kramers-Kronig equation is expressed as follows (Hawranek et al. 1976),

$$n(\nu_i) = n_r + \frac{2}{\pi}\,[P\int_0^\infty \frac{\nu k(\nu)}{\nu^2-\nu_i^2}\,d\nu - P\int_0^\infty \frac{\nu k(\nu)}{\nu^2-\nu_r^2}\,d\nu\,] \tag{11}$$

where n_r and ν_r are the anchor point refractive index and wavenumber (cm^{-1}) respectively.

In practice, the anchor value of n_f was taken from the prediction of the Swanepoel method (see Section 3.2.2). For our calculations, we used the value of n_f at 2000 nm. The accuracy of the anchor point is critical as it will be the main source of error propagating in the entire range (Hawranek & Jones 1976). As the integrands in Eq.11 are not defined in the entire range of frequencies, we calculate the Cauchy principal value using Maclaurin's formula that was found to be the most reliable method (Ohta & Ishida 1988).

As more reliable n values are retrieved for the film in the IR, a new simulated absorption-free spectrum is derived (see Fig.5) and k is re-calculated with the Beer-Lambert equation. This iterative procedure is performed until the mean variation of k between two successive iterations becomes $\leq 1\%$. In practice, 3 iterations are sufficient, the main change occurs at the first iteration, around 6 microns where n changes significantly in response to the strong hetero-aromatic features. This iterative method prevents the propagation of interference fringes in the k spectra. We present and discuss the results in Section 5.

3.4. UV-Vis ellipsometry

3.4.1. Measurements

In standard ellipsometry, we measure the ratio of specular reflectance between perpendicular (s) and parallel (p) polarization. In polar coordinates, we express it as follows,

$$\rho = \frac{r_p}{r_s} = \tan(\Psi)\,e^{i\Delta} \tag{12}$$

where Ψ and Δ are the ellipsometric angles representing the amplitude ratio and phase difference respectively.

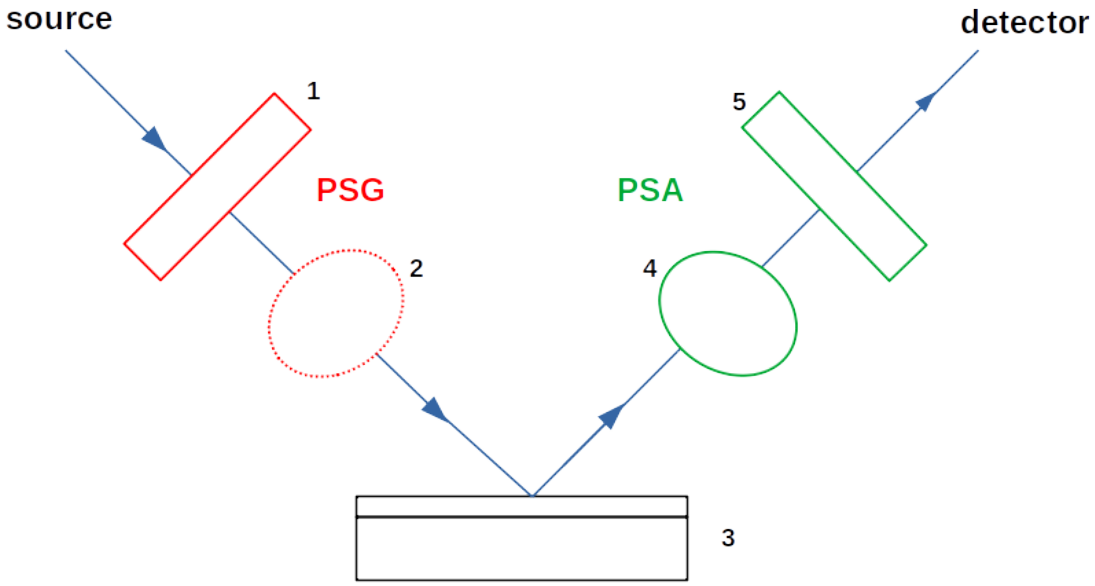

Fig. 6: General principle of our ellipsometric measurements. (1) and (5) are the linear polarizers of the polarization state generator (PSG) and polarization state analyzer (PSA) respectively. (2) and (4) are the modulators of the PSG and PSA respectively. (3) is the sample described in Fig.1.

We performed ellipsometric measurements from 300 to 830 nm using a Jobin-Yvon UVISEL ellipsometer at the LPICM (Laboratoire de Physique des Interfaces et des Couches Minces) laboratory, in Palaiseau (France). The operating principle of the ellipsometer is illustrated in Fig.6. Radiation produced by the halogen lamp is transmitted through an optical fiber to then reach the polarization state generator (PSG) made of a simple linear polarizer. This specific type of instrument does not use a modulator (or retarder) on the PSG. The beam width can be adjusted at the exit of the PSG to reduce the spot size on the sample. A grazing geometry of 70° is used for reflection on the sample. The reflected beam then transfers through the polarization state analyzer (PSA) consisting of a photo-elastic modulator followed by a linear polarizer. This specific instrument is called a phase-modulated ellipsometer. The photo-elastic modulator is a material (fused silica) that exhibits birefringence upon mechanical stress thus creating a phase difference as light splits and transmits through its different optical axes. The beam is spectrally resolved following the PSA. A photo-multiplier detector is used for this optical range.

The azimuths of the linear polarizers (P for the PSG and A for the PSA) and modulator (M) are set. Two configurations are used to retrieve the ellipsometric angles Δ and Ψ : P = 45°, M = 0°, A = 45° and P = 45°, M = 45°, A = 90°.

3.4.2. Optical models

In ellipsometry, the spectral dispersion of the dielectric constant (Section 3.1.2) is expressed using parameterized functions which are derived from the various theoretical descriptions of dielectric polarization. For the present study, a non-exhaustive list of functions were used. We emphasize that several other descriptions exist and their validity mainly depends on the optical range as we move from electronic to atomic polarization.

For ellipsometric measurements, we used the doped Si sample (Table 1). Silicon is highly reflective thus enhancing the sensitivity of our measurements. The dielectric function of the Si substrate is well-known in the UV-Vis range and therefore used as an input parameter. Reflection at the back of the substrate is negligible given the opacity of Si and the rugged back surface of our wafer. The substrate was therefore modeled as an infinite medium.

For the haze analog (film), we use three different dielectric functions that are described below. The aim is to assess the accuracy of the retrieved optical constants using these different descriptions.

In the UV-Vis range, it is common to use the Tauc-Lorentz description to quantify absorption near the bandgap. The bandgap energy marks the onset of UV absorption in response to electronic polarization. The Tauc-Lorentz function expresses the imaginary part of the dielectric constant (ε_2, see Section 3.1.2) as the product of Tauc's equation with the classical Lorentz oscillator (Tauc et al. 1966; Campi & Coriasso 1988) :

$$\varepsilon_2(E) = \begin{cases} 0 & \text{for } E \leqslant E_g \\ \frac{A\ Eo\ C\ (E-E_g)^2}{E\ ((E^2-Eo^2)^2\ +\ C^2\ E^2)} & \text{for } E > E_g \end{cases} \quad (13)$$

where E is the energy (eV), E_g is Tauc's bandgap energy (eV). A, Eo and C are respectively the strength (eV), peak energy (eV) and width (eV) of the Lorentz oscillator.

It efficiently reproduces the extinction slope near the bandgap although it is not valid at lower energies (higher wavelengths). The real part of the dielectric constant is derived to satisfy the Kramers-Kronig relation (Jellison & Modine 1996).

As ε_2 (or k) approaches 0, the Tauc-Lorentz formalism reduces to an expression of n as a power law known as the Sellmeier equation :

$$n^2(\lambda) = K \frac{\lambda^2}{\lambda^2 - \lambda_0^2} \tag{14}$$

where K is a constant and λ_0 a constant wavelength (in μm).

Although this description assumes k = 0 in the spectral range of interest, it still considers absorption at lower wavelengths and its forcing on the spectral dispersion of n in the optical and UV range. We use this description in practice to retrieve d_f and n_f in the transparent spectral region of the analog film.

The absorbent Cauchy description can also be used to reproduce the onset of absorption at optical and UV wavelengths. It conveniently provides estimations of k below the bandgap but lacks a physical meaning compared to the Tauc-Lorentz description. The absorbent Cauchy functions are expressed as follows,

$$\begin{aligned} n(\lambda) &= n_\infty + \frac{B.10^4}{\lambda^2} + \frac{C.10^9}{\lambda^4}, \\ k(\lambda) &= D + \frac{E.10^4}{\lambda^2} + \frac{F.10^9}{\lambda^4}, \end{aligned} \tag{15}$$

where B, C, D, E and F are constants. The units of these parameters can be deduced easily to ensure that n and k are dimensionless.

The dielectric function of our reduced haze analog is first expressed using a transparent Sellmeier model in the spectral region between 600 and 830 nm. Absorption by our haze analog is negligible in this optical window providing reliable estimations of the film thickness d_f and refractive index n_f. The dielectric function is then expressed following the Tauc-Lorentz and absorbent Cauchy descriptions in the entire spectral range from 300 to 830 nm.

Data analysis is performed using the Horiba DeltaPsi2 commercial software. The optical constants and film thickness of the haze analog are retrieved using iterative least-square fitting between our experimental data and the theoretical model. The model uses I_c and I_s as fitting quantities, they are expressed using the ellipsometric angles as $\cos(2\Psi)\cos(\Delta)$ and $\cos(2\Psi)\sin(\Delta)$ respectively. The quality of the fit is described by the square residual :

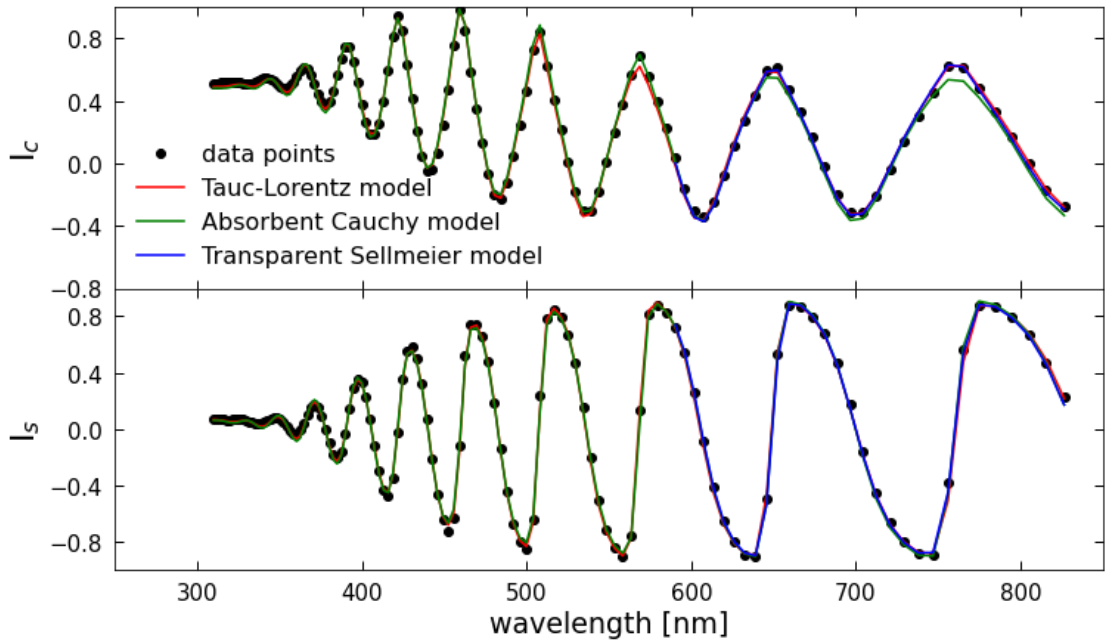

Fig. 7: Fit of ellipsometric data in the UV-Vis range for the reduced haze analog (deposited on a doped Si substrate). The transparent Sellmeier model (blue curve) is only used between 600 and 830 nm as it assumes k=0. The fitted Sellmeier parameters are : K = 2.569, λ_0 = 138.2 μm and d_f = 1568.6 nm. The Tauc-Lorentz model is shown by the red curve, the fitted parameters are : ε_∞ = 1.98, E_g = 2.01 eV, A = 10.58 eV, Eo = 5.88 eV, C = 2.52 eV and d_f = 1574.6 nm. The absorbent Cauchy model (green curve) fits best with n_∞ = 1.619, D = 9.63E-3, E = -0.314 μm^2, F = 1.148 μm^4, B = 1.544 μm^2, C = 0.21 μm^4 and d_f = 1558.7 nm. The square residuals χ^2 are 0.03, 0.15 and 0.25 respectively.

$$\chi^2 = \sum_j [(I_c^{\text{theo}} - I_c^{\text{exp}})^2 + (I_s^{\text{theo}} - I_s^{\text{exp}})^2] \tag{16}$$

where the summation over j refers to the number of data points.

The fit of experimental data with the three different models is shown in Fig.7. The fitted parameters and square residuals are given in the caption. We present and discuss the retrieved optical constants in Section 4.2.

3.5. MIR ellipsometry

3.5.1. Measurements

Measurements were performed at the SMIS beamline of Synchrotron SOLEIL, in Saint-Aubin (France), using Mueller ellipsometry. The optical system of the Mueller ellipsometer is described in detail in Garcia-Caurel et al. (2015). The SiC Globar light source is provided by a Jobin Yvon FTIR spectrometer. The layout of the optical system is similar to the phase-modulated ellipsometer (Section 3.4.1) with an additional retarder on the PSG as illustrated in Fig. 6. The PSG consists of a linear

polarizer followed by a rhombohedric ZnSe retarder. Multiple reflections within the two ZnSe prisms create an achromatic retardation that elliptically polarizes the beam before reflection on the sample at angle of 60.5°. The PSA is similar to the PSG with the optical components in a reversed order. The retarders of the PSG and PSA are mounted onto mobile holders to change the azimuth and create different polarization states. The optical path ends with a MCT detector cooled with liquid nitrogen.

Standard ellipsometry previously used in the UV-Vis range is based on the Jones formalism that only stands for fully polarized light. The Stokes-Mueller formalism however applies for any polarization state including partial polarization. In this case, the polarization state of the beam is characterized using the Stokes vector as follows,

$$S = \begin{pmatrix} I_x + I_y \\ I_x - I_y \\ I_{45^\circ} - I_{-45^\circ} \\ I_L - I_R \end{pmatrix} \tag{17}$$

where x and y are two linear and orthogonal polarization states. L and R refer to left and right circular polarization respectively. I_{45° and I_{-45° refer to two other linear polarization states.

Reflection on the sample introduces a linear transformation of the Stokes vector that can be retrieved from the measured intensities (Azzam 1977). It is the basic principle of Mueller ellipsometry that stands for any type of sample (isotropic or anisotropic). The linear coefficient of the transformation is expressed in the form of a 4×4 matrix called the Mueller matrix that satisfies the following :

$$S_f = MS_p, \tag{18}$$

where S is the Stokes vector preceding (S_p) and following (S_f) reflection on the sample. M is the Mueller matrix.

The Mueller matrix holds the properties of the sample including optical constants and film thickness. In practice, 16 PSG-PSA configurations are required to retrieve every coefficient of the Mueller matrix. We used four azimuths for the PSG and PSA retarders. In other words, each of the 4 polarization states generated by the PSG and transformed by the sample is analyzed by 4 configurations of the PSA. We performed a calibration of the optical system to measure the Stokes vector of the PSG and PSA for each azimuth used. We therefore obtained two matrices of S_p (Eq.18) and directly measured

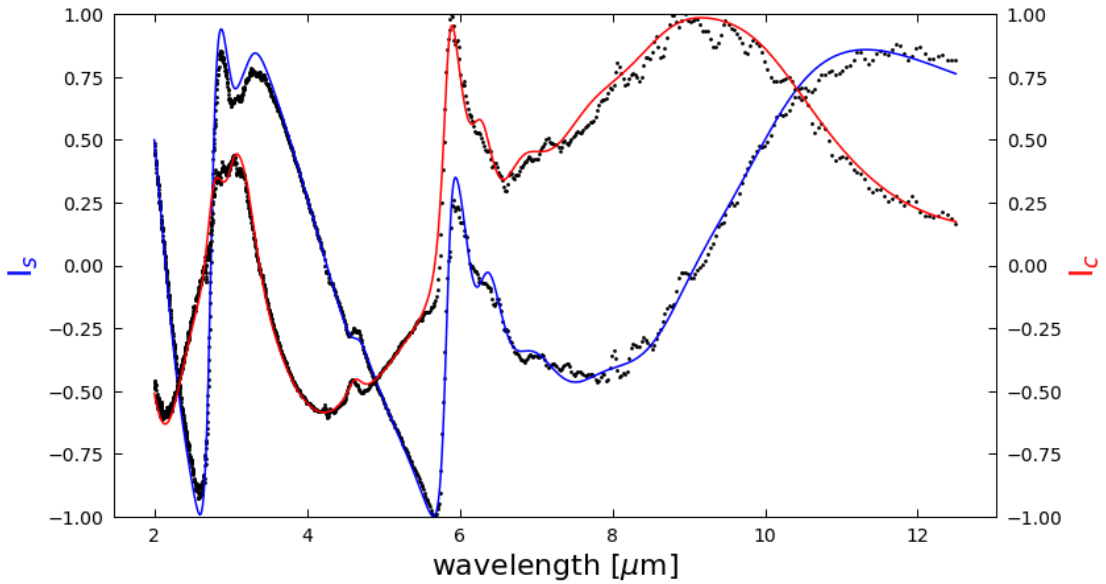

Fig. 8: Fit of MIR ellipsometric data for the reduced haze analog (deposited on a doped Si substrate). The best fit (χ^2 = 4.32) suggests an incident angle of 60.48°, d_f = 1804 nm and ε_∞ = 2.24 with 9 oscillators. The fitted parameters of the oscillators are listed in Table 2.

a 4×4 matrix of intensities from the 16 PSG-PSA configurations. Using this approach, the Mueller matrix is easily recovered using an algebraic matrix inversion.

For an isotropic sample, the Mueller matrix becomes solely function of the ellipsometric angles (Garcia-Caurel et al. 2013, 2015) :

$$\mathbf{M} = \begin{pmatrix} 1 & -\cos(2\Psi) & 0 & 0 \\ -\cos(2\Psi) & 1 & 0 & 0 \\ 0 & 0 & \cos(2\Psi)\cos(\Delta) & \cos(2\Psi)\sin(\Delta) \\ 0 & 0 & -\cos(2\Psi)\sin(\Delta) & \cos(2\Psi)\cos(\Delta) \end{pmatrix} \tag{19}$$

The isotropic nature of the sample is therefore inferred directly if our experimental Mueller coefficients satisfy the diagonal form in Eq.19. One can see that the Mueller coefficients can be written using I_c and I_s only. In a manner similar to UV-Vis ellipsometry, we then fit our measured I_c and I_s with a model to retrieve the optical constants of our haze analog.

3.5.2. Optical model

As we are now in the range of atomic polarization, we use different physical descriptions to parameterize the dielectric function. In the mid- and far- Infrared, absorption is caused by free charge carriers and vibrations of chemical bonds.

Although the dielectric function of Si is well-known in principle, we used a P-doped substrate to increase its IR opacity and thus reduce reflection at the back of the wafer. The boron atoms diluted in the structure of the semiconductor create new energy states near the valence and conduction bands. As a consequence, the conduction band is reached around FIR frequencies. Absorption occurs as free electrons collide and scatter with the background of silicon atoms. The Drude description expresses the dielectric function on the basis of kinetic theory as follows,

$$\varepsilon(\omega) = \varepsilon_\infty \, (1 - \frac{\omega_p^2}{\omega^2 - i \, \omega \, \Gamma}) \tag{20}$$

where ω is the angular frequency (s^{-1}), ω_p is the plasma angular frequency (s^{-1}), and Γ is a damping coefficient (s^{-1}).

We therefore first performed measurements on our blank Si substrate to derive its optical properties affected by the concentration of boron atoms. The parameters of the Drude model are fitted (ω_p and Γ), only the plasma frequency is significantly changed as it is function of the dopant concentration. Once the dielectric function of our Si wafer is known, we use it as an input parameter for the analysis of the film/substrate sample.

Absorption by the haze analog results from bending and stretching of its covalent bonds. The Lorentz formalism describes resonant oscillations by assimilating electric dipoles to strings in a viscous fluid. Compared to gaseous molecules, the bonded structure of the material creates an opposite force to atomic oscillations quantified by a damping factor. For a complex material with several vibrational modes, the dielectric function is expressed using the sum of all classical oscillators. The Lorentz model only stands near the natural frequencies and cannot describe the intrinsic properties in the absence of absorption. The dielectric function is therefore scaled to its limit at infinite frequency as follows,

$$\varepsilon(E) = \varepsilon_\infty + \sum_j \frac{F_j \; Eo_j}{Eo_j^2 - E^2 + i \; D_j \; E}, \tag{21}$$

where F, Eo and D are the strength (eV), peak energy (eV) and width/damping (eV) of the oscillator respectively. ε_∞ is the dielectric constant at infinite wavenumber. The summation over j refers to the number of oscillators.

In the ellipsometric model, the different modes that mirror the composition of our haze analogs are fitted using Lorentz oscillators. The fitted parameters are : ε_∞, d_f, the incident angle and the constants of each oscillator (F, Eo and D). The incident angle is known in principle but might be slightly changed as we adjust the position of the sample. We therefore add this parameter in the fit but constrain it in a 60-61° range.

Given the complexity of our material and the large number of stretching modes, the fit exhibits a strong degeneracy. Our main aim is to avoid reaching an unphysical numerical solution that would not accurately characterize the composition of the material. For that purpose, the natural frequencies (Eo) are kept constant, guided by our spectroscopic measurements (Fig. 5) and previous data on Titan haze analogs (Gautier et al. 2012; Mahjoub et al. 2012; Gavilan et al. 2018).

Deconvolution of hetero-aromatic features around 6-7 microns is difficult given the large number of overlapping modes (Gavilan et al. 2018). We therefore simplify this region with fewer oscillators to reduce the number of fitted parameters. Although it also prevents us from reaching a completely accurate physical description of the different modes, it still provides accurate estimations of k_f. In this characterization of the reduced haze analog, we found that the sample was best fitted with 9 oscillators. The fitted parameters are listed in Table 2. The orders of magnitude of these parameters are physically sensible for atomic vibrations although the strength and width of the 9^{th} oscillator are unrealistically high. Here, the physical meaning of the last three oscillators is lost and only used to properly retrieve the continuum of k at FIR frequencies.

The fit of the Lorentz model to experimental data is shown in Fig.8. We discuss the retrieved optical constants in Section 5.

4. UV-Vis-NIR optical constants

4.1. Spectrophotometry

Using the goniometry method with different sets of reflectance spectra, a mean refractive index and film thickness are calculated in the NIR. We obtain a mean refractive index of 1.61 with an uncertainty of 0.09 (1 σ) and a mean thickness of 1364 nm with an error of 76 nm (1 σ). This simplest

position (eV)	position (μm)	strength (eV)	width/damping (eV)	vibration mode
0.411	3.02	0.0076	0.031	primary and secondary amines (-NH, -NH_2)
0.397	3.12	0.0395	0.072	primary and secondary amines (-NH, -NH_2)
0.267	4.64	0.0060	0.016	conjugated nitrile C=C-C≡N, isonitrile R-N≡C
0.205	6.05	0.0359	0.012	double bonds C=O (with carbonyl and carboxyl), C=N, C=C
0.193	6.42	0.0385	0.014	double bonds C=O (with carbonyl and carboxyl), C=N, C=C
0.178	6.96	0.0625	0.027	-$CH_{2,3}$, -NH_2, C-OH bending
0.157	7.9	0.0662	0.035	-
0.134	9.2	0.0399	0.032	-
0.090	13.8	0.2363	0.028	-

Table 2: Fitted parameters of the 9 Lorentz oscillators.

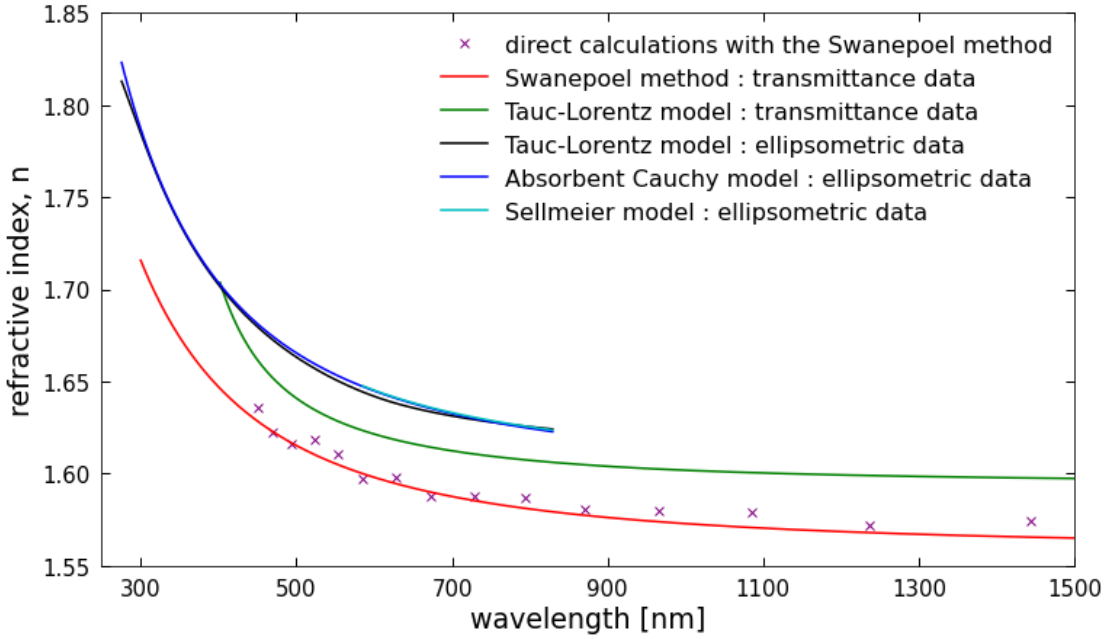

Fig. 9: Refractive index n of the reduced haze analog from UV to NIR retrieved with spectrophotometry on the MgF_2 sample and ellipsometry on the doped Si sample. Direct calculations from transmission (purple data points) with the Swanepoel method are fitted to a Cauchy law (red curve). Indirect calculations with a Tauc-Lorentz model are performed on transmision data (green curve) and ellipsometric data (black curve). n is also retrieved using a Sellmeier model (cyan curve) and a Cauchy model (blue curve) on our ellipsometric data.

analytical approach provides an average estimation of n between 0.9 and 1.1 microns that can be used as an anchor point for SSKK integration. However, the uncertainty on n and d with this approach is high as the calculation solely considers the spectral shift of fringe extrema and ignores the height of the interference fringes. The method is thus sensitive to measurement biases that leads to high uncertainties. Given the high angular precision of the TAMS module, these errors likely emerge from the focalisation of the beam.

On the other hand, the Swanepoel method is proven to be extremely accurate. Indeed, the error between the measured and simulated spectra shown in Fig.4 is below 0.4 % above 500 nm. The extrapolation of n at lower wavelengths leads to higher uncertainties although the error remains below 1.5%. The film thickness is estimated at 1375 nm with a maximum error below 1% (Table 1). It confirms the expected accuracy retrieved on simulated spectra in Swanepoel (1983). As our optical

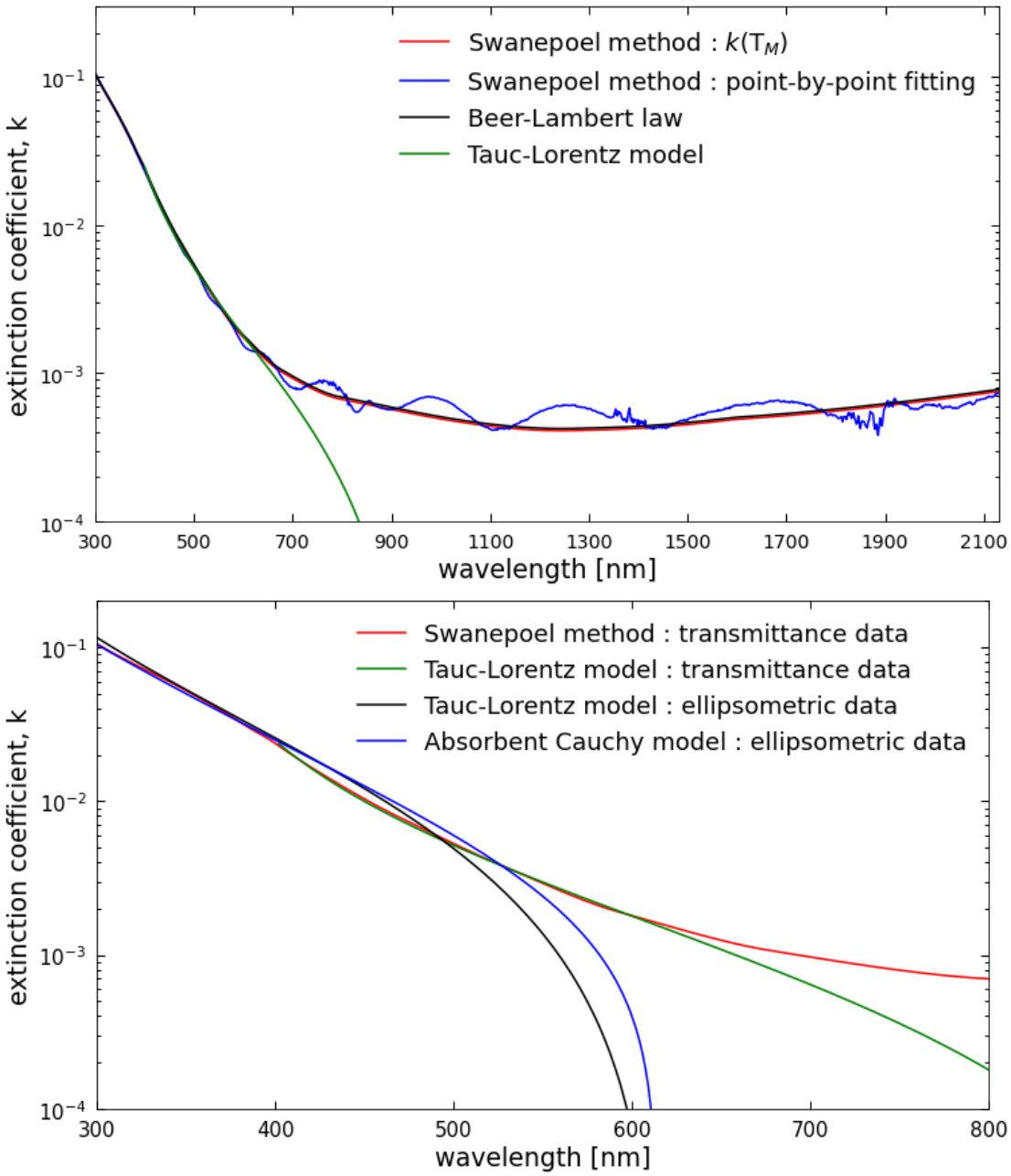

Fig. 10: Extinction coefficient k of the reduced haze analog from UV to NIR retrieved with spectrophotometry on the MgF_2 sample and ellipsometry on the doped Si sample. (top) Different spectrophotometric calculations of k from direct/analytical (Swanepoel, Beer-Lambert) and indirect/iterative (point-by-point fitting, Tauc-Lorentz) models. (bottom) k calculated using different models and different data (ellipsometric and spectrophotometric). The Swanepoel method shown on the bottom panel corresponds to the analytical expression on the top panel (red curve).

model improves the construction of transmission envelopes using a tangent point method similar to Jin et al. (2017), the refractive index shown in Fig.9 is analytically calculated in a large spectral range from 450 to 1500 nm. The low uncertainties on the thickness obtained by multiple measurements (Table 1) point to similarly reliable estimations of the refractive index n.

The Swanepoel method has also been applied to the analog deposited on the intrinsic Si substrate although measurements are limited above 1 μm as the Si wafer becomes opaque at lower wavelengths.

We find that the refractive index n estimated is similar, only a change in thickness is observed (see Table 1). It was previously suggested that variations in composition of the analog could arise from using substrates with different dielectric properties in the PAMPRE setup (Mahjoub et al. 2012). Our new result suggests that the composition is similar, we reaffirm this statement in Section 4.3 when comparing UV absorption.

Different spectrophotometric calculations of k were performed for the reduced analog (deposited on MgF_2 substrate), the results are shown in Fig.10 (top panel). We find that the analytical expression of the Swanepoel method (Eq.9) provides similar estimations of k compared to a Beer-Lambert law using the transmission of the substrate and the envelope of maxima (Eq.10). To evaluate the error on k in the transparent window of our haze analog, we used a point-by-point fitting of k using the measured transmission and the refractive index fitted from the Swanepoel method. With this approach, we observe oscillations in the k spectrum (Fig.10, top panel) resulting from very small errors on n and d. The propagation of interference fringes in the k spectrum is very weak in our case confirming the accuracy of the Swanepoel method.

In order to assess the effect of the model on the retrieved optical constants, we used an iterative Tauc-Lorentz model on our spectrophotometric data similar to the one used on our UV-Vis ellipsometric data (described in Section 3.4.2). The simulated transmission that best fits our data with a Tauc-Lorentz model is shown in Fig.4. The retrieved optical constants are shown in Fig.9 (for n) and 10 (for k). Above the retrieved bandgap energy (below 650 nm), we find similar k values compared to the analytical calculations with the Swanepoel method. We however note a 1% discrepancy on n and d between both models. This discrepancy can be explained by the strong correlation between n and d in the law of interference (Eq.3).

4.2. Ellipsometry

Ellipsometric data are fitted to the Sellmeier, absorbent Cauchy and Tauc-Lorentz models in Fig.7. The retrieved optical constants are shown in Fig.9 for n and 10 (bottom panel) for k. The models predict similar estimations of film thickness within a 20-nm error range (error below 1.5%). The thickness estimated at 1566 nm is thicker on the reduced haze analog deposited on Si substrate compared to the sample deposited on MgF_2 substrate (see Table 1). This difference was previously observed (Gautier et al. 2012; Mahjoub et al. 2012) and is thought to result from the dielectric properties of the substrate and the position of the sample in the non-homogenous plasma discharge during the experiment.

From 600 to 830 nm, the Sellmeier model that assumes k = 0 provides similar n values compared to the Cauchy and Tauc-Lorentz models. At lower wavelengths, the Cauchy and Tauc-Lorentz models predict a similar spectral dispersion of n and similar k values. The Cauchy model therefore satisfies the Kramers-Kronig causality as well as the Tauc-Lorentz model even though n and k are fitted with independent functions and parameters (see Eq.15). Although the Cauchy model is proven to be reli-

able, we are lacking a concrete physical meaning in the fitted parameters. Indeed, the k function of the Cauchy model is best fitted with a negative parameter. Both models are unable to quantify the weak absorption in the optical region. The Cauchy model indeed predicts negative values of k if not constrained, the reliability of the predictions are therefore lost in this optical range.

4.3. Spectrophotometry vs. Ellipsometry

We note a small discrepancy on the refractive index not only between both optical techniques but also using a similar data set with a different model (Fig.9). Our discrepancy between both techniques is $\sim 3\%$ around 800 nm which is generally lower than the variations observed by Tran et al. (2003). Two factors can explain this discrepancy : the strong anti-correlation between n and d seen with both methods, and the inhomogeneity of the film thickness. Indeed, our ellipsometric data in the optical region could still be fitted efficiently using different values of n and d. We also observed this correlation when comparing the Swanepoel method and Tauc-Lorentz model on our spectrophotometric data (Section 4.1). As for the second hypothesis, surface roughness does not improve the analysis on our ellipsometric data. Additionally, our spectrophotometric model is unable to converge to an estimation of roughness as the spectrum does not exhibit the shrinking of fringes expected for a non-homogeneous film. We therefore have several arguments suggesting that our estimations of n are not affected by the homogeneity of the film thickness. The small discrepancies in n are likely caused by its strong correlation with the film thickness. Given the small variations of n reported in the literature, one must be careful when comparing and correlating to the gas composition as these discrepancies might come from the measurements and calculations used.

In the UV, the different calculations provide extremely similar estimations of k with both data sets (Fig.10, bottom panel). The high accuracy of both methods in this spectral range is expected given the large strength of UV features. Additionally, these new results support the statement made in Section 4.1 saying that the composition of the haze analog is similar for both the Si and MgF_2 samples. Previous studies taught us that the change in gas composition lead to significant variations in the UV slope of k (Khare et al. 1984; Ramirez et al. 2002; Mahjoub et al. 2012; Jovanović et al. 2021; He et al. 2022). If changes in composition were to be expected between the Si and MgF_2 samples, changes in k would be observed in the UV.

k values in the optical region could only be calculated with the Swanepoel method. We predict an extinction coefficient close to 2-4.10^{-4} in agreement with previous measurements on Titan haze analogs (Khare et al. 1984; Ramirez et al. 2002; Imanaka et al. 2012). Our spectrophotometric estimations of k in that spectral range might be overestimated given the very small difference in transmission between the sample and substrate (Vuitton et al. 2009).

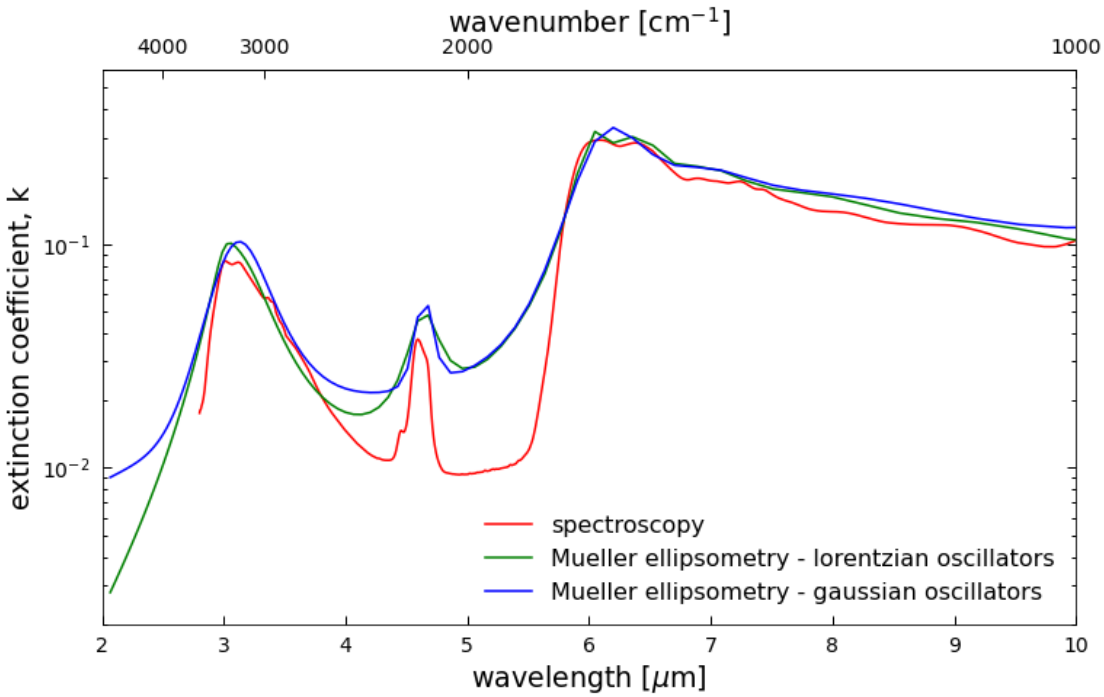

Fig. 11: Mid-Infrared extinction coefficient of the reduced haze analog determined with spectroscopy on the MgF_2 and intrinsic Si samples, and with Mueller ellipsometry on the doped Si sample. The different modes used for the ellipsometric Lorentz model are listed in Table 2. Gaussian and lorentzian damping are considered to assess the impact on the inter-band k values.

5. Mid-Infrared optical constants : spectrophotometry vs. ellipsometry

The MIR extinction coefficients (k) calculated from Fourier-transform spectroscopy and Mueller ellipsometry are shown in Fig.11. The general trend of k is similar between both methods and reflects the different vibrational modes characterizing our CHON haze analog. The different modes are described in detail in Gavilan et al. (2018) and categorized using the three following groups: amines (2.9-3.5 μm), nitriles (4.4-4.9 μm) and hetero-aromatics (5.8-8.3 μm). The oscillators used for the ellipsometric Lorentz model are attributed to the corresponding vibrational modes in Table 2. We note that IR reflection ellipsometry is not sensitive enough to efficiently detect weak absorption features as evidenced by the absence of C=H aliphatic (3.4 μm) or R-C≡N nitrile (4.5 μm) signatures which are observed in transmission.

Spectrophotometric and ellipsometric k values are very similar around the natural frequencies. We however observe variations in the inter-band regions as k is solely affected by the wings of the nearby oscillators. This discrepancy appears clearly in Fig.11 on a logarithmic scale. In these inter-band regions, accurate estimations of k require a good knowledge of the structural order in the material. The ordered structure of semiconductors is very well described with the Lorentz oscillators. For more disordered isotropic material, the Kim oscillator conveniently allows the damping factor (Eq.21) to vary from gaussian to lorentzian. In Fig.11, both descriptions provide similar estimations of k although we

notice a slight difference in the region between amine and nitrile absorption. The persisting discrepancy on k compared to direct spectroscopic calculations stems from the use of a simplified Lorentz description with fewer oscillators to reproduce the hetero-aromatic features. Although this simplified model reduces degeneracy while maintaining a partially accurate physical description, it also forces the width of oscillators to increase thus overestimating the inter-band extinction coefficients. Indeed, the Lorentz model does not fit accurately the steep slopes separating nitrile and hetero-aromatic features observed in the ellipsometric data (Fig.8) and confirmed in transmission spectroscopy (Fig.5).

The Lorentz model predicts a film thickness d of 1804 nm (Fig.8). The film thickness and thus the refractive index are significantly different than predictions with UV ellipsometry on a similar sample (Section 4.2). It suggests that the strong n-d correlation discussed in Section 4.3 is not resolved in the Lorentz model because of a strong degeneracy with the fitted parameters of the oscillators. The discrepancies observed in the MIR inter-band regions can therefore also be caused by errors in n-d values leading to an incorrect correction of interference fringes that propagates in the k spectrum. Measurements in the Vis-NIR spectral range are therefore crucial to retrieve accurate n-d values and efficiently correct the effect of multiple reflection in the data analysis. Given the complexity of our material, we conclude that direct spectrophotometric calculations are more suited to retrieve accurate estimations of k in the MIR inter-band regions.

6. Optical constants in the spectral range of JWST : implications for future observations

In Fig.12, we report new optical constants from UV to FIR for exoplanet haze analogs. The refractive indices compiled in this work are available in the Optical Constants Database.

As we increase the CO_2 to CH_4 ratio, our measurements and calculations point to higher intrinsic IR absorption properties confirming previous finding by Gavilan et al. (2018). Additionally, the increased CO_2 abundance in the gas phase results in a wider absorption peak regrouping hetero-aromatic modes around 6-8 μm. Additional work is required to assess the detectability of this strong feature in transit spectra. For the oxidized analog, we note that the slope of k on the high-frequency end of the hetero-aromatic group (around 6 microns) is shifted towards lower wavelengths compared to the reduced analog. This points to the presence of the C=O stretching band (at 5.8-5.9 microns) confirming the increasingly oxygenated nature of our exoplanet haze analogs. In the weakly absorbing NIR region, the extinction coefficient is similar for both analogs. The oxidized analog is less absorbing in the visible. In the UV, we note a stronger increase of the absorption slope for the oxidized analog

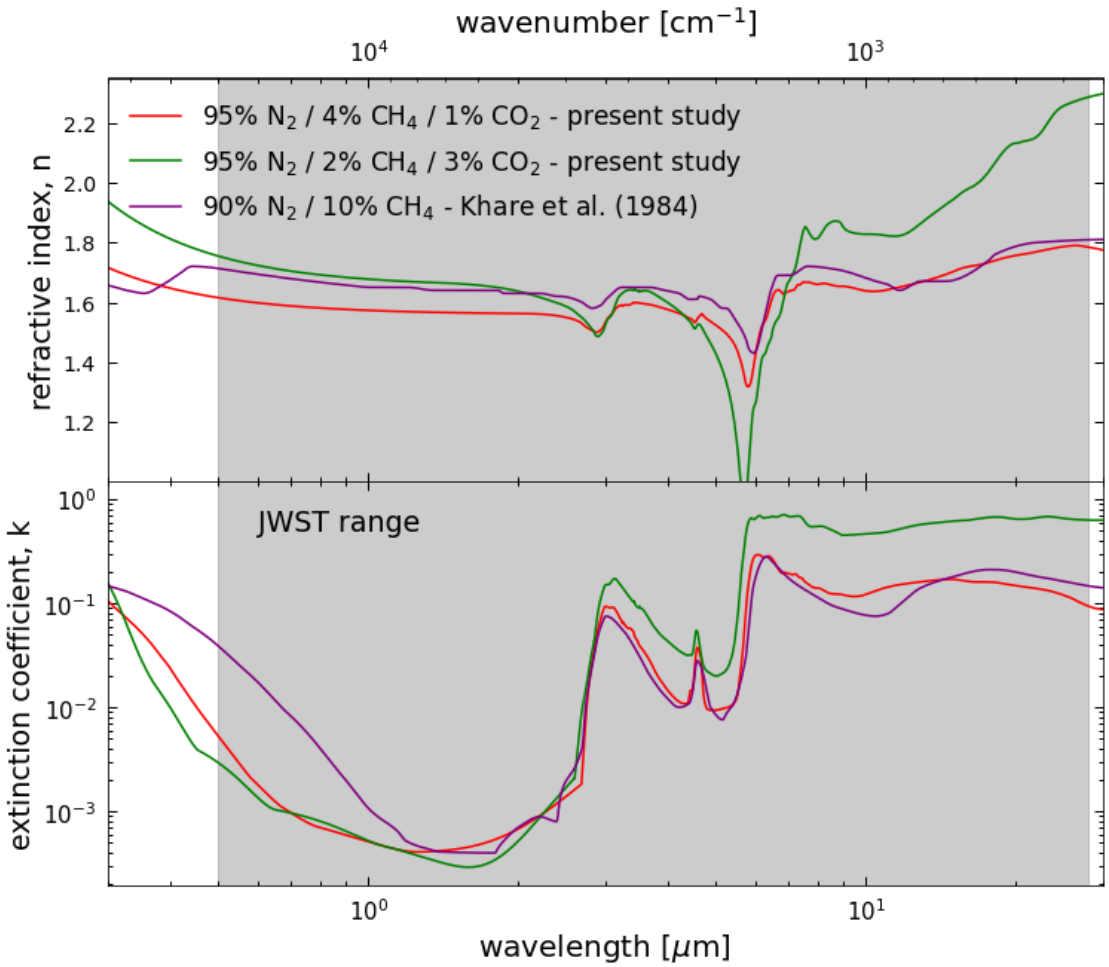

Fig. 12: Optical constants (n and k) measured from 0.3 to 30 μm on two exoplanet haze analogs. The analogs are produced from a 95% N_2 gas mixture with different CO_2 to CH_4 ratios (see Table 1). The seminal data of Khare et al. (1984) for Titan haze analogs is shown in comparison.

which might be caused by the presence of stronger high-energy UV features revealed in Gavilan et al. (2018).

We observe a significantly higher bandgap energy compared to Khare et al. (1984) that leads to variations of k by up to one order of magnitude in the Vis-NIR spectral range. In the MIR, our oxidized analog exhibits higher absorption compared to Khare et al. (1984). As shown by He et al. (2023), transit spectra are strongly affected by variations in the refractive indices of photochemical hazes. The data presented in this paper should therefore be used to interpret observations of CO_2-rich rocky exoplanet atmospheres.

7. Conclusions

We comparatively assessed the accuracy of ellipsometric and spectrophotometric measurements to retrieve the optical constants of haze analogs. In the UV, k values are similar using both techniques. The variations of k between ellipsometric and spectroscopic calculations in the MIR are explained

by the limitations of the Lorentz model. In the UV and MIR, the large variations of k reported in the literature largely overcome the error caused by the optical method and calculation. It thus likely results from the composition of the haze analogs although we cannot definitely conclude on the primary factor causing the change in composition as it can be caused by the gas composition or experimental conditions (residence time of the gas, pressure, temperature). We note a strong uncertainty in the k values with both techniques in the Vis-NIR as absorption is weak. We therefore expect this sensitivity to contribute significantly to the large discrepancies reported in the literature. As for the refractive index n, we find discrepancies of 1 to 3% between the different measurements and calculations at visible wavelengths. Small variations of n in the existing data could therefore stem from errors in the optical method and calculation. We confirm the strong accuracy of the Swanepoel method on our haze analogs in the UV-Vis-NIR. Reflection ellipsometry however constrains more efficiently the dispersion of n at UV-Vis wavelengths. Direct spectrophotometric calculations are preferred in the MIR region given the strong degeneracy observed in the analysis of ellipsometric data. We therefore recommend UV-Vis reflection ellipsometry to retrieve accurate values of refractive index and film thickness. This comparative optical study aims to guide the choice of future calculations and measurements to retrieve the refractive indices of exoplanet aerosol analogs.

Optical constants of haze analogs produced in a simulated N_2-dominated / CO_2-rich atmosphere are measured from 0.3 to 30 μm. We confirm the expected increased absorption for higher abundances of CO_2. Our data predicts weaker absorption in the NIR and optical range compared to the first analogs of Khare et al. (1984). The different data sets obtained in a broad spectral range on haze analogs suggest strong variations of the optical properties depending on the atmospheric composition. To better constrain retrieval models and correctly interpret future observations of oxidized exoplanet atmospheres, we encourage modelers to use these new data.

References

Al-Ani, S.K. 2008, Iraqi J. of Appl. Phys., 4(1)
Alves, L.L., Marques, L., Pintassilgo, C.D., et al. 2012, Plasma Sources Sci. Technol., 21, DOI : 10.1088/0963-0252/21/4/045008
Arney, G., Domagal-Goldman, S.D., Meadows, V.S., et al. 2016, Astrobiology, 16(11), DOI: 10.1089/ast.2015.1422
Arney, G., Domagal-Goldman, S.D., Meadows, V.S. 2018, Astrobiology, 18(4), DOI: 10.1089/ast.2017.1666
Ayupov, B.M., Sulyaeva, V.S., Shayapov, V.R., et al. 2011, J. Opt. Technol., 78(6), DOI : 10.1364/jot.78.000350
Azzam, R.M.A. 1977, Ellipsometry and polarized light, Elsevier North-Holland
Bakr, N.A., Funde, A.M., Waman, V.S., et al. 2011, Pramana - J. Phys., 76(3), DOI : 10.1007/s12043-011-0024-4
Beichman, C., Benneke, B., Knutson, H., et al. 2014, PASP, 126, DOI : 10.1086/679566
Berry, J.L., Ugelow, M.S., Tolbert, M.A., Browne, E.C. 2019, ApJl, 885, DOI : 10.3847/2041-8213/ab4b5b
Brassé, C., Muñoz, O., Coll, P., Raulin, F. 2015, PSS, 109, DOI : 10.1016/j.pss.2015.02.012
Bruno, G., Lewis, N.K., Stevenson, K.B., et al. 2018, AJ, 155(2), DOI : 10.3847/1538-3881/aaa0c7
Campi, D. & Coriasso, C. 1988, Materials Letters, 7(4)
Deng, J., Du, Z., Karki, B.B., Ghosh, D.B., Lee, K.K.M. 2020, Nat. Com., 11(1), DOI : 10.1038/s41467-020-15757-0

Dodge, M.J. 1984, Appl. Opt., 23
Dorranian, D., Dejam, L., Mosayebian, G. 2012, J. Theo. Appl. Phys., 6, DOI : 10.1186/2251-7235-6-13
El-Naggar, A.M., El-Zaiat, S.Y., Hassan, S.M. 2009, Optics & Laser Technology, 41, DOI : 10.1016/j.optlastec.2008.05.022
Fujiwara, H. 2007, Spectroscopic Ellipsometry : Principles and Applications, John Wiley & Sons Ltd, The Atrium, Southern Gate, Chichester, West Sussex PO19 8SQ, England
Gaillard, F. & Scaillet, B. 2014, EPSL, 403, DOI : 10.1016/j.epsl.2014.07.009
Gaillard, F., Bernadou, F., Roskosz, M., et al. 2022, EPSL, 577, DOI : 10.1016/j.epsl.2021.117255
Gao, P., Thorngren, D.P., Lee, G.K.H, et al. 2020, Nat. Astron., 4(10), DOI : 10.1038/s41550-020-1114-3
Gao, P., Wakeford, H.R., Moran, S.E., Parmentier, V. 2021, JGR : Planets, 126(4), DOI : 10.1029/2020JE006655
Garcia-Caurel, E., De Martino, A., Gaston, J.-P., Yan, L. 2013, Applied Spectroscopy, 67(1), DOI : 10.1366/12-06883
Garcia-Caurel, E., Lizana, A., Ndong, G., et al. 2015, Applied optics, 54(10), DOI : 10.1364/AO.54.002776
Gautier, T., Carrasco, N., Mahjoub, A., et al. 2012, Icarus, 221, DOI : 10.1016/j.icarus.2012.07.025
Gavilan, L., Broch, L., Carrasco, N., Fleury, B., Vettier, L. 2017, ApJL, 848(1), DOI : 10.3847/2041-8213/aa8cc4
Gavilan, L., Carrasco, N., Hoffmann, S.V., Jones, N.C., Mason, N.J. 2018, ApJ, 861(2), DOI : 10.3847/1538-4357/aac8df
Grigorovici, R., Stoica, T., Vancu, A. 1982, Thin Solid Films, 97, DOI : 10.1016/0040-6090(82)90226-7
Hawranek, J.P. & Jones, R.N. 1976, Spectrochimica Acta, 32A
Hawranek, J.P., Neelakantan, P., Young, R.P., Jones, R.N. 1976, Spectrochimica Acta, 32A
He, C., Hörst, S.M., Lewis, N.K., et al. 2018, ApJL, 856, DOI: 10.3847/2041-8213/aab42b
He, C., Hörst, S.M., Lewis, N.K., et al. 2018, ACS Earth and Space Chemistry, 3(1), DOI : 10.1021/acsearthspacechem.8b00133
He, C., Hörst, S.M., Radke, M., Yant, M. 2022, PSJ, 3(1), DOI : 10.3847/PSJ/ac4793
He, C., Radke, M., Moran, S.E., et al. 2023, under review in Nat. Astron., DOI : 10.48550/arXiv.2301.02745
Heng, K., Lyons, J.R., Tsai, S.-M. 2016, ApJ, 816(2), DOI : 10.3847/0004-637X/816/2/96
Heng, K. & Showman, A.P. 2015, Annu. Rev. Earth Planet. Sci., 43, DOI : 10.1146/annurev-earth-060614-105146
Hörst, S.M., He, C., Lewis, N.K., et al. 2018, Nat. Astron., 2(4), DOI : 10.1038/s41550-018-0397-0
Imanaka, H., Cruikshank, D.P., Khare, B.N., McKay, C.P. 2012, Icarus, 218, DOI : 10.1016/j.icarus.2011.11.018
Jellison, G.E. & Modine, F.A. 1996, Appl. Phys. Lett., 69, DOI : 10.1063/1.118064
Jin, Y., Song, B., Jia, Z., et al. 2017, Optics Express, 25(1), DOI : 10.1364/OE.25.000440
Jovanović, L., Gautier, T., Vuitton, V., et al. 2020, Icarus, 346, DOI : 10.1016/j.icarus.2020.113774
Jovanović, L., Gautier, T., Broch, L., et al. 2021, Icarus, 362, DOI : 10.1016/j.icarus.2021.114398
Kawashima, Y. & Ikoma, M. 2018, ApJ, 853(1), DOI : 10.3847/1538-4357/aaa0c5
Kawashima, Y. & Ikoma, M. 2019, ApJ, 877(2), DOI : 10.3847/1538-4357/ab1b1d
Khare, B.N., Sagan, C., Arakawa, E.T., et al. 1984, Icarus, 60, DOI : 10.1016/0019-1035(84)90142-8
Kitzmann, D. & Heng, K. 2018, MNRAS, 475(1), DOI : 10.1093/mnras/stx3141
Kramers, M.H.A. 1927, Atti cong intern Fis. 2
Krissansen-Totton, J., Olson, S., Catling, D.C. 2018, Science Advances, 4(1), DOI: 10.1126/sciadv.aao5747
Kronig, R. De L. 1926, Journal of the Optical society of America and Review of Scientific Instruments, 12, DOI : 10.1364/JOSA.12.000547
Lacy, B.I. & Burrows, A. 2020, ApJ, 904(1), DOI : 10.3847/1538-4357/abbc6c
Lavvas, P. & Koskinen, T. 2017, ApJ, 847, DOI : 10.3847/1538-4357/aa88ce
Mahjoub, A., Carrasco, N., Dahoo, P.-R., et al. 2012, Icarus, 221, DOI : 10.1016/j.icarus.2012.08.015
Mai, C. & Line, M.R. 2019, ApJ, 883(2), DOI : 10.3847/1538-4357/ab3e6d
Manifacier, J.C., Gasiot, J., Fillard, J.P. 1976, J. Phys. E: Sci. Instrum., 9(11), DOI : 10.1088/0022-3735/9/11/032
Mikal-Evans, T. 2022, MNRAS, 510(1), DOI : 10.1093/mnras/stab3383
Moran, S.E., Hörst, S.M., Vuitton, V., et al. 2020, PSJ, 1, DOI : 10.3847/PSJ/ab8eae
Morley, C.V., Fortney, J.J., Marley, M.S., et al. 2015, ApJ, 815, DOI : 10.1088/0004-637X/815/2/110
Nuevo, M., Sciamma-O'brien, E., Sandford, S.A., et al. 2022, Icarus, 376, DOI : 10.1016/j.icarus.2021.114841
Ohta, K. & Ishida, H. 1988, Applied Spectroscopy, 42(6), DOI : 10.1366/0003702884430380
Ozharar, S., Akcan, D., Arda, L. 2016, Journal of Optoelectronics and Advanced Materials, 18
Perrin, Z., Carrasco, N., Chatain, A., et al. 2021, Processes, 9, DOI : 10.3390/pr9060965
Pinhas, A. & Madhusudhan, N. 2017, MNRAS, 471(4), DOI: 10.1093/mnras/stx1849
Ramirez, S.I., Coll, P., da Silva, A., et al. 2002, Icarus, 156(2), DOI : 10.1006/icar.2001.6783
Rannou, P., Cours, T., Le Mouélic, S., et al. 2010, Icarus, 208, DOI : 10.1016/j.icarus.2010.03.016
Reizman, F. 1965, J. Appl. Phys., 36(12), DOI : 10.1063/1.1713951
Sciamma-O'Brien, E., Carrasco, N., Szopa, C., Buch, A., Cernogora, G. 2010, Icarus, 209, DOI : 10.1016/j.icarus.2010.04.009

Sciamma-O'Brien, E., Dahoo, P.-R., Hadamcik, E., et al. 2012, Icarus, 218, DOI : 10.1016/j.icarus.2011.12.014

Sciamma-O'Brien, E., Upton, K.T., Salama, F. 2017, Icarus, 289, DOI : 10.1016/j.icarus.2017.02.004

Sing, D.K., Fortney, J.J., Nikolov, N., et al. 2016, Nature, 529, DOI : 10.1038/nature16068

Stenzel, O., Hopfe, V., Klobes, P. 1991, J. Phys. D: Appl. Phys., 24(11), DOI: 10.1088/0022-3727/24/11/028

Swanepoel, R. 1983, J. Phys. E: Sci. Instrum., 16(12), DOI: 10.1088/0022-3735/16/12/023

Swanepoel, R. 1984, J. Phys. E: Sci. Instrum., 17(10), DOI : 10.1088/0022-3735/17/10/023

Szopa, C., Cernogora, G., Boufendi, L., Correia, J.J., Coll, P. 2006, Planetary & Space Science, 54(4), DOI : 10.1016/j.pss.2005.12.012

Tauc, J., Grigorovici, R., Vancu, A. 1966, phys. stat. sol., 15, DOI : 10.1002/pssb.19660150224

Tian, M. & Heng, K. 2023, https://arxiv.org/abs/2301.10217

Tompkins, H.G.& Irene, E.A. 2005, Handbook of Ellipsometry, William Andrew Inc.

Tran, B.N., Joseph, J.C., Ferris, J.P., Persans, P.D., Chera, J.J. 2003, Icarus, 165, DOI : 10.1016/S0019-1035(03)00209-4

Vuitton, V., Tran, B.N., Persans, P.D., Ferris, J.P. 2009, Icarus, 203, DOI : 10.1016/j.icarus.2009.04.016

Wakeford, H.R. & Sing, D.K. 2015, A&A, 573, DOI : 10.1051/0004-6361/201424207

Woitke, P., Herbort, O., Helling, C. 2021, A&A, 646, DOI : 10.1051/0004-6361/202038870

Zellem, R.T., Swain, M.R., Cowan, N.B., et al. 2019, PASP, 131, DOI : 10.1088/1538-3873/ab2d54

Astronomy & Astrophysics manuscript no. output
November 27, 2024
©ESO 2024

Chapter 6 : Refractive indices of photochemical haze analogs for Titan, Pluto and Exoplanet applications - a cross-laboratory comparative study

T. Drant[1,2], E. Sciamma-O'Brien[3], Z. Perrin[1], L. Maratrat[1], L. Vettier[1], D.H. Wooden[3], C.L. Ricketts[3], L. Jovanovic[3], J.-B. Brubach[4], and E. Garcia-Caurel[5]

[1] University of Paris Saclay, OVSQ, LATMOS, CNRS, 11 Boulevard d'Alembert, 78280 Guyancourt, France.
e-mail: thomas.drant@latmos.ipsl.fr

[2] Ludwig Maximilian University, Faculty of Physics, Observatory of Munich, Scheinerstrasse 1, Munich D-81679, Germany.

[3] NASA Ames Research Center, Space Science and Astrobiology Division, Code ST, Moffett Field, CA 94035, USA.

[4] Synchrotron SOLEIL, L'Orme des Merisiers, 91190 Saint-Aubin, France.

[5] Ecole Polytechnique, LPICM, Route de Saclay, 91120 Palaiseau, France.

ABSTRACT

Previous observations of Titan, Pluto and Solar System gas giants along with recent observations of exoplanet atmospheres with the James Webb Space Telescope taught us that photochemical hazes are ubiquitous and form in various environments. Despite being crucial to understand their impact on observations and on the radiative budget, the composition of these haze particles is unknown and strongly influenced by the gas phase chemistry. We perform a cross-laboratory study to assess the effect of the experimental setup and gas composition on the refractive indices of Titan, Pluto and exoplanet haze analogs. We report new data in a broad spectral range from UV to far-IR (up to 200 μm) for future use in climate models and retrieval frameworks. The data is available on the Optical Constants Database (https://ocdb.smce.nasa.gov/). We compare the refractive indices of analogs produced with the PAMPRE setup at LATMOS (France) and the COSmIC facility at the NASA Ames Research Center (USA) from similar gas compositions. We observe strong variations of the bandgap energy and k values in the range from UV to near-IR between the different samples. We note a clear correlation between the gas phase N_2 abundance and the material's bandgap energy. We also confirm the stronger UV-Visible absorbing properties of the Pluto analogs. The experimental setup is the primary factor affecting the refractive indices confirming that the gas residence time, irradiation and temperature are important parameters influencing the composition of the solid analog. The higher n and k values in the UV-Visible and the stronger amine signatures relative to aliphatics in the mid-IR for the COSmIC analogs suggest a stronger incorporation of nitrogen compared to the PAMPRE analogs. The strong amine signature strength on the Pluto analogs along with the observation of the C-O band suggest a stronger incorporation of N and O in the Pluto analogs compared to the Titan analogs, in agreement with previous elemental analyses. Given the strong effect of the setup

on the refractive indices and more specifically on the bandgap energy, one must be cautious when trying to infer atmospheric properties such as C/O from transit spectra of hazy exoplanet atmospheres.

Key words. atmospheres, terrestrial planets

1. Introduction

Photochemical hazes are currently observed in the atmospheres of the different Solar System objects (Kim et al. 1991; Ortiz et al. 1996; Gladstone et al. 2016) and in exoplanet atmospheres (Gao et al. 2021, 2023). Their formation is triggered by a complex organic radical chemistry driven by Vacuum Ultraviolet (VUV) photons in the upper layers of planetary atmospheres. The chemical pathways leading to haze formation and the composition of the resulting solid material remain largely unknown. Insights on these mechanisms are provided by laboratory experiments to support modelling efforts and help interpret observations.

Laboratory experiments revealed that hazes form under a broad variety of gas composition including CO_2- and H_2O-rich mixtures (He et al. 2018; Gavilan et al. 2018). The formation pathways and gas phase precursors are known to vary with the gas composition, the concentration of methane for example controls the transition between aliphatic and polycyclic aromatic hydrocarbon (PAH) pathways (Trainer et al. 2004). In N_2-rich mixtures representative of Titan and Pluto's atmosphere, nitrile chains form at high abundances contributing to the formation of these aerosols (Gautier et al. 2011; Sciamma-O'Brien et al. 2014; Hörst et al. 2018; Perrin et al. 2021). Ion chemistry also leads to formation of charged hydrocarbon and nitrile chains acting as precursors to these haze particles during their formation in the ionosphere (Vuitton et al. 2009; Dubois et al. 2020). The composition of the solid analog is strongly affected by the gas phase chemistry, it is thus controlled by the initial gas composition but also by the experimental conditions (Sciamma-O'Brien et al. 2014; Jovanovic et al. 2020; Carrasco et al. 2016; Nuevo et al. 2022). No model currently exists to link the gas phase chemistry to the composition of the solid haze particles. This composition must however be considered as it significantly affects the optical properties of the haze particles and thus strongly impact observations of planetary atmospheres (see review of Brassé et al. (2015)).

In radiative transfer models, the haze composition is accounted for using the material's refractive indices, n and k, describing dispersion and absorption respectively. Khare et al. (1984) provided the first refractive indices of laboratory-generated haze analogs for a Titan-like gas mixture with 90% N_2 and 10% CH_4. Their data is widely used in the community for the broad spectral range never reproduced to this day. There currently exists several groups able to produce laboratory haze analogs and

measure their refractive indices. Among them, we identify the NASA Ames group (Sciamma-O'Brien et al. 2023), the John Hopkins group (He et al. 2022b, 2023) and the LATMOS group (Sciamma-O'Brien et al. 2012; Mahjoub et al. 2012; Gavilan et al. 2017; Jovanovic et al. 2021; Drant et al. 2024). This massive work developed throughout the past decades revealed that the refractive indices of the haze analogs are strongly influenced by the initial gas composition but also by the experimental setup. The lack of cross-laboratory comparative studies limits our understanding on the effect of the setup as each group focuses on different gas compositions. In addition, most data are only available in the UV-Visible and near-IR (NIR) range (Mahjoub et al. 2012; Sciamma-O'Brien et al. 2012; Gavilan et al. 2017; He et al. 2022b; Sciamma-O'Brien et al. 2023). For that reason, they cannot be used in radiative transfer models to assess the role of hazes on the radiative budget or assess their impact on IR occultation observations as performed for exoplanets with the James Webb Space Telescope (JWST).

Observations of Titan's atmosphere and surface revealed the strong impact of atmospheric hazes on the spectra (Kim et al. 2011; Rannou et al. 2010, 2022). Early analyses showed that the data is best explained with fractal aggregates instead of spherical particles suggesting that a complex microphysical evolution is taking place (West & Smith 1991; Tomasko et al. 2008; Lavvas et al. 2009). This lead to the development of complex models to simulate the photochemistry, mixing and microphysics in Titan's atmosphere and thus explain the haze extinction controlling the observation (e.g. Wilson & Atreya (2004) and Lavvas et al. (2008a,b)). The different remote-sensing observational data obtained during the Cassini-Huygens mission showed a strong sensitivity to the spectral variations of haze extinction allowing us to retrieve haze properties such as fractal dimension and monomer size of the particles (e.g. Rannou et al. (2010, 2022)). The different measurements from UV to NIR constrained the monomer size to 10-60 nm (Liang et al. 2007; Bellucci et al. 2009; Tomasko et al. 2009) and the fractal dimension is estimated at 2 (Rannou et al. 1997; Sciamma-O'Brien et al. 2023) or 2.3-2.4 (Coutelier et al. 2021; Rannou et al. 2022; Es-sayeh et al. 2023) depending on the observation. Given the strong effect of haze extinction on the spectra, the imaginary part of the refractive index k is also constrained allowing comparison with laboratory-generated analogs (Rannou et al. 2010; Vinatier et al. 2012; Rannou et al. 2022). The composition of Titan's aerosols is still unknown, recent work suggested that N-rich analogs best explain the VIMS Visible-NIR observations of Titan's surface (Sciamma-O'Brien et al. 2023) although VIMS and CIRS IR observations point to a N-poor composition of Titan's aerosols (Kim et al. 2011; Vinatier et al. 2012). More laboratory work is needed to understand the influence of the gas composition, irradiation, temperature and mixing rate on the refractive indices of Titan haze analogs.

The more recent observations of Pluto's atmosphere during the flyby of the New Horizons probe taught us that the haze properties are similar to Titan hazes with a monomer size around 10-20 nm and a fractal dimension around 2 (Gao et al. 2017; Fan et al. 2022). Modelling of Pluto's atmospheric chemistry suggests a high production of C2 hydrocarbon species which strongly interact with the solid haze particles (Luspay-Kuti et al. 2017; Wong et al. 2017; Krasnopolsky 2020). Observations of Pluto's surface revealed a strong heterogeneity in the geological terrains with darker regions likely explained by the presence of photochemical hazes mixed with the ice (Stern et al. 2015; Grundy et al. 2018; Scipioni et al. 2021; Lauer et al. 2021). These observations of Pluto's surface are strongly affected by the haze refractive indices and more specifically by the spectral dispersion of k (Protopapa et al. 2020). The work of Jovanovic et al. (2021) on laboratory analogs revealed an increase of k caused by the presence of CO in the initial gas mixture. Gas and solid phase analyses revealed that the formation of oxygenated compounds and the inhibition of complex hydrocarbon chains caused by the presence of CO in the gas phase ultimately leads to an increase in N and O abundances relative to C in the solid analog (Jovanovic et al. 2020; Moran et al. 2022). Although the refractive indices of Jovanovic et al. (2021) gave promising results for the analyses of the Pluto surface observations, more data obtained with different experimental conditions are needed to assess the effect on the UV-Visible absorbing properties derived from observations. In the IR, thermal cooling by photochemical hazes is expected to control the temperature in Pluto's atmosphere (Zhang et al. 2017; Wan et al. 2023). The data is however lacking, there are no available IR refractive indices for Pluto haze analogs.

Early observations with the Hubble space telescope revealed that aerosols are ubiquitous in exoplanet atmospheres (Gao et al. 2021). Photochemical hazes are expected as the primary aerosols for objects with equilibrium temperatures <1000K where condensates are unlikely (Gao et al. 2020). Hazes strongly influence the thermal profile by heating the upper atmosphere and cooling the lower atmosphere (Lora et al. 2018; Lavvas & Arfaux 2021). They also significantly impact transit spectra observations through Rayleigh scattering (Ohno & Kawashima 2020; Gao et al. 2021). Contrary to Titan and Pluto observations, haze properties are more difficult to retrieve from transit spectra observations as strong degeneracy arises from the different haze properties contributing to extinction, i.e. vertical density distribution, particle size and refractive index of absorption k (Lavvas & Koskinen 2017). Lavvas & Arfaux (2021) and Steinrueck et al. (2023) showed that haze refractive index k strongly influences the radiative budget. Additionally, mid-IR (MIR) vibrational modes of these organic hazes should be observable if the haze extinction is relatively low (Kawashima & Ikoma 2019; He et al. 2023) . Only He et al. (2023) and Drant et al. (2024) recently provided refractive indices from UV to far-IR (FIR) covering the entire operating range of JWST. Given the strong correlation between gas composition and refractive indices, future observations of hazes can help constrain atmospheric parameters such as C/O as suggested by Corrales et al. (2023). Recent observations of GJ

Analog	Gas composition	Setup	Production (hours)	Substrates	Measurements
Titan 1	95% N_2 - 5% CH_4	PAMPRE	3	Si(d), Si(i), MgF_2	TS, RE, FTIRS(*)
		COSmIC	10	Si(d), Si(i)	RS, RE, FTIRS(*)
Titan 2	90% N_2 - 10% CH_4	PAMPRE	3	Si(d), Si(i), MgF_2	TS, RE, FTIRS
		COSmIC	8.5	Si(d), Si(i)	RS, RE, FTIRS
Pluto	99% N_2 - 1% CH_4 - 0.05% CO	PAMPRE	2	Si(i), Si(d)	RS, FTIRS
		COSmIC	11	Si(i), MgF_2	RS, FTIRS
Exoplanet	95% Ar - 5% CH_4	PAMPRE	5	Si(i), Si(d), MgF_2	TS, RE, FTIRS(*)
		COSmIC	11	Si(i), Si(d)	RS, RE, FTIRS

Table 1: Summary of the different analogs. The production refers to the duration of the experiment. For the substrates, we used : MgF_2 optical window for UV-NIR transmission spectroscopy (TS) measurements, doped silicon wafer Si(d) for reflection spectrocopy (RS) and ellipsometry (RE) measurements, and intrinsic silicon wafer Si(i) for Fourier-Transform IR spectroscopy (FTIRS) measurements. The analogs for which the FTIRS measurement is marked with (*) means that temperature-dependent transmission spectra were acquired from 40 to 300K (see Section 4).

1214b for example revealed the presence of a thick haze cover suggesting a high atmospheric metallicty (Kempton et al. 2023; Gao et al. 2023). As we gain understanding on the correlation between gas composition, experimental conditions and refractive indices of haze analogs, we will be able to further improve the interpretation of observations.

In the present study, we aim to assess the influence of the gas composition and experimental setup on the refractive indices of haze analogs in a broad spectral range from UV to FIR. We provide new data for Titan and Pluto analogs useful for re-analysis of previous observations and to develop observational strategies for future missions. With these new data, we aim to assess how significant variations of n and k can be depending on the gas composition and experimental setup used. These data will be essential to assess the influence of the refractive indices on transit spectra observations and to further optimize the retrieval of haze properties from JWST spectra.

The different gas composition and experimental setups used for the production of our haze analogs are described in Section 2. Section 3 and 4 present the measurements and models used to derive the refractive indices from UV to FIR. The results are summarized in Section 5 along with implications for observation and modelling frameworks.

2. Our haze analogs

2.1. Gas mixtures

We produced analog samples using various gas compositions to mimic conditions found in the atmospheres of Titan, Pluto and exoplanets. Table 1 summarizes the gas composition used for the different analogs. The exoplanet analog is produced from a mixture with methane as the only reactive gas. This sample is a reference to assess the optical properties of photochemical haze analogs in N-poor mixtures relevant for Solar System gas giants and exoplanet atmospheres. The Titan analogs are

produced from a mixture of N_2 and CH_4. We consider two different abundance ratios of these main molecules to assess the impact of a higher nitrogen content on the analog refractive indices. Mahjoub et al. (2012) addressed this issue for the PAMPRE Titan analogs but only in the range from UV to NIR. This effect was not yet studied for the COSmIC analogs. The nitrogen incorporation in the solid haze material is believed to vary from our laboratory analogs compared to the aerosols found in Titan's atmosphere (Rannou et al. 2010), it is thus essential to provide data produced with different N_2/CH_4 to better understand and interpret observations. In addition, important variations of N_2/CH_4 were observed with altitude in Titan's atmosphere (Niemann et al. 2005, 2010; Maltagliati et al. 2015; Gautier et al. 2024). For the Pluto analog, we further add 500ppm of CO in the N_2-CH_4 gas mixture as predicted by CRIRES/VLT (Lellouch et al. 2011) and ALMA (Lellouch et al. 2016) observations of Pluto's atmosphere. We aim to assess the influence of CO on the refractive indices of oxygenated haze analogs following the work by Jovanovic et al. (2021) limited to the UV-NIR spectral range.

2.2. Experimental setups

One aim of this study is to assess the influence of the experimental setup on the refractive indices of the haze analogs. For that purpose, the PAMPRE setup at LATMOS (France) and the COSmIC facility at the NASA Ames Research Center (USA) were used to produce analogs from similar gas compositions (see Table 1).

The PAMPRE (french acronym for production of aerosols in micro-gravity by a reactive plasma) setup described in details in Szopa et al. (2006) was designed to produce Titan aerosol analogs. A 13.56 MHz radio-frequency (RF) plasma discharge generated with a power of 30W allows dissociation and ionization of the main gas species (N_2 and CH_4 for Titan) from electron impact. This initiates a complex radical chemistry similar to the one driven by VUV photons in the upper layers of planetary atmospheres. The properties of the plasma source was studied in details, analyses revealed that the electron energy distribution is relatively similar to the Solar spectrum with a more significant contribution at high energies favoring dissociation and ionization mechanisms (Alves et al. 2012). The gas mixture (e.g. 95% N_2 - 5% CH_4 for the Titan 1 conditions, see Table 1) is injected in the PAMPRE chamber at a controlled flow rate of 55 sccm (standard cubic centimeter per minute). The continuous injection and pumping in the chamber create a gas flow and stabilize the pressure around 1 hPa. In these conditions, the initial species and the chemical products remain in the reactive medium for ≈30s before being pumped out of the chamber. We will refer to this parameter as the gas residence time. A stainless steel cage is placed around the upper electrode of the PAMPRE chamber to confine the plasma in a smaller volume. We place optical substrates at the bottom of the cage here acting as the grounded electrode. During the experiment, the proximity to the reactive medium will allow the

Fig. 1: Photographs of the Titan haze analogs produced with the PAMPRE (top) and COSmIC (bottom) setups from a mixture of 95% N_2 and 5% CH_4. The thin organic film is deposited onto MgF_2 and silicon substrates.

growth of an organic film directly onto the optical substrate. Samples are exposed to the atmosphere for a short time during collection at the end of the experiment. Fig.1 (top) shows the inside of the cage at the end of the experiment with the different substrates now covered by an organic film. After collection, the samples are kept under primary vacuum to avoid continuous oxidation. After the samples have been collected, the PAMPRE chamber is pumped to a secondary vacuum ($\approx 10^{-6}$ hPa) to prevent contamination for the next experiment.

The COsmic SImulation Chamber (COSmIC) facility described in Salama et al. (2018) and Sciamma-O'Brien et al. (2023) was designed to study the solid and gas phase chemistry for applications to planetary and astrophysical environments. The chosen gas mixture is injected in the

Parameters	PAMPRE	COSmIC
Discharge	Radio frequency	Direct-current
Pressure	≈1 hPa	≈30 hPa
Gas flow rate	55 sccm	2000 sccm
Gas residence time	≈30 s	≈3μs
Temperature	≈300 K	≈200 K

Table 2: Main differences between the PAMPRE and COSmIC experimental conditions.

chamber at a rate of 2000 sccm under atmospheric pressure and at room temperature. The gas flows through a thin slit (127 μm x 10 cm) using a pulse of 1.28 ms creating a supersonic jet expansion cooling the temperature adiabatically to ≈ 150K and reducing the pressure to ≈ 30 mbar. In the stream of the expansion, a pulsed direct-current (DC) plasma discharge is created along the slit to trigger dissociation of the main gas species and initiate chemical reactions leading to the formation of haze analogs. Emission spectroscopy measurements confirmed that the temperature remains at ≈200K in the plasma discharge (Sciamma-O'Brien et al. 2017). The supersonic speed of the gas limits the residence time to ≈ 3μs in the reactive medium which is still sufficient to produce small organic particles with sizes ranging from 20 to 500 nm depending on the initial gas composition (Sciamma-O'Brien et al. 2017; Gavilan Marin et al. 2020; Sciamma-O'Brien & Salama 2020). These small particles are transported in the jet expansion and deposited onto optical substrates placed vertically on the walls, 5 cm downstream of the electrodes. The continuous stacking of particles at jet speed onto the optical substrate creates a film-like layer similar to the analogs produced in the PAMPRE setup. Fig.1 (bottom) shows the samples collected at the end of the experiment.

The main differences between the PAMPRE and COSmIC setups are summarized in Table 2. The differences in temperature, plasma discharge (and thus irradiation) and residence time affect the chemistry and more specifically the formation of gas phase haze precursors. As a result, differences in composition and thus optical properties are expected between the PAMPRE and COSmIC analogs. Our aim is to quantify these variations with the refractive indices (n and k) used as input parameters in radiative transfer models.

3. Measurements from UV to near-IR

3.1. Measurements and model

We performed different spectroscopic measurements in the range from UV to NIR to obtain high quality data and optimize the data analysis and the accuracy of the retrieved refractive indices. We used three measurements providing different data : transmission spectroscopy, reflection spectroscopy and reflection ellipsometry. Table 1 summarizes the various measurements performed on each analog.

Whether we use spectrophotometry or ellipsometry, we measure the reflection and/or transmission of our haze analog sample. For a thin film overlaying an optical substrate, the theoretical transmission and reflection of the sample can be expressed following (Stenzel et al. 1991; Imanaka et al. 2012) :

$$
\begin{aligned}
T_{fs} &= \frac{|t_{afs}|^2 |t_{sa}|^2 e^{-2\beta_{s,im}}}{1 - |r_{sfa}|^2 |r_{sa}|^2 e^{-4\beta_{s,im}}} \\
R_{fs} &= |r_{afs}|^2 + \frac{|t_{afs}|^2 |r_{sa}|^2 |t_{sfa}|^2 e^{-4\beta_{s,im}}}{1 - |r_{sfa}|^2 |r_{sa}|^2 e^{-4\beta_{s,im}}} \\
\text{With : } \beta &= \frac{2\pi d}{\lambda} \sqrt{n^2 - \sin(\theta_i)^2}
\end{aligned}
\tag{1}
$$

where T_{fs} and R_{fs} are respectively the transmission and reflection of the film/substrate sample, β is the phase, $\beta_{s,im}$ is the imaginary part of the phase for the substrate, t and r are the transmission and reflection Fresnel coefficients between the different media (air, film, substrate). The phase of the thin film is included in the expression of these Fresnel coefficients.

These equations are the basis of our theoretical model. The parameter space includes : angle of incidence used for the measurement, refractive indices of the substrate, thickness of the substrate, refractive indices of the haze film, and the thickness of the haze film. Some of these parameters must be constrained a priori to retrieve the refractive indices of the haze analog (film). We emphasize that this theoretical description (Eq.1) describes an ideal scenario where the film thickness is homogeneous and the light beam is collimated. In practice, the film thickness varies following the production procedure specific to each setup, and the light beam of the instrument is focalized. In Table 1, not every measurement is listed for each analog. We performed initial tests to identify the technique providing conditions as close as possible to this ideal theoretical description in order to retrieve reliable refractive indices. Our choices of measurement for the different analogs are explained in the following sections.

The typical approach to retrieve the refractive indices of thin films overlaying a substrate is to fit the data to the theoretical model (i.e. Eq.1). We developed a model based on non-linear iterative least-square fitting with the python scipy packages to retrieve the film thickness and refractive indices from different types of data. The model is functional for both ellipsometric and spectrophotometric measurements. The iterative core is similar regardless of the data type. Different libraries were made for the theoretical expression of the data. The iterative fitting is performed in the entire chosen spectral range. The spectral dispersion of the refractive indices is thus expressed using parameterized functions. The parameters of the functions are fitted to reproduce the data efficiently.

The Tauc-Lorentz formalism is often used to describe the spectral dispersion of n and k in the transition between electronic and atomic polarization. The Tauc-Lorentz equation expresses the imaginary part of the dielectric constant ε_2 as the product of Tauc's equation with the classical Lorentz oscillator (Tauc et al. 1966; Campi & Coriasso 1988) :

$$\varepsilon_2(E) = \begin{cases} 0 & \text{for } E \leqslant E_g \\ \frac{A\ Eo\ C\ (E-E_g)^2}{E\ ((E^2-Eo^2)^2\ +\ C^2\ E^2)} & \text{for } E > E_g \end{cases} \quad (2)$$

where E is the energy (eV), E_g is Tauc's bandgap energy (eV). A, Eo and C are respectively the strength (eV), peak energy (eV) and width (eV) of the Lorentz oscillator.

The real part of the dielectric constant ε_1 can be expressed analytically from ε_2 (Jellison & Modine 1996) following Kramers-Kronig causality (Kronig 1926; Kramers 1927). The new parameter ε_∞ appears in the expression of ε_1, it scales the dielectric constant at infinite energy (or wavenumber). n and k are derived directly from the dielectric constant ($\varepsilon = \varepsilon_1$ - i ε_2) following (Fujiwara 2007):

$$\begin{aligned} n &= [[\varepsilon_1 + (\varepsilon_1^2 + \varepsilon_2^2)^{1/2}]/2]^{1/2} \\ k &= [[-\varepsilon_1 + (\varepsilon_1^2 + \varepsilon_2^2)^{1/2}]/2]^{1/2} \end{aligned} \quad (3)$$

Since k $\rightarrow$ 0 by definition below the bandgap energy, accurate k values of our haze analogs are not retrieved in the NIR range (Gavilan et al. 2017; Jovanovic et al. 2021; Drant et al. 2024). As the UV-NIR spectral range only reveals the absorption slope caused by electronic transitions at higher energies, one approach is to express the refractive indices with power law functions. With this Cauchy formalism, n and k are expressed following (Jenkins & White 1981) :

$$\begin{aligned} n(\lambda) &= n_\infty + \frac{\lambda_{n,1}}{\lambda^2} + \frac{\lambda_{n,2}}{\lambda^4}, \\ k(\lambda) &= k_\infty + \frac{\lambda_{k,1}}{\lambda^2} + \frac{\lambda_{k,2}}{\lambda^4}, \end{aligned} \quad (4)$$

where n_∞ and k_∞ are constants used to scale n and k respectively. $\lambda_{n,1}$, $\lambda_{n,2}$, $\lambda_{k,1}$, $\lambda_{k,2}$ are additional constants to describe the dispersion of n and k at lower wavelengths. The units of these parameters can be deduced easily to ensure that n and k are dimensionless.

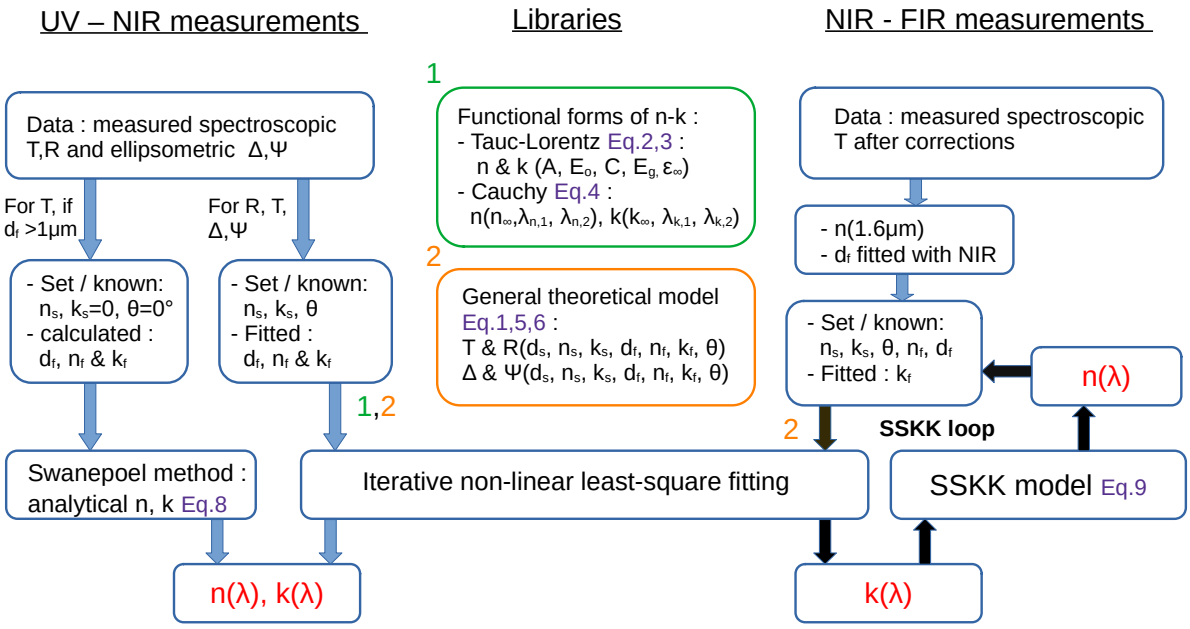

Fig. 2: Schematic summarizing the different procedures applied to retrieve refractive indices using spectroscopic and ellipsometric data from UV to far-IR. f and s refer to film and substrate respectively. θ is the angle of incidence during the measurement. d is the thickness.

The schematic in Fig.2 illustrates the principle of our model to derive refractive indices from different data in the UV-NIR spectral range. More details on each measurement and the data analysis are provided in the following sections.

3.2. Reflection ellipsometry

The previous work of Drant et al. (2024) observed a reasonable agreement between refractive indices derived from reflection ellipsometry and transmission spectroscopy in the UV-visible range. Only a small discrepancy around 3-4% was seen on the refractive index n. To ensure the reliability of our refractive indices in the present work, reflection ellipsometric measurements were performed on almost each analog (see Table 1). The wavelength range is limited to 0.27-0.8 μm. The transmission and reflection measurements described in the following sections provide data at higher wavelengths in the NIR. The ellipsometric measurements are thus only used to ensure reasonable agreement between the refractive indices retrieved with spectroscopy and ellipsometry.

For these measurements, we use the sample deposited onto a doped Si substrate with one side polished only. The organic film is deposited onto the polished side. The strong absorption by Si in the UV-Visible range prevents multiple reflection within the substrate. In this configuration, the reflection

of the sample in Eq.1 simplifies to :

$$R_{fs} = \frac{|r_{af}|^2 + |r_{fs}|^2 e^{-2\beta_{f,im}}}{1 + |r_{fa}|^2 |r_{fs}|^2 e^{-2\beta_{f,im}}} \tag{5}$$

This approach allows us to reduce the parameter space avoiding the use of the substrate thickness which can now be modeled as a semi-infinite layer. Its refractive indices are however still needed to consider reflection at the interface with the organic film.

Using standard ellipsometry, we measure reflection of the sample using two polarization states to retrieve the ellipsometric angles Δ and Ψ describing the phase shift and amplitude ratio respectively. The ratio of parallel (p) and perpendicular (s) reflectance can be expressed using these ellipsometric angles :

$$\rho = \frac{r_p}{r_s} = \tan(\Psi)\, e^{i\Delta} \tag{6}$$

In the theoretical expression library of our model (see Fig.2), Eq.6 is added for this data analysis.

We used the Jobin-Yvon UVISEL ellipsometer at the LPICM (Laboratoire de Physique des Interfaces et des Couches Minces) laboratory, in Palaiseau (France), to measure the ellipsometric angles of our samples from 0.27 to 0.83 μm. The instrument and the operating configurations are described in Drant et al. (2024). The measured ellipsometric angles are shown in Fig.3 (black) for the COSmIC Titan 2 analog and PAMPRE exoplanet analog (see Table 1). For each analog, we perform measurements at three different positions on the sample to derive an uncertainty on the retrieved refractive indices.

For the data analysis, only the refractive indices of the analog layer and the film thickness are unknown parameters of the theoretical model (Eq.5 and Eq.6). The substrate is modeled as a semi-infinite layer, its refractive indices are well-known in this spectral range. An analysis of the blank Si substrate alone allowed us to constrain the angle of incidence precisely (at 69.9°), this parameter is set in the model. The data is fitted to the theoretical model using Cauchy and Tauc-Lorentz functions in Fig.3. The results are discussed in Section 5.1.

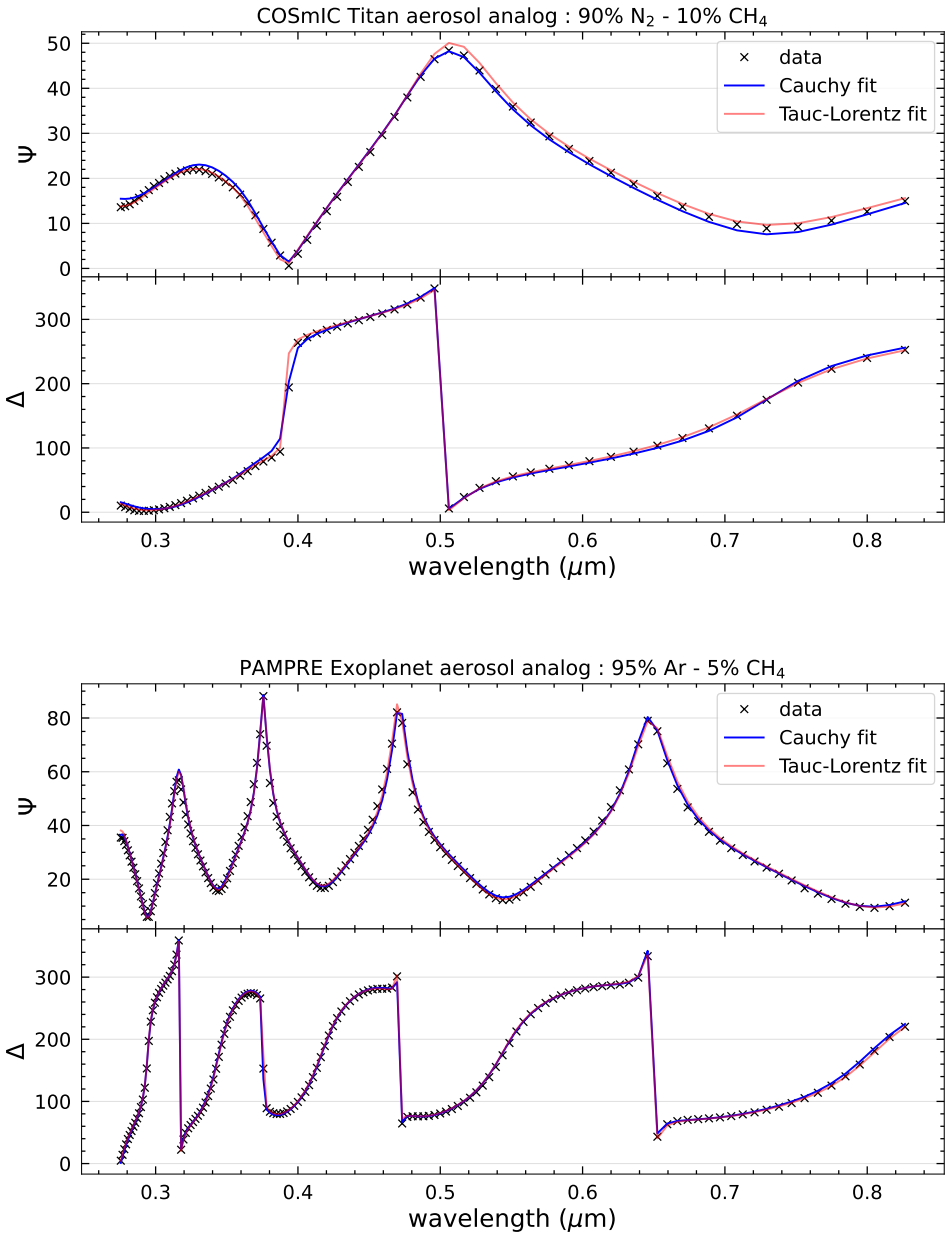

Fig. 3: Reflection ellipsometric data for the COSmIC Titan 2 analog (top panel) and PAMPRE exoplanet analog (bottom panel). The data is fitted to a Cauchy and Tauc-Lorentz model to derive the refractive indices.

3.3. Transmission spectroscopy

Previous work by Drant et al. (2024) revealed that the Swanepoel method (Swanepoel 1983) or iterative least-square fitting of transmission data can provide reliable refractive indices on laboratory haze analogs. The reliability of this approach is limited to homogeneous samples within the size of the beam spot, around 3-4 mm with our instrument. Our initial tests revealed that the strong film thickness variability on the COSmIC samples, also observed in Sciamma-O'Brien et al. (2023), significantly affects the measured spectrum and reduces the accuracy of the retrieved refractive indices. For that

reason, transmission measurements from UV to NIR were only performed on the PAMPRE samples.

For these measurements, we use the sample deposited onto an optical MgF_2 window as Si absorbs below 1μm. Since MgF_2 is transparent from UV to NIR and its refractive index n_s (≈ 1.38) is lower than the haze refractive index (expected $\approx$ 1.5-1.8), the theoretical expression of transmission in Eq.1 simplifies to (Swanepoel 1983) :

$$
\begin{aligned}
&T_{fs} = \frac{A\ x}{B - C\ x\ \cos(2\beta) + D\ x^2} \\
&\text{With :}\ \ A = 16\ n_f^2\ n_s \\
&\qquad B = (n_f + 1)^3\ (n_f + n_s^2) \\
&\qquad C = 2\ (n_f^2 - 1)\ (n_f^2 - n_s^2) \\
&\qquad D = (n_f - 1)^3\ (n_f - n_s^2) \\
&\qquad x = e^{-\alpha_f d_f} \\
&\qquad \alpha_f = \frac{4\ \pi\ k_f}{\lambda}
\end{aligned}
\tag{7}
$$

where α is the absorption coefficient. The f and s indices are used to distinguish between the thickness and refractive indices of the film and the substrate respectively.

Swanepoel (1983) showed that n and k can be retrieved analytically from the data in this condition following :

$$
\begin{aligned}
&n_f = \sqrt{C + \sqrt{(C^2 - n_s^2)}} \\
&k_f = \frac{-\lambda}{4\ \pi\ d_f} \ln\left(\frac{E_M - \sqrt{E_M^2 - (n_f^2 - 1)^3 (n_f^2 - n_s^4)}}{(n_f - 1)^3\ (n_f - n_s^2)}\right) \\
&\text{With :}\ \ C = 2\ n_s\ \frac{T_M - T_m}{T_M T_m} + \frac{n_s^2 + 1}{2} \\
&\qquad\qquad E_M = \frac{8\ n_f^2\ n_s}{T_M} + (n_f^2 - 1)(n_f^2 - n_s^2)
\end{aligned}
\tag{8}
$$

Where T_m and T_M are the constructed transmission envelopes.

The transmission measurements were performed using the PerkinElmer Lambda 1050+ High Resolution Spectrophotometer operating from UV to NIR. We used the Three Detector Module combining photomultiplier and InGaAs detector to cover a broad spectral range from 0.2 to 2.5 μm. This

module can be used for transmission measurements only. We make several measurements at different positions on the sample to account for small thickness variations and derive an uncertainty on the refractive indices. Fig.4 shows the transmission spectra obtained on the Titan 2 and exoplanet analogs, both produced with the PAMPRE setup.

For the data analysis, the analog refractive indices and the film thickness are the unknown parameters. We used normal incidence for the measurements, this parameter is set in the model. Depending on the analog, we used two different approaches to derive the refractive indices. For the Titan analogs, we use the Swanepoel method as the thick film thickness (around 1.5-1.7 μm) allows us to construct efficiently the transmission envelopes (see Fig.4, top panel). Film thickness and refractive indices can thus be derived analytically with great precision. Fig.4 (top panel) shows the analysis of the transmission data with the Swanepoel method for the PAMPRE Titan 2 analog. For the exoplanet analog, the lower film thickness around 0.7 μm make the construction of the envelopes more difficult leading to more significant errors on the retrieved refractive indices. We thus apply the iterative approach using Eq.1 for the theoretical expression of transmission. The exoplanet analog transmission spectrum is fitted with the Tauc-Lorentz and Cauchy models in Fig.4 (bottom panel). The two approaches used to analyze the transmission spectra and retrieve n-k are summarized in Fig.2. The results are discussed in Section 5.1 and 5.2.

3.4. Reflection spectroscopy

Reflection spectroscopic measurements are performed from 0.2 to 1.65 μm using the Filmetrics F40-UVX microscope spectrometer at the NASA Ames Research Center. The measurements are performed at normal incidence using 5X and 10X reflective microscope objectives to obtain a very high spatial resolution on the sample with a spot size around 25-50μm. Within this small spot size, the film thickness of the COSmIC samples is homogeneous. These measurements were only performed on the COSmIC analogs with the exception of the PAMPRE Pluto analog which seemed to present more significant thickness variations (see Table 1). For each analog, 2-3 measurements are taken at different locations on the sample to derive an uncertainty on the retrieved refractive indices. This approach was successfully used in Sciamma-O'Brien et al. (2023) to retrieve refractive indices on haze analogs. Following this study, we further improved the focalization of the beam during the measurement to approach the theoretical description of the model (Eq.1) and retrieve accurate k values in the entire spectral range.

Similar to the ellipsometric measurements, we use the sample deposited on the doped Si substrate to remove the effect of multiple reflection within the substrate and simplify the data analysis. The data is shown in Fig.5 for the Titan 2 and exoplanet analogs, both produced with the COSmIC setup.

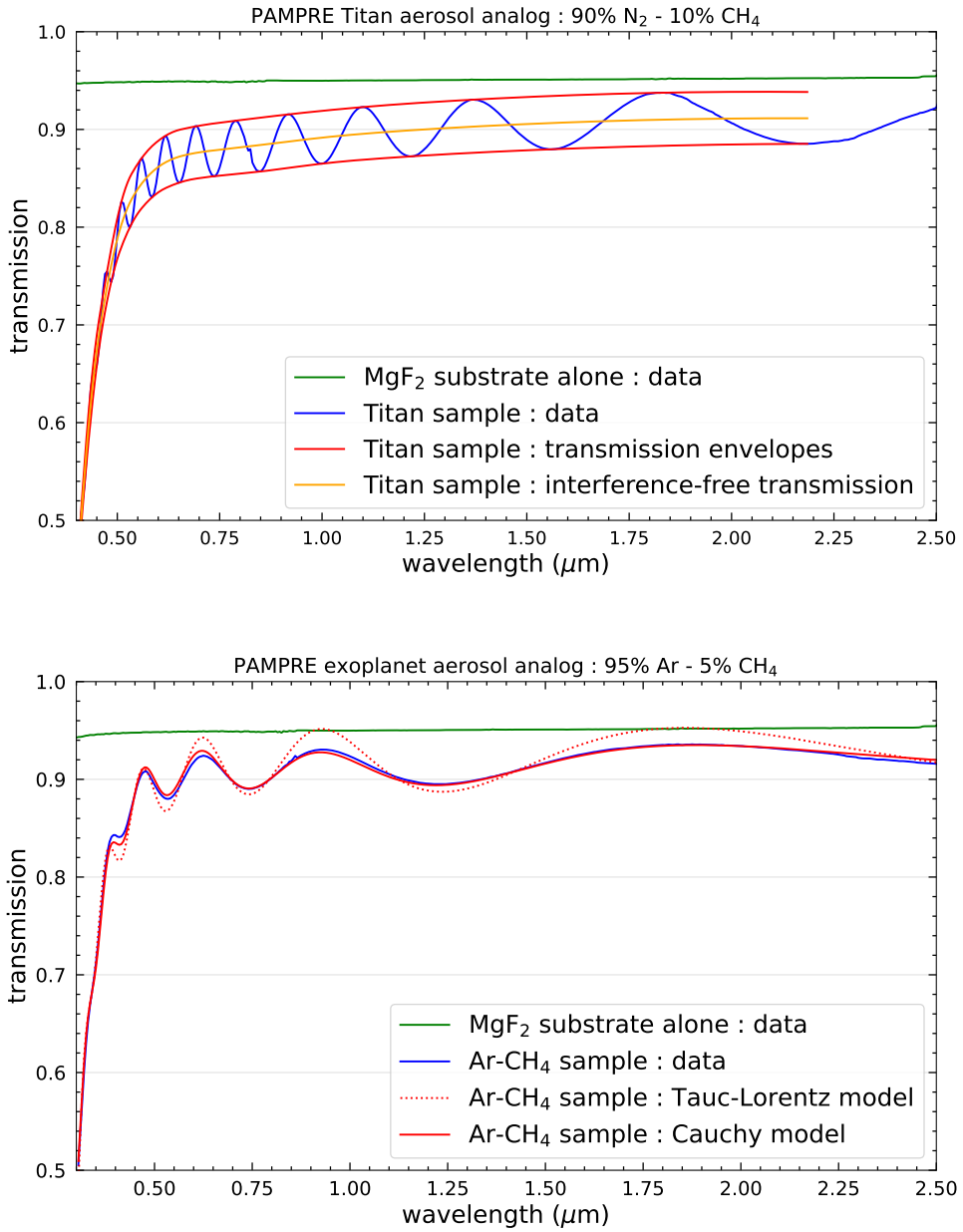

Fig. 4: Transmission spectroscopic data for the PAMPRE Titan and exoplanet analogs from 0.3 to 2.5 μm. (top) Data and analysis using the Swanepoel method for the Titan sample produced with 90% N_2 and 10% CH_4. (bottom) Data and best fit using Cauchy and Tauc-Lorentz models for the exoplanet analog produced with 95% Ar and 5% CH_4.

Data analysis is performed with the iterative approach described in Section 3.1 using Eq.5 as the theoretical expression of reflection. The thickness and refractive indices of the film analog are the unknown and fitted parameters. The data is fitted to the theoretical model with the Cauchy and Tauc-Lorentz expressions of n-k in Fig.5. The iterative procedure used on reflection data is summarized in Fig.2. We limit the fit to the spectral range with visible interference fringes and high signal to noise ratio to avoid errors during the fit. The lower wavelength limit depends on the film thickness and the absorbing properties of the sample, it therefore varies depending the analog. Results are discussed in Section 5.1 and 5.2.

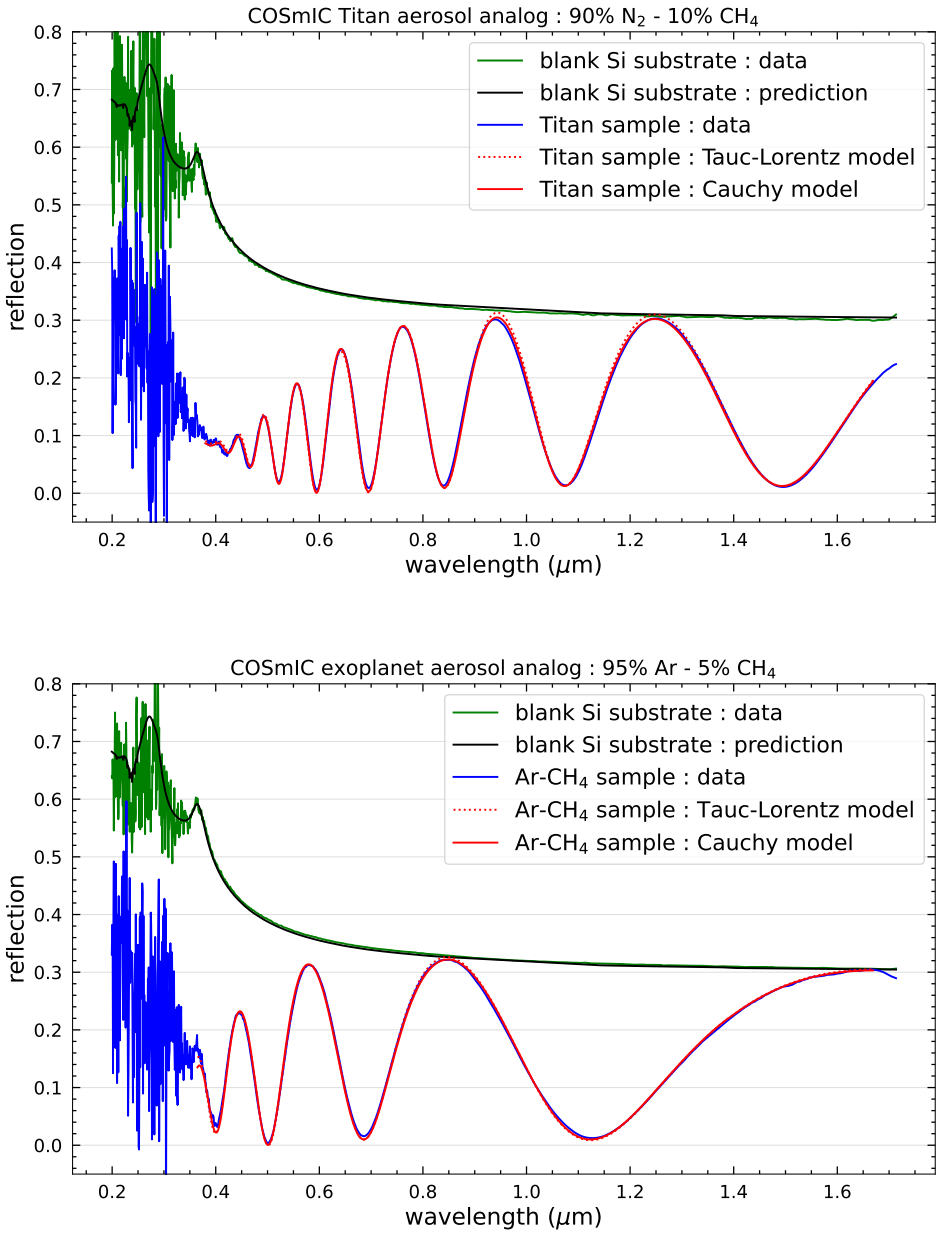

Fig. 5: Reflection spectroscopic data for the COSmIC Titan 2 and exoplanet analogs (see Table 1) from ≈0.4 to 1.65 μm. The data is fitted with both Tauc-Lorentz and Cauchy models.

4. Measurements from near-IR to far-IR

Measurements were performed from NIR to FIR (from 1.5 to 200 μm) using the Bruker IFS125HR Fourier-Transform (FTIR) spectrometer at the Ailes beamline of synchrotron SOLEIL. As we change the beamsplitter and detector between the MIR and FIR, independent measurements are required to cover the entire range. For the MIR, we use a KBr beamsplitter and a MCT detector cooled with liquid nitrogen. For the FIR, we use a 6-micron multilayer mylar beamsplitter and a bolometer detector cooled with liquid helium. The optics aperture is set to 1mm ensuring a small beam spot size on the

sample. Only transmission measurements are performed at normal incidence. For each measurement, the entire instrument is pumped down to $\approx 5.10^{-3}$ hPa to optimize the stability of the source and avoid the presence of atmospheric gaseous signatures on the spectra. We acquired spectra at two different positions on the sample for each analog in the MIR range. In the FIR, we obtained a spectrum for one position on each analog. We ensured using one similar position between the MIR and FIR measurements to have a similar thickness.

In addition, we performed MIR transmission measurements at low temperature using the same instrument with a helium-based cryostat. Temperature is varied from 40 to 300K using several steps. To avoid condensation of water, the instrument is pumped to $\approx 6.10^{-6}$ hPa. These experiments are expensive in time as the temperature must be stabilized accurately at each step. For that reason, we limited the steps to 40, 90, 130, 190 and 300K. These temperatures are relevant for high-altitude conditions in planetary atmospheres and for the low temperatures found at the surface of Titan and Pluto. At each temperature step, a spectrum is acquired in transmission, only for the MIR range. The low temperature measurements were not performed on each analog. We specify in Table 1 for which analogs these measurements were performed.

For these measurements, we use the analog deposited onto the intrinsic Si substrate with both sides polished (see Table 1) as this material is transparent in the entire IR range. As stated in Drant et al. (2024), FTIR measurements do not directly provide absolute data, the measured intensity is very sensitive to variations of the source intensity over time. Several corrections must be performed on the data to obtain an absolute transmission which is essential to retrieve accurate n and k values. First, the intensity spectra of the blank substrate and samples are divided by an open-beam reference spectrum to obtain an 'uncorrected' transmission. A reference spectrum was acquired regularly (every three hours approximately) to account for variations of the source intensity over time. Interference fringes caused by multiple reflection within the substrate are corrected following the procedure with transmission envelopes described in Swanepoel (1983). Given the 300-μm thick substrate, the fringes are very close spectrally and therefore easily distinguished from the fringes caused by multiple reflection within the film.

The first correction factor is obtained using the ratio of the measured 'uncorrected' interference-free transmission for the Si substrate and its expected transmission. Intrinsic Si is indeed transparent and its IR refractive index n is well-known allowing us to derive a theoretical transmission. This correction factor is wavelength-dependent, it also allows us to correct the small absorption features by silicon oxides observed in both the analog samples and the blank substrate. In theory, this correction should suffice if there were no variations of the source intensity between the measurement of the blank Si substrate and the haze analog sample. In practice, this assumption is not always valid and another correction is required.

For this second and last correction, we first fit the film thickness using the NIR range from 1.5 to 3 μm with the refractive index n derived with the UV-NIR measurements (see Section 3). Once the film thickness is known, we use the refractive indices n-k of the analog obtained by our previous UV-NIR measurements (see Section 3) to simulate the expected NIR transmission. If there were variations of the source intensity between the measurement of the blank substrate and analog sample, we observe a vertical shift in the measured transmission compared to the expected transmission. If not corrected, this shift will lead to strong biases in the retrieved k values. The ratio of the measured and expected NIR transmission provides the last correction factor to obtain an actual absolute transmission. The absolute transmission spectra of the COSmIC Titan 2 analog and PAMPRE exoplanet analog are shown in Fig.6. Concatenation between MIR and FIR spectra is performed at 15 μm. The absolute MIR transmission spectra obtained at different temperatures on the PAMPRE Titan 1 analog are shown in Fig.7.

For the data analysis, the aim is to fit the absolute IR transmission with the theoretical expression described in Eq.1. For the fit, one could describe n and k by a set of different Lorentz oscillators following the procedure in Drant et al. (2024) and Perrin et al. (2024) used to analyze MIR Mueller ellipsometric data. In practice, too many model parameters have to be fitted depending on the number of absorption features and strong model degeneracy can bias the results (Drant et al. 2024). We therefore use a different approach where only k is retrieved iteratively and n is calculated using a singly-substrative Kramers-Kronig (SSKK) model.

The model described in Drant et al. (2024) is similar to the approach of Imanaka et al. (2012). k is first retrieved for each data point. At this stage, k is the only unknown variable. The film thickness was already derived using interference fringes in the NIR. n is assumed constant following the NIR value derived with our UV-NIR measurements (see Section 3). A first spectrum of k is obtained based on the assumption that n is constant. Fig.6 shows the first simulated absorption-free (k=0) transmission spectrum for the PAMPRE exoplanet and COSmIC Titan 2 analogs (black curve).

Using the retrieved k values and an anchor refractive index n at a specific wavelength, the n spectrum can be derived from the SSKK model following (Hawranek et al. 1976):

$$n(\nu_i) = n_r + \frac{2}{\pi}\,[P\int_0^\infty \frac{\nu k(\nu)}{\nu^2-\nu_i^2}\,d\nu - P\int_0^\infty \frac{\nu k(\nu)}{\nu^2-\nu_r^2}\,d\nu\,] \tag{9}$$

where n_r and ν_r are the anchor point refractive index and wavenumber (cm^{-1}) respectively. P is the Cauchy principal value of the integral.

Our model was constructed following Maclaurin's formula as it was previously identified by Ohta & Ishida (1988) as the most reliable numerical approach to perform the integral in Eq.9. We use n derived at 1.6 μm with our UV-NIR measurements as an anchor point. Once the IR n spectrum is

obtained, we repeat the first procedure to derive the k spectrum now accounting for spectral variations of n in the IR. We repeat this procedure until the difference in n and k between two iterations is below 1%. In practice, 6 iterations are sufficient as the main variations occur during the first iteration. This iterative procedure used to derive the refractive indices from IR transmission data is summarized in Fig.2. Fig.6 shows the simulated absorption-free (k=0) transmission spectrum after SSKK correction for the PAMPRE exoplanet and COSmIC Titan 2 analogs (red curve). For the PAMPRE exoplanet analog, the SSKK correction has little impact on the transmission as absorption features are relatively weak (Fig.6, bottom panel). On the other hand, we observe an important impact of the SSKK correction for the COSmIC Titan 2 analog (Fig.6, top panel) as the strong hetero-aromatic features lead to strong variations of n around 6 μm. This result emphasizes that spectral variations of n in the IR impact the transmission spectrum. In other words, one should use an iterative model with SSKK correction instead of a standard Beer-Lambert model if one wants to retrieve accurate k values in the entire IR range. The results are discussed in Section 5.3, 5.4 and 5.5.

5. Results and Discussions

5.1. Identifying the best technique to retrieve refractive indices from UV to near-IR

Early work by Khare et al. (1984) and Tran et al. (2003) revealed significant variations of the refractive index n between spectrophotometric and ellipsometric measurements. Drant et al. (2024) also observed a small discrepancy around 3%. In the present work, we found that the discrepancy in n is mainly caused by the difficulty in retrieving accurate k values from reflection measurements in the Visible-NIR spectral range. Reflection measurements (spectroscopy and ellipsometry) are mainly sensitive to variations of n between the film and the substrate. The very weak absorption by the film in the Visible-NIR range is difficult to quantify from reflection measurements and strongly sensitive to the focalization of the beam. For our more absorbing samples, k values could be retrieved in the entire UV-Visible range from our ellipsometric measurements. Fig.8 compares the refractive indices derived from reflection spectroscopy and reflection ellipsometry on the COSmIC Titan analog produced with 90% N_2 and 10% CH_4. We find a strong agreement between both data sets within the range of uncertainty. For our less absorbing samples, the analysis of ellipsometric data is not able to constrain k in the entire UV-Visible range. If k is unconstrained by the data and approximated to 0 in the region of weak absorption (far-Visible and NIR for the PAMPRE analogs), it creates an error on the retrieved n values.

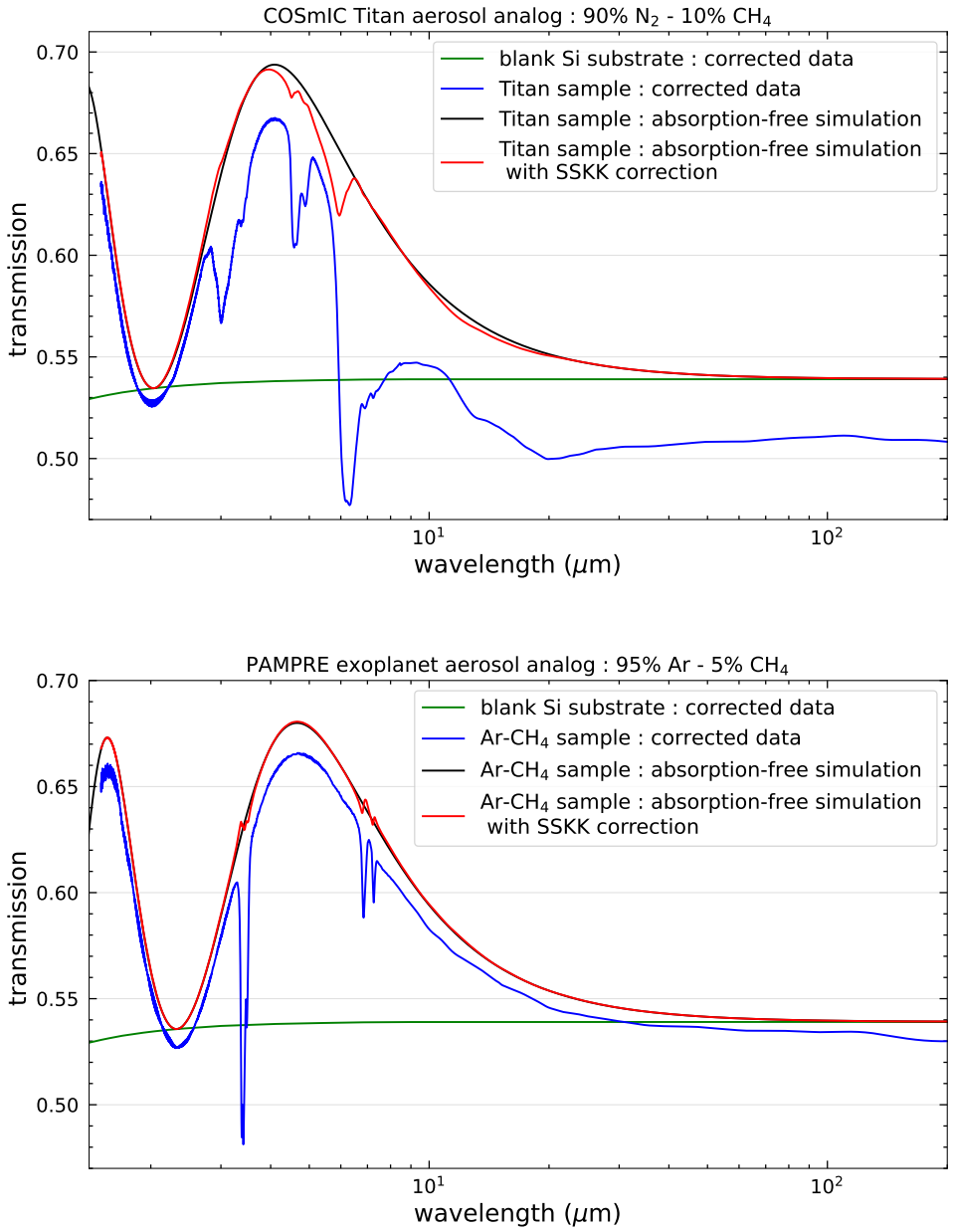

Fig. 6: FTIR spectroscopic transmission spectrum for the COSmIC Titan 2 analog (top) and PAMPRE exoplanet analog (bottom). The simulated absorption-free transmission assuming a constant refractive index n is shown (black curve). The film thickness was fitted in the NIR to match the observed interference fringes. The simulated absorption-free transmission spectrum now considering spectral variations of n (with SSKK model) is also shown (red curve).

Using transmission spectroscopy, the data is more sensitive to absorption. k is constrained more efficiently as it directly correlates to the difference between the transmission of the substrate and the transmission envelopes in Fig.4. The choice of description for n-k (Tauc-Lorentz or Cauchy) with the iterative approach however significantly influences the fit (see Fig.4, bottom panel) and the retrieved n values. Even if we have k<10^{-2} in the far-Visible and NIR range, the measured transmission is still sensitive to this parameter. The assumption of k=0 in the Tauc-Lorentz model leads to an artificial increase of the interference fringes' height during the fitting procedure (see Fig.4, bottom panel).

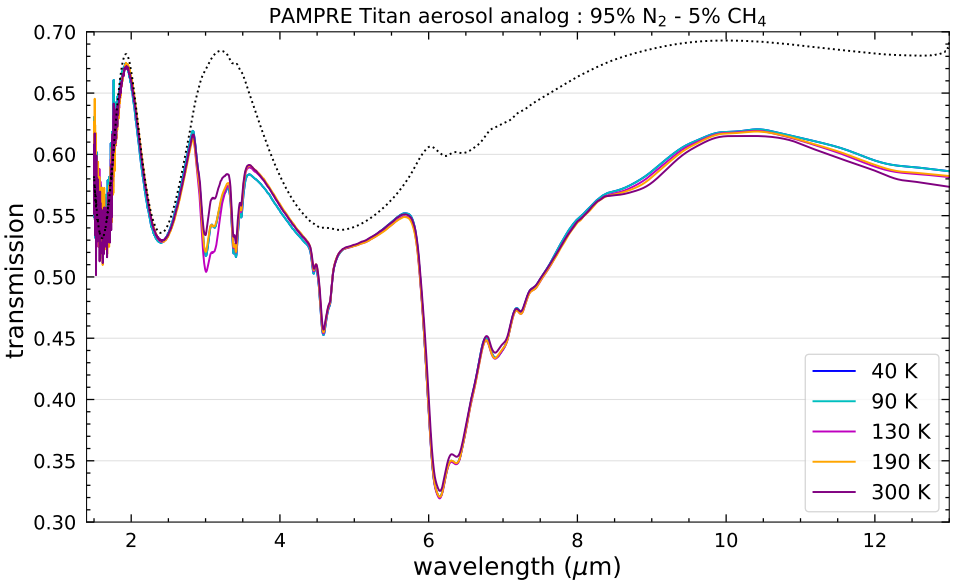

Fig. 7: MIR transmission spectra of the PAMPRE Titan analog produced with 95% N_2 and 5% CH_4. Measurements are performed at different temperatures using the cryostat setup (see Section 4). The simulated absorption-free transmission is shown (black dotted curve) considering spectral variations of n derived with the SSKK model.

In practice, this increased height of interference fringes is the result of a higher refractive index n. In other words, the assumption of k=0 below the bandgap energy in the Tauc-Lorentz model is not appropriate for transmission data, even in the NIR range, as it leads to over-estimations of n to improve the goodness of fit. Given the strong correlation between refractive index n and film thickness d in the law of interference (phase parameter in Eq.1), the over-estimation of n also leads to an under-estimation of the film thickness to preserve the product n x d. A similar effect is observed with reflection spectroscopic measurements. For the more absorbing COSmIC samples (e.g. COSmIC Pluto analog), the analysis of the reflection data with a Tauc-Lorentz model becomes reliable as the bandgap energy is outside of our available spectral range and non-zero k values are retrieved. This analysis emphasizes that the Cauchy model is generally more reliable for weakly absorbing samples in the Visible-NIR spectral range.

5.2. UV-Vis-NIR refractive indices : influence of gas composition and experimental setup

Fig.9 shows the refractive indices of the different analogs from UV to NIR, retrieved with reflection spectroscopy measurements on the COSmIC samples and transmission spectroscopy measurements on the PAMPRE samples (with the exception of the Pluto analog, see Section 3.4). For the refractive indices retrieved using iterative least-square fitting (see Section 3.3 and 3.4), only the predictions of the Cauchy model are shown as they provide more reliable k values in the Visible-NIR (see Section 5.1). For the NIR k values, higher uncertainties are observed for the COSmIC samples compared to

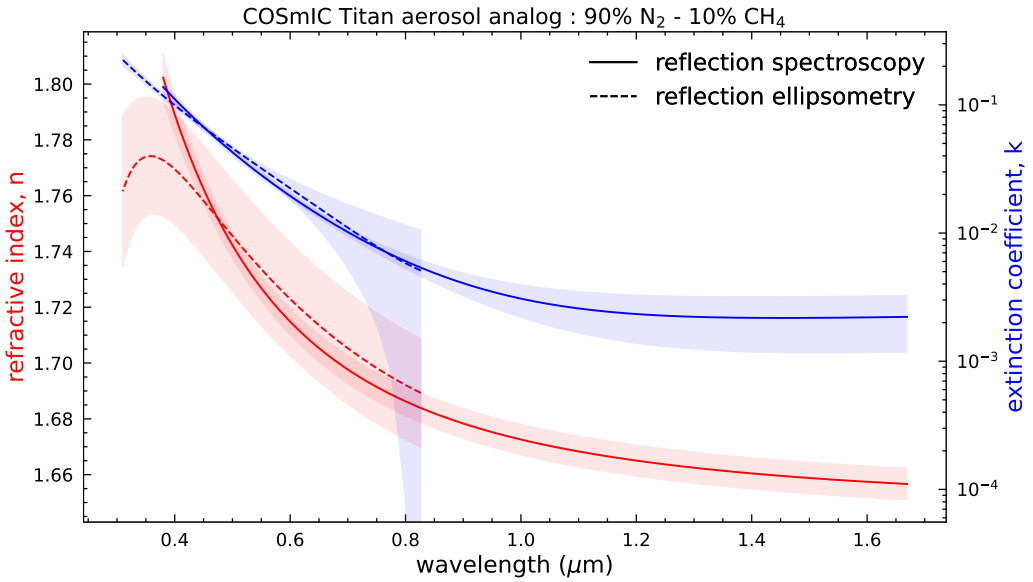

Fig. 8: Comparison between the refractive indices derived by reflection spectroscopy and ellipsometry from UV to near-IR for the COSmIC Titan analog (90% N_2 - 10% CH_4).

the PAMPRE samples as reflection spectroscopy is less sensitive to absorption and more sensitive to measurements biases caused by the focalization of the beam.

Our results reveal a broad range of optical properties affected by both the gas composition and experimental setup (see Fig.9). k varies by up to two orders of magnitude and n varies by up to 0.3-0.4 depending on the wavelength. Both the gas composition and experimental setup introduce a spectral shift of the absorption slope. We can quantify it by a change of the bandgap energy in the Tauc-Lorentz formalism (Eq.2). Previous work revealed that the bandgap energy is affected by the initial gas composition and more specifically by the abundance ratio of CO_2 and CH_4 (Gavilan et al. 2017). The change of optical properties between our exoplanet and Titan analogs clearly reveal a decrease in the bandgap energy as we increase the N_2 abundance in the initial gas mixture. This behavior is observed on both the PAMPRE and COSmIC analogs. A similar effect was observed by Mahjoub et al. (2012) on PAMPRE Titan analogs. The addition of CO seems to further decrease the bandgap energy and generally produce more absorbing analogs in the UV-Visible range. Our n and k values for the PAMPRE Pluto analog are in agreement with the previous ellipsometric measurements by Jovanovic et al. (2021). Gavilan et al. (2018) performed VUV transmission spectroscopy on Early-Earth haze analogs and observed stronger features associated to carbonyl and carboxyl functional groups when CO_2/CH_4 increases. The increase of these functional groups in the presence of CO might explain this increase of k in the near-UV and visible range. Additional VUV constraints are required to confirm this hypothesis and clarify if the increased absorption in the UV-Visible range is caused by stronger VUV features and/or by the appearance of new VUV features at longer wave-

lengths related to oxygenated functional groups. Variations of n with nitrogen content are less clear although higher n values are obtained for the Pluto analogs.

The change of experimental setup for a similar gas composition has an even more significant effect on the optical properties. For a similar analog, we observe a significantly higher bandgap energy for the PAMPRE analogs compared to the COSmIC analogs (see Fig.9, top panel). n and k values are generally higher for the COSmIC samples in the entire UV-NIR spectral range. The strong shift in the bandgap energy between the PAMPRE and COSmIC exoplanet analogs shows that the experimental conditions affect the solid's composition even in the absence of nitrogen. The short gas residence time in the COSmIC setup results in a more simple gas phase chemistry, preventing the formation of complex carbon chains (Sciamma-O'Brien et al. 2014). For the Titan and Pluto analogs, one could expect that the simple chemistry in the COSmIC setup leads to higher N/C in the solid relative to PAMPRE analogs. Previous work taught us that the change in N incorporation can be explained by variations of the temperature (He et al. 2022) or by the properties of the plasma source (Sciamma-O'Brien et al. 2023). More work is needed to assess the effect of the residence time. By changing the plasma discharge voltage, the work of Sciamma-O'Brien et al. (2023) suggests a positive correlation between the incorporation of N and the n-k values of the solid analog. The higher n and k values observed for the COSmIC analogs indeed point to a higher N/C. The higher N/C is however not the only factor influencing the n and k values as we still observe an increase of the optical properties for the COSmIC analogs even in the pure CH_4 exoplanet analogs.

Corrales et al. (2023) suggested that the shift in haze bandgap energy can help constrain C/O in exoplanet atmospheres following the correlation observed in Gavilan et al. (2017). In this present work, we emphasize that the bandgap energy is not only affected by the gas composition but also by the experimental conditions and the resulting effect on the gas phase chemistry. In the laboratory, it is thus controlled by the gas flow rate, the properties of the plasma source, the temperature and the gas residence time. In an atmosphere, it would be controlled by stellar irradiation, vertical mixing and temperature profile. The bandgap energy alone is thus not a reliable tracer of atmospheric C/O. More work focusing on the link between the bandgap energy and the gas phase chemistry could help improve and constrain the choice of refractive indices for exoplanet applications.

Below the bandgap energy, all samples exhibit k values around 1-6.10^{-3}. In this NIR range, variations of the k slope is also primarily influenced by the experimental setup. Observations of Titan's surface by the VIMS instrument onboard the Cassini probe revealed that the slope of the haze extinction coefficient k in the NIR range strongly impacts observations (Sciamma-O'Brien et al. 2023). In general, our NIR k values are lower than the predictions for Titan aerosols constrained by observa-

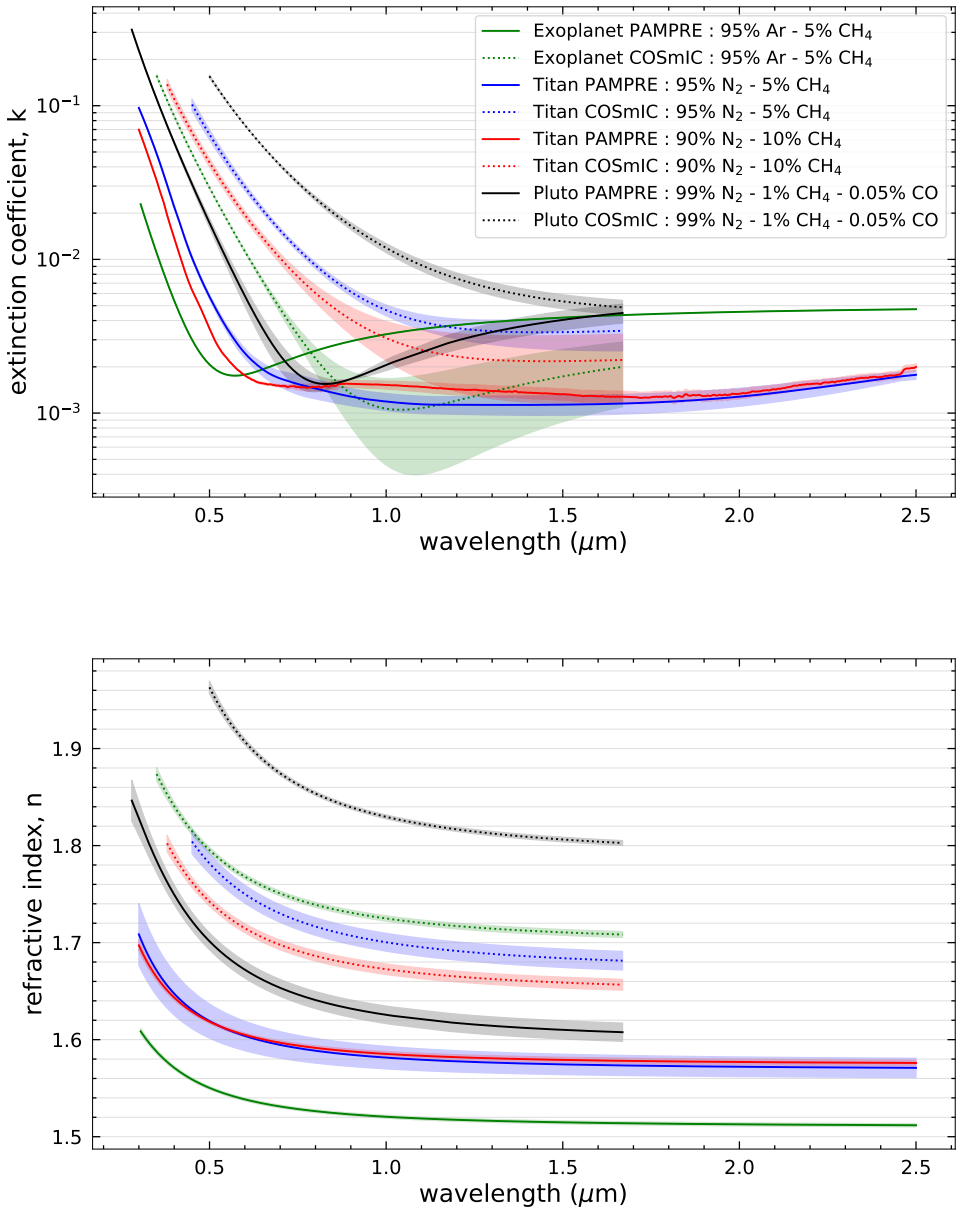

Fig. 9: Refractive indices of the different analogs produced with PAMPRE and COSmIC (see list in Table 1) from UV to NIR. The n-k values are retrieved from transmission spectroscopic data for the PAMPRE analogs and reflection spectroscopic data for the COSmIC analogs.

tions to $\approx 10^{-2}$ (Rannou et al. 2010, 2022). The UV-Visible absorption slope and the lower bandgap energy of the COSmIC Titan analogs are closer to the properties of Titan's aerosols in comparison to the properties of the PAMPRE analogs.

5.3. Titan refractive indices

Fig.10 shows the refractive indices of the different Titan analogs from UV to FIR (up to 200 μm). The seminal work of Khare et al. (1984) is shown in comparison. For the PAMPRE analogs, we

observe an increase of the amine signature strength relative to aliphatics as N_2/CH_4 increases, confirming previous results by Mahjoub et al. (2012) and Gautier et al. (2012). k values related to amine absorption are stronger on the COSmIC analogs compared to the PAMPRE analogs also suggesting a higher N/C in the solid material. Strong similarities are observed between the optical properties of the COSmIC analogs and the samples of Khare et al. (1984). The UV-Visible absorption slope is very similar similar between these analogs although the stronger amine signatures in the Khare samples might suggest a higher incorporation of N. The MIR k values of the two COSmIC Titan analogs are extremely similar suggesting a low effect of the initial CH_4 abundance. It suggests that the short gas residence time still prevents a complex hydrocarbon chemistry even when the CH_4 abundance reaches 10%. The MIR refractive indices of the Titan analogs were determined at different temperatures from 40 to 300K using the data shown in Fig.7. The condensation of water prevents us to accurately assess variations of amine signatures at similar wavelengths. The n-k values are unchanged by the temperature in the entire MIR range. This result confirms the reliability of previous MIR Titan analog refractive indices measured at room temperature (Khare et al. 1984; Imanaka et al. 2012). We find a steeper slope in the FIR k continuum of our analogs compared to Khare et al. (1984). These new data should be considered to re-evaluate the role of hazes in Titan's thermal budget.

We used the refractive indices of the Titan 1 analogs to estimate the extinction efficiency of haze particles with similar composition. This radiative parameter is calculated using Mie theory following the theoretical approach of Wiscombe (1979). In practice, we use the miepython package. To verify our results, we further use the LX-MIE model[1] described in Kitzmann & Heng (2018) developed to improve the numerical procedure for the broad range of particle sizes expected in exoplanet atmospheres. We consider spherical particles with a mean radius of 50 nm following previous determinations for Titan aerosols (e.g. Tomasko et al. (2009)). We consider a gaussian size distribution with a standard deviation of 5 nm. As previously stated, Titan aerosols are fractal aggregates of spherical monomers. We use the fractal optics model[2] following the mean-field approximation of Mie scattering described in Botet et al. (1997) to assess the difference with the prediction for spherical particles. Our parametrization is guided by the known properties of Titan aerosols retrieved from previous observations. We choose a fractal dimension Df of 2 and 3000 monomers with a radius of 50 nm (e.g. Rannou et al. (1997)).

The results are shown in Fig.13, we compare the predictions for spherical particles and fractal aggregates using the refractive indices of the PAMPRE and COSmIC Titan analogs produced from 95% N_2 and 5% CH_4. We show that the change in k values in the UV-Visible-NIR range affects the slope of extinction which can be constrained from observations of Titan's surface and atmosphere (e.g. Rannou et al. (2010)). IR extinction is slightly different between the COSmIC and PAMPRE

[1] https://github.com/NewStrangeWorlds/LX-MIE/
[2] https://github.com/storyofthewolf/fractal$optics_core shell$

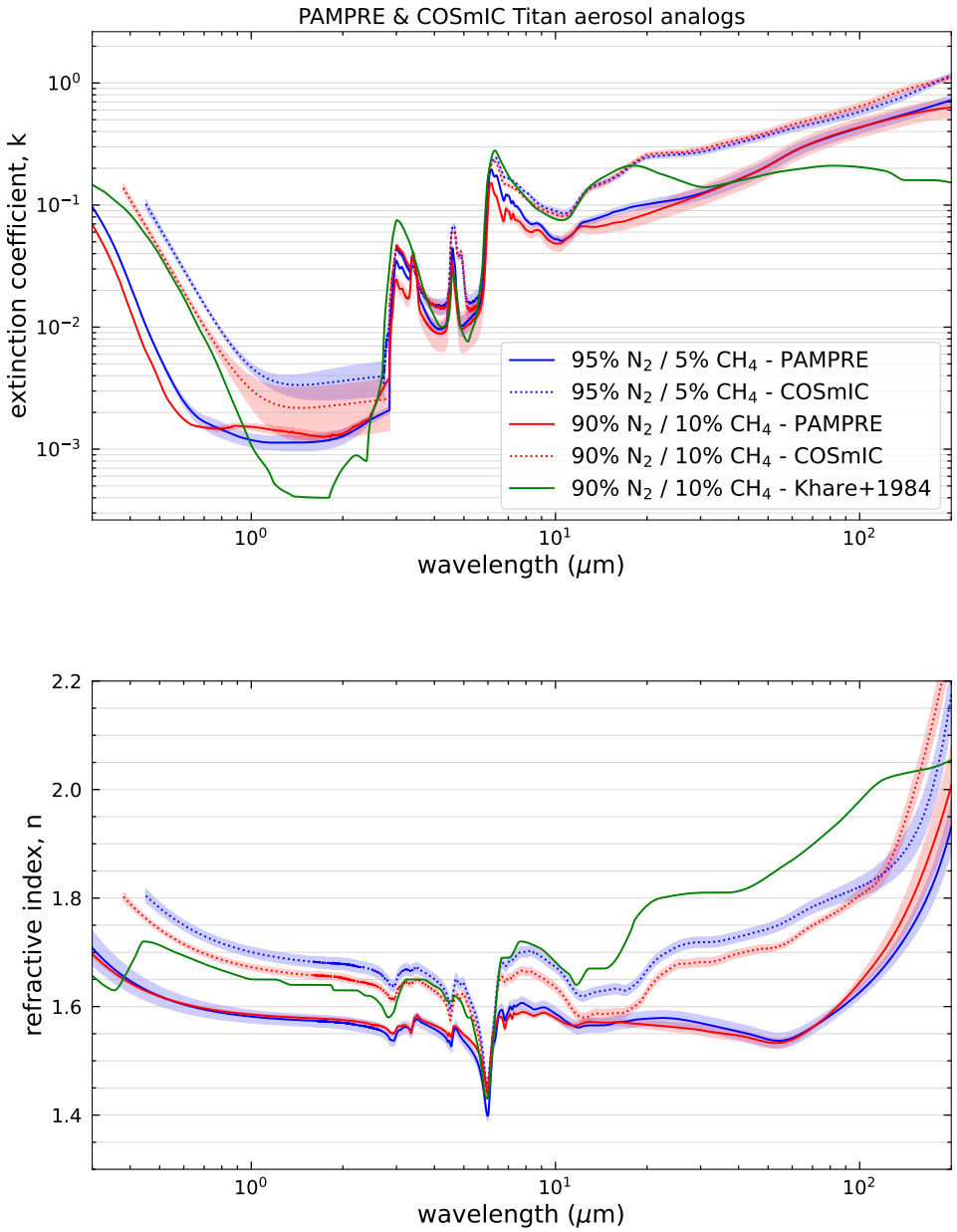

Fig. 10: Refractive indices of Titan aerosol analogs produced with two different ratios N_2/CH_4 using the PAMPRE and COSmIC setups. Data are available from UV up to 200 μm. The low wavelength limit depends on the sample as the strong absorption by COSmIC analogs constrains the spectral range of the data analysis . The refractive indices of Khare et al. (1984) are shown in comparison.

analogs with MIR vibrational modes clearly resolved, providing crucial information on the composition. Previous observations of Titan's atmosphere with VIMS and CIRS indicated that C-H haze features dominate the spectrum (Kim et al. 2011, 2018; Vinatier et al. 2012). We encourage the use of our new refractive indices to re-analyse IR observations and identify the analog that best reproduces the data.

5.4. Pluto refractive indices

The retrieved refractive indices of the PAMPRE and COSmIC Pluto analogs are shown in Fig.11 in the entire range from UV to MIR. We note a relatively small difference of the MIR k values between the COSmIC and PAMPRE samples. In both analogs, the amine signature is much stronger than the aliphatic contribution. This result was also observed on oxygenated hazes produced with CO_2 (Gavilan et al. 2018; Drant et al. 2024). This result is likely caused by the formation of oxygenated C2 species inhibiting the formation of complex carbon chains participating in the formation and composition of reduced hazes (Moran et al. 2022). For both analogs, k values are higher than the corresponding Titan analogs produced without CO. These new data should be used to re-assess thermal emission and cooling by atmospheric hazes in Pluto's atmosphere (Zhang et al. 2017; Wan et al. 2023). The 6-μm C-O feature is observed in the Pluto haze analogs suggesting incorporation of O in agreement with the IR characterization of Jovanovic et al. (2020). The C-O feature is less clear on the COSmIC analogs suggesting a lower O content, this remains to be confirmed by elemental analysis measurements. Analyses of the Pluto analog's composition revealed a higher N and O incorporation compared to Titan analogs caused by the oxygenation of carbon chains (Jovanovic et al. 2020; Moran et al. 2022). These results explain well the MIR signatures observed in our data.

5.5. Exoplanet refractive indices

All of the Titan, Pluto and pure methane analogs are relevant to study the broad diversity of compositions expected for exoplanet atmospheres. For gas giant, sub-Neptune or H_2-rich Super-Earth atmospheres, hazes form in a N-poor environment. The refractive indices of the PAMPRE and COSmIC N-poor exoplanet haze analogs are shown in Fig.12 from UV to FIR. As expected, fewer and weaker features are observed in the MIR. The spectrum is dominated by C-H signatures with the 3-μm aliphatic group providing the highest MIR k values. The PAMPRE exoplanet analog generally exhibits low absorption in the entire range. Similar to the Titan analogs, we found no effect of temperature on the MIR refractive indices of the PAMPRE exoplanet analog. Among all the data sets provided in this work, one can identify end-member cases that can be used for applications to exoplanet atmospheres. The current data obtained with JWST does not provide strong constraints on the haze refractive indices, it rather provides an overall constraint on the haze extinction (Lavvas & Koskinen 2017).

In Fig.13, we compare the extinction efficiency obtained for three of our analogs including the PAMPRE exoplanet analog with Mie scattering models for both spherical particles and fractal aggregates (see Section 5.3). We find that the change in k slope between the different analogs (see Fig.9) modifies the extinction slope of Rayleigh scattering often observed in transit spectra and considered as the main evidence to infer the presence of haze. This extinction slope is used to constrain the particle

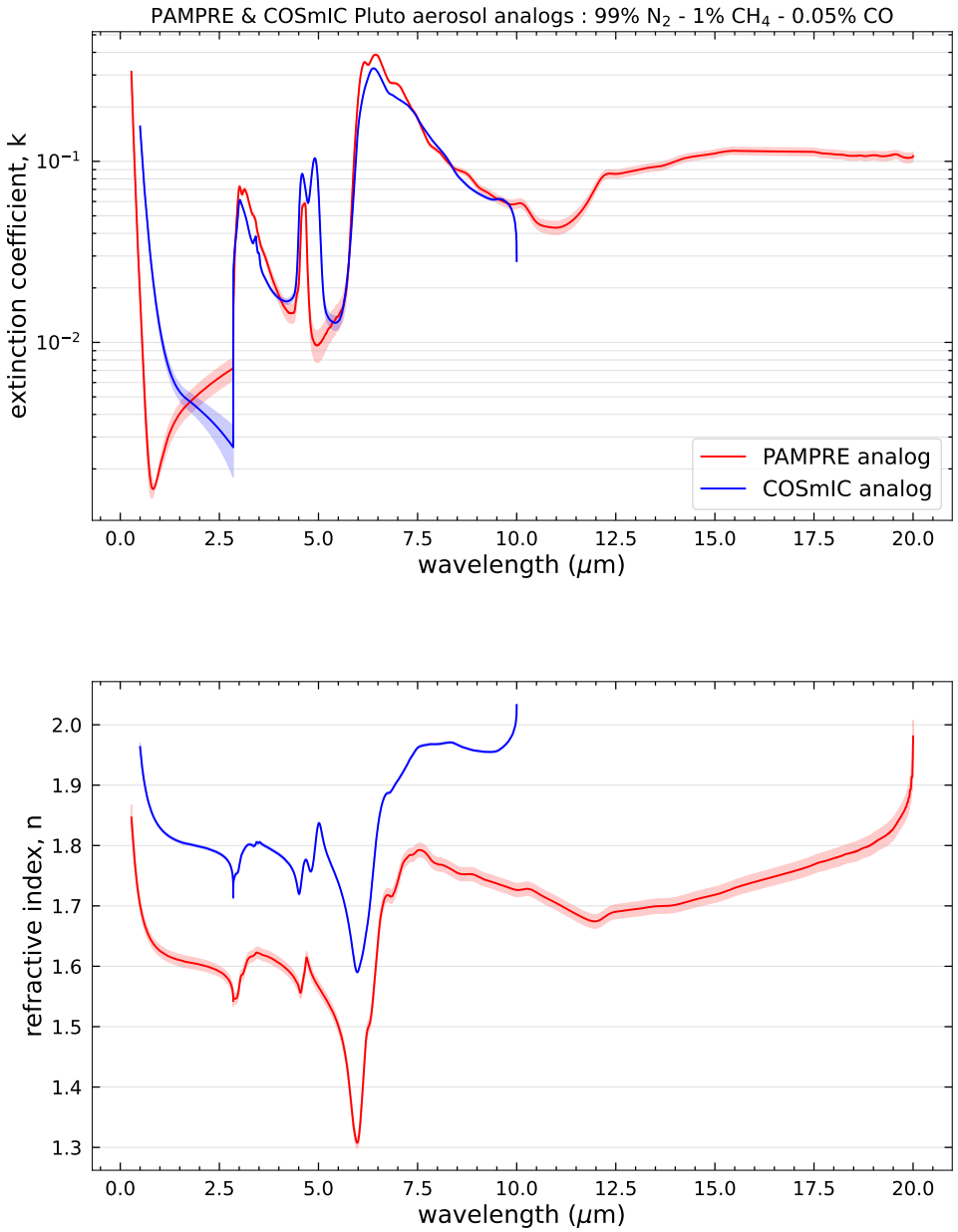

Fig. 11: Refractive indices of Pluto aerosol analogs produced using the PAMPRE and COSmIC setups from a gas mixture with 99% N_2 - 1% CH_4 - 0.05% CO. Data is available from UV to mid-IR.

size under the assumption that absorption is negligible in this Visible-NIR spectral range dominated by scattering (Kitzmann & Heng 2018; Gao et al. 2021). In the MIR, the vibrational modes of organic hazes are visible as extinction is dominated by absorption given the low particle size to wavelength ratio (r/λ). Following previous conclusions by He et al. (2023), our data suggest that MIR haze signatures should be observable in transit spectra of exoplanet atmospheres which could help constrain the haze composition. We note that the amine, aliphatic and nitrile bands are not as resolved if we consider fractal aggregates instead of spherical particles (see Fig.13). The consideration of micro-

physical mechanisms is thus essential as it will affect haze extinction and the detectability of MIR modes.

Previous work on Hot Jupiter hazes suggest a strong influence of the refractive indices / haze composition on the thermal structure of the atmosphere (Steinrueck et al. 2023). The extinction coefficient k of hazes can strongly affect transit spectra of sub-Neptune atmospheres (He et al. 2023). Using the different data provided in this work, more comparative studies should follow to (1) assess the impact of haze composition on the thermal structure of the atmosphere, (2) evaluate detectability of MIR modes against the gaseous background, and (3) assess the impact of refractive indices on the degeneracy of other haze properties (production rate, vertical distribution, fractal dimension) in retrieval frameworks.

6. Conclusions

We derive the refractive indices of Titan, Pluto and Exoplanet haze analogs using different gas compositions and two experimental setups (PAMPRE at LATMOS and COSmIC at NASA Ames). We find a significant effect of N_2 and CO abundances on the refractive indices of the solid analogs. The comparison between the analogs produced with COSmIC and PAMPRE confirms that the experimental conditions controlling the gas phase chemistry strongly influences the refractive indices. Refractive indices are derived in the MIR at different temperatures from 40 to 300K, we found no impact of temperature on the strength of the different stretching and bending modes.

These new data should be used in future work to re-analyze previous observations of Titan and Pluto's surface and atmosphere. The differences in the UV-Visible k values of our different analogs suggest that the heating of the upper atmosphere can strongly differ depending on the haze composition. Our higher k values in the MIR for the Pluto analogs compared to the Titan analogs calls to re-assess thermal cooling suggested as an important contributor to the temperature profile in Pluto's atmosphere. The different data sets highlight the strong variability in absorption from UV to MIR, it can be used to assess the impact of the haze composition on the detectability of haze signatures and the degeneracy of retrieved haze properties (e.g. production rate) during the analysis of JWST data. Recent work revealed that the addition of sulfur in the gas mixture increases the haze production rate (He et al. 2020; Reed et al. 2022) leading to solid analogs with a strong sulfur abundance (Vuitton et al. 2021) and higher n-k values in the Visible range (Reed et al. 2023). Future work should further assess the impact of sulfur on the refractive indices of CHNS and CHNOS hazes in a broad spectral range.

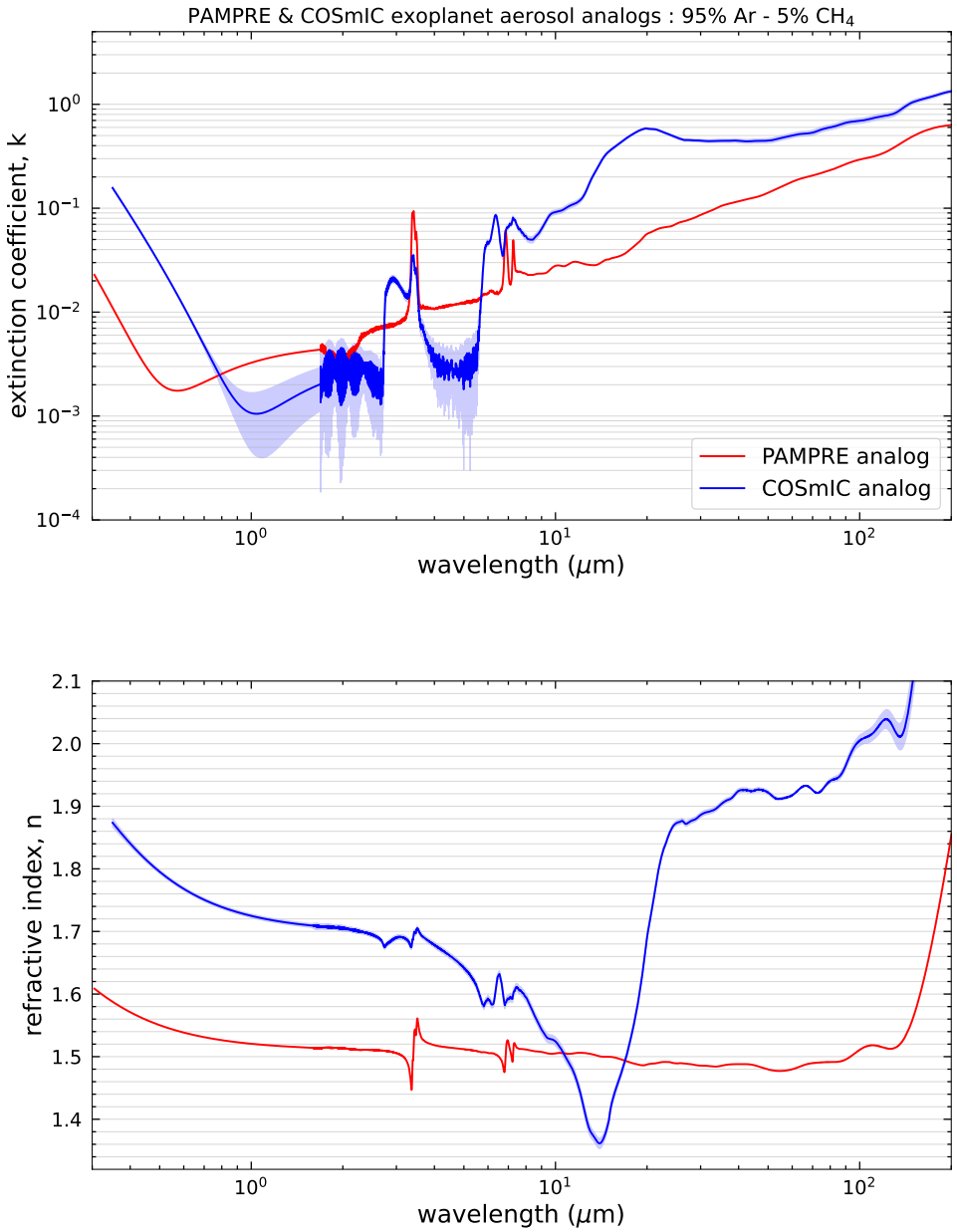

Fig. 12: Refractive indices of Exoplanet aerosol analogs produced using the PAMPRE and COSmIC setups from Ar-CH_4 gas mixtures representative of N-poor atmospheres. Data is available from UV to Far-IR.

References

Alves, L.L., Marques, L., Pintassilgo, C.D., et al. 2012, Plasma Sources Science and Technology, 21, doi : 10.1088/0963-0252/21/4/045008

Bellucci, A., Sicardy, B., Drossart, P., et al. 2009, Icarus, 201, doi : 10.1016/j.icarus.2008.12.024

Botet, R., Rannou, P., Cabane, M. 1997, Applied Optics, 36, 8791-8797, doi :

Brassé, C., Muñoz, O., Coll, P., Raulin, F. 2015, Planetary and Space Science, 109-110, 159-174, doi : 10.1016/j.pss.2015.02.012

Campi, D. & Coriasso, C. 1988, Material Letters, 7, 134-137, doi : 10.1016/0167-577X(88)90169-3

Carrasco, N., Jomard, F., Vigneron, J., Etcheberry, A., Cernogora, G. 2016, Planetary and Space Science, 128, 52-57, doi : 10.1016/j.pss.2016.05.006

Corrales, L., Gavilan, L., Teal, D.J., Kempton, E.M.-R. 2023, ApJL, 943, doi : 10.3847/2041-8213/acaf86

Coutelier, M., Cordier, D., Seignovert, B., et al. 2021, Icarus, 364, doi : 10.1016/j.icarus.2021.114464

Drant, T., Garcia-Caurel, E., Perrin, Z., et al. 2024, A&A, 682, doi : 10.1051/0004-6361/202346820

Dubois, D., Carrasco, N., Jovanovic, L., Vettier, L., Gautier, T., Westlake, J. 2020, Icarus, 338, doi : 10.1016/j.icarus.2019.113437

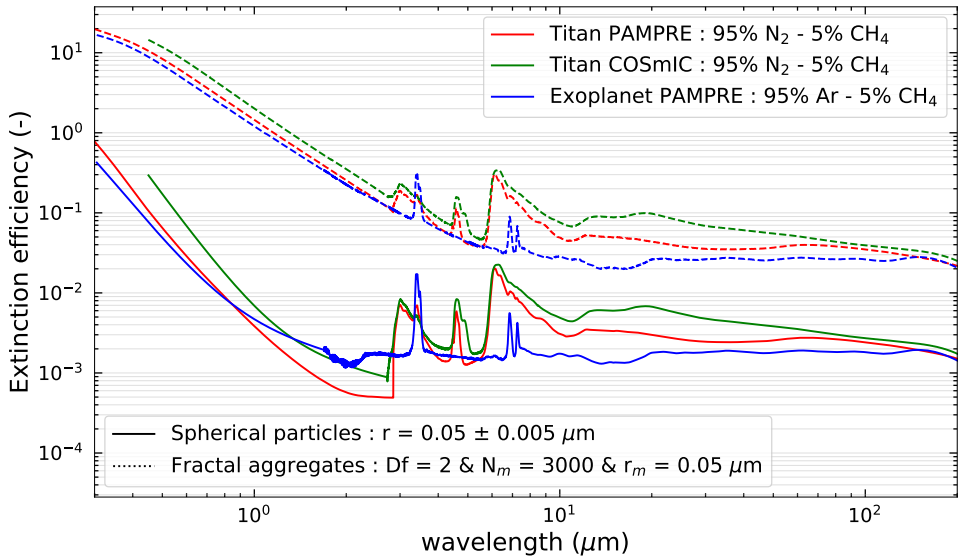

Fig. 13: Comparison of extinction efficiency for different PAMPRE and COSmIC haze analogs in the range from UV to far-IR. The difference between a prediction with spherical particles and fractal aggregates is shown. We consider a gaussian size distribution of spherical particles with a mean radius of 50 nm and a standard deviation of 5 nm. For the fractal aggregates, we consider 3000 monomers with a radius of 50 nm and a fractal dimension of 2.

Es-sayeh, M., Rodriguez, S., Coutelier, M., et al. 2023, Planetary Science Journal, 4, doi : 10.3847/PSJ/acbd37

Fan, S., Gao, P., Zhang, X., et al. 2022, Nature Communications, 13, doi : 10.1038/s41467-021-27811-6

Fujiwara, H. 2007, Spectroscopic Ellipsometry : Principles and Applications, John Wiley & Sons Ltd, The Atrium, Southern Gate, Chichester, West Sussex PO19 8SQ, England

Gao, P., Fan, S., Wong, M.L., et al. 2017, Icarus, 287, 116-123, doi : 10.1016/j.icarus.2016.09.030

Gao, P., Piette, A.A.A., Steinrueck, M.E., et al. 2023, ApJ, 951, doi : 10.3847/1538-4357/acd16f

Gao, P., Thorngren, D.P., Lee, G.K.H., et al. 2020, Nature Astronomy, 4, 951–956, doi : 10.1038/s41550-020-1114-3

Gao, P., Wakeford, H.R., Moran, S.E., Parmentier, V. 2021, JGR planets, 126, doi : 10.1029/2020JE006655

Gautier, T., Carrasco, N., Buch, A., Szopa, C., Sciamma-O'Brien, E., Cernogora, G. 2011, Icarus, 213, 625-635, doi : 10.1016/j.icarus.2011.04.005

Gautier, T., Carrasco, N., Mahjoub, A., et al. 2012, Icarus, 221, 320-327, doi : 10.1016/j.icarus.2012.07.025

Gautier, T., Serigano, J., Das, K., et al. 2024, A&A, in Review.

Gavilan Marin, L., Bejaoui, S., Haggmark, M. 2020, ApJ, 889, doi : 10.3847/1538-4357/ab62b7

Gavilan, L., Broch, L., Carrasco, N., Fleury, B., Vettier, L. 2017, ApJL, 848, doi : 10.3847/2041-8213/aa8cc4

Gavilan, L., Carrasco, N., Hoffmann, S.V., Jones, N.C., Mason, N.J. 2018, ApJ, 861, doi : 10.3847/1538-4357/aac8df

Gladstone, G.R., Stern, S.A., Ennico, K., et al. 2016, Science, 351, doi : 10.1126/science.aad8866

Grundy, W.M., Bertrand, T., Binzel, R.P., et al. 2018, Icarus, 314, 232-245, doi : 10.1016/J.ICARUS.2018.05.019

Hawranek, J.P., Neelakantan, P., Young, R.P., Jones, R.N. 1976, Spectrochimica Acta, 32A, 85-98, doi : 10.1016/0584-8539(76)80055-4

He, C., Hörst, S.M., Lewis, N.K., et al. 2018, ApJL, 856, doi : 10.3847/2041-8213/aab42b

He, C., Hörst, S.M., Lewis, N.K., et al. 2020, Nature Astronomy, 4, 986–993, doi : 10.1038/s41550-020-1072-9

He, C., Hörst, S.M., Radke, M., Yant, M. 2022, Planetary Science Journal, 3, doi : 10.3847/PSJ/ac4793

He, C., Radke, M. Moran, S.E., et al. 2023, Nature astronomy, 8, 182-192, doi : 10.1038/s41550-023-02140-4

He, C., Serigano, J., Hörst, S.M., Radke, M., Sebree, J.A. 2022, ACS Earth Space Chem., 6, 10, 2295-2304, doi : 10.1021/acsearthspacechem.2c00164

Hörst, S.M., Yoon, Y.H., Ugelow, M.S., et al. 2018, Icarus, 301, 136-151, doi : 10.1016/j.icarus.2017.09.039

Imanaka, H., Cruikshank, D.P., Khare, B.N., McKay, C.P. 2012, Icarus, 218, 247-261, doi : 10.1016/j.icarus.2011.11.018

Jellison, G.E. & Modine, F.A. 1996, Appl. Phys. Lett., 69, doi : 10.1063/1.118064

Jenkins, F.A. & White, H.E. 1981, Fundamentals of Optics (Auckland:McGraw-Hill), 482

Jovanovic, L., Gautier, T., Broch, L., et al. 2021, Icarus, 362, doi : 10.1016/j.icarus.2021.114398

Jovanovic, L., Gautier, T., Vuitton, V., et al. 2020, Icarus, 346, doi : 10.1016/j.icarus.2020.113774

Kawashima, Y. & Ikoma, M. 2019, ApJ, 877, doi : 10.3847/1538-4357/ab1b1d

Kempton, E.M.-E., Zhang, M., Bean, J.L., et al. 2023, Nature, 620, 67-71, doi : 10.1038/s41586-023-06159-5
Khare, B.N., Sagan, C., Arakawa, E.T., Suits, S., Callcott, T.A., Williams, M.W. 1984, Icarus, 60, 127-137, doi : 10.1016/0019-1035(84)90142-8
Kim, S.K., Drossart, P., Caldwell, J., et al. 1991, Icarus, 91, 145-153, doi : 10.1016/0019-1035(91)90133-E
Kim, S.J., Jung, A., Sim, C.K., et al. 2011, Planetary and Space Science, 59, 699-704, doi : 10.1016/j.pss.2011.02.002
Kim, S.J., Lee, D.W., Sim, C.K., Seon, K.I., Courtin, R., Geballe, T.R. 2018, Journal of Quantitative Spectroscopy & Radiative Transfer, 210, 197-203, doi : 10.1016/j.jqsrt.2018.02.024
Kitzmann, D. & Heng, K. 2018, MNRAS, 475, 94–107, doi : 10.1093/mnras/stx3141
Kramers, M.H.A. 1927, Atti. Cong. Intern. Fisica (Transactions of Volta Centenary Congress) Como, 2, p. 545.
Krasnopolsky, V.A. 2020, Icarus, 335, doi : 10.1016/j.icarus.2019.07.008
Kronig, R. de L. 1926, Journal of the optical society of America, 12, 547-557, doi : 10.1364/JOSA.12.000547
Lauer, T.R., Spencer, J.R., Bertrand, T., et al. 2021, Planetary Science Journal, 2, doi : 10.3847/PSJ/ac2743
Lavvas, P. & Arfaux, A. 2021, MNRAS, 502, 5643–5657, doi : 10.1093/mnras/stab456
Lavvas, P.P., Coustenis, A., Vardavas, I.M. 2008, Planetary and Space Science, 56, 27-66, doi : 10.1016/j.pss.2007.05.026
Lavvas, P.P., Coustenis, A., Vardavas, I.M. 2008, Planetary and Space Science, 56, 67-99, doi : 10.1016/j.pss.2007.05.027
Lavvas, P. & Koskinen, T. 2017, ApJ, 847, doi : 10.3847/1538-4357/aa88ce
Lavvas, P., Yelle, R.V., Vuitton, V. 2009, Icarus, 201, 626-633, doi : 10.1016/j.icarus.2009.01.004
Lellouch, E., de Bergh, C., Sicardy, B., Käufl, H.U., Smette, A. 2011, A&A, 530, doi : 10.1051/0004-6361/201116954
Lellouch, E., Gurwell, M., Butler, B., et al. 2016, Icarus, 286, 289-307, doi : 10.1016/j.icarus.2016.10.013
Liang, M.-C., Yung, Y.L., Shemansky, D.E. 2007, ApJ, 661, doi : 10.1086/518785
Lora, J.M., Kataria, T., Gao, P. 2018, ApJ, 853, doi : 10.3847/1538-4357/aaa132
Luspay-Kuti, A., Mandt, K., Jessup, K.-L., et al. 2017, MNRAS, 472, 104–117, doi : 10.1093/mnras/stx1362
Mahjoub, A., Carrasco, N., Dahoo, P.-R., et al. 2012, Icarus, 221, 670-677, doi : 10.1016/j.icarus.2012.08.015
Maltagliati, L., Bézard, B., Vinatier, S., et al. 2015, 248, 1-24, doi : 10.1016/j.icarus.2014.10.004
Moran, S.E., Hörst, S.M., He, C., et al. 2022, JGR planets, 127, doi : 10.1029/2021JE006984
Niemann, H.B., Atreya, S.K., Bauer, S.J., et al. 2005, Nature, 438, 779-784, doi : https://doi.org/10.1038/nature04122
Niemann, H.B., Atreya, S.K., Demick, J.E., et al. 2010, JGR, 115, doi : 10.1029/2010JE003659
Nuevo, M., Sciamma-O'Brien, E., Sandford, S.A., Salama, F., Materese, C.K., David, K.A.L. 2022, Icarus, 376, doi : 10.1016/j.icarus.2021.114841
Ohno, K. & Kawashima, Y. 2020, ApJL, 895, doi : 10.3847/2041-8213/ab93d7
Ohta, K. & Ishida, H. 1988, Applied Spectroscopy, 42, 952-957, doi : 10.1366/0003702884430380
Ortiz, J.L., Moreno, F., Molina, A. 1996, Icarus, 119, 53-66, doi : 10.1006/icar.1996.0002
Perrin, Z., Carrasco, N., Chatain, A., et al. 2021, Processes, 9, doi : 10.3390/pr9060965
Perrin, Z., Drant, T., Garcia-Caurel, E., et al. 2024, A&A, submitted.
Protopapa, S., Olkin, C.B., Grundy, W.M., et al. 2020, AJ, 159, doi : 10.3847/1538-3881/ab5e82
Rannou, P., Cabane, M., Botet, R., Chassefière, E. 1997, JGR, 102, 10,997-11,013, doi : 10.1029/97JE00719
Rannou, P., Cours, T., Le Mouélic, S., et al. 2010, Icarus, 208, 850–867, doi : 10.1016/j.icarus.2010.03.016
Rannou, P., Coutelier, M., Rey, M.M., Vinatier, S. 2022, A&A, 666, doi : 10.1051/0004-6361/202243045
Reed, N.W., Jansen, K.T., Schiffman, Z.R., Tolbert, M.A., Browne, E.C. 2023, ApJL, 954, doi : 10.3847/2041-8213/acf1a2
Reed, N.W., Wing, B.A., Tolbert, M.A., Browne, E.C. 2022, Geophysical Research Letters, 49, doi : 10.1029/2021GL097032
Salama, F., Sciamma-O'Brien, E., Contreras, C.S., et al. 2018, in IAU Proc., 13, 364-369, doi : 10.1017/S1743921317011619
Sciamma-O'Brien, E., Dahoo, P.-R., Hadamcik, E., et al. 2012, Icarus, 218, 356-363, doi : 10.1016/j.icarus.2011.12.014
Sciamma-O'Brien, E., Ricketts, C.L., Salama, F. 2014, Icarus, 243, 325-336, doi : 10.1016/j.icarus.2014.08.004
Sciamma-O'Brien, E., Roush, T.L., Rannou, P., Dubois, D., Salama, F. 2023, The Planetary Science Journal, 4, doi : 10.3847/PSJ/acd83f
Sciamma-O'Brien, E. & Salama, F. 2020, ApJ, 905, doi : 10.3847/1538-4357/abc00d
Sciamma-O'Brien, E., Upton, K.T., Salama, F. 2017, Icarus, 289, 214-226, doi : 10.1016/j.icarus.2017.02.004
Scipioni, F., White, O., Cook, J.C.C., et al. 2021, Icarus, 359, doi : 10.1016/j.icarus.2021.114303
Steinrueck, M.E., Koskinen, T., Lavvas, P., et al. 2023, ApJ, 951, doi : 10.3847/1538-4357/acd4bb
Stenzel, O., Hopfe, V., Klobes, P. 1991, J. Phys. D: Appl. Phys., 24, 2088-2094, doi : 10.1088/0022-3727/24/11/028
Stern, S.A., Bagenal, F., Ennico, K., et al. 2015, Science, 350, doi : 10.1126/science.aad1815
Swanepoel, R. 1983, J. Phys. E: Sci. Instrum., 16, doi : 10.1088/0022-3735/16/12/023
Szopa, C., Cernogora, G., Boufendi, L., Correia, J.J., Coll, P. 2006, Planetary and Space Science, 54, 394–404, doi : 10.1016/j.pss.2005.12.012
Tauc, J., Grigorovici, R., Vancu, A. 1966, phys. stat. sol., 15, 627-637, doi : 10.1002/pssb.19660150224
Tomasko, M.G., Doose, L., Engel, S., et al. 2008, Planetary and Space Science, 56, 669-707, doi : 10.1016/j.pss.2007.11.019
Tomasko, M.G., Doose, L.R., Dafoe, L.E., See, C. 2009, Icarus, 204, 271-283, doi : 10.1016/j.icarus.2009.05.034

Trainer, M.G., Pavlov, A.A., Jimenez, J.L., et al. 2004, Geophysical Research Letters, 31, doi : 10.1029/2004GL019859

Tran, B.N., Joseph, J.C., Ferris, J.P., Persans, P.D., Chera, J.J. 2003, Icarus, 165, 379-390, doi : 10.1016/S0019-1035(03)00209-4

Vinatier, S., Rannou, P., Anderson, C.M., et al. 2012, Icarus, 219, 5-12, doi : 10.1016/j.icarus.2012.02.009

Vuitton, V., Lavvas, P., Yelle, R.V., et al. 2009, Planetary and Space Science, 57, 1558–1572, doi : 10.1016/j.pss.2009.04.004

Vuitton, V., Moran, S.E., He, C., et al. 2021, Planetary Science Journal, 2, doi : 10.3847/PSJ/abc558

Wan, L., Zhang, X., Hofgartner, J.D. 2023, ApJ, 955, doi : 10.3847/1538-4357/ace9d5

West, R.A. & Smith, P.H. 1991, Icarus, 90, 330-333, doi : 10.1016/0019-1035(91)90113-8

Wilson, E.H & Atreya, S.K. 2004, JGR, 109, doi : 10.1029/2003JE002181

Wiscombe, W.J. 1979, University Corporation for Atmospheric Research, doi : 10.5065/D6ZP4414

Wong, M.L., Fan, S., Gao, P., et al. 2017, Icarus, 287, 110-115, doi : 10.1016/j.icarus.2016.09.028

Zhang, X., Strobel, D.F., Imanaka, H. 2017, Nature, 551, 352-355, doi : 10.1038/nature24465

Conclusions and perspectives

JWST observations of exoplanet atmospheres are continuously coming. The retrieval community now focuses on a more quantitative analysis of the model parameters to better constrain the properties of the atmosphere and assess the validity of theoretical predictions. The field progresses fast, we are at a time where several groups possess tools to analyze JWST data with various techniques, e.g. bayesian statistics or more recently machine learning. The community is starting to perform comparative studies to better understand the limitations of retrieval models and better quantify the reliability of retrieved atmospheric properties such as temperature or C/O. The data analysis also reveals the lack of experimental data, e.g. gas cross sections or aerosol refractive indices. This lack of data limits the analysis and the interpretation but it also limits the feasibility of new predictions. The community is now identifying all the data needs to prepare future observations with JWST and to prepare the ARIEL mission.

The different projects I led during this PhD revealed the importance of laboratory experiments and the crucial data and information they provide to understand chemical processes occurring in exoplanet atmospheres. My work showed that refractive indices of photochemical haze analogs vary significantly with gas composition and experimental conditions (energy distribution of the source, temperature, gas residence time). I lead a new comparative study between two laboratories to better understand the origin of the discrepancies and quantify the effect of experimental conditions compared to the gas composition. The change in experimental conditions lead to significant variations of the UV-Visible absorption properties of these haze analogs. In addition, the incorporation of nitrogen in the solid has a similar effect on the absorption properties. The effect of nitrogen is however not limited to the UV-Visible range. It also influences the absolute absorption, mirrored in the k values of the refractive indices, in the MIR through the amine and aliphatic features. This new cross-laboratory comparative study showed that the experimental conditions have a dominant impact on the refractive indices in the UV-Visible range. In the IR, the refractive indices are mainly affected by the presence/absence of nitrogen in the gas mixture. It is rather difficult to imagine

changing freely and independently several experimental parameters such as the energy distribution of the source (irradiation spectrum) and the amount of time the gas spends in the reactive medium (residence time). There are however ways to change irradiation by varying the voltage of the plasma discharge for example. More work is needed in the future to assess the effect of irradiation alone, without changing the residence time. The refractive indices data provided in this thesis have already clear implications that should be tested in future modelling work. For habitable words, the strong variations of absorption in the UV-Visible range likely has a significant impact on the temperature profile in the atmosphere and on the surface temperature. Hazes produced with and without nitrogen have clearly different absorbing properties in the MIR. Future work should assess the detectability of the different features for hazy exoplanet atmospheres. Since the production rate and micro-physical evolution are also crucial to characterize the extinction of hazes in exoplanet atmospheres, more experimental work is needed to assess the role of oxygen on the gas phase chemistry and more specifically on the haze precursors. To better quantify the production rate of haze particles as a function of gas composition in atmospheric models, more experimental work is needed to understand the correlation between the gas phase chemistry and the growth of aerosols. The challenge is to identify a clear experimental procedure and strategy that can provide data useful in modelling and retrieval frameworks.

My work on the photochemistry of CO_2-H_2 atmospheres revealed a strong correlation between the abundance of high-altitude water vapor and the bulk density of molecular hydrogen. For a C-H-O system, the analysis and interpretation of the results helped identify the dominant chemical network for these worlds. This detailed analysis help simplify the problem and provide general trends that can be used in complex models and help interpret observations. My study is a proof of concept for a simple gas mixture still representative of secondary atmospheres expected around exoplanets (and early Mars). In the future, the same procedure can be applied to more complex mixtures to better understand the various chemical pathways controlling the evolution of secondary atmospheres since exoplanets can exhibit a broad diversity of atmospheric composition. Another perspective is to assess in details the detectability of the wapor vapor signatures above the cloud layer and identify the conditions needed for its detection (stellar radius,

atmospheric temperature, vertical extension of cloud layer, etc). This would require a thorough analysis with retrieval models.

For warm rocky exoplanet atmospheres (temperature between 400 and 1600K approximately), our reasoning is quite different. The atmospheric composition is less sensitive to evolution caused by plate tectonics and the carbon cycle or condensation/evaporation cycles. The characterization of the atmospheric composition can thus provide crucial information on its origin. Secondary atmospheres are formed by geochemical outgassing, the composition is mainly controlled by the redox state of the planetary interior quantified with the oxygen fugacity. In this scenario, relative molecular abundances of simple species (e.g. CO_2, CO, H_2O or CH_4) retrieved from JWST observations can help constrain the redox state of the planetary interior. During my PhD, I explored the parameter space in a complex 1D atmospheric model including radiative transfer, atmospheric chemistry and geochemical outgassing to assess the bias caused by atmospheric chemistry (photochemistry and equilibrium chemistry). The latter is indeed modifying the initial state of the atmosphere set by geochemical outgassing. I particularly focused on the effect of atmospheric temperature, pressure and mixing. I mainly conclude that an accurate retrieval of CO_2/CO from observations can help constrain interior oxygen fugacity (fo_2) efficiently despite the effect of atmospheric chemistry. The bias caused by atmospheric chemistry should remain below a factor of 2-3 in most cases. Since the presence of CO might be difficult to infer from observations, we find CO_2/CH_4 to be a better indicator of oxygen fugacity although methane abundances will likely be undetectable for $fo_2 \geq$ IW. The accumulation of CH_4 to detectable abundances requires a low redox state and the presence of a surface pressure and temperature high enough to have reasonably low timescales of thermochemistry (T $\geq$ 700-800K). For lower temperatures, photochemistry has a more significant effect although the timescales needed to change relative molecular abundances above the order of magnitude is very long (several hundreds of thousands of years). Since the theory tells us that these relative molecular abundances contain a lot of information, it is now time to perform an assessment of detectability and accuracy with retrievals. The accuracy of the retrieved relative molecular abundances should be assessed in details since it's affected by both the error bar of the current data and the model degeneracies.

In this thesis, I report experimental and modelling results pointing to interesting atmospheric tracers (gas or aerosols) that can provide important information on the planet's surface conditions and the atmosphere's properties. Now remains the need to perform sensitivity studies with retrieval models to ensure that the data quality and the correlation between model parameters does not introduce large errors that could affect the outcome of the retrieval and bias our interpretation.